

Numerical Simulation of Biomimetic self-healing cementitious materials

PhD Thesis



Sina Sayadi

School of Engineering, Cardiff University

September 2024

For my dearest sister and my mom
Thank you for your infinite love and support

Acknowledgements

This journey would not have been possible without the advice, help, support, and guidance of the people who accompanied me throughout this project. It is my pleasure to acknowledge their contributions and support.

I would like to thank my main supervisors at Cardiff University. I am deeply grateful for their invaluable and continuous support during my PhD. I was fortunate to have Prof. Tony Jefferson and Dr. Iulia Mihai on my supervisory board. In particular, I would like to thank them for their help and understanding during difficult times.

I am grateful for the fruitful and amazing experiences I had during my secondments in Delft and Milan. Special thanks to Prof. Erik Schlangen and Liberato Ferrera for hosting me. The wonderful research group atmosphere provided me with a great opportunity to explore and enhance my research. Prof. Frank Dehn, thank you for hosting me at KIT and for sharing your insights and advice on the design aspects of this research.

As a member of the SMARTINCS project, I met and became friends with fantastic people from all over the world, for which I extend my special thanks to the SMARTINCS consortium. I enjoyed every moment of my time during training, collaborations, and conferences with each of the ESRs: Yasmina, Clair, Mert, Harry, Suelen, Shan, Gabriele, Niranjan, Vaness, Pardis, Kiran, Davide, and Lais, as well as our project manager, Tim.

Thanks to all the people in our office at Cardiff University for the good times, technical discussions, and great coffee breaks: Amrit, Louis, Shahram, Ahmad, Zebang, Ziang, Nirthiha, Aymen, and Ebrahim. A special thanks goes to my research associate colleagues and friends, Brubeck, Cristina, and Evan, for the excellent collaboration. I am so grateful to have you as my colleagues and friends.

I acknowledge the financial support from the SMARTINCS project, an EU Horizon 2020 research and innovation program under the Marie Skłodowska-Curie grant agreement no. 860006. I also acknowledge the support of the Supercomputing Wales project, which is part-funded by the European Regional Development Fund (ERDF) via the Welsh Government.

Finally, I would like to thank my parents and my sister for their unconditional love and support. Without their encouragement, I would not be where I am today. Thanks to my sister Maryam for all the love and chats, whether online or in person, which provided a much-needed distraction.

A final special thanks goes to my mum, Narges, who has given me her immense love and support. Every single step of my life and any accomplishment would not have been possible without her.

Sina, June 2024

Table of Contents

_Summary	i
_List of Symbols.....	iii
Chapter 1 Introduction	1
1-1 Overall aims and objective.....	2
1-2 List of publication.....	2
1-2-1 List of journal papers.....	3
1-2-2 List of conference paper	3
1-3 Outline of the thesis.....	4
Chapter 2 Modelling self-healing concrete: a state-of-the-art review.	7
2-1 Self-healing cementitious materials.....	8
2-2 Mechanistic models for cementitious composite materials.....	9
2-2-1 Elastic moduli of composite materials	10
2-2-2 Mechanical behaviour of cementitious composite materials	16
2-3 Review of theoretical framework for modelling self-healing	27
2-3-1 Continuum damage healing mechanics and micromechanics	27
2-3-2 Discrete crack-healing methods.....	32
2-4 Coupled Multiphysics models	36
2-5 Discussion.....	39
Chapter 3 Lattice beam method	41
3-1 Introduction	41
3-2 Lattice beam network model	41
3-3 Standard LBM fracture model.....	46
3-4 Progressive damage.	47

3-4-1	Incremental damage	49
3-5	Time dependent healing	50
3-5-1	Damage-healing solution algorithm	53
3-5-2	Formulation for 1D case.....	55
3-6	Computational solution parameters	57
3-7	Model calibration	58
3-8	Illustrative damage healing responses for different uniaxial strain paths	58
3-9	Examples based on experiments	60
3-9-1	Direct tensile test	60
3-9-2	3-Point bending test.....	63
3-10	Additional applications of the Lattice model	65
3-10-1	Mesostructure effect on fracture characteristics	66
3-10-2	A study on microcapsule activation	69
3-11	Conclusions	73
Chapter 4	Micromechanical model	75
4-1	Introduction	75
4-2	Micromechanical formulation for microcracking and healing.....	76
4-3	Directional microcracking	76
4-3-1	Microcrack evolution function	78
4-4	Healing simulation	81
4-4-1	Time dependent healing evolution	84
4-4-2	Healing strain computation.....	87
4-5	Numerical implementation	92
4-5-1	Calibration	95
4-6	Volumetric response	96

4-7	Single point simulations	97
4-7-1	Parametric study	99
4-7-2	Microencapsulated uniaxial test	101
4-8	Conclusions	102
Chapter 5	Finite element implementation and boundary value problems.....	105
5-1	Introduction	105
5-2	Finite element implementation	106
5-3	Numerical examples and model validation.....	107
5-3-1	One-element illustration.....	108
5-3-2	Petersson test.....	110
5-3-3	3-point bending test CA	116
5-3-4	3-point bending test vascular	123
5-3-5	Encapsulated self-healing_ Lattice vs micromechanics	129
5-4	Conclusions	135
Chapter 6	Conclusion and recommendations for future work.....	137
6-1	Discussion and conclusions.....	138
6-2	Recommendations for future work.....	140
_	References.....	143
_Appendix A	Elastic tensors component.....	165
_Appendix B	Eshelby tensor.....	166
_Appendix C	weights and corresponding direction for numerical integration.....	167
_Appendix D	Tensorial notation	169

List of Figures

Figure 2-1 Different types of self-healing systems, a) micro encapsulated self-healing, b) vascular network.....	9
Figure 2-2. Constraint strain derivation procedure involving the cutting and welding method.....	11
Figure 2-3 Multiscale homogenization method for estimating concrete elastic moduli. (Reproduced from (Bernard et al., 2003; Pichler & Hellmich, 2011; Sanahuja et al., 2007))	13
Figure 2-4 Passing parameter used in Lattice simulation (reproduced from Qian et al. (2017)).....	13
Figure 2-5 Schematic methodology adopted by Quayum et al. (2015) for hierarchical homogenization.	15
Figure 2-6. Effect of microcapsules dosage on mechanical properties, a) Young's modulus, b) tensile strength, c) compression strength	16
Figure 2-7 Discontinuity consideration in displacement formulation, a) strong form in displacement, b) weak form of discontinuity, c) strong jump in strain and d) strain corresponding the weak form of displacement discontinuity.	17
Figure 2-8 Schematic micromechanical approaches for microcrack simulation	18
Figure 3-1 Illustration of the LBM, a) 2D lattice network with elements and Voronoi cells, b) 3D Lattice structure and c) an element in 3D space	42
Figure 3-2. Effect of randomness on Lattice mesh, a) randomness=0.5 , and b) no randomness.....	43
Figure 3-3 Lattice meshing example for heterogenous system, a) irregular inclusions, and b) embedded microcapsules.....	45
Figure 3-4 Stepped softening approach. a) schematic procedure and b) the softening representation of the considered materials in this study.....	49

Figure 3-5 Comparison of classical and incremental damage model for Lattice beam method, a) Force-deformation, and b) stress-strain.....	50
Figure 3-6 Schematic illustration of healing for a partial damaged element, a) partially damaged element at time of healing, and b) healed element.	54
Figure 3-7 Sequence stiffness regain due to rate dependent healing procedure.	55
Figure 3-8 Schematic procedure for fracture process in Lattice.....	56
Figure 3-9 Schematic procedure for healing implementation in the Lattice.....	56
Figure 3-10 Constitutive behaviour of self-healing materials derived with the enhanced Lattice model, a) boundary conditions, b) $\sigma_{av}-\epsilon_{nom}$ curves for single healing scenario, c) $\sigma_{av}-\epsilon_{nom}$ curves for re-healing re-damaging scenarios and d) Lattice mesh at different phases of healing	59
Figure 3-11 Experimental arrangement for notched cube tests Selvarajoo, et al. (2020), a) 3D schematic representation, b) front view and c) section view.....	61
Figure 3-12 Boundary condition and mesh configuration, a) mesh and boundary conditions and b) perspective 3D view of the mesh, and c) Multilinearised segmented behaviour for set-wise damage.....	61
Figure 3-13 Numerical simulation results for stress-CMOD of the DT series tests, a) loading protocol, b) stress-CMOD for DT-300 test and c) Stress-CMOD for DT-600 test...	62
Figure 3-14 Damage and healing patterns for DT-600 test, a) damaged state at CMOD=0.1mm, b) curing phase at CMOD=0.1mm. and c) fully healed phase at CMOD=0.1mm.	63
Figure 3-15 Experimental setup for notched beam tests, a) 3D schematic view, b) front view and c) beam section.	63
Figure 3-16 Notched beam test simulation results, a) SF-120 test results, b) SO series with loading rate 0.0005mm/s and c) SO series with loading rate 0.002mm/s.	64
Figure 3-17 Crack pattern and system phase in deformed state, a) damaged state CMOD 0.075 mm, b) healed phase CMOD 0.12mm and c) re-damage-re-healed CMOD 0.2mm. (all deformations are magnified for clarity)	65

Figure 3-18 Meso structure configuration with different geometry, a) $v_f=29.26$ and b) $v_f=31.2$	66
Figure 3-19 Boundary condition and mesh resolution illustration.....	67
Figure 3-20 Stress-displacement curve for a) irregular shape inclusion, b) circular, and c) mix of polynomial	68
Figure 3-21 Crack pattern and propagation with different microstructure.....	68
Figure 3-22 Schematic illustration of microcapsules within the cementitious matrix. a, b and c 1%; d, e and f are 3% volume fraction.	70
Figure 3-23 Maximum healing probability for different capsules arrangement	71
Figure 3-24 Average of maximum healing probability for different capsules volume fraction	72
Figure 3-25 Percentage of capsules breakage for different arrangement.....	72
Figure 4-1 Schematic representation of RME. a) Coordinate system: b) illustration of microcracked (left) and partially healed (right), material states.	76
Figure 4-2 Microcracking strain surface, b) parallel set of microcracks	79
Figure 4-3 Microcracking evolution response with respect to different material parameters.....	80
Figure 4-4 RME behaviour under different microcrack configurations, a-c) microcracking alignment, d-f) compliance matrix variation for different microcracking alignments, and g-f) corresponding constitutive behaviour.....	81
Figure 4-5 Curing function illustration, a) different τ , and b) different healing activation times.....	84
Figure 4-6. schematic representation of material states in successive microcracking and healing cycles.	87
Figure 4-7 Illustration of stress-strain responses and stress changes during a healing increment, in global and local coordinates according to the method of Davies & Jefferson (2017).....	89

Figure 4-8 Stress state at healing step for fully microcracked and fully unloaded case..	89
Figure 4-9 Comparing the difference in responses between method with modification factor and without.	92
Figure 4-10 Volumetric stress-strain response	97
Figure 4-11 Computed uniaxial responses, a) variation of stress with time, b) re-microcracking variables.....	98
Figure 4-12 Microcracking and healing vectors evolution, a) virgin microcrack b) virgin healing, c) re-microcrack for single healing and d) re-microcracking-re-healing-re-microcracking variables for multiple healing case	99
Figure 4-13 Parametric study results.....	100
Figure 4-14 Experimental validation, a) loading protocol, b) stiffness recovery comparison	102
Figure 5-1 8 node hexahedral element	106
Figure 5-2 The boundary condition for the single element example, a) tension uniaxial, b) confined compression, and c) uniaxial compression	109
Figure 5-3 Responses computed with one finite element for a range of tension and compression loading paths	110
Figure 5-4 Petersson's direct tension test setup a) dimensions and boundary conditions, b) finite element mesh (all dimensions in this figure are in mm).....	111
Figure 5-5 Numerical and experimental average stress-displacement responses for the Petersson's experiments	112
Figure 5-6 Original microcracking distribution, a) elevation view at top displacement equal to 0.002mm, b) displacement equal to 0.01mm, c) displacement equal to 0.04mm, and d) localised damage	113
Figure 5-7 Load path and stress-displacement curve, a) load path, and b) stress-displacement curve for the crack-healing case.....	114
Figure 5-8 Healing state at different prescribed displacements at the top of the specimen, a) 0.04 mm, b) 0.055, c) 0.07, and d) 0.076 mm.....	115

Figure 5-9 Re-microcracking variables distribution at different prescribed displacement, a) elevation view for 0.05 mm, b) elevation view for 0.06mm, and c) 3D isometric view for 0.07mm	116
Figure 5-10 a) beam geometry and boundary conditions, b) finite element mesh	117
Figure 5-11 Mesh convergency test with different number of elements, a) 336, b) 972, c) 1452, d) 2160, and e) Force-deflection response.	118
Figure 5-12 Experimental and numerical control beam responses, a) Load v CMOD response, b) microcracking variables at a CMOD of 150	119
Figure 5-13 Force-CMOD response for WCAD samples (a-c) and WCAW (d-e), a)reference sample loading unloading curve, b) reloading process with healing, c) magnified illustration of (b), d)reference loading-unloading for WCAW, e)reloading with healing and f) magnified illustrating of (e)	120
Figure 5-14 Force-CMOD response for samples with CA cured in dry (CAD) (a-c) and wet conditions (d-e) (CAW), a) reference sample loading-unloading curve, b) reloading process with healing, c) magnified illustration of (b), d) reference loading-unloading for CAW, e) reloading with healing and f) magnified illustrating of (e)	120
Figure 5-15 Healed material status after reloading a) healing at CMOD=275 μm , b) re-damage at CMOD=310 μm c) re-damage at CMOD=350 μm , d) overlapping damage and healing illustration, and e) the force-CMOD for CAW	122
Figure 5-16 Rob's test setup (Davies et al., 2021) , a) dimension and boundary conditions, and b) mesh	123
Figure 5-17 Comparing the course and fine mesh response.....	124
Figure 5-18 Force-CMOD curve for self-healing cases.....	126
Figure 5-19 Matrix damage variables at different CMOD, a) 50 μm , b) 100 μm , and c) 200 μm	127
Figure 5-20 Healing and re-microcracking variables at different CMOD, a) 250 μm , b) 290 μm , and c) 300 μm	128

Figure 5-21 Boundary condition and meshing type, a) structured mesh, and b) Dulaney triangulation.....	129
Figure 5-22 Considered RVE for: a) computational microstructure, b) Lattice mesh in the highlighted region	130
Figure 5-23 Uniaxial responses, a) MM approach, and b) Lattice approach.....	131
Figure 5-24 The rendering of the crack pattern generated by morphological operations at the collapsed stage, a) without the operation, and b) after the operation.....	132
Figure 5-25 Crack pattern and microcracking variable (ω_1) distribution at different strains level, a) Lattice method at $\varepsilon=0.00005$, b) Lattice method at $\varepsilon=0.00015$, c) MM method at $\varepsilon=0.00005$ and d) MM method at $\varepsilon=0.00015$	133
Figure 5-26 The crack pattern after healing and re-microcracking variables. a) MM method at $\varepsilon=0.0002$, b) MM method $\varepsilon=0.0003$ c) Lattice method at $\varepsilon=0.0002$, and d) Lattice method $\varepsilon=0.00025$	134
Figure C-1 Schematic numerical points, a) 3D figure, b) direction and weight for numerical integration.....	168

List of Tables

Table 2-1 Methods for considering microcracks through Eshelbian approach.	21
Table 2-2 Methods for considering cracking using Budiansky and O'Connell approach (direct).....	24
Table 2-3 Different configuration for considering discrete crack.	26
Table 2-4. Different configuration for considering healing.....	31
Table 2-5. Methods and configuration for simulating triggering process	33
Table 2-6 Summary of existing models for capturing mechanical regain due to healing mechanism.....	35
Table 2-7 Coupled modelling approaches.	38
Table 3-1 Mechanical properties	50
Table 3-2 Material properties for uniaxial example test	59

Table 3-3 Experiment details and the material properties used for modelling.	60
Table 3-4 Cementitious matrix and aggregate properties.....	67
Table 3-5 Material properties*	70
Table 4-1 RME characteristics used for simulation in Figure 4-4.....	80
Table 4-2 Mechanical parameter for controlling the stress-free condition	88
Table 4-3. material properties for the volumetric model.....	96
Table 4-4 Material properties	97
Table 4-5 Material properties for parametric study	100
Table 4-6 Material properties	101
Table 5-1 Summary of the numerical example details	108
Table 5-2 Material properties used as an input for EX_1.	109
Table 5-3 Peterson specimen material input.....	111
Table 5-4 Material properties for EX-3	117
Table 5-5 Mechanical properties	125
Table 5-6 Material mechanical properties.....	130
Table D-1 Tensorial notation.....	169

Summary

The biomimetic approach to enhance the performance of material has been attracting attention for decades, especially in cementitious materials such as concrete, in which they have shown promising results in terms of mechanical recovery after damage. The crack healing process is multiscale in nature and involves various mechanical and chemical mechanisms, which need to be taken into account in order to accurately predict the behaviour of these materials. Two distinct frameworks are chosen to represent the rate-dependent crack-healing effect on the mechanical characteristics of self-healing materials. The discrete Lattice approach and micromechanical model are employed. The former represents the explicit random distribution of self-healing meso and microstructures, whilst the latter gives an overall form of constitutive behaviour of the system. The new micromechanical model simulates self-healing rate dependency as well as allowing for healing under loaded conditions. Moreover, continuous cycles of crack-healing and their effect on the mechanical performance of self-healing materials were considered through a novel micromechanical framework which satisfies the second thermodynamics law. The proposed constitutive formulation was implemented in the Cardiff finite element code Cardinal for simulating boundary value problems. The Lattice approach, on the other hand, includes element-level healing and considers the damage-healing effect on the updated overall stiffness matrix as well as the healed element. This method provides detailed information on fracture process zones and associated crack-healing regions. A range of self-healing scenarios and systems were simulated in this study and the proposed numerical methods were successfully validated against experimental data.

List of Symbols

A	Beam element cross section area
\mathbf{A}^{dill}	Dilute strain concentration
a	Representative material area
a_h	Healed portion of Representative material are
a_ω	Cracked portion of representative material area
\mathbf{B}	Shape functions derivatives matrix
\mathbf{C}^{eff}	Effective compliance tensor of a composite material
\mathbf{C}_L	Crack plane compliance tensor of original material
\mathbf{C}_m	Matrix fourth order compliance tensor
\mathbf{C}_{Lh}	Crack plane compliance tensor of healed material
c	Microcrack evolution constant
\mathbf{D}	Original material elastic stiffness tensor
\mathbf{D}^{eff}	Effective equivalent composite stiffness matrix
\mathbf{D}_L	Local elastic tensor
\mathbf{D}_{Lh}	Local healed elastic tensor
\mathbf{D}_m	Matrix elastic tensor
\mathbf{D}_{sec}	Secant stiffness tensor
\mathbf{D}_{sech}	Healed secant stiffness tensor
\mathbf{D}_Ω	Inclusion stiffness tensor
E	Young modulus
E_0	Initial elastic modulus
E_h	Healing material elastic modulus
E_i	Secant elastic moduli in step-wise damage method
\mathbf{f}	Nodal force vector in global coordinate
f	Crack density parameter
f_Ω	Inclusion volume fraction
F_ζ	Directional micro-cracking function
f_b	Body force
f_c	Compressive strength of original material
f_t	Tensile strength of original material
f_{th}	Tensile strength of healed material
f_{ti}	Tensile strength for first microcracking initiation
\mathbf{f}_{uh}	Internal force vector after healing
$\hat{\mathbf{f}}$	Local nodal force vector
$\hat{\mathbf{f}}_h$	Healed element force vector
G	Shear modulus
H_{pr}	Healing probability
h_r	Re-healed portion
h_v	Healed portion
\mathbf{I}^{4s}	Symmetric part of fourth order identity tensor
I	Second moment of inertia
i	Time step index
\mathbf{j}	Matrix flux
j	Microcracking direction index
\mathbf{K}	Element stiffness matrix

\mathbf{K}_{G0}	Initial element stiffness matrix in global coordinate
$\mathbf{K}_{G\omega}$	Damaged element global stiffness matrix
\mathbf{K}_h	Healed stiffness matrix
$\mathbf{K}_{\omega h}$	Updated global stiffness matrix during a damage-healing cycle
$\hat{\mathbf{k}}_0$	Undamaged local stiffness matrix
$\hat{\mathbf{K}}_\omega$	Damaged stiffness matrix
$\hat{\mathbf{K}}_h(t)$	Element healing matrix at time t
$\hat{\mathbf{K}}_{h\infty}$	ultimate healing matrix
L	Element length
M	Bending moment
\mathbf{N}	Stress transformation tensor
\mathbf{N}_ε	Strain Transformation tensor
N_i	Shape function of node i
N	Axial force
\mathbf{n}	Crack plane surface normal vector
n_j	Total directional microcracking integration points
r, s, t	Local coordinate system
P	pressure
q	Internal shear force
q_s	Interface shear strength to matrix tensile strength
Q	Shear force at boundaries
r	Crack radius
\mathbf{s}_L	Local stress tensor
\mathbf{s}_{Lh}	Local stress tensor after healing
\mathbf{S}	Eshelby fourth order tensor
t	Time
t_c	Current curing time
t_{c0}	Healing initiation time
u_o	Displacement at the end of softening
u	Nodal displacement
\mathbf{u}	Displacement field
\mathbf{u}_h	global healed displacement vector
$\hat{\mathbf{u}}$	Local displacement vector
$\hat{\mathbf{u}}_h$	Local healed displacement vector
$\dot{\mathbf{u}}$	Velocity
x	Position in continuum medium
α	Microcrack interaction modification factor
α	Normal force influence factor
β	Moment influence factor
Δ	Increment symbol
Δh	Healing increment
Δt	Time increment
$\bar{\varepsilon}$	Far field strain tensor
ε	Strain tensor
ε_{ah}	Total additional healed strain
ε_L	Local strain tensor
ε_{Lh}	Local healed strain tensor

$\boldsymbol{\varepsilon}_\alpha$	Additional strain due to a microcrack
$\boldsymbol{\varepsilon}_a$	Total additional strain
ε	One dimensional Strain variable
ε_0	Strain at fully microcracked state
ε_t	Strain at first microcrack
η	Local coordinate of an isotropic element
κ	Shear factor in Timoshenko beam
μ	Shear modulus ratio in micromechanical model
μ_s	Friction angle between matrix and aggregate
ν	Poisson ratio
ξ	d
ρ	Material density
Σ	Summation of discrete number operator
$\boldsymbol{\sigma}$	Stress tensor
$\bar{\boldsymbol{\sigma}}$	Far field stress tensor
σ	One dimensional stress variable
ζ	microcracking strain parameter
ζ_{heff}	Effective microcracking strain for healed material
τ	Curing constant coefficient
ϕ_h	Curing degree
ϕ_{he}	Healing efficiency
ψ, θ	Spherical coordinate reference angle
ϕ_h	Curing degree
ϕ_{he}	Healing efficiency
$\boldsymbol{\Psi}$	Potential energy
Ω	Continuum domain
ω	Microcracking variable
ω_h	Re-microcracking variable
ω_{heq}	Equivalent re-microcracking variable
$\bar{\omega}$	Average damage parameter

Chapter 1

Introduction

Cementitious materials, owing to the energy intensive methods used in their production and their widespread use, are a significant contributor to global carbon emissions. The most widely used cementitious material is concrete but this material is susceptible to cracking because of its relatively low tensile strength. This susceptibility gives rise to durability problems which can either reduce the lifespan of a structure or necessitate frequent maintenance interventions. The associated environmental and economic impacts of such required repairs are substantial. Furthermore, conventional repair practices disrupt the normal function of a structure, e.g., cause traffic congestion due to a full or partial concrete bridge closure.

To tackle these issues, researchers have drawn inspiration from nature and developed biomimetic solutions for the production of cementitious materials (De Belie et al., 2018). This innovative approach has the potential to detect and repair damage in cementitious structures in a way that is akin to the regenerative properties observed in biological tissues and bones. Despite the novelty and interest surrounding the self-healing concept, it is currently applicable only in specific cases and remains far from practical implementation on a large scale.

Understanding and modelling self-healing behaviour is one of the challenges facing researchers. Despite several studies dedicated to developing models for self-healing phenomena (Jefferson et al., 2018), much work needs to be undertaken before such models are ready for engineers to apply to real structures. Therefore, the development of a robust, physically based model applicable across a broad spectrum of scenarios is essential. Such a model would empower engineers to incorporate this technology into the design of their structures.

1-1 Overall aims and objective.

The main objectives and aims of this study are listed below:

- Understanding the mechanisms and physics associated with self-healing processes in quasi-brittle materials.
- Finding a tractable mathematical formulation to represent microcracking in self-healing cementitious materials.
- Developing a 3D micromechanical formulation which represents time dependent mechanical regain due to the self-healing action.
- Enhancing the developed formulation for multiple damage-healing cycles and overlapping damage-healing conditions.
- Implementing the developed formulation in a 3D finite element program to simulate boundary value problems and model structural elements made with biomimetic self-healing materials.
- Enhancing the Lattice beam model to simulate self-healing action in the context of discrete crack-healing mechanisms.
- Simulating self-healing problems with Lattice model to investigate the microstructural effects on the self-healing response and studying the fracture process zone during damage-healing event.
- Validating and assessing the performance of the proposed numerical frameworks against experimental data available from previous work.
- Investigating the possibility of incorporating the proposed model into design codes.

1-2 List of publication

Throughout this PhD and research journey, the primary findings and methodology presented in Chapters 3, 4, and 5 have been disseminated through publications in international journals. Additional results have also been shared in international conferences. The following is a list of journal articles and conference papers:

1-2-1 List of journal papers

- Sayadi,S., Chang,Ze., Shan,H., Schlangen,E., Mihai,I., Jefferson, AD. "*An enhanced lattice beam element framework for numerical simulation of rate-dependent self healing processes in cementitious materials*" <https://doi.org/10.1016/j.engfracmech.2023.109632>.

Under review papers

- Sayadi,S., Mihai,I.,Jefferson,AD. "*Rate dependent self-healing model for composite cementitious materials*. International journals of solids and structure (2024).
- De Nardi,C., Sayadi,S., Mihai,I., Jefferson, AD. "*Simulation of autogenous self-healing in lime-based mortars*". Numerical and Analytical Methods in Geomechanics (2024).

1-2-2 List of conference paper

- Sayadi,S., Ricketts,E., Schlangen,E., Cleall,P., Mihai,I., Jefferson, AD. "*Effect of microstructure heterogeneity shapes on constitutive behaviour of encapsulated self-healing cementitious materials*". MATEC Web Conf. Volume 378, 2023, <https://doi.org/10.1051/mateconf/202337809004>.
- Shan,H., Sayadi,S., Chang,Ze., Schlangen,E., Jefferson., Mihai,I. "*Experimental validation of a discrete lattice model for simulating mechanical regains in a vascular self-healing cementitious material*". 8th International Conference on Self-Healing Materials ICSHM Politecnico di Milano, Milan, Italy,
- Sayadi,S., Chang,Ze., Shan,H., Schlangen,E., Jefferson., Mihai,I. "*Microcapsules triggering probability in self-healing cementitious material: A parametric study*". 8th International Conference on Self-Healing Materials ICSHM Politecnico di Milano, Milan, Italy,
- Sayadi,S., Jefferson,AD, Mihai,I. "*Time dependent micromechanical self-healing model for cementitious material.*" Edited by R. Maddalena and M. Wright-Syed (2021): 105.",RM4L2020 International Conference.
- Sayadi,S., De Nardi,C., Jefferson,AD, Mihai,I, Gardner,D. " *Enhanced micromechanical formulation for capturing permanent strain in lime materials*" UK association for computational mechanics University of Nottingham, Nottingham,UK.

- Sayadi,S., Davolio,M., Al Obaidi,S., Ferrara,L., Mihai,I., Jefferson,AD. " *Constitutive formulation for self-healing fibre-reinforced concrete*" UK association for computational mechanics, Warrick University, Warrick, UK.

1-3 Outline of the thesis

This thesis is structured into six main chapters. Within these chapters, comprehensive information and details pertaining to existing models for capturing the constitutive behaviour of self-healing systems are presented. Additionally, the procedural aspects leading to the development of formulations and approaches proposed in this research are thoroughly discussed.

Chapter two presents a comprehensive review of the models for capturing the mechanical behaviour of self-healing cementitious materials. It elucidates two primary mechanistic approaches for mathematically describing the fracture process in cementitious materials. The chapter also highlights several studies dedicated to capturing mechanical regain resulting from the healing process. In this review, the state of the art in self-healing modelling is discussed, and the primary research gaps identified. The chapter underscores the need for a reliable, widely applicable model to capture realistic self-healing actions in cementitious materials with sufficient accuracy.

One of the novel approaches reported in this research is presented in chapter three. The methodology, formulation, development and numerical implementation of the model are described in this chapter. The chapter outlines the enhancement of the TUDelft Lattice framework to capture rate-dependent damage-healing cycles in cementitious materials. The model introduced in this chapter provides a valuable tool for simulating self-healing behaviour at the structural level. This is further expanded in Chapter 5 by the exploration of a micro encapsulated self-healing composite material.

In Chapter Four, another framework which provides a continuum representation of crack-healing effects on mechanical properties of the system, is introduced. This chapter details the development of a 3D micromechanical method designed to capture rate-dependent damage-healing mechanisms. It specifically explores the suitability of this formulation for capturing mechanical regain in diffuse crack-healing systems, such as materials with embedded microcapsules. The theoretical formulation is presented and the

ability of the model to capture multiple and overlapping damage-healing cycles is assessed. Furthermore, a numerical framework is introduced to tackle the computational challenges associated with thermodynamic consistency.

The implementation of the model in a finite element framework is described in detail in Chapter 5. This chapter explains how the new material is added to a hexahedral element for simulating boundary value problems. The behaviour of a number of experiments are replicated in this chapter. Finally, for a heterogenous microstructural case, the responses provided by the Lattice approach and micromechanical approach are presented and compared in this chapter.

Finally, conclusions derived from each of the preceding chapters are summarised in Chapter 6. This chapter describes the main outcomes of this research in the context of the overall aims and objectives. Recommendations for future work are discussed at the end of this chapter.

Chapter 2

Modelling self-healing concrete: a state-of-the-art review.

In this review the essential developed concepts and theories alongside the efforts that have been made to model self-healing cementitious materials (SHCM) are discussed. This section emphasises models that follow mechanistic approaches. Many studies have explored different aspects of self-healing cementitious materials. These studies covered a vast range of topics from experimental investigations to analytical and numerical modelling. Some of these studies were focused on macroscopic response whilst others explored microlevel processes in these systems. This chapter presents a brief overview of self-healing concepts in cementitious materials. An overview of self-healing concepts alongside different types of self-healing and associated mechanisms are discussed in section 2-1. Section 2-2 explains mechanistic-based approaches for modelling mechanical behaviour of cementitious materials. In this section, the main focus is on understanding and modelling the cracking process and its effect on compliance tensors, strength and constitutive formulations. The section reviews the methods and formulations that shaped current research methodologies. After addressing the damage process, section 2-3-2 explains different self-healing frameworks, with a focus on mechanistic approaches. Section 2-4 highlights challenges and new problems in modelling self-healing systems and finally a discussion (section 2-5) is given in which research gaps are identified.

2-1 Self-healing cementitious materials

Most construction materials, specifically those being used for carrying and resisting significant loads, are susceptible to cracking and damage. These reduce structural and material durability (Cappellesso et al., 2023) and result in degradation of structural performance, as well as a reduction in longevity and safety. The desire to produce materials with a better functionality under harsh conditions, and to tackle durability concerns linked to cracking in brittle materials, has led scientists to come up with the idea of mimicking the self-healing abilities of biomaterials (W. Zhang et al., 2020). For cementitious materials, as discussed comprehensively in review articles by the UGent university team (Li et al., 2018; Van Tittelboom & De Belie, 2013), self-healing is defined as sealing the crack and regaining the lost mechanical properties. Self-healing systems in cementitious materials are categorized as either autogenous or autonomous self-healing. The self-healing action that happens due to the cementitious system's intrinsic self-healing capability is called autogenous self-healing. The other self-healing category (autonomic) involves external materials and devices being embedded in the original matrix. Healing is provided by external materials that participate in the healing action (Joseph et al., 2011). Some specific self-healing systems include microencapsulation (Xue et al., 2019), vascular network (Shields et al., 2021), bacteria based (Luhar et al., 2022) and fibre-reinforced self-healing systems (Wu et al., 2012). Numerous experimental investigations have been conducted to comprehend the mechanisms underlying each of the self-healing systems mentioned above. Some of these studies are focused on characterizing the properties of self-healing materials, while others explore the self-healing mechanisms (De Belie et al., 2018; Ferrara et al., 2018). From a modelling perspective, it is crucial to identify and understand the mechanisms involved in damage-healing cycles. The first step in this identification process is assessing the impact of self-healing material components on the initial mechanical properties of the system. The second involves studying the mechanical behaviour of the system, including crack formation and the overall response of the system prior to the healing activation. The third encompasses the healing itself, which is a multi-physics process often associated with chemo-transport processes and the restoration of mechanical properties. For different self-healing systems, these mechanisms are schematically illustrated in Figure 2-1.

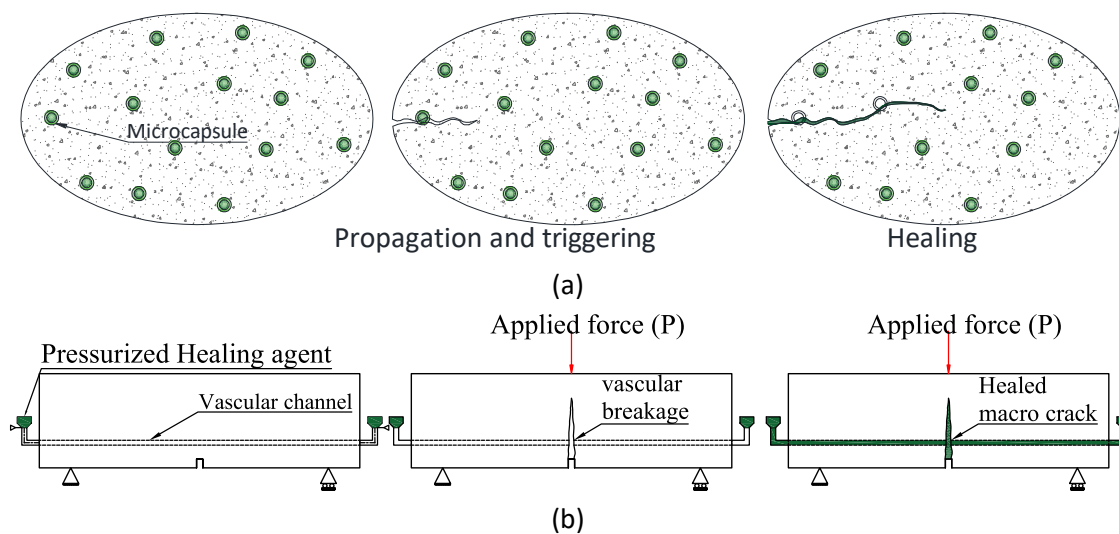


Figure 2-1 Different types of self-healing systems, a) micro encapsulated self-healing, b) vascular network.

The aforementioned mechanisms might occur at different lengths scales, and these also depend on the type of self-healing system. The microstructure of self-healing systems is influenced by the corresponding healing mechanisms. Hence, despite the existence of many macroscopic constitutive frameworks for modelling cementitious materials such as plasticity and damage mechanics (Luhar et al., 2022), which are based on phenomenological assumptions, mechanistic approaches are used in the current research to capture the behaviour of self-healing systems.

2-2 Mechanistic models for cementitious composite materials

The overall response of cementitious composite materials is based on micro-scale mechanisms. These characteristics, which encompass the initial properties and potential microcracking, need to be accounted for in the constitutive formulation (van Mier, 2017). The behaviour of these materials depends on the microstructural properties and the mechanical processes that take place at microscale level. Multiscale approaches provide effective tools for considering the role of each individual constituent in the response of the system (Van der Giessen, 2019). These approaches either model each process and constituent at lower scales explicitly and then pass information to the upper scale, as is the case in multiscale analysis finite element and Lattice procedures, or they employ homogenization techniques through micromechanical formulations.

The methods for estimating the overall elastic moduli of composite materials as well as their application for microencapsulated self-healing cementitious materials are presented in section 2-2-1. Section 2-2-2 summaries constitutive models for cementitious materials and explains both discrete and continuum frameworks respectively.

2-2-1 Elastic moduli of composite materials

Typically, at the mesoscale, cementitious composite materials have two main phases, namely, the cementitious matrix and aggregate. The cementitious matrix, which may be considered at the microscale, consists of different phases such as hydrated clinker, unhydrated particles and pores. The make-up of these phases greatly influences the mechanical properties of the overall cementitious composite.

The micromechanical approach provides a bridge between different length scales. It allows the macroscopic response to be computed from information provided by microconstituent properties through homogenization schemes (Böhm, 1998; Van der Giessen, 2019). Different methods have been developed for estimating the overall properties of composite materials including upper and lower bound approaches (Reuss, 1929; Voigt, 1889), Hill's theory (Hill, 1965). Eshelby (Eshelby, 1957, 1959) derived a closed form formulation to calculate the response of an elastic medium with an inclusion. Later, for systems with multiple inclusions like systems with heterogeneity, some approximation methods, in which the homogenisation approach is used, were proposed. These homogenisation methods include Mori-Tanaka (Mura, 1982), self-consistent, Ponte-Castaneda and Willis schemes ((Mura, 1982), Nemat-Nasser & Hori, 2013). The choice of the most suitable technique depends on the type of heterogeneity and the distribution of inclusions.

The basic Eshelby solution (Eshelby & Peierls, 1957) is illustrated in Figure 2-2. This shows that if a subregion inside a matrix experiences a spontaneous deformation, it would no longer fit in its original space and will experience a constraint strain which is uniform inside the inclusion. The relationship between this eigen strain and constraint strain is defined with a fourth order constant tensor \mathbf{S} introduced by Eshelby. This tensor depends only on the shape of the inclusion and its elastic properties.

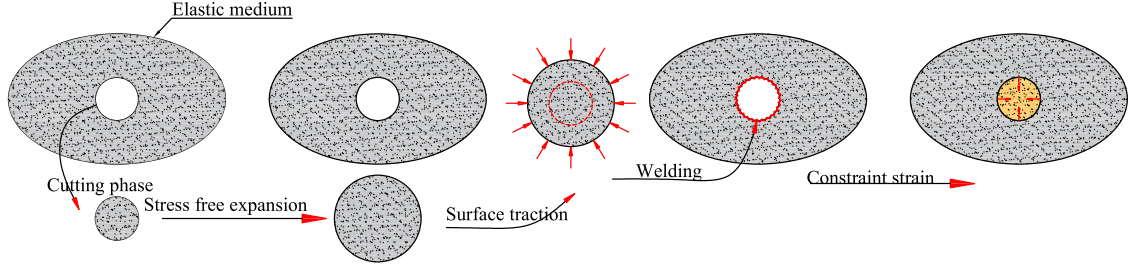


Figure 2-2. Constraint strain derivation procedure involving the cutting and welding method.

The averaging theory gives an analytical formulation for estimating the overall properties of composite systems. For a two-phase dilute composite system, in which the interaction between inclusions is negligible, the effective stiffness matrix is calculated by the following equation (Benveniste, 1987).

$$\mathbf{D}_{\text{eff}} = \mathbf{D}_m + f_{\Omega}(\mathbf{D}_{\Omega} - \mathbf{D}_m) \cdot \mathbf{A}^{\text{dill}} \quad (2.1)$$

in which \mathbf{D}_{eff} , \mathbf{D}_m , f_{Ω} , \mathbf{D}_{Ω} , and \mathbf{A}^{dill} are equivalent composite stiffness, matrix stiffness, inclusion volume fraction, inclusion stiffness and dilute strain concentration tensors respectively. The strain concentration tensor for a two-phase matrix inclusion system is as follows:

$$\mathbf{A}^{\text{dill}} = [\mathbf{I}^{4s} + \mathbf{S} \cdot \mathbf{C}_m \cdot (\mathbf{D}_{\Omega} - \mathbf{D}_m)]^{-1} \quad (2.2)$$

where \mathbf{I}^{4s} is the symmetric part of the fourth order tensor, \mathbf{S} is the Eshelby tensor, and \mathbf{C}_m is the matrix elastic compliance tensor which equal to \mathbf{D}_m^{-1} . The derivation of the above-mentioned tensors is given in the Appendix A and Appendix B. Some approximative solutions have been developed for non-dilute cases, in which the interactions between inclusions are non-negligible. These approximate methods are generally categorized into effective field and medium approaches. One of the most straight forward methods is the Mori-Tanaka approach (Benveniste, 1987; Mori & Tanaka, 1973). In this method, a double inclusion system with inclusions denoted Ω_1 and Ω_2 , where Ω_1 includes Ω_2 , and this inclusion is subjected to a uniformly eigenstrain is considered. These inclusions are within an infinite domain named Λ . It is observed that the volume average ($\langle \cdot \rangle_v$) of the strains and stresses induced by the Ω_2 over the subtracted domain ($\Omega_1 - \Omega_2$) is zero. As a result, the average far field stress or strain is replaced by the matrix average strain or stress tensor. Equation (2.3) shows the resulting effective stiffness matrix of a two-phase system.

$$\mathbf{D}_{\text{eff}} = \mathbf{D}_m + [f_{\Omega}(\mathbf{D}_{\Omega} - \mathbf{D}_m) \cdot \mathbf{A}^{\text{dill}}] \cdot [(1 - f_{\Omega})\mathbf{I}^{4s} + f_{\Omega}\mathbf{A}^{\text{dill}}]^{-1} \quad (2.3)$$

The second group of mean-field estimates for overall mechanical properties of composite materials have been named effective medium approaches. In these approaches, it is assumed that the inclusions are embedded in effective field for which the properties are not known in advance. Classical and generalized self-consistent scheme are the most important types of homogenization scheme within this category (Mura, 1982). As shown in the equation (2.4) the effective properties derived through an iterative procedure.

$$\mathbf{D}_{\text{eff}} = \mathbf{D}_m + f_{\Omega}[\mathbf{D}_{\Omega} - \mathbf{D}_m] \cdot [\mathbf{I}^{4s} + \mathbf{S}^{\text{eff}} \cdot \mathbf{C}_{\text{eff}} \cdot (\mathbf{D}_{\Omega} - \mathbf{D}_{\text{eff}})]^{-1} \quad (2.4)$$

where \mathbf{S}^{eff} is the Eshelby tensor of inhomogeneities embedded in the effective medium and $\mathbf{C}_{\text{eff}} = \mathbf{D}_{\text{eff}}^{-1}$. For cementitious matrices, researchers have employed micromechanical formulations to estimate the overall elastic properties of the cement matrix from microstructural properties. (Achour et al., 2020; Bernard et al., 2003; Königsberger et al., 2017, 2020; Nguyen-Sy et al., 2020; Pichler & Hellmich, 2011; Sanahuja et al., 2007). The procedure for multiscale homogenization used in these studies is illustrated in Figure 2-3 for a model that considers hierarchical homogenisation assuming spherical inclusions (Bernard et al., 2003). Later, detailed images derived from electron microscopic devices, revealed that hydrate products are needle shaped. Sanahuja et al. (2007) applied a modification to achieve a more realistic simulation and a better prediction of representative material element properties at different scales. Figure 2-3 illustrates some specific homogenisation techniques along with the scales and configurations considered. This figure illustrates how different researchers used homogenisation methods to link lower scales (micro or nano) to higher scales (meso or macro). Mostly, the Mori-Tanaka scheme is applied to cases that have a dominant matrix phase and clearly distinct inclusions. The self-consistent scheme tends to be used for configurations with multiple phases where no one particular phase is dominant (Bernard et al., 2003; Pichler & Hellmich, 2011).

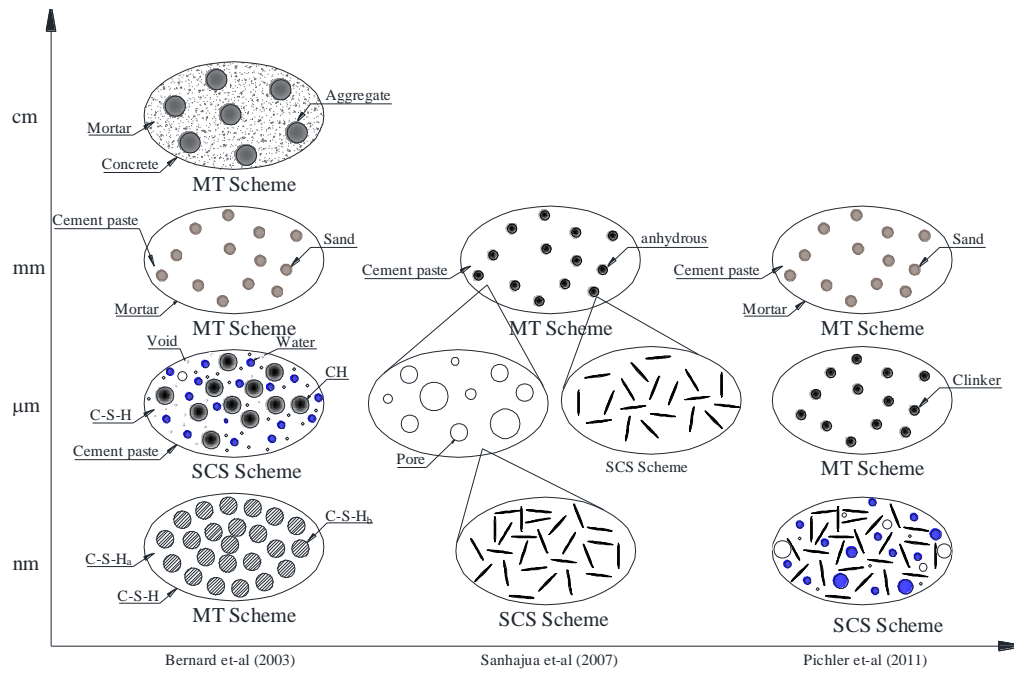


Figure 2-3 Multiscale homogenization method for estimating concrete elastic moduli. (Reproduced from (Bernard et al., 2003; Pichler & Hellmich, 2011; Sanahuja et al., 2007))

The homogenization approach provides a computationally convenient method for multiscale analysis. Alternative approaches have been explored in a few studies. For example, Qian et al. (2011, 2017) employed the lattice method for multiscale analysis. The authors established a parameter passing methodology (see Figure 2-4) for modelling multiscale integrated systems such as cement paste, mortar and aggregate. They used their method to simulate a uniaxial tensile test specimen and thereby derive the mechanical properties at each scale. For a more accurate response, the solution derived from a lower scale should undergo an additional multiscale homogenisation to bridge between the different scales.

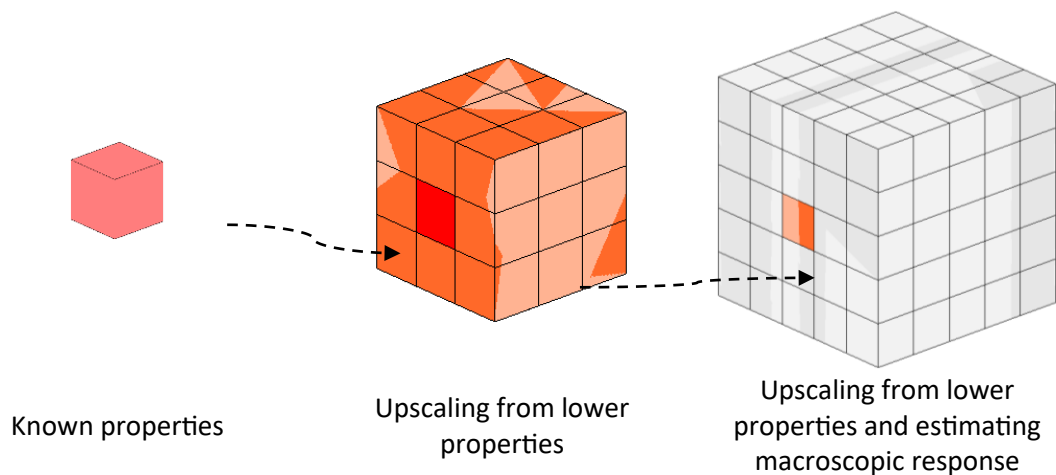


Figure 2-4 Passing parameter used in Lattice simulation (reproduced from Qian et al. (2017))

Whilst the homogenization techniques were used for the macroscopic responses of cementitious composite, some studies followed the same method for microencapsulated self-healing systems (Ahmed & Sanada, 2019; Kanellopoulos et al., 2016; Li et al., 2016; Quayum et al., 2015; Zhou et al., 2020). Concrete, at mesoscale, inherently is a two-phase composite heterogeneous material. Introducing microcapsules filled with healing agent transforms it into a multiphase composite material. Such inhomogeneous materials comprise a variety of sub-materials at different scales.

Wu et al., (1997) and Yang et al., (2007) employed both analytical and experimental methods to examine the influence of microcapsule inclusions on the initial properties of the cementitious matrix. The studies indicated that inclusions within the matrix can lead to a reduction in overall mechanical properties, resulting in stress concentrations and anisotropic behaviour. Abaimov et al. (2019) obtained the overall mechanical properties of a representative volume of multiphase material using the hierarchical approach, which is essentially a multistep homogenization scheme. They also compared their results with the one-step homogenisation technique and check the accuracy of those methods against the experimental data. They found that for the overall elastic properties using multistep procedure for system with the higher volume of fraction led to a better approximation.

The initial elastic properties of a self-healing cementitious system were estimated using a linear micromechanical model by Quayum et al. (2015). They utilised a two-step homogenisation technique (see Figure 2-5) to determine the elastic properties of cementitious composites containing embedded microcapsules. They also examined the impact of volume fractions of different constituents and the size of the Representative Volume Element (RVE). The results were compared with finite element solutions, leading to the conclusion that further research on the application of linear homogenisation, as well as further experimental investigations for validation, were necessary to address these issues.

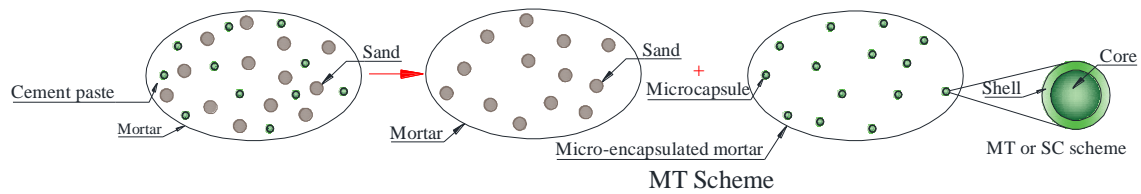


Figure 2-5 Schematic methodology adopted by Quayum et al. (2015) for hierarchical homogenization.

In an experimental-numerical study, Li et al. (2016) investigated the effect of adding spherical microcapsules to a concrete matrix on the elastic properties of SH concrete. Using Eshelby theory and assuming that cracks are randomly positioned over the medium with uniform orientation, and that the healing agent only flowed to the cracks because of capillary action, they studied the dependency of matrix parameters on self-healing mechanical behaviour. This also included the portion of cracks to be potentially healed. They showed that crack healing could cause more anisotropy as the load increases. By measuring the amount of water absorption on a pre-cracked sample they realized that cracks were healed partially and not fully.

Later, Ahmed & Sanada (2019) treated the cores and shells of microcapsules as separate matrix-inclusion systems. They undertook the same hierarchical averaging procedure for the cement-capsules system and for the matrix-inclusion system. They assumed that each material phase behaved as an elastic isotropic material. They compared experimental data with the results from a series of finite element analyses of an RVE consisting of microcapsules and cementitious composite matrix. They showed that their proposed analytical model can predict the elastic properties of encapsulated self-healing systems. They claimed that some parameters especially shell elastic modulus effect on effective elastic properties is insignificant up to a certain limit of volume fraction. However, according to the Mori-Tanaka scheme the inclusion mechanical parameters is explicitly included in the formulation. The authors conclusion was due to the fact that they normalized their results and they needed to examine different types of microcapsules with different properties. As expected, the results showed that the elastic property of the composite system is dependent on the volume fraction of capsules. Following this research, Zhou et al. (2020) investigated the global sensitivity of polymeric microcapsules in a self-healing cementitious composite. They used an Extended Fourier Amplitude Sensitivity test to find the most influential parameters on the effective properties of SHCM materials. They

concluded that identifying the most influential parameters should lead to more precise prediction. They showed that the volume fraction of capsules is the most sensitive parameter, and that the effect of interfacial interaction could not be ignored. Figure 2-6 shows the variation of matrix properties with changing microcapsule volume fractions. The results of the different homogenization techniques are also compared in this Figure.

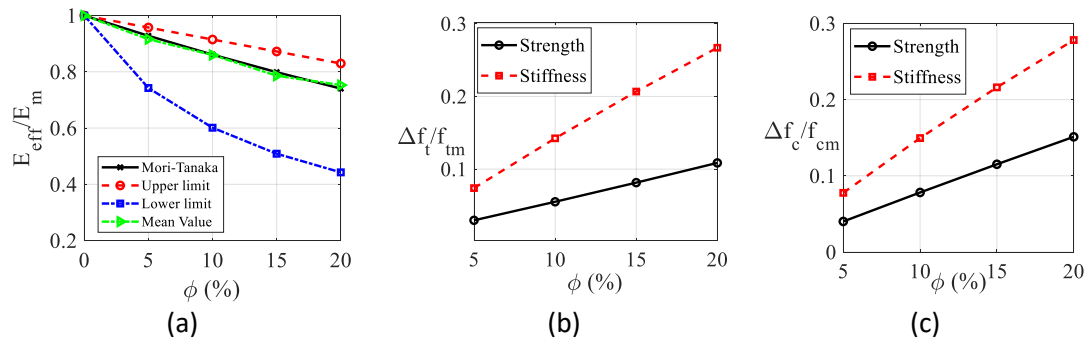


Figure 2-6. Effect of microcapsules dosage on mechanical properties, a) Young's modulus, b) tensile strength, c) compression strength

2-2-2 Mechanical behaviour of cementitious composite materials

The mechanical behaviour of materials, such as cementitious, rock, ceramics and most composites, is classified as quasi-brittle (Cornelissen et al., 1985; Labuz et al., 1985; Van Mier & Van Vliet, 2001). These are typically heterogenous materials composed of brittle constituents in which some of them have a lower tensile strength than others. Consequently, the failure mode in these materials is attributed to degradation and fracture of those weak brittle phases. In contrast to ductile materials, they don't have significant strain hardening, and often exhibit a marked softening response after reaching the ultimate strengths (Huang & Karihaloo, 1993).

There are many studies on the macroscopic modelling of fracture of quasi-brittle materials through both smeared and discrete approaches (Rashid, 1968; Rots et al., 1985; Rots & Blaauwendraad.,1989). The choice between employing a smeared or discrete method for capturing fracture processes is contingent upon the specific nature of the process under consideration, and opinions vary on which is the superior approach (Borst et al., 2004; Cervera & Chiumenti, 2006; Jendele et al., 2001; Noghabai, 1999; Willam & Carol, 2014). With the discrete category, a discontinuity may be represented by a strong jump in the displacement field within a cracked element or by a soft displacement transition function to represent a weak form of discontinuity, as depicted in Figure 2-7.

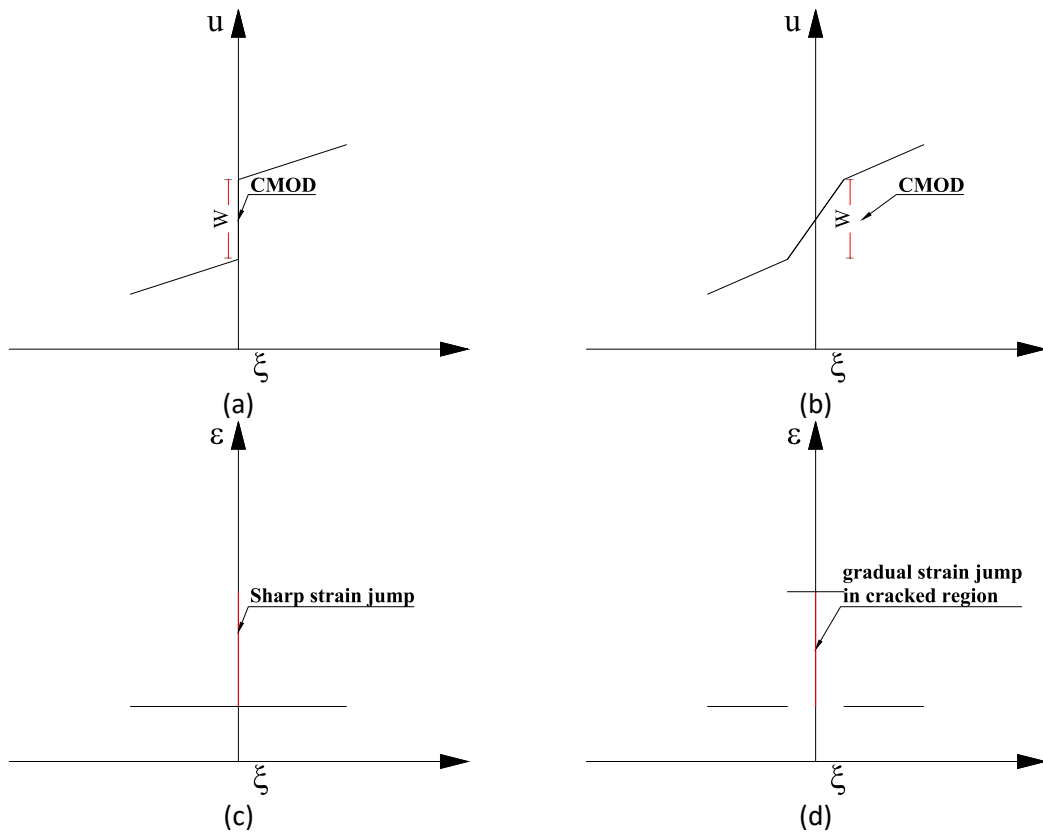


Figure 2-7 Discontinuity consideration in displacement formulation, a) strong form in displacement, b) weak form of discontinuity, c) strong jump in strain and d) strain corresponding the weak form of displacement discontinuity.

The earliest model for simulating damage in quasi-brittle materials, especially cementitious ones, based on micromechanical principles, originated from the work of Bazant's team (Bazant, 1984; Bažant et al., 1984; Bazant et al., 1991; Bažant & Oh, 1983) between 1980 and 1990. He introduced the concept of the microcrack plane, wherein the microcracks are distinctively aligned with an arbitrary plane (Caner & Bažant, 2013). Ortiz (1985 and 1988) employed homogenisation techniques, incorporating the role of microcracks as a degradation mechanism coupled with a plasticity formulation, to enhance the representation of concrete behaviour in the compression regime. In this model, the additional macroscopic strain energy is derived from the average strain energy, as noted in equation (2.5). This is computed using information from all active microcrack planes.

$$\bar{\boldsymbol{\sigma}} : \bar{\boldsymbol{\varepsilon}} = \int_{\Omega} \boldsymbol{\sigma}(\mathbf{x}) : \boldsymbol{\varepsilon}(\mathbf{x}) d\Omega \quad (2.5)$$

where $\bar{\boldsymbol{\sigma}}$ and $\bar{\boldsymbol{\varepsilon}}$ are far field averaged stress and strain derived from stress and strain tensor over the Ω domain.

In the homogenization scheme, the influence of microcracks on the overall elastic moduli of cementitious system is calculated through two primary methods. The direct method, which involves adding the effect of microcracks directly to the constitutive formulation. This method introduced by (Budiansky and O’Connell 1976) for estimating overall moduli of elastic solid with microcracks defects (Nemat-Nasser & Hori, 1993), has been subsequently adopted and refined by numerous researchers. Particularly, it has been used for the development of constitutive models for cementitious materials (Davies & Jefferson, 2015, 2017; A. Jefferson & Bennett, 2007; I. C. Mihai & Jefferson, 2011, 2017). The second approach involves employing the classical two phase Eshelbian formulation, treating the microcracks as ellipsoidal void inclusions with zero stiffness properties. However, employing the Eshelbian solution for estimating the overall behaviour of microcracked medium encounters difficulties. Following the initiation of multidirectional cracking, the isotropic medium changes into an anisotropic medium, consequently, the initial standard Eshelby tensor is not valid anymore and an iterative procedure for the calculation of the Eshelbian tensor at each microcracking event is required. Figure 2-8 shows schematically the procedure for deriving the effective properties of quasi brittle materials with microcracks through the direct and Eshelbian approaches.

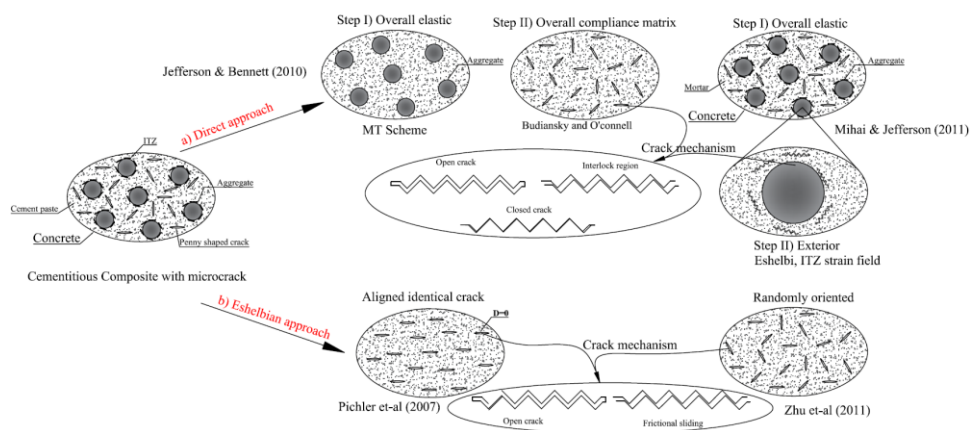


Figure 2-8 Schematic micromechanical approaches for microcrack simulation

For quasi-brittle materials, (Pensée et al., 2002) formulated both direct and Eshelbian approaches to determine the influence of microcracking on overall system properties. They showed that, taking the crack interactions into account might be a complex process and involve difficulties since it requires the numerical computation of the Eshelby matrix every time the crack density parameter changes in any direction. Later on, Q. Zhu et al.

(2008) studied the effect of microcracks on effective properties using various homogenization schemes. They proposed equations for calculating overall elastic moduli. These equations are applicable to both open and closed crack conditions. Following the decomposition method, the overall macroscopic strain was derived through homogenising the strain field over the decomposed domains of closed and open cracks. Equation (2.6) shows this process mathematically.

$$\bar{\boldsymbol{\varepsilon}} = \frac{1}{\Omega} \int_{\Omega} \boldsymbol{\varepsilon}_c(\mathbf{z}) d\Omega + \boldsymbol{\varepsilon}_m \quad \forall \mathbf{z} \in \partial\Omega \quad (2.6)$$

in which $\boldsymbol{\varepsilon}_c(\mathbf{z})$ represents the strain tensor at the domain boundary containing microcracks. $\boldsymbol{\varepsilon}_m$ denotes the uniform strain across the matrix. It was suggested that due to the spatial distribution of microcracks, the interaction between them is captured more accurately through the homogenisation technique suggested by Ponte Castañeda (2002) (PCW scheme) rather than the Mori-Tanaka (Q. Zhu et al., 2008). This is because in Mori-Tanaka's scheme, the homogenization procedure is solely a function of the crack density parameter. The PCW scheme considers the interaction of sliding and damage evolution in a constitutive relationship derived from the following thermodynamic potential:

$$\Psi = \frac{1}{2} (\bar{\boldsymbol{\varepsilon}} - \bar{\boldsymbol{\varepsilon}}_c) : \mathbf{D}_m : (\bar{\boldsymbol{\varepsilon}} - \bar{\boldsymbol{\varepsilon}}_c) - \frac{1}{2\Omega} \int_{\Omega} \boldsymbol{\varepsilon}_m : \mathbf{D}_m : \boldsymbol{\varepsilon}_c d\Omega \quad (2.7)$$

In this equation, Ψ is potential energy, $\bar{\boldsymbol{\varepsilon}}_c$ is the average strain of medium containing open crack.

Similarly, Pichler et al. (2007) employed Eshelby's inclusions principle, treating microcracks as empty inclusions. They assumed that the microcracks within an RVE are penny-shaped cracks with identical size and orientation. To predict brittle behaviour, they integrated classical fracture mechanics with micromechanics.

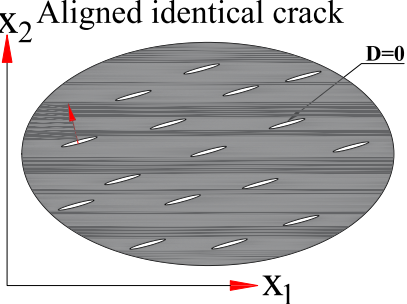
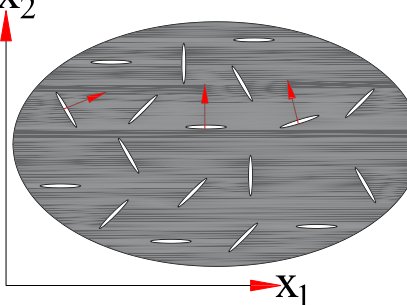
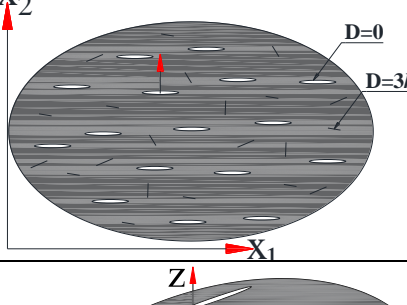
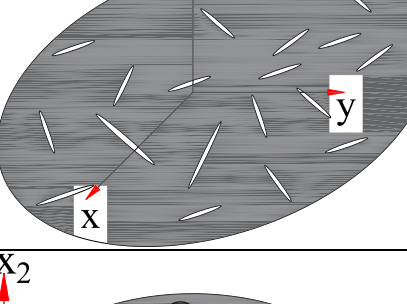
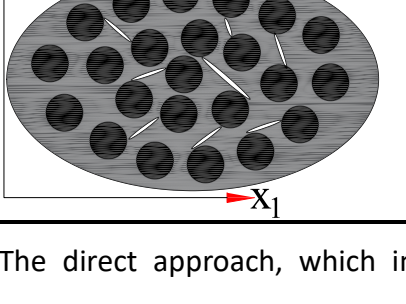
To enhance their former approach, Zhu et al. (2009) developed an anisotropic damage model based on a homogenization scheme. They utilized the thermodynamic framework for damage evolution function proposed by Pensée et al. (2002). Subsequently, they proposed a simplified method for an isotropic case, assuming a uniform distribution of

microcracks. In this way they derived the homogenized stiffness tensor for an isotropic damage case (Zhu et al., 2011).

In another study, Levasseur et al. (2015), formulated a micromechanical model that coupled the material initial anisotropy and the damage-induced anisotropy while accounting for ‘unilateral’ (crack closure) effects of evolving microcracks. They employed a thermodynamic framework to derive the model variables from a micromechanical free energy closed-form equation. They showed that their 2D model can capture the initial anisotropy and damage growth in argillite material with good accuracy compared to experimental data from uniaxial tensile tests. This model was extended to 3D by Zhu & Shao (2015) Zhu & Shao (2015). They determined the free enthalpy of representative element volume consisting of a family of randomly oriented penny shaped microcracks based on the Mori-Tanaka homogenisation scheme. The aforementioned methodologies and approaches, along with their schematic configurations, are summarised in Table 2-1.

It is important to note that in the current study, a representative volume element (RVE) was assumed to characterize the average elastic properties of the composite. However, its validity becomes highly questionable once macrocracking occurs. Gitman et al. (2007) demonstrated that, in the context of cracking, the concept of an RVE loses its significance. Therefore, in this study, the term ‘representative material element’ (RME) is used to describe an RVE specifically for elastic properties.

Table 2-1 Methods for considering microcracks through Eshelbian approach.

Configuration	Methods and results	Assumptions	references
 <p>Aligned identical crack</p>	<ul style="list-style-type: none"> • MT • Decomposition • Frictional and sliding cracks 	<ul style="list-style-type: none"> • No crack interaction • 2D formulation • Uniformly distributed cracks 	(Pensée et al., 2002; Zhu et al., 2008)
	<ul style="list-style-type: none"> • PCW • Crack interaction • Coupling of crack sliding and damage evolution 	<ul style="list-style-type: none"> • Homogenous material • Uniform stress • 2D formulation • Spatial distribution 	(Pichler et al., 2007; Zhu et al., 2009)
	<ul style="list-style-type: none"> • PCW • Closed crack effect on stiffness • Coupled formulation 	<ul style="list-style-type: none"> • Crack interaction • 2D formulation • Uniform direction 	(Zhu et al., 2011)
	<ul style="list-style-type: none"> • PCW • Friction and sliding 	<ul style="list-style-type: none"> • Homogenous material • Uniform stress • 3D formulation • Random orientation 	(Zhu & Shao, 2015)
	<ul style="list-style-type: none"> • MT and PCW • Spherical inclusions for aggregate 	<ul style="list-style-type: none"> • Crack interaction • 2D formulation • Randomly oriented directions • Cracks formed between inclusions 	(Levasseur et al., 2015)

The direct approach, which involves incorporating the additional directional strain (Equation (2.8)) resulting from microcracks, allows for the calculation of the overall homogenised cracking medium. A notable advantage of the direct is its ability to

circumvent the need for numerical solutions in evaluating the Eshelby tensor for anisotropic cases (Deseumaux, et al., 2001).

$$\varepsilon_{\alpha} = \frac{\mathcal{N}_c}{r^3} \int_{\partial\Omega} \mathbf{n} \otimes [\mathbf{u}] + [\mathbf{u}] \otimes \mathbf{n} dS \quad (2.8)$$

where \mathbf{n} is crack plane surface normal vector, $[\mathbf{u}]$ is the crack opening displacement vector and \mathcal{N}_c is the number of cracks within RME.

The direct approach has been investigated by many authors (Mura, 1982; Němeček et al., 2013; Pensée et al., 2002) and yields a 3D anisotropic damage model for estimating the effective elastic solid moduli with combined penny-shaped open and closed cracks. Feng et al. (2004), combined the micromechanical framework and phenomenological approach to capture the behaviour of quasi-brittle materials. They proposed a quasi-micromechanical model that characterises microcracks using two terms: the orientational domain of microcrack growth and a scalar crack density parameter representing the isotropic part of the damage. Additionally, they proposed an approximation to account for microcrack interactions on overall elastic moduli and compared their results with effective field and effective medium approaches.

Jefferson & Bennett (2007) followed a mechanistic approach to derive a micromechanical formulation for microcracking in a cementitious materials incorporating the rough contact mechanism due to crack closure. Extending their analysis, A. D. Jefferson & Bennett (2010) enhanced their previous work to cementitious composite materials. They used Eshelby theory to simulate the aggregate phase in the cementitious materials and Mori-Tanaka to consider the interactions between inclusions for volume fractions greater than 10 percent. Building upon this foundation, I. C. Mihai & Jefferson (2011) improved the microcrack initiation criteria by employing the Eshelby exterior tensor ((Eshelby & Peierls, 1959) to compute the strain and stress fields at the boundary of the inclusions. Experimental evidence highlighted the fact that microcracking mostly occurs in interfacial transition zone (ITZ), therefore using the exterior Eshelby tensor could increase simulation accuracy and make it closer to reality.

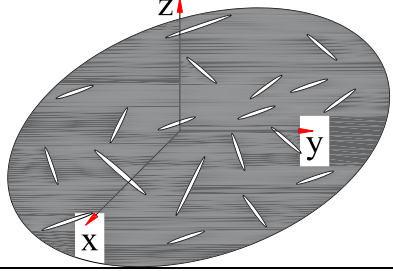
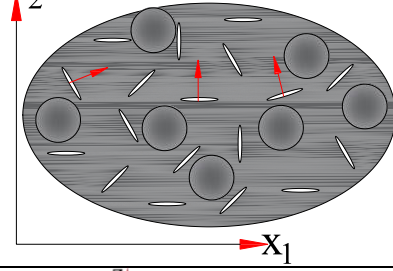
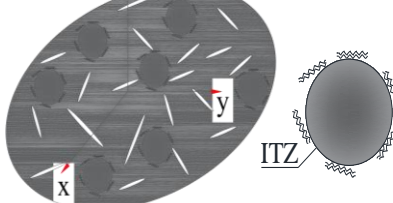
Similar research conducted to investigate the effect of the ITZ and the interaction between aggregate particles with ITZ on the macroscopic response of concrete was

undertaken by Königsberger et al., (2013a and 2013b). They derived a stress concentration tensor related to the ITZ, and assumed that cracking in the ITZ was responsible for the nonlinear stress-strain behaviour in the pre-peak regime. Considering the microstructural properties of this region, Sharma & Bishnoi (2020) showed that the ITZ properties affect the overall macroscopic response of cementitious materials. Recently, Dutta & Chandra Kishen (2018) investigated the progressive damage between matrix and inclusions. They assumed that three consecutive mechanisms happen during a damage event. Their model included microcrack propagation along the interface, kinking of the interface into the matrix, and subsequent propagation. The model was developed in 2D and the Mori-Tanaka homogenisation scheme was employed for upscaling from micro to mesoscale. In their model, the cracks were assumed to be open and arc shaped.

Following that study, Dutta & Kishen (2019) suggested a 2D micromechanical damage model considering the crack propagation within matrix using thermodynamics-based strain energy released function. They assumed the microcracks are slits that are distributed isotropically within a representative material domain. Due to uncertainty in estimation of each phase parameters, Chen, et al. (2022), followed a stochastic micromechanics-based approach to derive a constitutive formulation for cementitious materials.

The schemes for damage evolution in several studies discussed in this chapter were based on energy potentials along with yield and damage state concepts. By contrast, Jefferson & Bennett (2007) suggested that a strain-based damage formulation, which utilises an exponential function, provides a more accurate representation of the damage evolution in cementitious materials with a few parameters that have physically meaning representations. Mihai and Jefferson (2013) introduced a smoothing function to simulate gradual microcrack closure. This not only improved the accuracy of their model but also helped alleviate some numerical problems, namely 'chatter', associated with abrupt crack opening and closing behaviour. The summary of the models that employed a direct approach is presented in Table 2-2.

Table 2-2 Methods for considering cracking using Budiansky and O’Connell approach (direct)

Configuration	Methods and results	Assumptions	references
	<ul style="list-style-type: none"> • Additional strain • Adding contact 	<ul style="list-style-type: none"> • No crack interaction • Randomly distributed cracks • Homogenous medium 	(Pensée et al., 2002; Q. Zhu et al., 2008)
	<ul style="list-style-type: none"> • MT • Coupling of cracks sliding and damage evolution 	<ul style="list-style-type: none"> • Uniform stress • 2D formulation • Aligned cracks • Spatial distribution 	(Pichler et al., 2007; Q. Z. Zhu et al., 2009)
	<ul style="list-style-type: none"> • MT • Exterior Eshelby • Coupled formulation 	<ul style="list-style-type: none"> • 3D formulation • Penny shaped cracks • Standard loading-unloading condition is applied 	(Mihai and Jefferson 2013)

Despite the popularity of homogenisation schemes for predicting the mechanical response of materials, modelling the explicit formation of micro and macrocracks remains challenging problem for researchers.

Several numerical techniques have been developed to augment classical finite element formulations for capturing discontinuities within solid media arising from fracture action. The Extended Finite Element Method (XFEM) addresses displacement discontinuity by introducing an additional degrees of freedom and assigning an appropriate interpolation formulation. To mitigate mesh dependency issues, the Enriched Finite Element Method (EFEM) was devised. This method incorporates an additional displacement field to better approximate cracks through the enrichment of degrees of freedom (Feng et al., 2023).

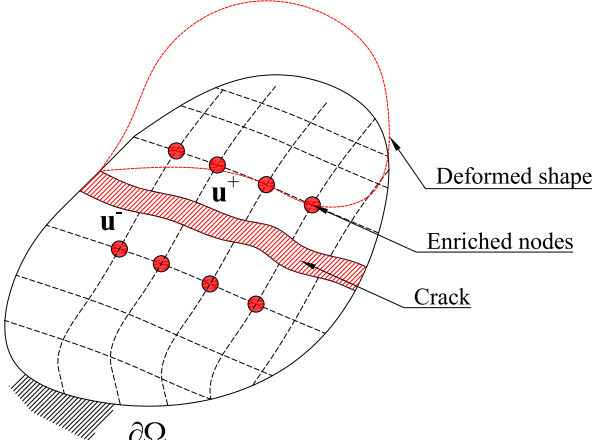
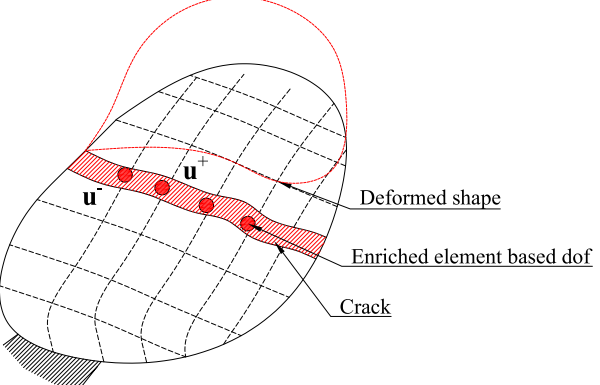
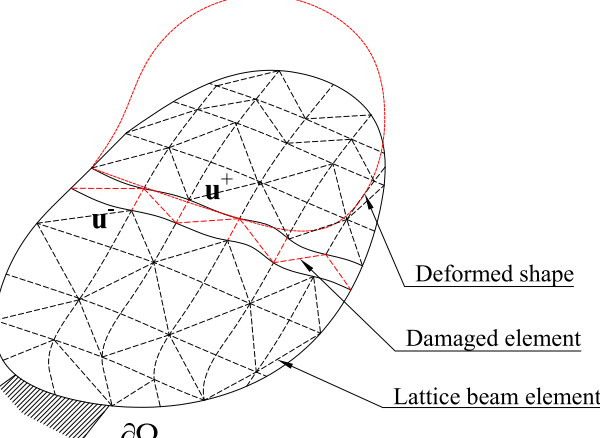
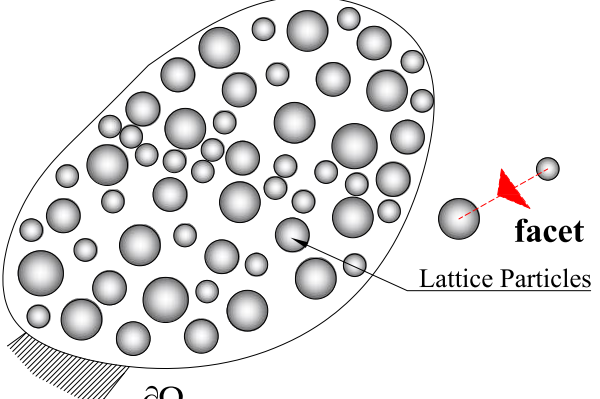
Another approach in capturing crack initiation, and propagation which is mostly applicable for quasi-brittle material is the cohesive-zone models (Alfano, 2006). It is assumed that in this zone, the tractions gradually decrease from a peak value to zero. In this zone, at microscale level, the decohesion occurs due to microcracks nucleation. The

macrocracks formation is mainly because of progressive interface damage corresponding to microcrack growth and coalescence (Alfano & Sacco, 2006).

One of the pioneering and highly effective methods employed for modelling cementitious materials at micro- and mesoscale is the Lattice approach, initially developed by Schlangen & van Mier (1992). Their initial 2D work was extended to 3D and expanded to include heterogeneous systems (Qian et al., 2011). This latter 3D version has been named the 'TUDelft Lattice model'. Other investigators have developed lattice-type approaches and there are now three main categories of Lattice model; the Lattice Spring Model (LSM) (Bolander & Saito, 1998), the Lattice Discrete Particle model (LDPM) (Cusatis et al., 2011) and the original Lattice Beam network Model (LBM) (Alessandro et al., 2018). The LBM has been used extensively to investigate fracture and transport processes in cementitious materials (Athanasiadis et al., 2018; Šavija et al., 2012; Schlangen & Garboczi, 1996; Schlangen & van Mier, 1992; Vidya Sagar et al., 2019).

Qian et al. (2017) furthered the scope of LBM models by showing that they could be used as a sub-scale model that governs the effective constitutive behaviour of an upscaled macroscopic analysis. They generated cement paste microstructures using the HYMOSTRUCT3D model (van Breugel, 1995). In some studies, the geometry and positioning of aggregate particles were determined by using X-ray computed tomography (XCT) techniques (Zhang et al., 2016, 2018). Other investigators used computational based algorithms for generating and positioning the aggregate particles; for example, Qian et al (2016) used the ANM computer model to generate a randomly positioned irregular shaped meso structure within a representative composite cementitious material. In their study, at each scale and for each phase, the mechanical properties were derived using nano indentation tests (Hu & Li, 2014). More recent work has shown that the lattice framework can successfully describe the multiphase microstructure of cement paste (Xu et al., 2022). In this work, the authors assigned material properties according to the level of hydration of each cement-paste phase and compared experimentally observed fracture processes with model results. These aforementioned studies proved the efficacy of the lattice approach for simulating damage processes at multiple scales in cementitious materials. The different approaches discussed in this chapter for capturing discrete cracking problem are presented in Table 2-3.

Table 2-3 Different configuration for considering discrete crack.

Name	Configuration	Assumptions and references
XFEM	 <p>The diagram shows a domain $\partial\Omega$ with a crack. Nodes near the crack are marked as 'Enriched nodes' (red dots). The displacement field is shown as u^+ and u^-. The deformed shape is indicated by a red outline. Labels include 'Deformed shape', 'Enriched nodes', and 'Crack'.</p>	<ul style="list-style-type: none"> • Additional degree of freedom added to the nodes • The crack initiation should be known • The accuracy of the solution is dependent on an enrichment function • Mesh density and nodal distribution near discontinuity can affect the crack path
EFEM	 <p>The diagram shows a domain $\partial\Omega$ with a crack. Elements near the crack are marked as 'Enriched element based dof' (red dots). The displacement field is shown as u^+ and u^-. The deformed shape is indicated by a red outline. Labels include 'Deformed shape', 'Enriched element based dof', and 'Crack'.</p>	<ul style="list-style-type: none"> • The displacement jump is considered through heavy side or other appropriate functions • Discontinuity intersect is considered
LBM	 <p>The diagram shows a domain $\partial\Omega$ with a crack. Elements near the crack are marked as 'Damaged element' (red dots). The displacement field is shown as u^+ and u^-. The deformed shape is indicated by a red outline. Labels include 'Deformed shape', 'Damaged element', and 'Lattice beam element'.</p>	<ul style="list-style-type: none"> • Multilateralization • Full or partial element removal to simulate damage • Mesh generated by the triangulation technique
LDPM	 <p>The diagram shows a domain $\partial\Omega$ with lattice particles. A facet is shown as a red triangle. Labels include 'facet' and 'Lattice Particles'.</p>	<ul style="list-style-type: none"> • Particles are connected by a Lattice strut • Mechanical interaction between particles is characterized by normal and shear stresses

In this research, the TUDelft Lattice beam approach was extended and enhanced to allow the explicit representation of the crack-healing process. The formulation and corresponding algorithm for the numerical implementation is fully described in Chapter 4.

2-3 Review of theoretical framework for modelling self-healing

A number of studies have been dedicated to modelling self-healing cement-based materials (SHCM). These materials comprise various phases at different length scales. Damage and healing within these materials involves several multi-physics processes. Consequently, different frameworks tailored to specific self-healing mechanisms have emerged over the past two decades. In general, there are two primary theoretical frameworks commonly used as the foundation for modelling the mechanical behaviour of self-healing systems. The first category is continuum damage healing mechanics (CDHM) (Barbero et al., 2005). This method gives the overall response of a representative material element by including damage and healing processes in the constitutive formulation. This approach mainly considers macroscopic material information. Another category is the discrete approach, in which a model is formulated in a way that considers explicitly the crack-healing process inside a discrete crack.

In section 2-3-1, CDHM related models are presented. This section explains how these models consider healing and mechanical recovery. Also, ways of including chemo-physical phenomena in these models, such as curing and transport processes, are explained. The section also discusses how former studies shaped the development of the proposed micromechanical formulation for multiscale mechanistic approach developed in this research.

Section 2-3-2 is devoted to discrete methods and their application. It explains how healing processes in discrete cracks are considered. The section also discusses the secondary problems associated with healing, such as the triggering of an embedded healing system.

2-3-1 Continuum damage healing mechanics and micromechanics

The models within the category of CDHM are constructed upon the foundation of the Continuum Damage Mechanics (CDM) framework (Voyiadjis et al., 2022). This method

offers a convenient framework for incorporating damage into quasi-brittle material models by embedding the effects of cracking within the constitutive formulation, as demonstrated by (Cervera & Chiumenti, 2006; Rots et al., 1985). CDM theory considers the effect of damage on the constitutive response by applying a damage variable, or tensor, which in this work is denoted ω (or $\boldsymbol{\omega}$, if in tensor form). The damage variable is assumed to be the ratio of damaged area (a_ω) of a representative material element to the total area (a), as noted below:

$$\omega = \frac{a_\omega}{a} \quad (2.9)$$

Extending Hooke's law (Malvern, 1969) to account for anisotropic damage gives the following stress-strain relationship:

$$\boldsymbol{\sigma} = \mathbf{D}: (\mathbf{I}^{4s} - \boldsymbol{\omega}): \boldsymbol{\varepsilon} \quad (2.10)$$

The majority of CDHM formulations consider healing in one of two ways. The first of these involves explicitly accounting for healing by incorporating the contribution of the healed material component into the original constitutive equation, as initially suggested by (Schimmel & Remmers, 2006) for a one dimensional domain. The following equation proposed by (Schimmel & Remmers, 2006) shows the stress variable in a 1D system after a single damage-healing cycle.

$$\sigma = (1 - \omega)E\varepsilon + h(1 - \omega_h)E_h(\varepsilon - \varepsilon_h) \quad (2.11)$$

where σ and ε are the 1D stress and strain variables, E and E_h are Youngs' moduli of the original material and the healed material respectively, h is the healing variable contribution which varies from 0 to 1, ω_h is the redamage variable applied to the healed material and ε_h is the healing strain variable, which makes sure that the healed material forms in a stress-free condition and allows for the permanent strain that results from healing agent curing in open cracks.

The h variable is defined as the ratio of the healed (a_h) to damaged relative areas (a_ω), as follows:

$$h = \frac{a_h}{a_\omega} \quad (2.12)$$

The second option introduces an effective damage parameter (ω_{eff}) to simulate the healing effect. Darabi et al., 2012; Voyiadjis et al., 2011, 2012 use an effective configuration and the concept of effective stress space for self-healing materials, such that the nominal strain energy is equal to the effective strain energy. To derive the constitutive formulation, they assumed the following power equivalence hypothesis:

$$\frac{\partial \sigma_{eff}}{\partial t} = (1 - \omega(1 - h))E \frac{\partial \varepsilon}{\partial t} \quad (2.13)$$

where σ_{eff} is effective stress configuration of healing state. The healing evolution function was adopted from a phenomenological equation proposed by (Mergheim et al., 2012).

The healing potential in a few studies (Abu Al-Rub & Darabi, 2012; Barbero et al., 2005) was driven by applying a thermodynamics framework to satisfy a potential energy dissipation criterion. In these studies, due to the lack of experimental data, the authors decided to consider the healing potential function in an analogous way to the damage potential function. An example potential is given in the equation below:

$$\Psi = \frac{1}{2}(\varepsilon - \varepsilon_p):D:(\varepsilon - \varepsilon_p) + \Pi_d + \Pi_p + \Pi_h \quad (2.14)$$

$$\mathbf{F}_h = \frac{\partial \Psi}{\partial h} \quad (2.15)$$

where Ψ is the potential energy, Π is a driving force potential and \mathbf{F}_h is the healing force potential. In this equation, the subscript d , p and h refer to the damaged, plasticity and healing components of the potential energy respectively.

In most of real self-healing cases, healing does not occur instantaneously. To address this challenge, Mergheim et al., (2012) and Mergheim & Steinmann (2013) proposed a method for considering healing time dependency and simultaneous damage-healing processes. They developed the following equation assuming that, during healing, the mechanical response does not change unless the strain field changes:

$$h(t) = \int_{s=t_0}^t \omega(s)\phi(s) e^{-(t-s)/\tau} ds \quad (2.16)$$

Oucif et al. (2019) looked into the super-healing concept with CDHM theory in which the material strengths increase beyond the original values. They extended the classical definition to generalized nonlinear and quadratic super healing based on elastic stiffness strengthening.

Recent efforts in modelling self-healing behaviour, employing the CDHM, reveal that the majority of these models are grounded in the frameworks developed by Voyiadjis teams. Some of these studies extended the work for healing under cyclic loading (Subramanian & Mulay, 2020). Other studies coupled the healing evolution function to a hydration degree derived from experimental data in order to represent hydration induced healing (Q. Chen et al., 2021). Shojaei & Voyiadjis (2023) introduced a statistical perspective to the CDHM framework. For modelling multiple self-healing cycles, Sanz-Herrera et al. (2019) developed a framework that assumes that healing occurs under fully unloaded conditions, allowing for the estimation of the overall material response during the multiple cycle loading history where healing initiated at fully unloaded phase at each cycle.

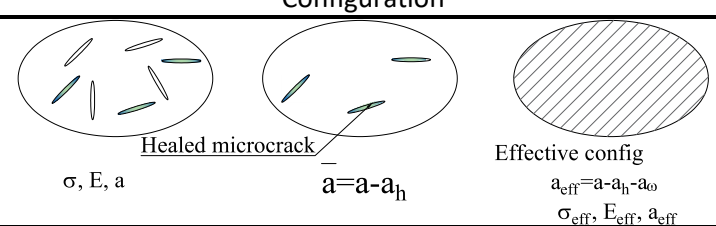
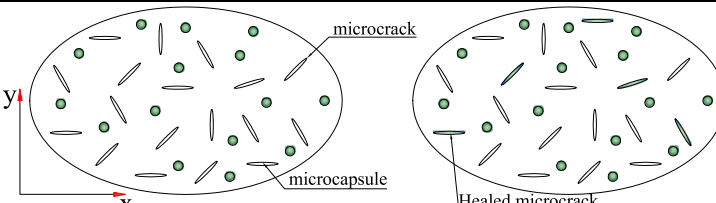
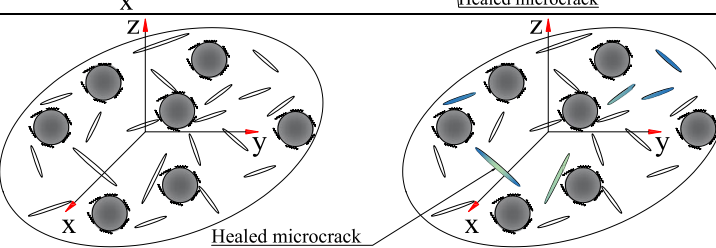
Nevertheless, a subset of these studies incorporates a mechanistic trace in their methodology, predominantly relying on experimentally informed parameters for deriving their model parameters. Additionally, a limited number of studies have endeavoured to simulate the mechanical behaviour of self-healing cementitious systems through micromechanical formulations. For instance, in the case of a dilute distribution of 2D ellipsoidal cracks, Li et al. (2016) calculated the homogenized compliance matrix of a representative self-healing material. Zhu's team employed micromechanical simulations to deduce the constitutive material behaviour. They applied a micromechanical framework in a two-dimensional space to simulate the behaviour of self-healing systems incorporating microencapsulation under both tension and compression loads (H. Zhu et al., 2015, 2016). They assumed a random distribution of microcapsules (Zemskov et al., 2011) within their representative material domain to estimate the portion of healed microcracks.

Davies & Jefferson (2017) enhanced the direct micromechanical approach to derive a constitutive formulation to represent healing in randomly distributed microcracks. Their formulation assumed that crack healing occurs in the interfacial transition zone, modelled through the Exterior Eshelbian method (Eshelby & Peierls, 1959; I. C. Mihai & Jefferson, 2011). They also assumed that healing action occurs only once and instantaneously.

In other studies, (K. Han, Ju, Zhang, et al., 2021; K. Han, Ju, Zhu, et al., 2021; T. Han et al., 2021) a 3D evolutionary micromechanical damage-healing formulation was derived to predict the healing effect by estimating the effective compliance matrix. Self-healing due to crystallization on the overall elastic moduli of cementitious materials was estimated using the homogenization technique presented by Q. Chen, Li, et al. (2022). In this study, cracks were assumed to be penny-shaped inclusions and parallel to a defined material axis. The healing process was considered to create another inclusion inside the penny-shaped cracks, leading to a double inclusion homogenization problem.

Most of these micromechanical based studies examined encapsulated self-healing systems in which the damage-healing process distributed throughout a representative volume of material. The summary of configurations used in the CDHM and micromechanics approaches discussed above are illustrated in Table 2-4.

Table 2-4. Different configuration for considering healing

Method	Configuration	References
CDHM	 <p> σ, E, a Healed microcrack $a = a - a_h$ Effective config $a_{eff} = a - a_h - a_0$ $\sigma_{eff}, E_{eff}, a_{eff}$ </p>	(Abu Al-Rub et al., 2010; Abu Al-Rub & Darabi, 2012; Darabi et al., 2012)
MM2D	 <p> microcrack microcapsule Healed microcrack </p>	(Li et al., 2016)
MM3D	 <p> Healed microcrack </p>	(Davies & Jefferson, 2017)

2-3-2 Discrete crack-healing methods

In the context of modelling healing in an open crack, the discrete modelling framework (van Mier, 2012) serves as the foundation for the development of self-healing formulations. This approach involves the explicit representation of macro cracks and simulation of healing processes, such as the transport flow of healing agents (Alsheghri & Abu Al-Rub, 2016; Ponnusami et al., 2015, 2018). There are different techniques for incorporating discrete cracks into numerical models, such as the extended finite element (XFEM) (Cervera et al., 2022), finite elements with embedded discontinuities (EFEM) (Freeman & Jefferson, 2022), cohesive elements, and lattice methods (Cibelli et al., 2022).

The discrete approach provides the option to consider the triggering mechanism of self-healing systems, offering essential insights into crack nucleation and propagation (Ponnusami et al., 2015, 2019). Ponnusami et al. (2015) employed a cohesive zone approach in 2D space to investigate the interaction between cracks and embedded microcapsules in the matrix. Their findings revealed that the main fracture mechanism results from strength and toughness mismatches between the particles and the matrix. Additionally, pre-existing defects were found to alter crack propagation, with potential implications for design applications.

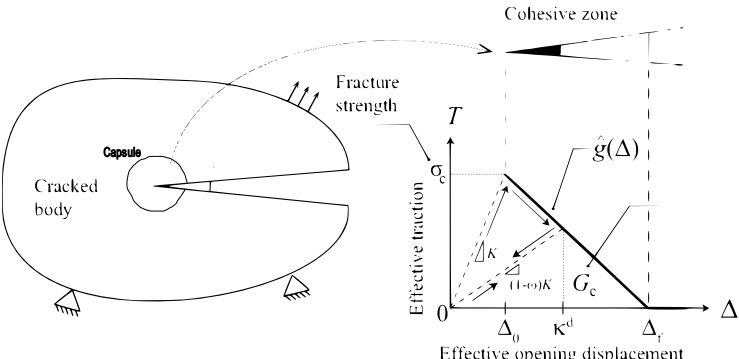
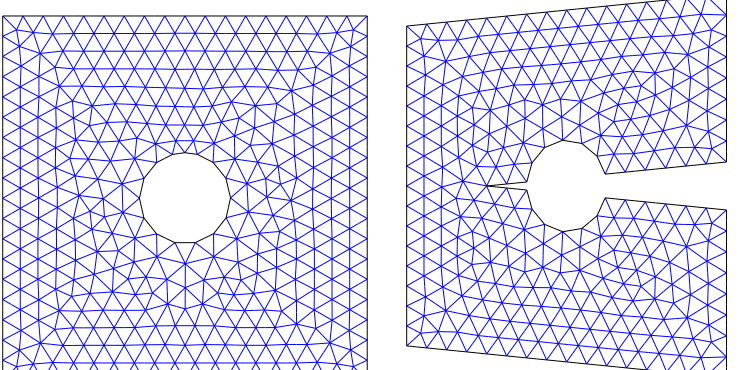
A similar study conducted by Šavija et al. (2016) explored the breakage of tubular capsules made of different polymers and wall thicknesses using a lattice beam approach. In a related experimental-numerical study, Lv et al. (2017) conducted a combined experimental numerical study to investigate crack behaviour for encapsulated systems. They constructed the mesh of a self-healing system using real microstructural information obtained from XCT scans. Zhou et al. (2016) employed PFC2D software to study the fracture process near microcapsules in 2D matrix-capsule idealisations, utilizing the discrete element method where the capsules were assumed to be bonded particles that followed standard laws of motion. In this way, the fracture process was modelled by the breakage of bonds between adjacent particles.

Mauludin & Oucif (2019) studied the effect of varying the interfacial strength on the fracture behaviour of microcapsules using the cohesive zone model. They embedded polymeric-based microcapsules in the centre of a 2D matrix domain and found that the

load-bearing capacity of the system depends on the interfacial strength, regardless of the core-to-shell thickness ratio of the microcapsules. Additionally, they demonstrated that the probability of triggering microcapsules under fixed interfacial fracture strengths depends on the core-to-shell thickness ratio.

Gilabert et al. (2017) presented a 3D XFEM based model in combination with the cohesive surface method to study the fracture process of encapsulated self-healing materials. They highlighted the role of bond strength between the capsule and matrix in the fracture process. The summary of methods and configurations used for simulating the triggering process involved in self-healing action is presented in Table 2-5.

Table 2-5. Methods and configuration for simulating triggering process

Method	Configuration	References
Cohesive XFEM, DEM	 <p>The diagram shows a cracked body with a capsule. A dashed line indicates the fracture path. To the right, a graph plots Effective traction (T) against Effective opening displacement (Δ). The graph shows a linear elastic region up to Δ₀ with stiffness K, followed by a softening region with peak traction σ_c and critical energy release rate G_c. The total displacement at failure is Δ_f. A dashed line represents the cohesive zone. The graph also shows a residual stiffness (1-α)K and a function g(Δ).</p>	(Ponnusami et al., 2015, 2019) (Mauludin & Oucif, 2019)
LBM	 <p>The diagrams show a lattice structure with a circular hole. The left diagram shows the lattice before fracture, and the right diagram shows the lattice after fracture, with the hole enlarged and the lattice structure distorted.</p>	(Šavija et al., 2016)

The finite element framework for simulating the damage-healing process using a phenomenological cohesive zone approach was adopted by Alshegri & Abu Al-Rub (2016). They assumed that healing occurs at the crack tip. Following this research, Ponnusami et al. (2018) extended their cohesive model (Ponnusami et al., 2015) to include healing variables for simulating the mechanical recovery. Their model proved capable of capturing multiple instantaneous healing events.

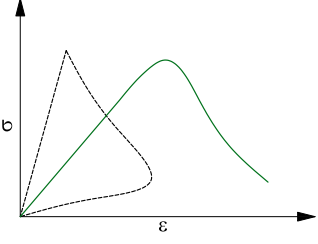
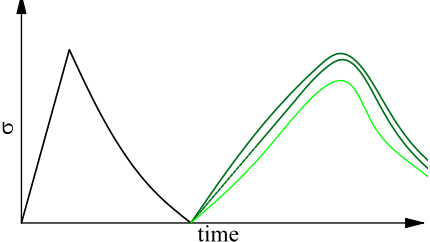
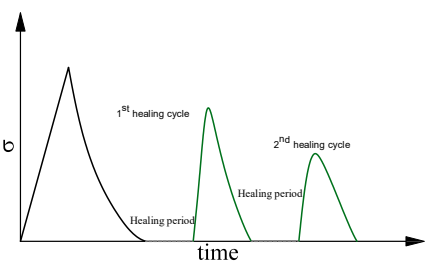
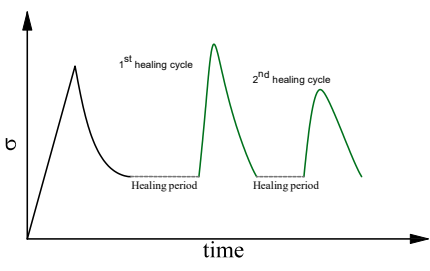
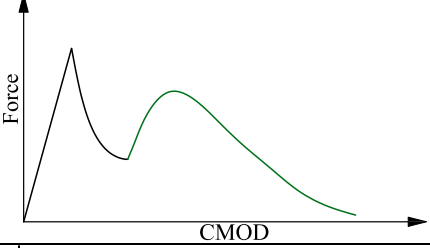
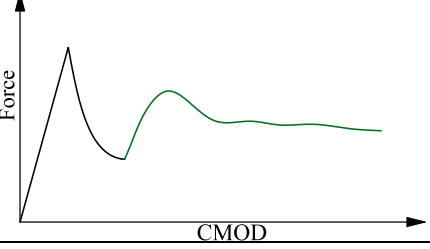
In a different approach, Caggiano et al. (2017) proposed a damage/plasticity interface model with a zero-thickness element to represent the post-cracking response before and after self-healing. They demonstrated that their model can effectively capture the concrete's post-peak strength after healing.

To extend the DEM method, Zhou et al. (2017) introduced a healing index derived from the number of broken bonds before and after healing. They concluded that the characteristics of self-healing depend on the initial damage and strengths, and that self-healing causes local contact instabilities which result in fluctuations in the stress-strain response after the peak-load has been reached. Also, they showed that healing may reduce the 'peak strain', which in this paper is defined as strain corresponding to the peak load.

In a distinct methodology within the context of discrete approaches, Chen & Ye (2019) utilized a Lattice Boltzmann single-component model to simulate healing caused by further hydration. Their model was employed to estimate healing efficiency as well as geometry changes.

Adopting a strong discontinuity framework called SDA, for considering crack-healing effects on global mechanical responses of cementitious materials, Y. Zhang & Zhuang (2018) obtained a general range of healing parameters through back analysis of a set of experiments on a self-healing beam subjected to bending and shear. They compared the crack path with and without healing and showed how healing action causes a deviation in the crack propagation direction.

Table 2-6 Summary of existing models for capturing mechanical regain due to healing mechanism

Description	Mechanical response	Range of applicability
<ul style="list-style-type: none"> • Healing commenced in a fully unloaded condition • Redamage is considered • Healing occurred instantaneously • Healing can occur once • Formulation derived based on damage models 		<ul style="list-style-type: none"> • Intrinsic and extrinsic self-healing with microcapsules, where healing occurs rapidly enough for healing to be complete
<ul style="list-style-type: none"> • Time dependency is included • Healing commenced in a stress free condition • Single healing event is considered 		<ul style="list-style-type: none"> • Single healing systems with healing agent with different curing times
<ul style="list-style-type: none"> • Multiple healing cycle is included • Healing should commence in stress free condition • At each cycle, healing commences instantaneously 		<ul style="list-style-type: none"> • Systems with multiple healing cycle potential, such as microbial systems.
<ul style="list-style-type: none"> • Healing occurs under sustained load • There is no overlap between healing and damage • Cohesive zone element method mostly used for this formulation 		<ul style="list-style-type: none"> • Systems with multiple healing cycle potential, such as microbial systems.
<ul style="list-style-type: none"> • Simultaneous damage and healing considered • Healing process time dependency is considered 		<ul style="list-style-type: none"> • Systems in which loading is resumed during the healing process, such as vascular networks and encapsulated systems.
<ul style="list-style-type: none"> • Re-healing feature and continuous damage-healing mechanism is considered. • Damage and healing is formulated in elements with strong discontinuities 		<ul style="list-style-type: none"> • Systems with a continuous healing agent supply, provided by, for example, a vascular network.

2-4 Coupled Multiphysics models

The prevalent and widely adopted theories for modelling damage-healing processes, aimed at capturing the mechanical recovery aspect in self-healing, have been outlined. However, as previously discussed, self-healing is a complex, multifaceted process. The transport of healing agents to the crack, chemical reactions, and the solidification process of the healing materials constitute sets of mechanisms associated with the self-healing phenomenon. Limited attention has been given to exploring and developing coupled chemo-physical-mechanical models of self-healing. The governing equations for discrete crack flow, diffusive and advection-diffusive processes, along capillary transport, are intertwined with mechanical frameworks, reflecting the essence of Multiphysics modelling in the context of self-healing.

In the context of flow within discrete crack, Freeman & Jefferson (2020) devised a numerical framework for crack flow simulation, specifically tailored to simulate the flow of healing agents inside a non-uniform crack. This involved coupling the Navier-Stokes formulation, as noted in equation (2.17), with the mass balance equation to comprehensively capture the flow of healing agents throughout the cementitious matrix.

$$\frac{\partial \dot{\mathbf{u}}}{\partial t} + (\dot{\mathbf{u}} \cdot \nabla) \dot{\mathbf{u}} = -\frac{\nabla P}{\rho} + \mu \nabla^2 \dot{\mathbf{u}} \quad (2.17)$$

where $\dot{\mathbf{u}}$ is velocity vector, P is pressure, μ is viscosity and ∇ is differential operator.

They applied the method proposed by Gardner et al. (2014) to incorporate the capillary flow action into their equation by introducing the viscous resistance force. Considering the fact that the transport properties of healing agent through time changes due to curing process, they described and modelled healing agent movement inside cracks of various geometries. The healing process is described by moving curing fronts within the body of healing agent, which is simulated using the following advection diffusion equation:

$$\frac{\partial \emptyset}{\partial t} + \nabla \cdot (\dot{\mathbf{u}} \emptyset) - \nabla \cdot (D_f \nabla \emptyset) = 0 \quad (2.18)$$

where \emptyset is curing degree and D_f is diffusive constant.

The transport flow of healing agent through the cementitious porous medium is modelled using the diffusive flux equation.

$$\frac{\partial S}{\partial t} + \nabla \cdot \mathbf{j} - Q = 0 \quad (2.19)$$

where S is saturation degree, \mathbf{j} is the matrix flux and Q is the discharge flow.

Employing the above-mentioned equation, and building on previous work on coupled models for self-healing materials (Di Luzio et al., 2014; Di Luzio & Cusatis, 2009b, 2009a) Di Luzio et al. (2018) introduced a model that captures solidification and crack-healing mechanisms through a coupled hygro-thermo-chemical approach. They described the driving force for self-healing as a reaction function of cement hydration, considering factors such as temperature, hydration degree, relative humidity, and crack width. A coupled diffusive-mechanical model was developed by Sanz-Herrera et al. (2019) which takes into account the chemical-diffusive action of mobile chemical species. The mechanical aspect of their model is developed based on the Continuum Damage Healing Mechanics (CDHM) model presented by Darabi et al. (2012).

Rodríguez et al. (2020) used the lattice framework for modelling the crack sealing process. They simulated the moisture transport within a cracked sample and considered the effects of cracking on diffusivity.

In a similar context, but with different Lattice framework approach, Cibelli et al. (2022) followed a lattice discrete particle approach to simulate autogenous healing in cementitious materials. Their model incorporated fracture, moisture transport, and hydration processes through a Hygro-Thermo-Chemical formulation. The authors applied this model to simulate self-healing in dog bone-shaped and double-edged notched prismatic specimens, demonstrating that the numerical results aligned well with experimental data.

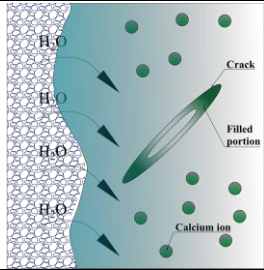
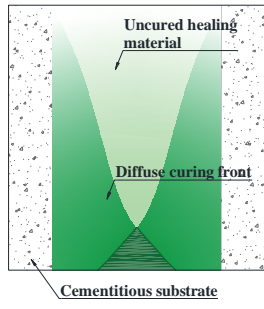
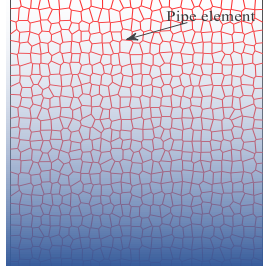
Recently, Freeman et al. (2020) integrated their transport model with a novel cohesive damage-healing mechanics model. They implemented their formulation into an element with strong discontinuity, defining all healing variables at that level. Expanding on their work, they considered healing in a crack with varying opening displacement over time, as detailed in (Jefferson & Freeman, 2022). In this extension, healing was simulated by

accounting the interaction of the curing front and the crack geometry. The model took into consideration the interaction of healing processes with the crack opening displacement and its rate. The authors demonstrated that their model accurately captures the mechanical and transport features of autonomous self-healing.

Building on their prior work, Freeman & Jefferson (2023) recently extended the model to a 3D domain for the simulation of realistic boundary value problems. Their simulations provide valuable insights into the transport of healing agents inside realistic crack geometries in a 3D domain.

The modelling approaches for simulating different mechanisms associated with coupled self-healing processes is summarised in the Table 2-7

Table 2-7 Coupled modelling approaches.

Coupled process	Configuration	Description	References
flux		The healing product forms inside the crack through coupling the flux mechanism and chemical process of carbonation.	(Ponnusami et al., 2015, 2019) (Mauludin & Oucif, 2019)
Moving curing front		The amount of healing material is determined through the advection-diffusion process. In this method the overlapping between curing fronts from opposing crack-surfaces determines the level of healing.	(Freeman & Jefferson, 2022, 2020; Jefferson & Freeman, 2022)
Explicit transport		The transport of healing materials is explicitly considered by adding pipe elements. These elements determine the level of saturation at each voronoi element.	(Rodríguez et al., 2020; Singla et al., 2022)

2-5 Discussion

The approaches used to simulate mechanical self-healing have been considered in this chapter. It has been shown that most of the previous research undertaken on simulating self-healing processes has employed empirical methods for deriving the healing and damage driving forces. This has resulted in the development of models that are limited to the range of the experimental data used for their derivation. Many of the existing mechanistic approaches are limited to certain damage-healing conditions, e.g. instantaneous self-healing, healing under zero-strain conditions or separate damage and healing processes.

Generally, it is shown that, depending on the self-healing system, either diffuse or discrete crack-healing is likely to occur. However, both can occur in the same structural element and therefore a comprehensive model would need to consider both scenarios. The continuum approach, as shown in the literature, can provide a convenient framework for capturing damage and healing processes. However, the currently proposed models are not able to consider three main features: i) the time dependency of the healing process, ii) simultaneous damage and healing processes, and iii) multiple re-healing events.

For cases where the explicit representation of the microstructure and fracture process zones is required, the Lattice method is attractive. However, to date, and to the best knowledge of the author of this thesis, no study has been devoted to considering mechanical aspects of self-healing in the Lattice formulation.

Although recently a few coupled models for representing discrete crack-healing systems have been developed, most of these models have defined explicitly the location and formation time of a principal crack. Therefore, existing models are not able to simulate accurately multiple and intersecting cracks and associated crack healing.

The research gaps identified in this literature review are addressed in the remainder of this thesis. The research described comprises an enhanced and updated micromechanical model as well as a new Lattice formulation for capturing self-healing effects on mechanical properties. These are validated against experimental data.

Chapter 3

Lattice beam method

3-1 Introduction

This chapter describes a new formulation for simulating time-dependent crack-healing in lattice models, which was implemented in the TUDelft Lattice program. The chapter provides detailed information on the nature and extent of damage and healing zones at the mesoscale in cementitious structural elements. The Lattice method enables complex heterogeneity of cementitious systems with a selected level of randomness to be captured. The addition of healing to the model in a way that allows the simulation of micro- and macro-crack healing, in both an open and closed states, adds a considerable degree of complexity to the formulation. The enhancement was applied to the existing TUDelft Lattice model. This enhanced Lattice model is able to predict the overall mechanical recovery and system behaviour due to the healing in addition of the micro and mesoscale responses.

In the remainder of this chapter, lattice beam theory and the meshing procedure are explained in sections 3-2 to 3-4. The healing formulation is described in detail in section 3-5 and the computational details are noted in section 3-6. The behaviour of proposed model is illustrated in Section 3-8. Section 3-9 gives numerical examples to show the typical responses that would be derived from the proposed model. A range of numerical examples that considers meso and microstructural Lattice representations are provided in section 3-10. Section 3-11 is devoted to discussion and conclusion.

3-2 Lattice beam network model

In the lattice method, a domain is discretised with beam elements which connect a set of randomly positioned nodes. The mesh of beam elements is generated using a Delaunay triangulation algorithm which simultaneously determines the corresponding Voronoi cells

(Qian et al., 2011), as illustrated in Figure 3-1. This procedure involves dividing the domain into cubic sub-cells of specified size. The mesh nodes are then positioned based on the desired level of randomness in each sub-cell. Subsequently, nodes are connected using Delaunay triangulation (Chang, Liang, et al., 2022; Chang, Zhang, et al., 2022). The cross section of the element is chosen such that it is equivalent to the common surface area between the two Voronoi cells (see Figure 3-1d). In this way, the whole discretised system approximately represents the continuum. In addition, it is necessary to adjust the radius of the sphere associated with each cell so that the initial stiffness of the lattice model matches that of the elastic system. This is part of the calibration procedure, which is explained in more detail in section 3.7.

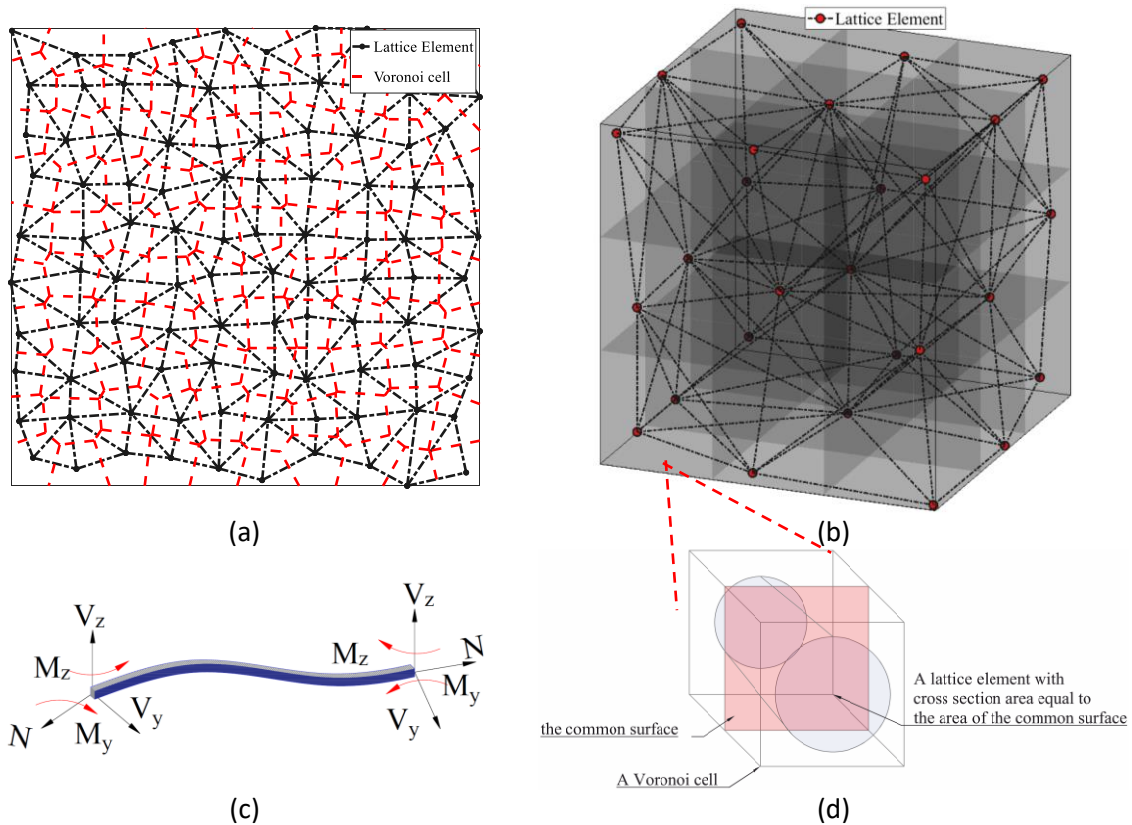


Figure 3-1 Illustration of the LBM, a) 2D lattice network with elements and Voronoi cells, b) 3D Lattice structure and c) an element in 3D space

The level of randomness determines the mesh irregularity as depicted in Figure 3-2.

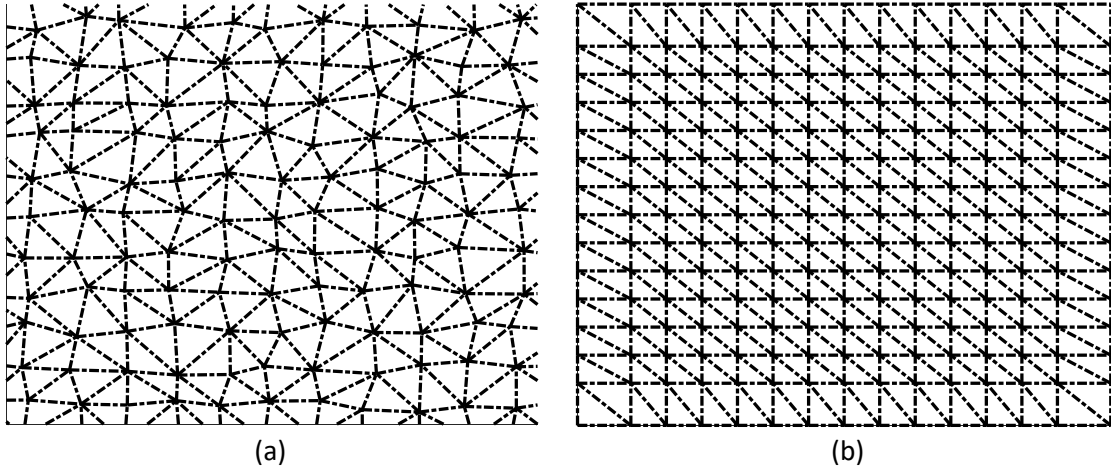


Figure 3-2. Effect of randomness on Lattice mesh, a) randomness=0.5 , and b) no randomness

For a Lattice beam element in 3D space, the 12×12 stiffness matrix is derived from applying the standard Galerkin weak form to the axial, bending, torsional and shear components of the beam governing equations. The governing equilibrium, compatibility and constitutive equations for a continuum solid, as well as the associated Neumann and Dirichlet boundary conditions, are as follows:

$$\begin{cases} \nabla \cdot \boldsymbol{\sigma} + \mathbf{f}_b = 0 \\ \mathbf{u} = \mathbf{u}_0 \\ \boldsymbol{\sigma} \cdot \mathbf{n} = \mathbf{T} \\ \boldsymbol{\sigma} = \mathbf{D} : \boldsymbol{\varepsilon} \\ \boldsymbol{\varepsilon} = \frac{1}{2}(\nabla \mathbf{u} + \nabla \mathbf{u}^T) \end{cases} \quad (3.1)$$

where \mathbf{T} is the traction vector on the boundary and \mathbf{D} is stiffness matrix of the continuum media.

Applying Timoshenko's beam theory to a lattice beam element with 12 degrees of freedom, generated using the discretisation process for continua described above, gives the following governing differential equation:

$$\begin{cases} EA \frac{d^2 u}{dx^2} + f_x = 0 \\ EI \frac{d^4 v}{dx^4} - f_y + \frac{EI}{\mathcal{K}AG} \frac{d^2 f_y}{dx^2} = 0 \end{cases} \quad (3.2)$$

where u is axial displacement field and v is vertical displacement field I is the second moment of inertia, f_x and f_y are force in x and y direction respectively. G is the material shear modulus and \mathcal{K} is the Timoshenko shear coefficient.

Expanding the boundary conditions for each degree of freedom on $\partial\Omega$ gives

$$\begin{cases} u(x) = u_0 \\ v(x) = v_0 \\ \theta(x) = \theta_0 \\ m(x) = M_0 \\ q(x) = Q_0 \end{cases} \quad (3.3)$$

where $u(x)$, $v(x)$ and $\theta(x)$ are axial, shear and rotational displacement components at an arbitrary coordinate x , and $m(x)$ and $q(x)$ are the applied moment and force vectors respectively.

By multiplying the governing equations by a weight function and integrating over the beam domain the weak form is derived. The following are the proposed shape functions for the solution of the Galerkin problem:

$$\begin{cases} u(x) = \sum_{i=1}^2 L_i u_i \\ v(x) = \sum_{i=1}^2 N_i v_i + \sum_{i=1}^2 M_i \theta_i \end{cases} \quad (3.4)$$

Shape functions for the axial and transverse components of displacement comprise linear and cubic polynomials respectively.

$$\begin{cases} L_1 = 1 - \frac{x}{l} \\ L_2 = \frac{x}{l} \\ N_1 = 1 - \frac{3x^2}{l^2} + \frac{2x^3}{l^3} \\ N_2 = \frac{3x^2}{l^2} - \frac{2x^3}{l^3} \\ M_1 = x - \frac{2x^2}{l} + \frac{x^3}{l^2} \\ M_2 = -\frac{x^2}{l} + \frac{x^3}{l^2} \end{cases} \quad (3.5)$$

For a Timoshenko beam element, the stiffness matrix is finally calculated as shown:

$$\hat{k}_0 = \begin{bmatrix} \frac{EA}{l} & 0 & 0 & 0 & 0 & 0 & -\frac{EA}{l} & 0 & 0 & 0 & 0 & 0 \\ \frac{12EI_z}{l^3(1+\phi)} & 0 & 0 & 0 & \frac{6EI_z}{l^2(1+\phi)} & 0 & \frac{-12EI_z}{l^3(1+\phi)} & 0 & 0 & 0 & \frac{6EI_z}{l^2(1+\phi)} \\ \frac{12EI_y}{l^3(1+\phi)} & 0 & \frac{-6EI_z}{l^2(1+\phi)} & 0 & 0 & 0 & \frac{-12EI_y}{l^3(1+\phi)} & 0 & \frac{-6EI_y}{l^2(1+\phi)} & 0 & 0 \\ \frac{GJ}{l} & 0 & 0 & 0 & 0 & 0 & 0 & 0 & -\frac{GJ}{l} & 0 & 0 \\ \frac{(4+\phi)EI_y}{l(1+\phi)} & 0 & 0 & 0 & 0 & 0 & \frac{6EI_y}{l^2(1+\phi)} & 0 & \frac{(2-\phi)EI_y}{l(1+\phi)} & 0 & 0 \\ \frac{(4+\phi)EI_z}{l(1+\phi)} & 0 & 0 & 0 & 0 & 0 & \frac{-6EI_z}{l^2(1+\phi)} & 0 & 0 & 0 & \frac{(2-\phi)EI_z}{l(1+\phi)} \\ \frac{EA}{l} & 0 & 0 & 0 & 0 & 0 & \frac{EA}{l} & 0 & 0 & 0 & 0 \\ \frac{12EI_z}{l^3(1+\phi)} & 0 & 0 & 0 & 0 & 0 & \frac{12EI_z}{l^3(1+\phi)} & 0 & 0 & 0 & \frac{-6EI_z}{l^2(1+\phi)} \\ \frac{12EI_y}{l^3(1+\phi)} & 0 & \frac{6EI_y}{l^2(1+\phi)} & 0 & 0 & 0 & \frac{12EI_y}{l^3(1+\phi)} & 0 & \frac{6EI_y}{l^2(1+\phi)} & 0 & 0 \\ \frac{GJ}{l} & 0 & 0 & 0 & 0 & 0 & \frac{GJ}{l} & 0 & 0 & 0 & 0 \\ \frac{(4+\phi)EI_y}{l(1+\phi)} & 0 & 0 & 0 & 0 & 0 & \frac{(4+\phi)EI_y}{l(1+\phi)} & 0 & \frac{(4+\phi)EI_y}{l(1+\phi)} & 0 & 0 \\ \text{sym} & & & & & & & & & & \frac{(4+\phi)EI_z}{l(1+\phi)} \end{bmatrix} \quad (3.6)$$

A full derivation is given in Logan (2002) and Qian (2012a).

The microstructure geometry can be determined using X-ray, electron microscopic images or by utilizing computational codes. The latter produce random shapes (inclusions) and positions them within a domain (cementitious matrix) thereby replicating the cementitious material’s microstructure. Figure 3-3 shows different types of Lattice meshes. The mechanical properties of each beam element are determined from experimental tests on concrete specimens (e.g. cylinder compression, cylinder splitting and direct tension tests).

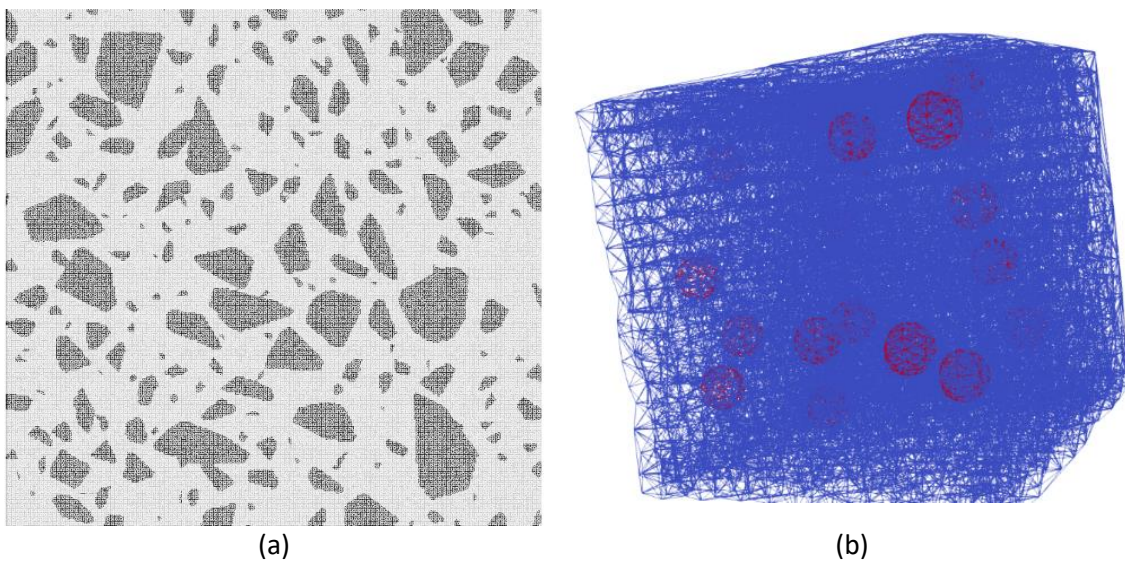


Figure 3-3 Lattice meshing example for heterogenous system, a) irregular inclusions, and b) embedded microcapsules

The skeletal finite element system, which is sparse in nature, is assembled in compressed row format (Barrett et al., 1994; Zienkiewicz et al., 2013). Initially, the sequential linear solution procedure was used to solve the nonlinear system of equations, but this was later modified to accommodate the new healing procedure, as explained in Section 3-5. The linearised equation system for each iterative step is solved using a Jacobi preconditioned conjugate gradient solver.

The basic method used to simulate damage in the conventional Lattice model is to remove elements from the structural system when the internal representative stress, defined in equation (3.11), exceeds the damage threshold strength (Section 3-3). This is in contrast to continuum damage mechanics in which a damage variable (ω) varies continuously from zero (no damage) to unity (fully damage) at a material point. In damage mechanics terms, the classical lattice approach would be consistent with the damage variable for an entire element changing instantaneously from zero to one when the element fracture criterion is met. In this study, the conventional lattice approach has been modified to simulate progressive element-level damage in a step-wise (or segmented) fashion for incremental prescribed displacements. This involves the element damage variable being increased in discrete steps from zero to one. Details of this procedure are provided in Section 3-4. In addition, rate dependent damage and healing behaviour has been introduced into the model, as explained in Sections 3-4-1 and 3-5.

3-3 Standard LBM fracture model

For a standard LBM mesh, as illustrated in Figure 3-1, the static equilibrium equation for an undamaged linear elastic lattice beam element is as follows:

$$\hat{\mathbf{K}}_0 \hat{\mathbf{u}} = \hat{\mathbf{f}} \quad (3.7)$$

where $\hat{\mathbf{K}}_0$, $\hat{\mathbf{u}}$ and $\hat{\mathbf{f}}$ are the element undamaged stiffness matrix (as illustrated in equation 3.6), nodal displacement vector and force vector respectively, noting that $\hat{}$ denotes element level variables.

The global equation system is obtained by assembling the contributions from each beam element, as follows:

$$\mathbf{K}_{G0} \mathbf{u} = \mathbf{f} \quad (3.8)$$

where \mathbf{K}_{G0} is the intact global stiffness matrix, and \mathbf{u} and \mathbf{f} are the global displacement and force vectors respectively.

Lattice beam elements are removed when the representative stress (σ), as given by equation (3.9), exceeds the damage threshold strength of the element (f_t).

$$\sigma = \alpha_N \frac{N}{A} + \beta \times \max\left(\frac{|M_i|}{W_i}\right) \quad (3.9)$$

where N and M are the maximum axial force and bending moment of the beam section respectively, A is the cross-sectional area and W is elastic section modulus; α_N and β govern the normal and flexural stress contributions to the equivalent stress respectively, and are set to $\alpha_N = 1$ and $\beta = 0.05$, based on the values suggested by Chang (2019), through experimental and numerical validation for cementitious materials.

Beam elements are removed sequentially such that, at any point in the analysis, the element with the highest representative stress is removed. The solution procedure is sequentially linear with one element being removed per iteration until there are no beams left that exceed the damage threshold.

The assembled equilibrium equation system from equation (3.8), modified to account for fractured elements, is as follows:

$$\mathbf{K}_{G\omega} \mathbf{u} = \mathbf{f} \quad (3.10)$$

where $\mathbf{K}_{G\omega}$ is the global stiffness matrix updated for damaged (or fractured) elements.

It is noted that in the standard LBM fracture approach, the stiffness matrix of a fractured beam element is null, i.e. $\hat{\mathbf{K}}_{\omega} = \mathbf{0}$. Further details of how the standard LBM simulates the fracture behaviour of quasi-brittle materials can be found in (Chang et al., 2020).

3-4 Progressive damage.

The standard LBM was later extended by Schlangen and co-workers (Qian, 2012b; Schlangen, 2022; Schlangen & van Mier, 1992) to capture the softening behaviour of

concrete using a multi linear constitutive material law, which was assigned to each lattice beam element, such that an element can experience partial -rather than full- damage at a particular time. This method has now been extended to account for the softening behaviour of an element subjected to incremental prescribed displacements in a way that is compatible with incremental-iterative solution procedures.

The damaged element stiffness matrix is obtained from:

$$\hat{\mathbf{K}}_{\omega} = (1 - \omega)\hat{\mathbf{K}}_0 \quad (3.11)$$

ω varies in a step-wise manner and is related to the initial and secant elastic moduli (E_0 and E_i respectively), as follows:

$$\omega = 1 - \frac{E_i}{E_0} \quad (3.12)$$

where i denotes the step number.

The stepped damage procedure determines E_i from the corresponding representative strain (ε_i); noting that $\varepsilon_i = \tilde{u}_i/L_e$, where \tilde{u}_i is the representative element relative displacement and L_e the element length. According to the Timoshenko strain energy and fracture mechanics theory, the energy dissipation rate would be depends on the element length and which can be normalized by the unit volume of a lattice beam. This method employs a stress v representative-strain softening curve based on experimental data appropriate for the materials that have been considered in this work, as illustrated in Figure 3-4b. In this figure, the material tensile strength (f_t) and its corresponding secant elastic modulus (E) at each damage step ($i \in 1:n$) is presented. It is worth noting that, in this model, the variation of strain along the lattice beam section is not computed; rather, the maximum value is used. For more accurate strain tracking and computation, fibre beam models may be employed.

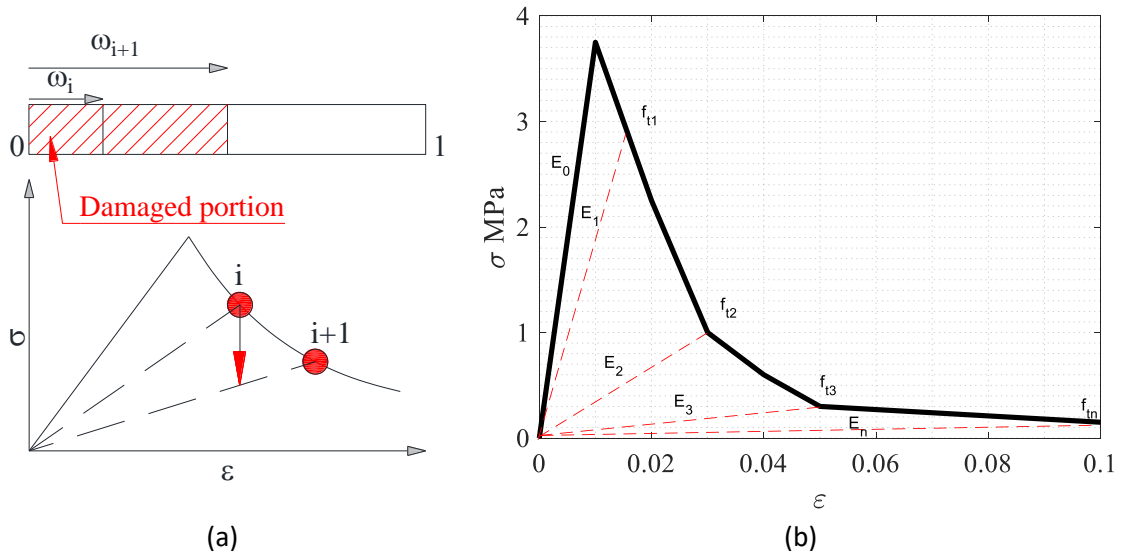


Figure 3-4 Stepped softening approach. a) schematic procedure and b) the softening representation of the considered materials in this study

In the progressive damage case, the global stiffness matrix ($\mathbf{K}_{G\omega}$) is formed from the assembled element matrices ($\hat{\mathbf{K}}_{\omega}$), noting that ω is null for undamaged elements.

3-4-1 Incremental damage

In the classical Lattice algorithm, the prescribed displacement is adjusted such that only one lattice element reaches the damage threshold in each mechanical step. In effect, the lattice structure is fully unloaded after each step, and/or after each lattice element fracture event, and then the fully reloaded. This loading-unloading sequence continues until the system reaches either the desired prescribed displacement (or load) with no more element fracture events, or it becomes unstable due to the formation of a fracture path that crosses the entire structure.

This approach is not suitable for simulating healing in loaded (displaced) lattice structures. Rather, to simulate healing under sustained load, as well as considering continuous damage healing cycles, the existing TUDelft lattice method was modified to an incremental damage formulation. In this approach, at each mechanical step, an increment of displacement is applied to the system. The new algorithm determines the critical element(s), if any, with respect to fracture. A multilinear iterative segment is added to make sure the system is in equilibrium after the system stiffness matrix has been updated for any new damage. The following figure shows a comparison between the computed responses for a uniaxial test specimen undertaken with (i) the incremental damage

method, and (ii) the classical loading-unloading approach. The material and geometric properties are given in Table 3-1. In this example the material parameters are chosen in a such way as to represent a typical cementitious mortar. Also, in this example, full damage is assumed to occur instantaneously and this is simulated by the removal of a lattice element when the failure criterion stress (equation (3.9) reaches to the strength threshold (f_t in Table 3-1).

As shown in Figure 3-5, the response envelopes obtained with the classical loading unloading method and the incremental damage model are essentially the same; however, the former includes some secant unloading-reloading branches. The responses have been plotted as both load-displacement and averaged stress-strain graphs. The stress (σ) and strain (ϵ) in this example are the average engineering stress and strain variables which were calculated from force divided by cross section area and displacement divided by specimen length respectively.

Table 3-1 Mechanical properties

E (MPa)	f_t (MPa)	ν	Sample dimensions (mm)
29501.6	3.4	0.25	$50 \times 50 \times 50$

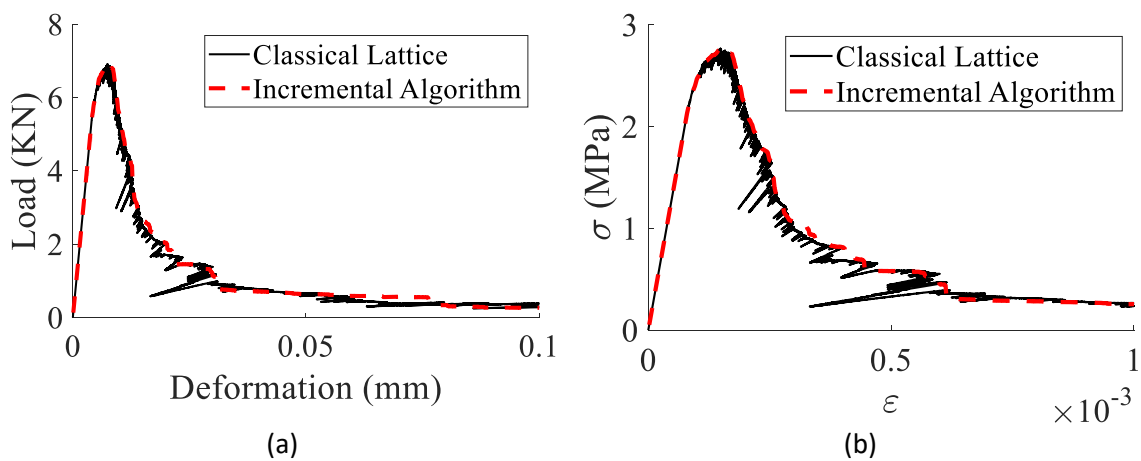


Figure 3-5 Comparison of classical and incremental damage model for Lattice beam method, a) Force-deformation, and b) stress-strain

3-5 Time dependent healing

Healing is associated with chemical processes that involve (i) healing agent curing in autonomic systems, or (ii) further hydration of unhydrated particles in autogenous self-healing. In both cases, healing is a time dependent phenomenon which involves the

diffusion and advection of healed material to and within the cracked area. It has been shown that the progress of healing in many biomimetic cementitious materials can be represented adequately with an exponential healing function (Freeman & Jefferson, 2023, 2020; Jefferson & Freeman, 2022).

This has been used in the present work to enhance the TUDelft-Lattice model to include transient healing. This is accomplished by recovering the properties of damaged elements over time and by allowing for the permanent relative displacements that occur when healing agent cures in an open crack. When damaged elements heal, the system stiffness matrix changes; however, the crucial point is that in a healing sub-step the internal forces should not be changed. This is because mechanical healing alone should not cause a change in the stress or strain energy. The basic assumption is that the healing agent in an open-crack cures in a stress-free condition. This ensures that the model does not violate the second law of thermodynamics (Jefferson et al., 2018) and, for a lattice system, this condition implies that the internal forces remain constant during a healing step. The model is based on the assumptions that (i) an adequate amount of healing agent is available to fill the crack fully, and (ii) the transport of healing agents to the crack is instantaneous.

To allow for healing, the basic element equilibrium equation (3.7) is modified, as follows:

$$\hat{\mathbf{K}}_{\omega} \hat{\mathbf{u}} + \hat{\mathbf{K}}_h (\hat{\mathbf{u}} - \hat{\mathbf{u}}_h) = \hat{\mathbf{f}} \quad (3.13)$$

where $\hat{\mathbf{K}}_h$ is the healed element stiffness matrix and $\hat{\mathbf{u}}_h$ is the element healed displacement vector. The normal component of $\hat{\mathbf{u}}_h$ physically represents the width of the cured healing agent zone in a crack (generally equal to the crack width at that position) at the time the crack is healed.

In the absence of re-damage, the element healing matrix at a time t is given by:

$$\hat{\mathbf{K}}_h(t) = \hat{\mathbf{K}}_{h\infty} (1 - e^{-(t-t_0)/\tau}) \quad (3.14)$$

where τ is a curing time constant, t is the current time, t_0 is the healing initiation time, $\hat{\mathbf{K}}_{h\infty}$ is the ultimate healing matrix and $\langle \rangle$ denote Macaulay brackets.

In order to allow for multiple healing cycles and account for the gradual accumulation of the healing displacement vector, equation (3.14) is introduced into equation (3.13) and

the second term in the latter is re-written as a summation of convolution integrals, as follows:

$$\hat{\mathbf{K}}_h(\hat{\mathbf{u}} - \hat{\mathbf{u}}_h) = \hat{\mathbf{f}}_{uh}(t) = \sum_{i=1}^n \int_{t_0(i)}^t \frac{\hat{\mathbf{K}}_{hi} e^{-\frac{(s-t_0(i))}{\tau}}}{\tau} (\hat{\mathbf{u}}(t) - \hat{\mathbf{u}}_h(s)) ds \quad (3.15)$$

where n represents the number of healing cycles, $\mathbf{u}_h(s)$ is the healed element displacement at the specific time of the curing (s), and the first term of the right hand side is based on the derivative of equation (3.14), i.e. $\frac{\partial \hat{\mathbf{K}}_h(t)}{\partial t} = \frac{\hat{\mathbf{K}}_h e^{-\frac{t}{\tau}}}{\tau}$, which represents the incremental stiffness regain.

The assembled equation system for the damage transient healing case is as follows:

$$\mathbf{K}_{G\omega} \mathbf{u} + \mathbf{K}_h(\mathbf{u} - \mathbf{u}_h) = \mathbf{f} \quad (3.16)$$

where \mathbf{u}_h is the global healed displacement vector and \mathbf{K}_h is the assembled healed stiffness matrix. As mentioned earlier, the internal forces in the system should not change during a healing step. This criterion imposes an extra constraint on the global and local equation systems. Theoretically, \mathbf{u}_h could be based on the relative displacement in an element at the time an increment of healing occurs, i.e. based directly on \mathbf{u}_h from the convolution integral in equation (3.15). However, this would involve storing a large amount of information and undertaking excessive computations involving the summation of all element healing displacement increments for all healing steps up to the step under consideration. An alternative, and far more tractable, solution is to apply the thermodynamic constraint (zero stress change at a healing step) to the global equilibrium equation. In this way there is no need to have a time history record of the element displacement vectors for the whole healing process and only the information from the previous step is required for an update. The internal force vector, allowing for the update in the global nodal healing displacement (\mathbf{u}_h), is given by:

$$\mathbf{f}_{uh} = \mathbf{K}_h(\mathbf{u} - \mathbf{u}_h) \quad (3.17)$$

Since there should be no change in nodal forces during a healing step, the virtual offset displacement can be derived from equation (3.17), as follows:

$$\mathbf{u}_h = \mathbf{u} - \mathbf{K}_h^{-1} \mathbf{f}_{uh} \quad (3.18)$$

3-5-1 Damage-healing solution algorithm

When solving the system, it proves convenient to group the stiffness terms from equation (3.13), that pre-multiply $\hat{\mathbf{u}}$ and $\hat{\mathbf{u}}_h$, separately and to shift the terms associated with $\hat{\mathbf{u}}_h$ to the righthand side of the equation, as follows:

$$\hat{\mathbf{K}}_{\omega h} \hat{\mathbf{u}} = \hat{\mathbf{f}} + \hat{\mathbf{f}}_h \quad (3.19)$$

$$\text{where } \hat{\mathbf{K}}_{\omega h} = \hat{\mathbf{K}}_{\omega} + \hat{\mathbf{K}}_h \text{ and } \hat{\mathbf{f}}_h = \hat{\mathbf{K}}_h \hat{\mathbf{u}}_h.$$

The global system counterpart to equation (3.16) is then:

$$\mathbf{K}_{\omega h} \mathbf{u} = \mathbf{f} + \mathbf{f}_h \quad (3.20)$$

$$\text{where } \mathbf{K}_{\omega h} = \mathbf{K}_{\omega} + \mathbf{K}_h \text{ and } \mathbf{f}_h = \mathbf{K}_h \mathbf{u}_h.$$

The overall problem is solved using a standard incremental-iterative solution algorithm (De Borst et al., 2012) with each increment of the solution being associated with a time step (p).

The healed stiffness matrix from the summed convolution integrals in equation (3.15) is evaluated at each time step using the recursive scheme described by Mergheim & Steinmann (2013). The elements available for healing include those that have partially healed but not re-damaged, as well as those newly damaged elements for which healing has been initiated. Allowing for the current and previous damage states, the healed stiffness matrix increments for the first and subsequent healing steps are given by equations (3.21) and (3.22) respectively, as follows:

$$\Delta \hat{\mathbf{K}}_{h_1} = \hat{\mathbf{K}}_{h\infty} (1 - e^{-\frac{\Delta t}{\tau}}) \omega_p, \quad (3.21)$$

$$\Delta \hat{\mathbf{K}}_{h_p} = \Delta \hat{\mathbf{K}}_{h_{p-1}} e^{-\frac{\Delta t}{\tau}} \frac{\omega_p}{\omega_{p-1}}, \quad (3.22)$$

The healed stiffness matrix increment is added to the current undamaged – healed stiffness matrix, as follows:

$$\hat{\mathbf{K}}_{\omega h_p} = \hat{\mathbf{K}}_{\omega h_{p-1}} + \Delta \hat{\mathbf{K}}_{h_p} \quad (3.23)$$

The healed element force vector is then calculated from the healed stiffness increment at each time step, as follows:

$$\hat{\mathbf{f}}_{hp} = \hat{\mathbf{f}}_{hp-1} + \Delta \hat{\mathbf{K}}_{hp} \hat{\mathbf{u}}_{hp} \quad (3.24)$$

When a healed element is re-damaged, the stiffness and healed internal force terms are updated proportionally to the level of re-damage thus, re-healing always commences from a null state. The calculation procedure is illustrated schematically in Figure 3-6. This figure shows the equivalent healed element status in terms of the regained stiffness and the internal stress. Since curing is assumed to be an exponential process, the stiffness regain increment is highest for the first step and then gradually reduces in subsequent steps. This is illustrated in Figure 3-7, in which the darker the colour the greater the proportion of healing over a time step. At a specific time-step, the overall regained healing stiffness is the summation of the stiffness increments throughout the healing history.

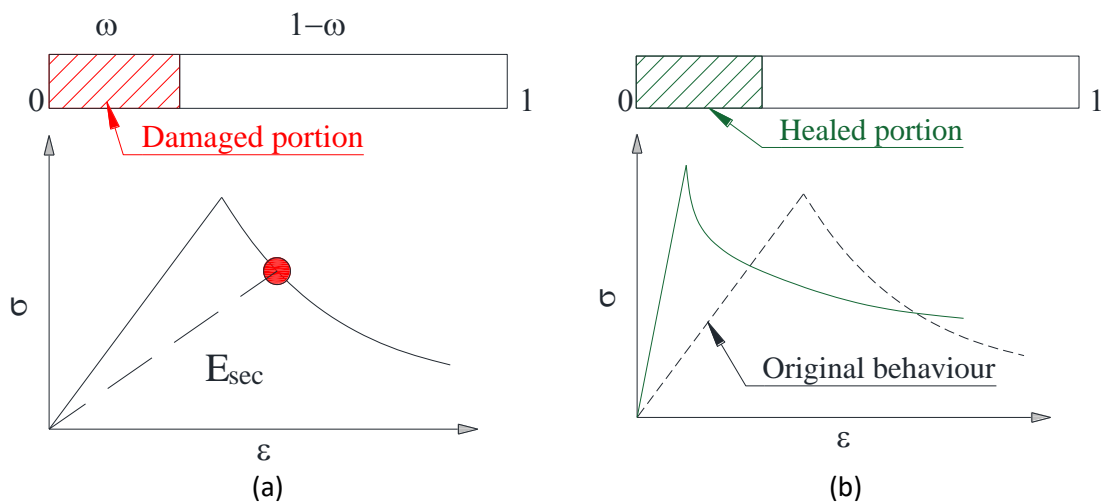


Figure 3-6 Schematic illustration of healing for a partial damaged element, a) partially damaged element at time of healing, and b) healed element.

The solution process comprises two sub-steps. The first sub-step, named the ‘mechanical step’, determines the global displacement vector and damage variable of each element. This requires iterations until the overall damage has reached a steady state. The second sub-step is the ‘healing step’. In this sub-step, the global displacements are assumed to remain constant whilst the stiffness matrices and \mathbf{u}_h are updated for healing. This procedure is shown schematically in Figure 3-7 and is illustrated for a one-dimensional problem in section 3-5-2.

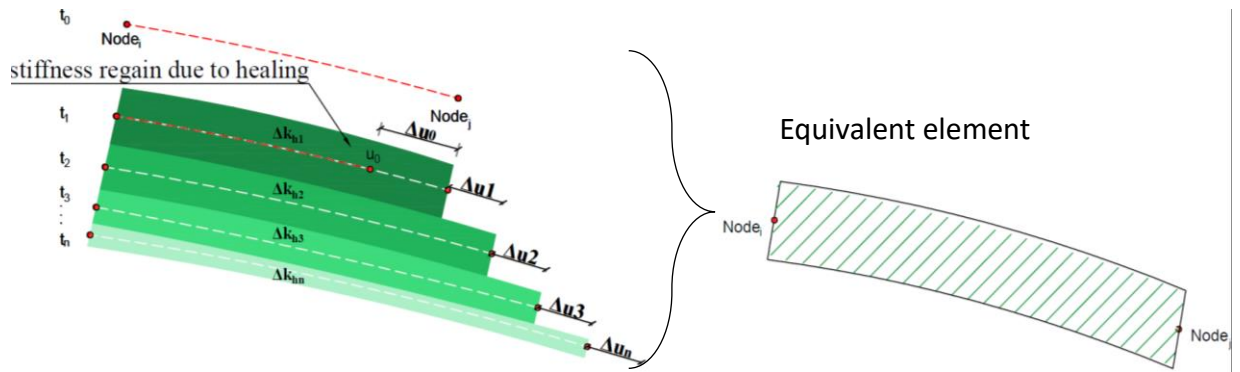


Figure 3-7 Sequence stiffness regain due to rate dependent healing procedure.

A preconditioned Conjugate Gradient solver is used to solve the assembled system of equations as well as to determine u_h at each healing step, the latter being the solution of equation ((3.18).

During a solution, the program stores only the current element damage and healing variables, nodal displacement vector and force vector. The global system stiffness matrix is assembled at each step prior to the solution of the current equation system. This makes the algorithm efficient in terms of memory storage and computational cost.

The following algorithm presents the steps of the numerical implementation of model for a general rate dependent healing scenario which considers the partial damage-healing case.

3-5-2 Formulation for 1D case

For a better understanding of how the presented method works, a simplified 1-D case is used to illustrate the formulation and implementation procedure. A one-dimensional model comprising 3 elements and 4 nodes is used in this example, as illustrated in Figure 3-8. As shown in the figure, the system is subjected to a force P in the direction shown in the Figure 3-8. At a selected displacement, it is assumed that element number 2 breaks and heals. The damage process is described in four stages (I-IV), each of which defines a different structural condition. Stage I is system just before loading. Stage II is the loaded system in elastic regime. At stage III the second spring (k_2) is assumed to fail and in stage IV this spring is instantaneously removed. For the sake of simplicity, in this illustration, it was assumed that the damaged element is instantaneously removed from the system.

The healing process may also be represented in four stages (I_h - IV_h), as follows: at stage I_h , the healed element is starting to form. Later the healed element is contributing in system

loading bearing for the Δu_1 increment (stage II_h). As loading resumes, the element number 3 reaches to its threshold (III_h) and is removed in stage IV_h.

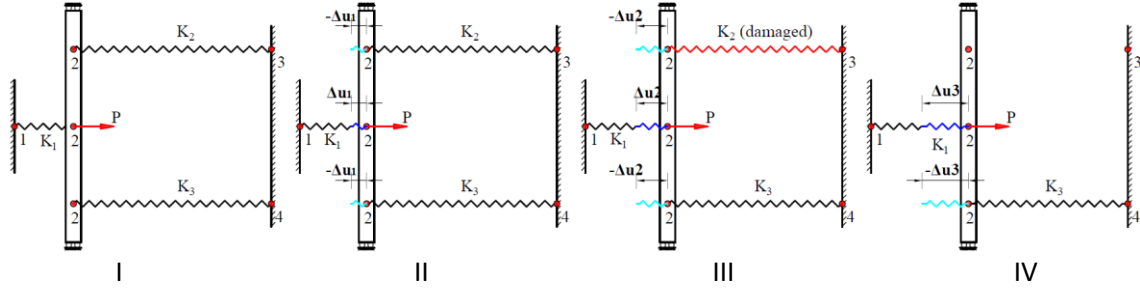


Figure 3-8 Schematic procedure for fracture process in Lattice

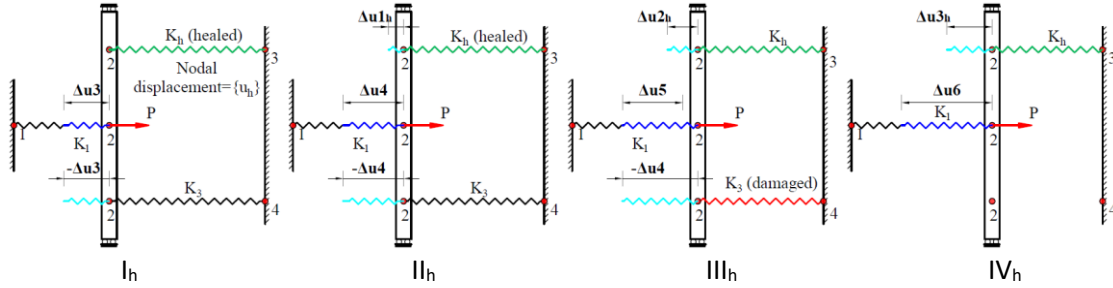


Figure 3-9 Schematic procedure for healing implementation in the Lattice.

In this example, the system initial stiffness and equilibrium equations can be written in the following matrix form:

$$\begin{bmatrix} k_1 & -k_1 & 0 & 0 \\ -k_1 & k_1 + k_2 + k_3 & -k_2 & -k_3 \\ 0 & -k_2 & k_2 & 0 \\ 0 & -k_3 & 0 & k_3 \end{bmatrix} \begin{Bmatrix} u_1 \\ u_2 \\ u_3 \\ u_4 \end{Bmatrix} = \begin{Bmatrix} R_1 \\ P \\ R_3 \\ R_4 \end{Bmatrix} \quad (3.25)$$

where k is the lattice beam element stiffness matrix, u is nodal displacement, R is reaction force and P is external force.

At stage III, where the second element is assumed to be broken, the system global stiffness matrix is updated as follows:

$$\mathbf{K}_{G\omega} = \begin{bmatrix} k_1 & -k_1 & 0 & 0 \\ -k_1 & k_1 + 0 + k_3 & 0 & -k_3 \\ 0 & 0 & 0 & 0 \\ 0 & -k_3 & 0 & k_3 \end{bmatrix} \quad (3.26)$$

At a specific stage (Like Figure 3-9) at which the nodal displacements are \mathbf{u}_{1h} , it is assumed that the healing commences. The equilibrium equations for such a system at the healing point are reformulated as noted in equation (3.27). Because the healed element is

generated in a deformed state, the internal force of healed element is calculated by $k_h(u_2 - u_{2h}) = f_2$.

$$\begin{cases} R_1 = K_1 u_1 - k_1 u_2 \\ P = -k_1 u_1 + k_1 u_2 + k_h(u_2 - u_{2h}) - k_h(u_3 - u_{3h}) + k_3 u_2 - k_3 u_4 \\ R_3 = -k_2(u_2 - u_{2h}) + k_h(u_3 - u_{3h}) \\ R_4 = -k_3 u_2 + k_3 u_4 \end{cases} \quad (3.27)$$

in which k_h is the healed element stiffness matrix. The matrix form of the above series of equations are rewritten, as follows:

$$\begin{bmatrix} k_1 & -k_1 & 0 & 0 \\ -k_1 & k_1 + k_h + k_3 & -k_h & -k_3 \\ 0 & -k_h & k_h & 0 \\ 0 & -k_3 & 0 & k_3 \end{bmatrix} \begin{Bmatrix} u_1 \\ u_2 \\ u_3 \\ u_4 \end{Bmatrix} - \begin{bmatrix} 0 & 0 & 0 & 0 \\ 0 & +k_h & -k_h & 0 \\ 0 & -k_h & k_h & 0 \\ 0 & 0 & 0 & 0 \end{bmatrix} \begin{Bmatrix} u_{1h} \\ u_{2h} \\ u_{3h} \\ u_{4h} \end{Bmatrix} = \begin{Bmatrix} R_1 \\ P \\ R_3 \\ R_4 \end{Bmatrix} \quad (3.28)$$

in which the adjustment healing force (f_h) is defined as follows:

$$f_h = \begin{bmatrix} 0 & 0 & 0 & 0 \\ 0 & +k_h & -k_h & 0 \\ 0 & -k_h & k_h & 0 \\ 0 & 0 & 0 & 0 \end{bmatrix} \begin{Bmatrix} u_{1h} \\ u_{2h} \\ u_{3h} \\ u_{4h} \end{Bmatrix} \quad (3.29)$$

3-6 Computational solution parameters

For all of the examples considered below, the starting value of the load step rate was set to 0.0001mm/sec. The relative convergence criterion used was the Euclidean norm of the residual force vector ($[r]$) derived from solving the linear system of equations ($\mathbf{R} = (\mathbf{K}\mathbf{u} - \mathbf{f})$) and then normalised as follows; $\mathbf{R}/(\mathbf{K}_0\mathbf{u}_1)$ where \mathbf{K}_0 is the initial stiffness matrix and \mathbf{u}_1 is the first displacement vector obtained before any nonlinearity occurs. The convergence criterion was set to 10^{-6} . The maximum number of iterations was set to 5000; however, for most of the cases, convergence was achieved within 300 iterations. For each iterative step, the previous response was always taken as the initial estimate for the CG solver.

The lattice method is most suited to meso-scale analysis; applying this method to full-scale structures would have a very high computational cost. In addition, a viable two-scale method, in which the lattice method is used for lower scale (constitutive) computations and a continuum method is used for the overall discretisation, would require a complex homogenisation scheme. The longest element length in all the meshes was 2.5 mm. This

ensures that the meso-scale meshes are sufficiently fine to capture the cracking process within the fracture process zone for concrete specimens for which the coarse aggregate size was 10mm.

3-7 Model calibration

The cross section area of lattice beams (see Figure 3-4d), and their strengths are the two parameters that need to be calibrated. For the validation examples, these parameters were calibrated to ensure that the elastic response derived from the model matched that from the experimental data for the control specimens. Additionally, the number of post-peak control curve dropping steps (Section 3-4-1 and Figure 3-4) for each material was adjusted to ensure that the post-peak behaviour obtained from the model accurately represented the observed experimental response in the post-peak regime.

3-8 Illustrative damage healing responses for different uniaxial strain paths

To illustrate the performance of the enhanced lattice model, the behaviour of a 50mm self-healing cementitious cube under tensile loading is considered for two different healing scenarios with three healing agents, each with different curing time properties. The first scenario is that healing agent is supplied to the system once at $t=400s$ and there is a single healing cycle. In the second case, the healing agent is supplied continuously, after its release at 200s, and multiple healing cycles occur. The properties of the cementitious matrix and the healing agent are given in Table 3-2. The input parameters required for these simulations are the elastic mechanical properties of cementitious mortar. The parameters used in this simulation, given in Table 3-2, were taken from the experimental measurements of Selvarajoo, et al (2020). It is assumed that lattice elements fully damage instantaneously when the damage criterion reaches the strength threshold. In this numerical example, an incremental displacement is applied to the top of the cube at a rate of 0.001mm/s. The boundary conditions maintain an average uniaxial state of stress across the specimen.

Table 3-2 Material properties for uniaxial example test

Properties Example	$E_{m,h}$ (MPa)	$f_{tm,h}$ (MPa)	$\nu_{m,h}$ (MPa)	t_{hi}^* (s)	τ (s)	Sample dimensions (mm)
Single healing	29501.6	3.4	0.25	400	1 100 2000	$50 \times 50 \times 50$
Re-healing	29501.6	3.4	0.25	200	1 60 1000	$50 \times 50 \times 50$

* t_{hi} = Time, after the start of the test, at which healing is initiated

The mesh used to represent the sample is shown in first image of Figure 3-10d. Figure 3-10b and c show the computed average stress (σ_{av}) and nominal strain (ϵ_{nom}) responses for three healing-agent cases. The average stress is computed from the total vertical reactions on the top face divided by the cross-sectional area and the strain measure is calculated by dividing the applied displacement by the specimen height. Figure 3-10d shows the state of the elements at different stages of the analysis. This figure shows, as expected for a constant loading rate, that the stiffness recovers and peak post-healed strengths reduce with the rate of healing.

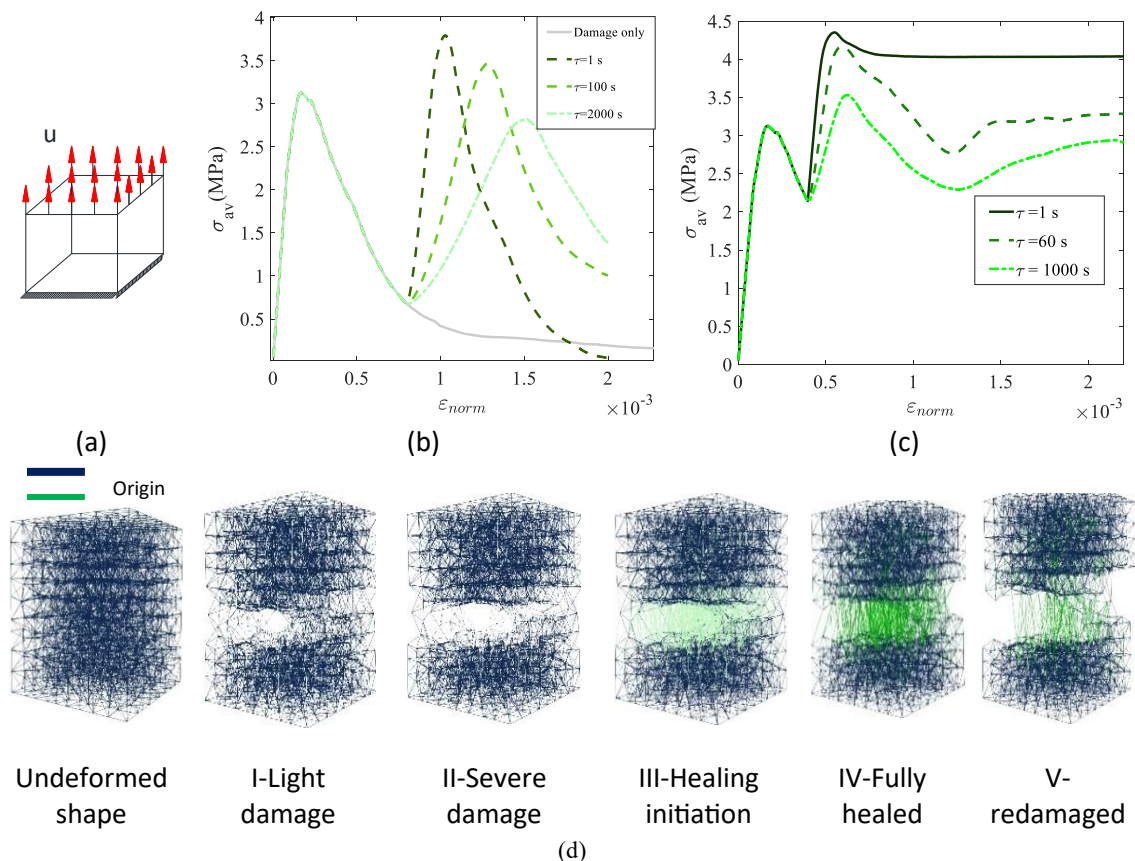


Figure 3-10 Constitutive behaviour of self-healing materials derived with the enhanced Lattice model, a) boundary conditions, b) σ_{av} - ϵ_{nom} curves for single healing scenario, c) σ_{av} - ϵ_{nom} curves for re-healing re-damaging scenarios and d) Lattice mesh at different phases of healing

3-9 Examples based on experiments

In order to assess the validity of the proposed approach for simulating the mechanical self-healing behaviour of structural elements formed from self-healing cementitious materials, the model was used to consider two series of experiments undertaken by Selvarajoo, et al. (2020). These tests comprised a set of notched cube specimens subject to tensile loading (DT series) and a series of notched beams subjected to 3-point loading with (i) a fixed crack width during the healing period (SF series) and (ii) continuous healing with varying crack opening displacement (SO series). The specimens were formed with an autonomic self-healing system that supplied healing agent to damaged zones from an external source.

The material properties used in the analyses are given in Table 3-3, along with the damage threshold used for the release of the healing agent in each case. The experimental arrangements are shown in Figure 3-11 and Figure 3-15 for the notched cube and beam specimens respectively.

Table 3-3 Experiment details and the material properties used for modelling.

Experiment name	$E_{m,h}$ (GPa)	f_{tm} (MPa)	f_{th} (MPa)	$\nu_{m,h}$	CMOD at releasing (mm)	Healing time (s)	τ (s)	Test type
DT-300	30	3.5	3.4	0.2	0.1	300	60	Direct Tension
DT-600	30	3.5	3.4	0.2	0.1	600	60	Direct Tension
SF-120	30	3.0	3.4	0.2	0.15	120	60	3-point bending
SO-0.0005	30	3.0	3.4	0.2	0.075	-*	60	3-point bending
SO-0.002	30	2.5	3.4	0.2	0.075	-*	60	3-point bending

* the healing time for the SO cases, starts from releasing action and continues until the end of the experiment.

3-9-1 Direct tensile test

A set of doubly notched 100mm cuboid samples were considered under uniaxial loading. Each sample was loaded in tension until the crack mouth opening displacement (CMOD) reached a limit of 0.1mm. At this point, the loading was paused and the valve of the pressurized healing agent (cyanoacrylate) supply system was opened. This released the healing agent through the channels embedded in the samples. The healing agent supply was maintained for healing periods of 300s or 600s, after which the healing agent supply ceased, and the loading resumed so as to maintain a constant CMOD rate of 0.0001 mm/s.

The healing agent properties were taken from (Jefferson & Freeman, 2022; Selvarajoo, et al., 2020; Selvarajoo, et al., 2020)

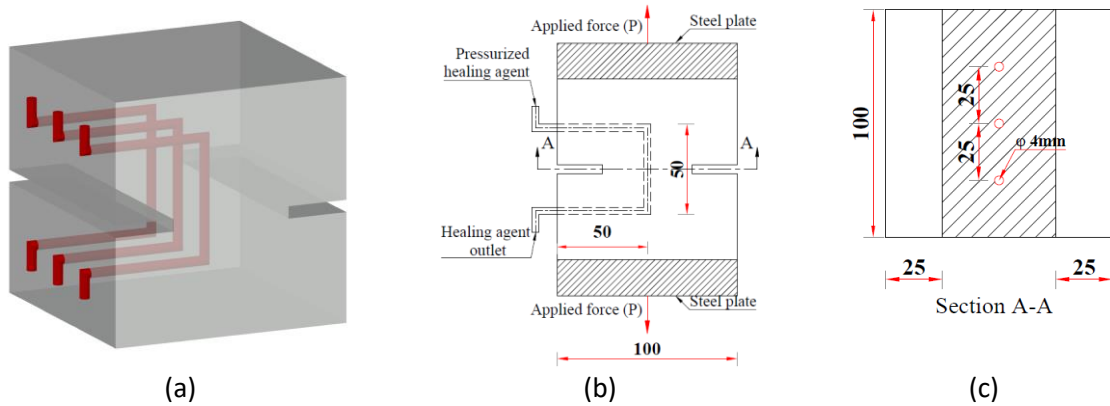


Figure 3-11 Experimental arrangement for notched cube tests Selvarajoo, et al. (2020), a) 3D schematic representation, b) front view and c) section view.

The mesh and boundary conditions used for the analysis are shown Figure 3-12. For simulating the post-peak behaviour, the elastic modulus at each damage step was calculated from the curve shown in Figure 3-12c. The control values $\left(\varepsilon_i, \left(\frac{E_i}{E_0}\right)\right)$ for each step damage point (i) in this figure were derived such that the post-peak response of the simulation matched that from the experimental reference data as closely as possible. The mechanical properties used for the cement matrix and healed material elements are given in Table 3-3.

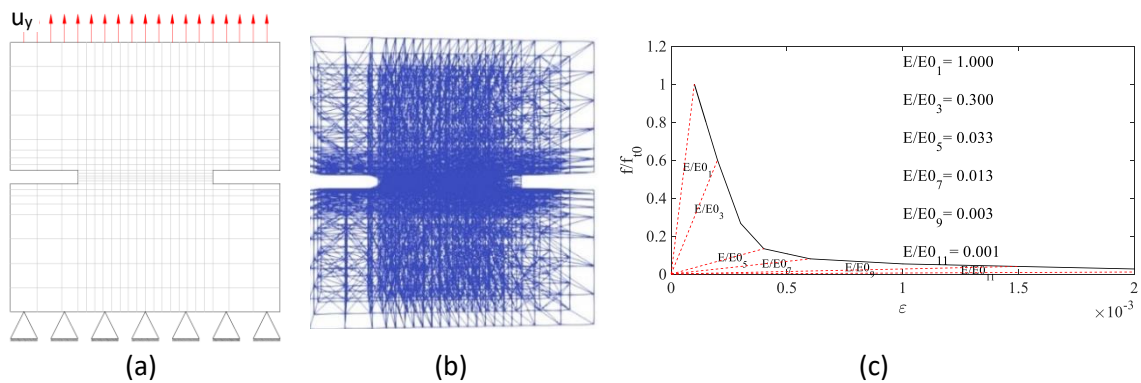


Figure 3-12 Boundary condition and mesh configuration, a) mesh and boundary conditions and b) perspective 3D view of the mesh, and c) Multi-linearised segmented behaviour for step-wise damage

The results for two different healing periods are presented in Figure 3-13. Based on experimental evidence (Selvarajoo, et al., 2020), it is assumed that the healing agent fully cures in a 0.1mm crack in 600s but that the curing process is incomplete after 300s. The

results are reported in the form of averaged stress vs CMOD. The average stress is calculated by dividing the normal force by the unnotched area. Plots that show damaged and healed elements before healing initiates (at CMOD=0.1) and during the healing period are shown in Figure 3-13. The experimental results in Figure 3-13 are denoted using the notation given in Table 3-3.

The results presented in Figure 3-13 show that stiffness and strength recoveries are in a good agreement with the experiments. The results (Figure 3-13b and c) confirm that the model is able to simulate partial healing and the response of specimens subject to different healing periods. It is noted that the numerical simulations allowed for the experimental observation that healing agent was transported to 60% of the crack area. The plots in Figure 3-14 show that the damage-healing zone extends above and below the notch with an overall characteristic dimension of approximately 15mm.

The information provided by analysing the fracture zone is used to estimate the amount of required healing agent. For the SF case, this calculation was based on the element healed displacement (\hat{u}_h) and the cross-sectional area. The calculated amount of healing agent for this case was 1045 mm³.

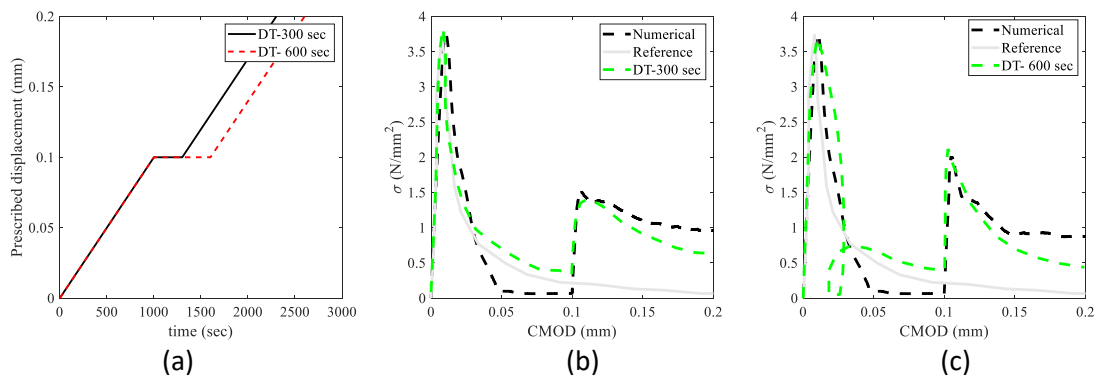


Figure 3-13 Numerical simulation results for stress-CMOD of the DT series tests, a) loading protocol, b) stress-CMOD for DT-300 test and c) Stress-CMOD for DT-600 test.

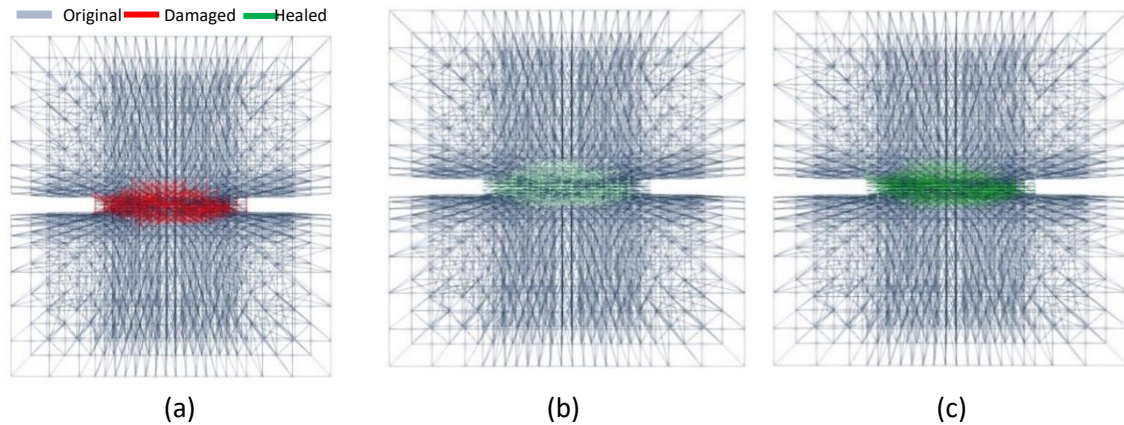


Figure 3-14 Damage and healing patterns for DT-600 test, a) damaged state at CMOD=0.1mm, b) curing phase at CMOD=0.1mm. and c) fully healed phase at CMOD=0.1mm.

3-9-2 3-Point bending test

The notched self-healing beam explored for the second example is illustrated in Figure 3-15. Two different healing scenarios were considered, one in which the crack opening displacement remained constant during the healing period (SF tests) and the other for which the CMOD was increased at a constant rate with healing agent supplied at a pressure of 0.5 bar (SO tests). For the former (SF) series, an analysis was undertaken until the CMOD reached 0.15mm. Healing agent was supplied for a period of 120 s while the CMOD was kept constant, after which, the loading was resumed at a CMOD rate of 0.001mm/s. For the latter (SO) series, post-crack CMOD rates of 0.0005 and 0.002 mm/s were used, with the analyses being continued until the CMOD reached 0.3mm. The reason for choosing these two different healing scenarios is to assess the ability of the proposed model to simulate healing for both fixed crack and moving crack scenarios, with the latter involving multiple and simultaneous damage and healing events. The material properties and test parameters are summarised in Table 3-3.

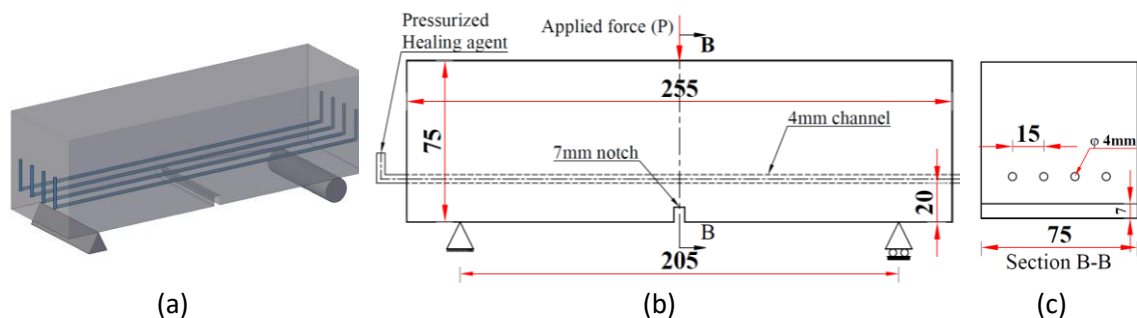


Figure 3-15 Experimental setup for notched beam tests, a) 3D schematic view, b) front view and c) beam section.

The results from the fixed crack (SF) analysis are compared with experimental data in Figure 3-16a. The numerical response in terms of stiffness and strength recovery is generally in good agreement with the experimental data, although the initial peak in the numerical simulation is slightly greater than the experimental average. The difference is considered to be within the natural variability level for this type of material. The results from the SO series analyses for the two different CMOD rates are compared to the experiment data from three tests with the same parameters in Figure 3-16b and c. This scenario is much more complex than the fixed crack case since healing and damage events overlap in time. The numerical responses are again in good general agreement with the experimental data and show the ability of the model to capture multiple re-damaging-re-healing events. This can be seen clearly at the end of the graph (Figure 3-16b and Figure 3-16c) where the numerical response tends to an asymptote, although the numerical plots do not exhibit the multiple peaks seen in the experimental data. Plots showing the extent of damage, healing, re-damage and re-healing are presented in Figure 3-17a to c. It may be seen from these plots that the fracture zone is relatively wide, with a characteristic dimension of approximately 20mm after the first cracking stage and 60mm at the final stage after re-healing and re-damage have occurred. It may also be seen also that healing extends to the far reaches of the fracture process zone.

Following the same approach as used in the previous example, the required healing agent volume is 234 mm^3 .

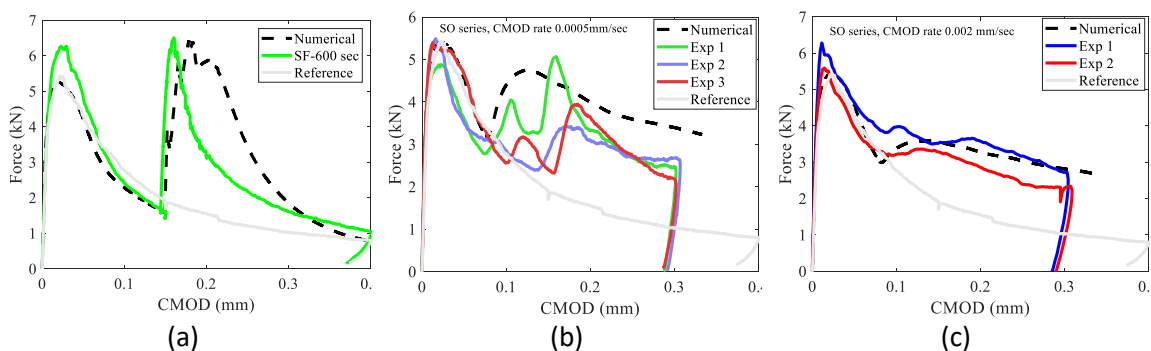


Figure 3-16 Notched beam test simulation results, a) SF-120 test results, b) SO series with loading rate 0.0005mm/s and c) SO series with loading rate 0.002mm/s.

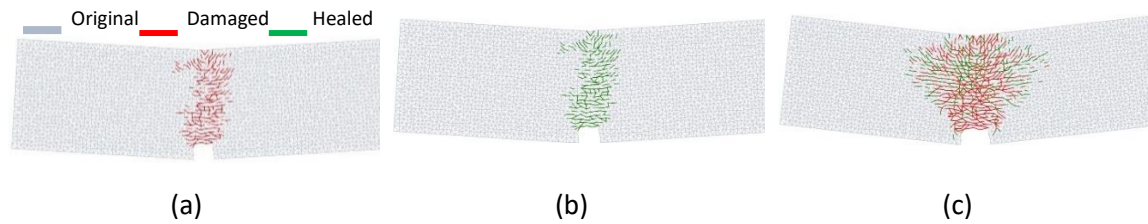


Figure 3-17 Crack pattern and system phase in deformed state, a) damaged state CMOD 0.075 mm, b) healed phase CMOD 0.12mm and c) re-damage-re-healed CMOD 0.2mm. (all deformations are magnified for clarity)

The examples presented in this chapter relate to an autonomic healing material; however, the proposed model framework is equally applicable to the simulation of autogenous healing processes. To apply the model to an autonomic problem the healing rate function would need to be determined from the hydration rate of unhydrated cement particles and the rate of formation of other cementitious healing compounds (e.g. portlandite) (Qian, 2012a).

The model provides detailed information on the distribution and size of damage and healing zones at the meso-scale, along with the associated volume of healing agent required at a particular time in the life of a structural element. These output data are far more refined than those provided by a comparable continuum model. This is essential information for the efficient design of a self-healing system and is also useful for researchers developing new self-healing systems.

The present chapter has concentrated on simulating time-dependent mechanical healing at the meso-scale but the model could be readily coupled to a transport model to simulate the movement of healing agent through the body of a structural element and within cracks (Freeman & Jefferson, 2020).

3-10 Additional applications of the Lattice model

Two studies are presented in this section, which used the lattice model to explore, (i) how changes in the meso-structure of mortar affect the predicted fracture behaviour and, (ii) how the degree of activation (or triggering) of embedded microcapsules varies with the volume fraction of capsules and with the relative strength of the microcapsule shell. In the first study, a series of irregular mesostructures representing a cementitious mortar were generated and the effects of varying the geometry and disposition of the inclusions

on the fracture path were examined. In the second study, the triggering mechanism for microencapsulated systems was studied. Multiple configurations with different volume fractions of microcapsules were considered to assess the probability of capsule breakage. In addition, the effect of varying the relative shell to matrix strength ratio on the capsule breakage behaviour was examined.

3-10-1 Mesostructure effect on fracture characteristics

In this section a study is reported that explored the effect of varying the microstructure geometry on the predicted cracking behaviour and mechanical response of a structural component. In this investigation, different inclusion geometries, from irregular-shapes to spheroids, were considered. Since the work reported in this section was conducted before the incremental method was implemented, the classical Delft Lattice method was used in the study.

The image segmentation technique was used to convert the actual aggregate shapes obtained from computationally generated images to their equivalent form in terms of regular shapes; namely circles, triangles, squares, pentagons and hexagons. Figure 3-18 shows the different shapes derived from the image of the mesostructure. The equivalent inclusions are depicted in various colour spectra since in image segmentation each individual inclusion is treated as a separate phase.

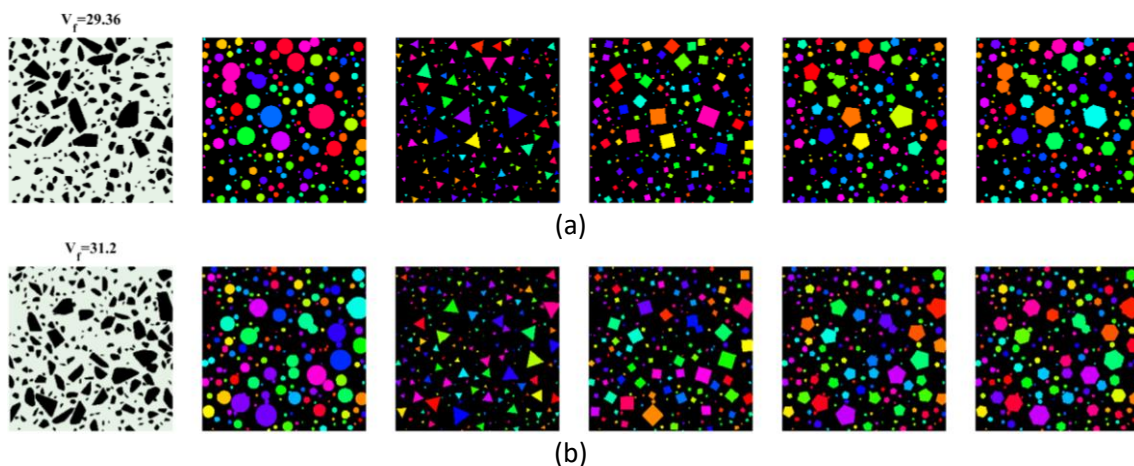


Figure 3-18 Meso structure configuration with different geometry, a) $vf=29.26$ and b) $vf=31.2$

The mechanical properties used in the investigation are given in Table 3-4. It is assumed that the material behaves in brittle way and that sudden and full damage occurs when a

lattice element reaches its threshold value. This results in the element being removed from the system.

Table 3-4 Cementitious matrix and aggregate properties.

E_m (MPa)	E_Ω (MPa)	f_{tm} (MPa)	ν_m	ν_Ω	Sample dimensions (mm)
32000	49000	0.75	0.1	0.28	40 × 40 × 40

*since this example consist of two phase, the subscript (m) specifies matrix and (Ω) shows the inclusions

It is assumed that micro- and macro-cracking only take place within the matrix and that the aggregate particles remain elastic throughout the simulation.

The numerical simulations were conducted in 2D. Figure 3-19a shows the boundary conditions for the test and the meshes are illustrated in Figure 3-19b . 186497 Elements and 62500 nodes were used to capture microcracking and cracking localization with a high resolution.

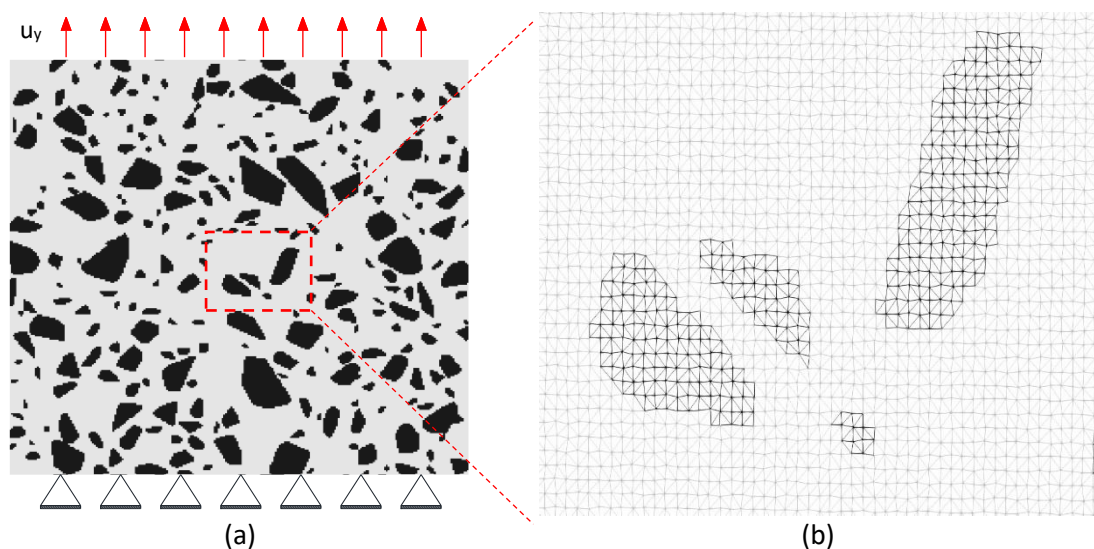


Figure 3-19 Boundary condition and mesh resolution illustration

The different stress-displacement curves (Figure 3-20) show that the responses computed using meshes with idealised regular shaped aggregate particles are very similar to those obtained from a mesh with irregular particles. In this illustrative example, the strengths of both the matrix and the ITZ were assumed to be relatively low (0.75 MPa), resulting in computed average peak strengths that were lower than those of standard concrete. However, as shown in Figure 3-21, the crack path and initial cracking zones are different. This highlights the importance of the inclusions' shape for studies that focus on crack patterns and propagation.

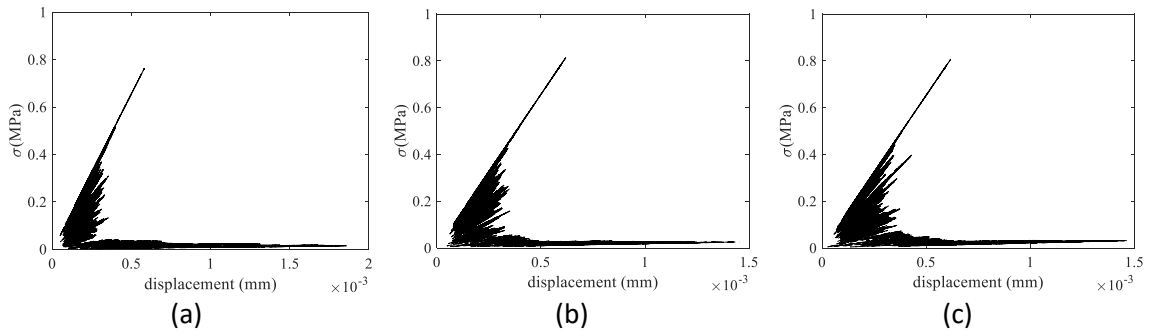


Figure 3-20 Stress-displacement curve for a) irregular shape inclusion, b) circular, and c) mix of polynomial

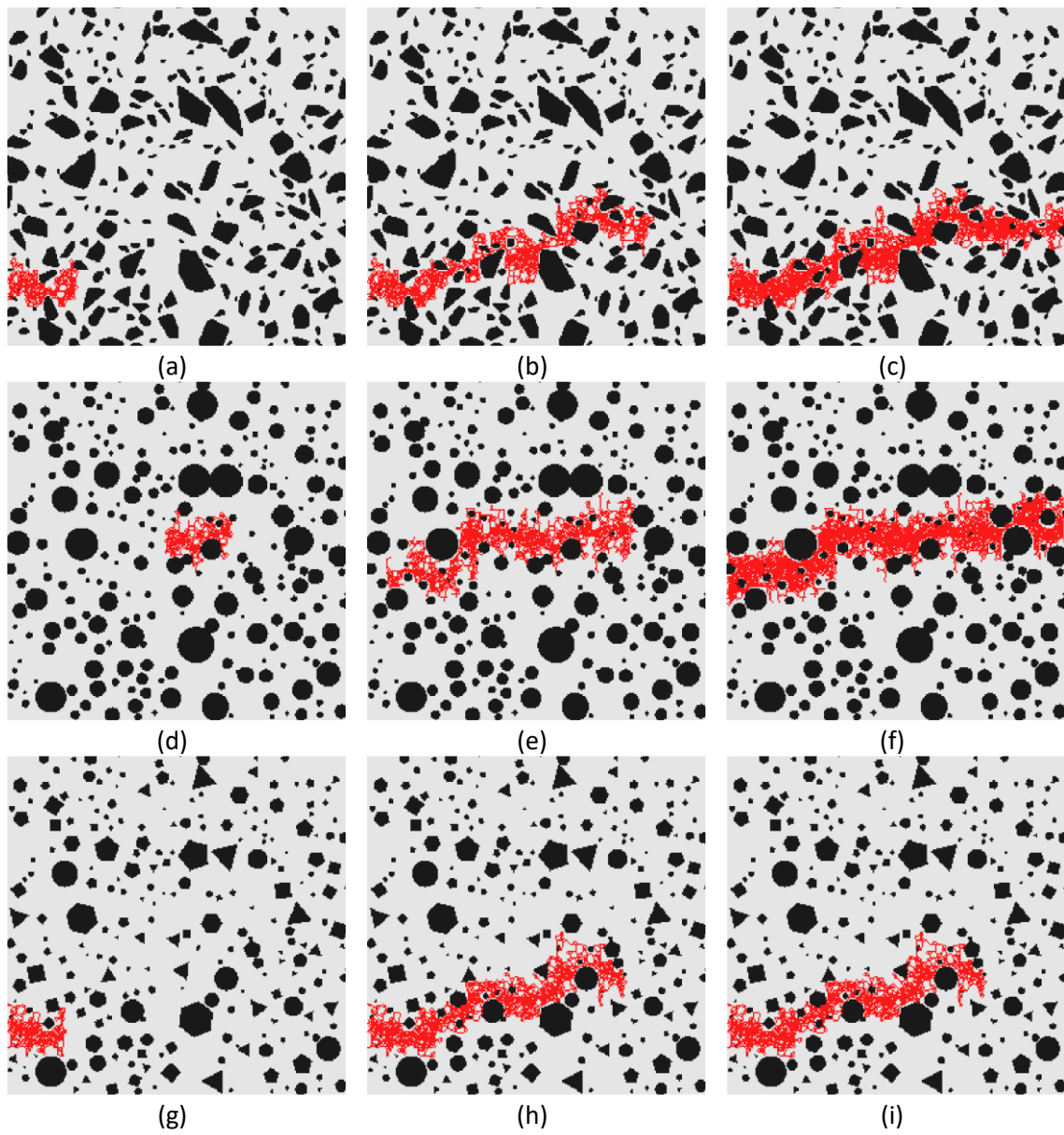


Figure 3-21 Crack pattern and propagation with different microstructure

3-10-2 A study on microcapsule activation

One of the primary issues in designing a microencapsulated self-healing system with randomly distributed microcapsules is whether the capsules will be activated (or 'triggered') by cracks within the cementitious matrix. Specifically, the issues are (i) will the shell of a microcapsule rupture when intersected by a crack in the cementitious matrix, and (ii) will the array of cracks within the matrix rupture sufficient microcapsules -and release sufficient healing agent- to bring about healing. These issues depend on the crack pattern, the location of the microcapsules, volume fraction of microcapsules, their mechanical properties, and the bond between the microcapsules and matrix (Zemskov et al., 2011).

To investigate the second of these issues, the probability of healing within an RVE of an encapsulated cementitious system is computed for 100 lattice meshes, each with a different volume fraction of microcapsules (Ω_c), as well as with different distributions of microcapsules. The RVE mesh was subjected to uniaxial tension loading. A framework is proposed to assess the maximum healing potential at each damage stage. Based on healing agent content and cracks near the microcapsules, the number of cracked elements that potentially could be healed was calculated. It is assumed that the bond between microcapsules and matrix is perfect, which means that once a crack intersects a capsule, it would break and release the healing agent. Also, it is assumed that an expansive healing agent is used; therefore, all of the healing agent would be released and would fill the cracks adjacent to capsules. The healing ratio is defined by equation (3.30).

$$H_{pr} = \frac{N_{Helement}}{N_{crack}} \quad (3.30)$$

where, $N_{Helement}$ is the number of healed elements, N_{crack} is the total number of damaged elements in each step and H_{pr} is the healing ratio. An average damage parameter ($\bar{\omega}$) is used in this study. This is defined as the ratio of the current number of damaged elements to the total number of damaged elements at the stage under consideration. This parameter varies from 0 to 1 (undamaged and fully damaged respectively) and represents an average of the damage variable for the whole domain. The

damage parameter is used to identify the healing ratio corresponding to the damage parameter.

In these examples, no notches or predefined cracks were introduced into the meshes. This meant that cracks initiated at random locations. A schematic showing how microcapsules are arranged within cementitious matrix is presented in Figure 3-22.

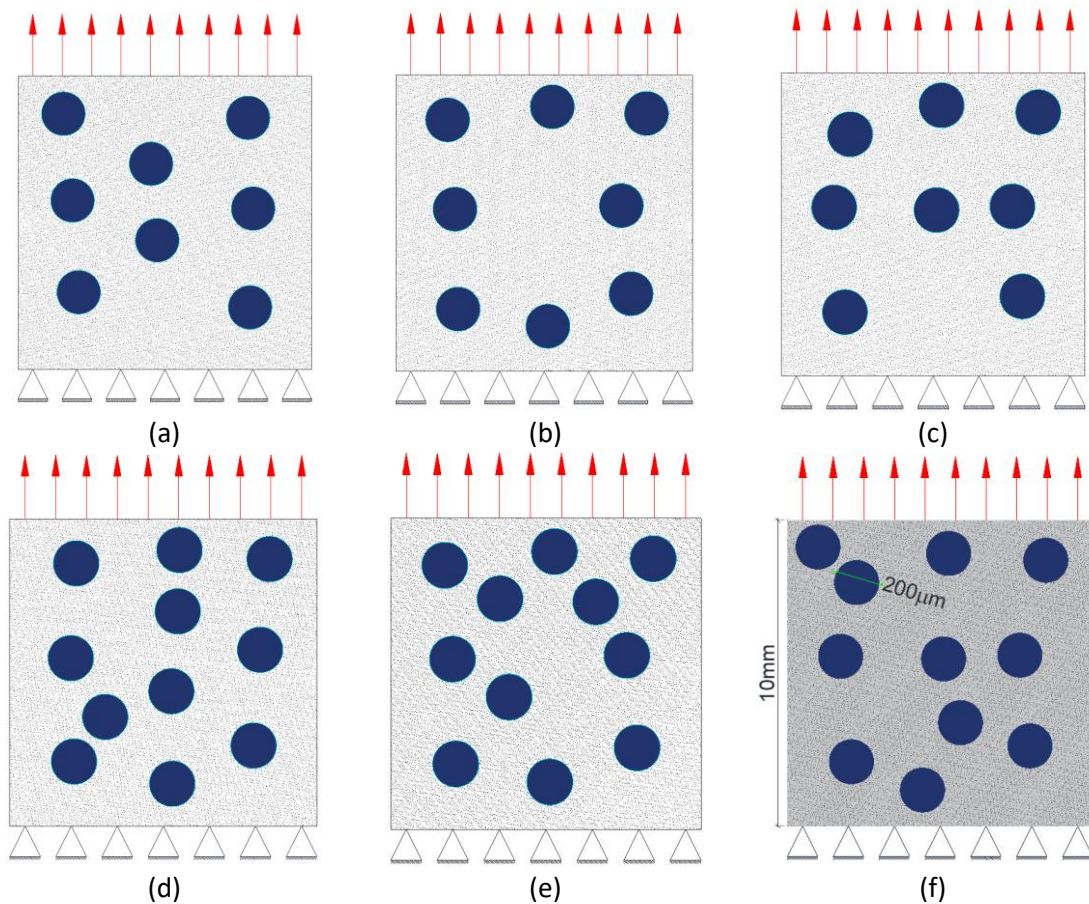


Figure 3-22 Schematic illustration of microcapsules within the cementitious matrix. a, b and c 1%; d, e and f are 3% volume fraction.

Figure 3-10 shows the different arrangements of microcapsules with different volume fractions. For these simulations, 10 volume fractions with 10 different random distributions were assessed and the maximum healing ratio calculated for each case. In all these simulations, the matrix and capsules properties were constant, as given in Table 3-5.

Table 3-5 Material properties*

Matrix			Interface			Capsule				
E	ν	f_t	E	ν	f_t	E	ν	f_t	Ω_c	Pos
31000	0.2	1	31000	0.2	1	3100	0.2	1	1-10%	10-Ran

* The unit of E , f_c and f_t is (N/mm^2)

The results from the series of analyses shows that the possibility of triggering capsules and healing the cracks strongly depends on the arrangement and number of capsules within the RVE. Figure 3-23 shows the maximum healing potential versus ($\bar{\omega}$) for different capsules arrangement. The mean probability of healing for each volume fraction of capsules was calculated by averaging the derived values (i.e. the number of damaged elements, number of healed elements and number of activated capsules through loading history) for different capsules positions. As shown, the average healing potential increases with the volume fraction of capsules. Although, beyond a volume fraction of 5% the healing ratio becomes constant. The graphs shown in Figure 3-24 suggest that the healing ratio initially decreases as the damage parameter increases but eventually reaches a plateau when the damage parameter reaches approximately 0.5

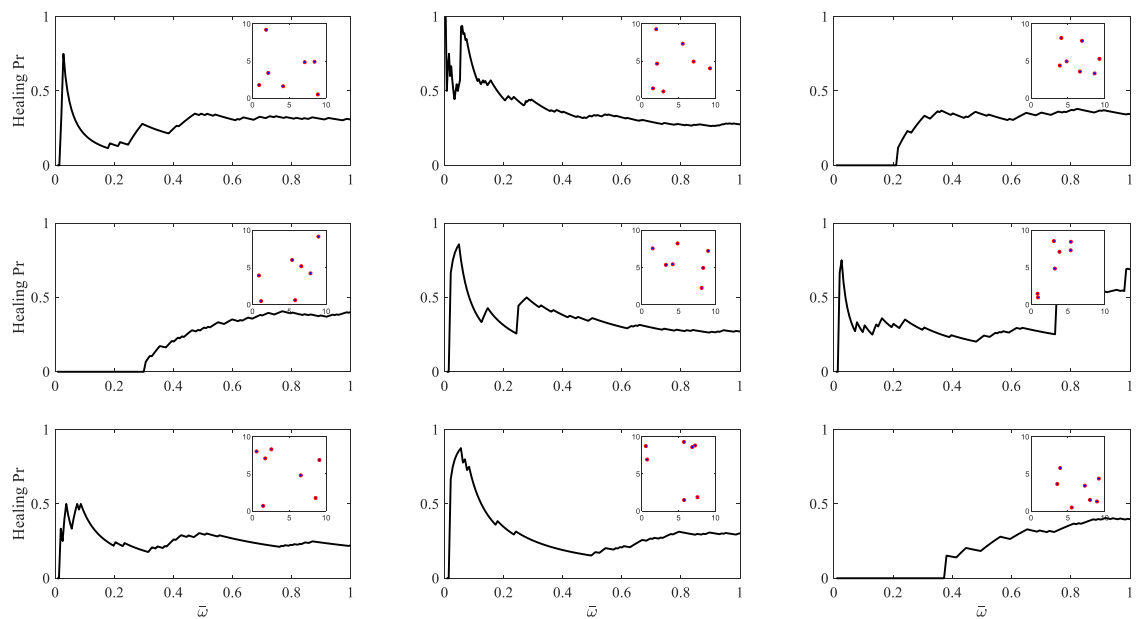


Figure 3-23 Maximum healing probability for different capsules arrangement

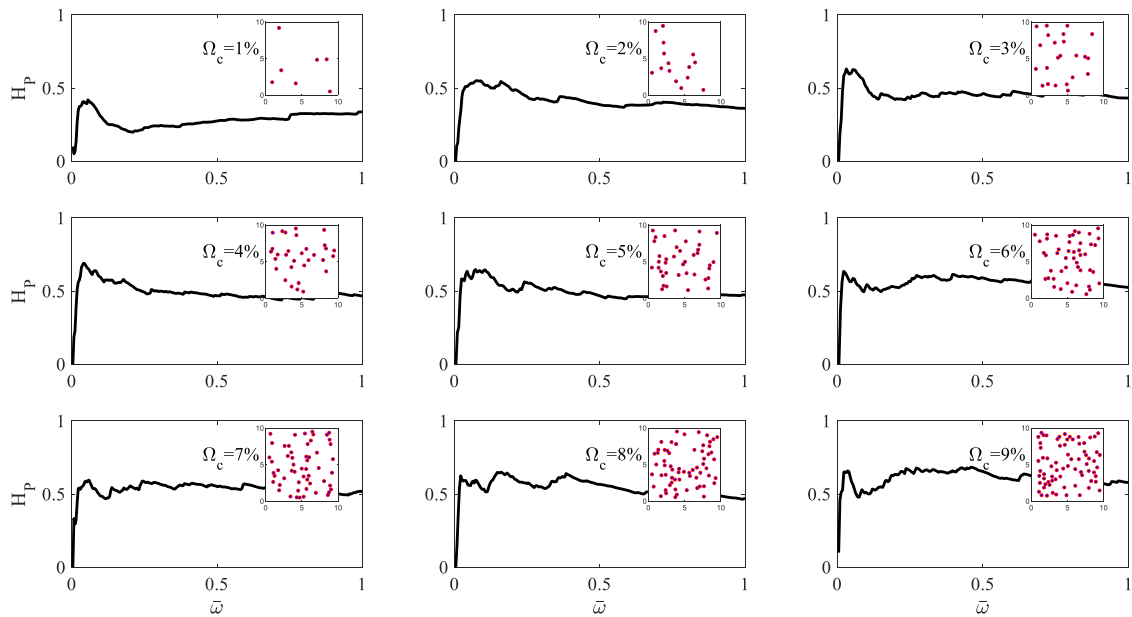


Figure 3-24 Average of maximum healing probability for different capsules volume fraction

The ratio of activated capsules to the total number of capsules in the RVE is presented in Figure 3-25. This shows that the ratio of capsules activated does not necessarily rise with the total number of capsules. These simulations suggest that the optimum range of microcapsules is between 3 and 5 percent for the cementitious material considered in this study.

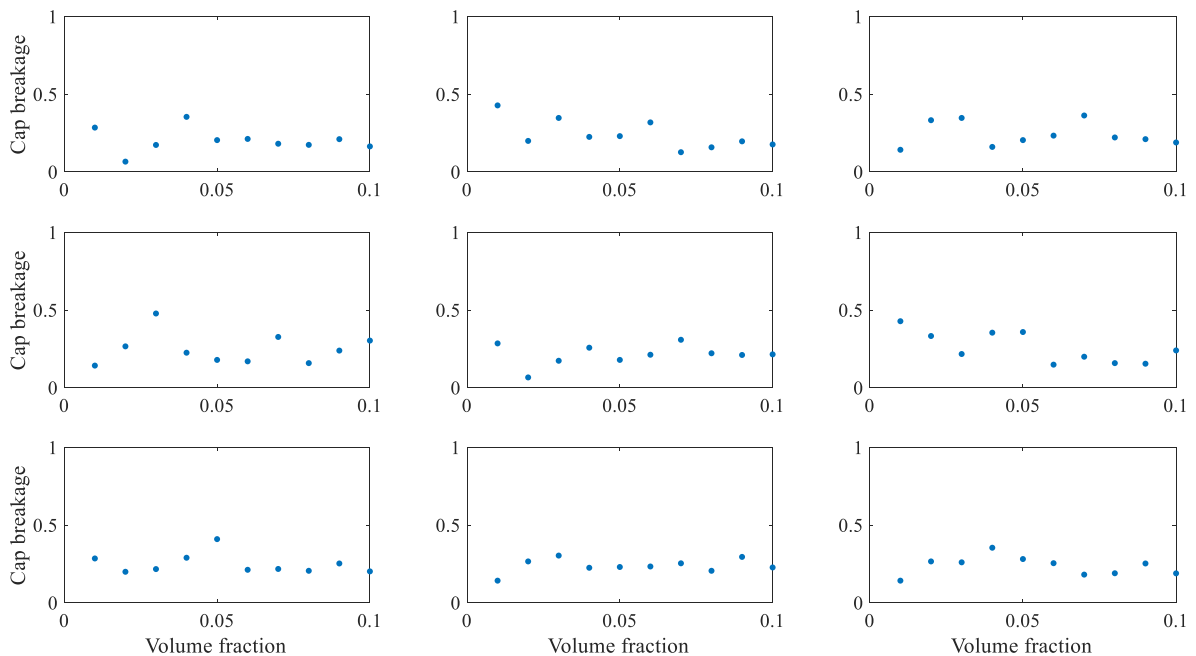


Figure 3-25 Percentage of capsules breakage for different arrangement

3-11 Conclusions

A model has been presented for simulating the response of structural elements formed from self-healing cementitious materials based on the TUDelft lattice framework. The existing LBM has been extended to account for simultaneous and rate-dependent damage and healing processes. The main conclusions from the present study are given below.

The model is able to replicate the mechanical response of self-healing cementitious materials with good accuracy, including fracture and rate-dependent healing behaviour.

It is able to simulate multiple healing cycles, as well as overlapping damage and healing processes.

The meso-scale lattice simulations provide valuable information on the size, geometry and disposition of the fracture and healing zones for the full history of a simulation. In addition, the model can be used to determine response data for regions that is hard to access and observe.

The method provides a viable means of computing the amount of agent required to produce healing at any time within an analysis.

The mechanical and chemical properties of healing agents have a significant influence on the degree of healing and on the overall response of a self-healing material.

The rate of applied loading and the healing rate of an agent both influence strongly the mechanical response of a self-healing structural element.

The experimental and numerical results indicate that, for multiple re-healing-re-damaging scenarios, the overall response reaches an asymptote in which healing and damage increments balance each other.

The detailed meso-scale data provided by the new lattice model would be of considerable value to researchers developing new self-healing material systems, as well as to engineers designing structural elements formed from self-healing materials.

The explicit mesostructural simulations show that using idealised regular shapes for inclusions, in place of more accurate irregular shapes, affects the crack pattern but has a negligible effect on overall mechanical response.

The disposition of capsules within a cementitious matrix has a significant influence on the degree of healing and on the probability that given percentage of capsules will be triggered. Also, the number of activated capsules does not necessarily increase with microcapsule dosage.

The optimal dosage of microcapsules was found to be approximately 5%. This percentage was found to maximize the probability of healing whilst minimizing the reduction in mechanical properties due to the presence of the microcapsules.

Chapter 4

Micromechanical model

4-1 Introduction

In this chapter, a new micromechanics-based constitutive model for self-healing cementitious materials is proposed. The model is aimed at self-healing materials with distributed healing mechanisms, such as materials with embedded microcapsules and enhanced autogenous healing capabilities. The model considers anisotropic microcracking and time-dependent healing with no restrictions on the number or timing of microcracking or healing events that can be simulated. An efficient two-level recursive scheme is adopted for computing the healing and re-microcracking state variables. The formulation ensures that the simulation of microcracking and healing is always consistent with the second law of thermodynamics. A series of single point simulations illustrate the versatile capabilities of the model, and the model is validated using experimental data. The experiments considered with the model include a set of cylindrical specimens formed of concrete with embedded microcapsules containing sodium silicate. The validations showed that the model is able to capture the characteristic mechanical behaviour of these structural elements.

In the remainder of this chapter, the overall micromechanical formulation for capturing microcracking behaviour is explained in sections 4-2 and 4-3. Section 4-4 describes in detail the derivation of the self-healing formulation. A new approach for ensuring that there is zero stress change during a pure healing increment is presented in subsection 4-4-2. Section 4-5 is devoted to the numerical implementation and sections 4-6 and 4-7 present different types of examples that describes single point and parametric simulations, along with a series of validation examples of the proposed constitutive formulation.

4-2 Micromechanical formulation for microcracking and healing

The main concepts of the constitutive model are presented in Figure 4-1. The cementitious composite is modelled as an elastic solid containing series of randomly distributed circular microcracks which can have any orientation, defined by ψ and θ (see Figure 4-1a). The model accounts for healing by simulating the filling of the microcracks with healing agent and subsequent curing of the agent (see Figure 4-1b). The model aims to represent the behaviour of a representative material element (RME).

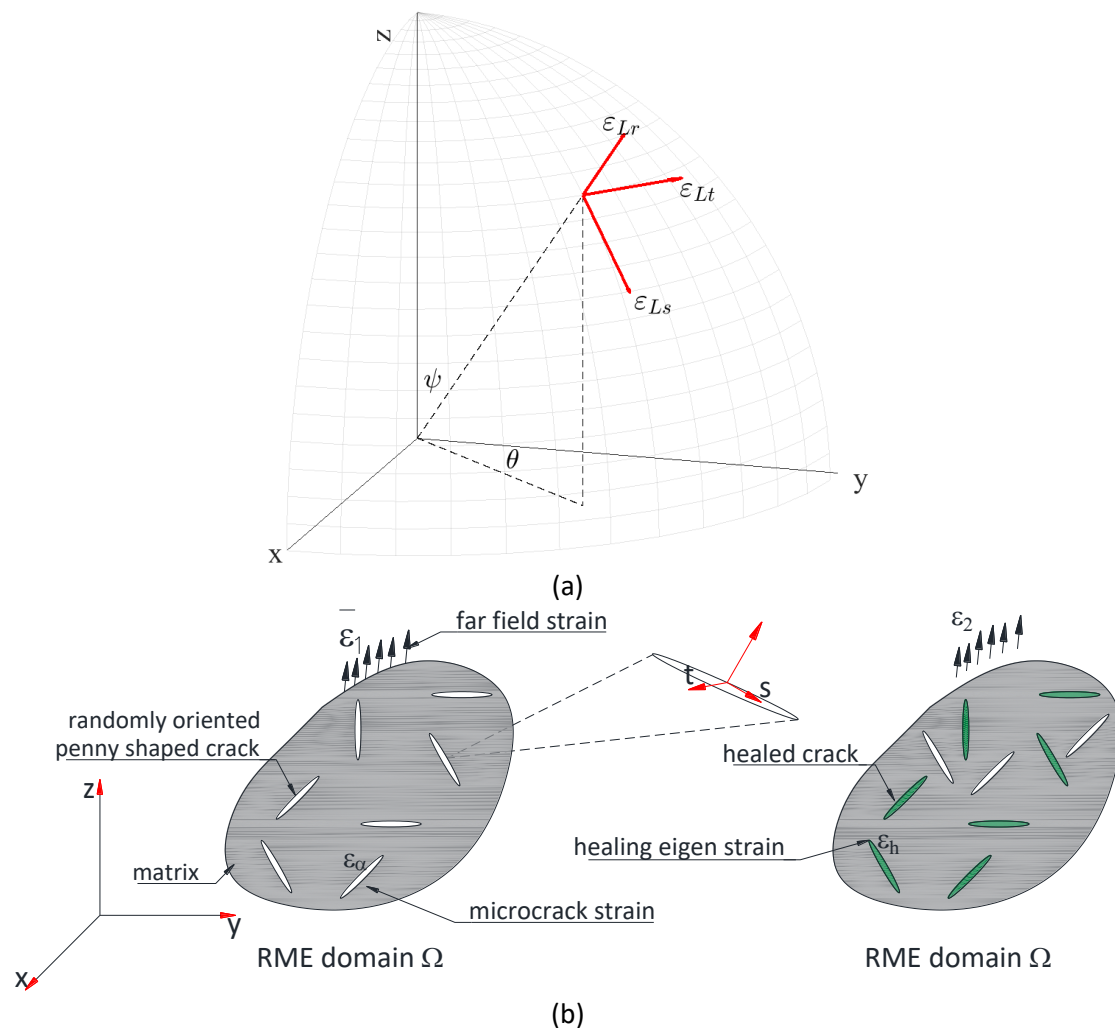


Figure 4-1 Schematic representation of RME. a) Coordinate system: b) illustration of microcracked (left) and partially healed (right), material states.

4-3 Directional microcracking

The model draws on a series of previous micromechanics-based constitutive formulations for cementitious materials (Davies & Jefferson, 2017; A. Jefferson & Bennett, 2007; I. C. Mihai & Jefferson, 2011). These authors, in turn, employed the model of Budiansky and

O'Connell (1976) (see also Nemat-Nasser & Hori, 1997) to represent microcracking. In this approach, the effects of multi-directional microcracking are represented by an additional strain tensor, $\boldsymbol{\varepsilon}_{\text{add}}$, in the following constitutive relationship:

$$\boldsymbol{\sigma} = \mathbf{D} : (\boldsymbol{\varepsilon} - \boldsymbol{\varepsilon}_{\text{add}}) \quad (4.1)$$

where $\boldsymbol{\varepsilon}_{\text{add}}$ is the overall additional strain due to microcracking, which can be initiated in any direction, $\boldsymbol{\sigma}$ and $\boldsymbol{\varepsilon}$ are the overall stress and strain tensors respectively, and \mathbf{D} is the elasticity tensor.

For a series of circular microcracks that have the same orientation, defined by (ψ, θ) , the non-zero components of the added strain tensor (Jefferson & Bennett, 2007) are given by:

$$\boldsymbol{\varepsilon}_{\alpha} = \mathcal{f} \frac{16(1-\nu^2)}{3E} \begin{bmatrix} s_{rr} \\ \frac{4}{2-\nu} s_{rs} \\ \frac{4}{2-\nu} s_{rt} \end{bmatrix} \quad (4.2)$$

where \mathcal{f} is the crack density parameter, ν and E are Poisson's ratio and Young's modulus of the elastic medium respectively. \mathbf{s} is the local stress tensor.

For convenience, in this chapter, a reduced form of tensors is given -as a vector or matrix- in which only those terms that can be non-zero are included e.g. $\mathbf{s} = [s_{rr} \ s_{rs} \ s_{rt}]^T$.

To account for the effects of all active microcracks, the added strains $\boldsymbol{\varepsilon}_{\alpha}$ from equation (4.2) are integrated over a hemisphere S (Nemat-Nasser & Hori, 1997) as follows.

$$\boldsymbol{\varepsilon}_{\text{add}} = \frac{1}{2\pi} \oint_S \mathbf{N}_{\varepsilon} : \boldsymbol{\varepsilon}_{\alpha} \quad (4.3)$$

where \mathbf{N}_{ε} is the strain transformation tensor (Jefferson, 2003).

In each direction, the crack density parameter is represented as a function of a directional microcracking variable (ω) which varies from 0 for intact material to 1 for fully microcracked material. The relationship between the microcracking variable and the crack density parameter was derived by Jefferson & Bennett (2007), and is given by:

$$\mathcal{f} = \frac{3}{16(1-\nu^2)} \left(\frac{\omega}{1-\omega} \right) \quad (4.4)$$

Substituting equation (4.4) into equation (4.2) gives

$$\boldsymbol{\varepsilon}_\alpha = \left(\frac{\omega}{1-\omega} \right) \mathbf{C}_L : \mathbf{s} \quad (4.5)$$

in which the local compliance tensor (\mathbf{C}_L), which relate rr , rs and rt strain to stress components, may be expressed by the following matrix: $\left(\frac{1}{E} \right) \begin{bmatrix} 1 & 0 & 0 \\ 0 & \frac{4}{(2-\nu)} & 0 \\ 0 & 0 & \frac{4}{(2-\nu)} \end{bmatrix}$

If the local strain tensor in each direction is defined as $\boldsymbol{\varepsilon}_L$, such that it comprises the sum of the added ($\boldsymbol{\varepsilon}_\alpha$) and the elastic ($\boldsymbol{\varepsilon}_{Le}$) local strain tensors, a local stress-strain relationship may be derived from (4.5) to be:

$$\mathbf{s} = (1-\omega) \mathbf{D}_L : \boldsymbol{\varepsilon}_L \quad (4.6)$$

where $\mathbf{D}_L = \mathbf{C}_L^{-1}$

The local variables (i.e. $\boldsymbol{\varepsilon}_\alpha$, \mathbf{s} and ω) are functions of direction (i.e. θ , ψ), and equation (4.6) has the form of a conventional isotropic damage mechanics stress-strain relationship (Krajcinovic, 1996) except that here it relates to local stress to local strain tensors.

4-3-1 Microcrack evolution function

The microcracking function, also termed the microcracking strain surface, given in equation (4.7) is taken from (Jefferson & Bennett, 2010).

$$F_\zeta(\boldsymbol{\varepsilon}_L, \zeta) = \zeta_{ef} - \zeta \quad (4.7)$$

in which $\zeta_{ef} = \left(\frac{\varepsilon_{Lrr}}{2} \left(1 + \left(\frac{\mu}{q} \right)^2 \right) + \frac{1}{2q^2} \sqrt{\varepsilon_{Lrr}^2 (q^2 - \mu^2)^2 + 4q^2 \gamma^2} \right)$, $\mu = \frac{\mu_s E}{G}$, $\gamma = \sqrt{\varepsilon_{Lrs}^2 + \varepsilon_{Lrt}^2}$, $q = \frac{q_s E}{G}$, ζ_{ef} is termed the effective microcracking strain and ζ is the microcracking strain parameter. μ_s is the friction angle between matrix and aggregate and q_s is the ratio of interface shear strength to matrix tensile strength.

The following loading-unloading conditions apply to equation (4.7) once the effective microcracking strain in a particular direction exceeds the crack initiation strain (ε_t):

$$F_\zeta \leq 0; \dot{\zeta} \geq 0; F_\zeta \dot{\zeta} = 0 \quad (4.8)$$

$\varepsilon_t = \frac{f_{t_i}}{E}$ and f_{t_i} is the uniaxial tensile stress at which microcracking initiates, noting that f_{t_i} is normally significantly lower than the uniaxial tensile strength of the cementitious composite (f_t).

The evolution of the microcracking variable is given by the following equation, taken from I. C. Mihai & Jefferson (2011):

$$\omega(\zeta) = 1 - \frac{\varepsilon_t}{\zeta} e^{-c \left(\frac{\zeta - \varepsilon_t}{\varepsilon_0 - \varepsilon_t} \right)} \quad (4.9)$$

in which c is the microcrack evolution constant, $\varepsilon_0 = \frac{u_o}{l_e}$ is the strain at the fully microcracked state, u_o is displacement at the end of the softening curve and l_e is the finite element characteristic length. This is based on Bažant & Oh (1983) crack-band model, which assumes that when softening commences, the strains will localise into a one-element-wide band within a finite element mesh. This ensures that the energy consumed in the formation of a crack (G_f) does not change with the mesh grading, noting that $G_f = f_t \int_0^\infty e^{-c \left(\frac{\zeta - \varepsilon_t}{\varepsilon_0 - \varepsilon_t} \right)} d\zeta$.

Figure 4-2b illustrates the microcracking strain surface (equation(4.7)) and shows a set of parallel microcracks in the cementitious composite.

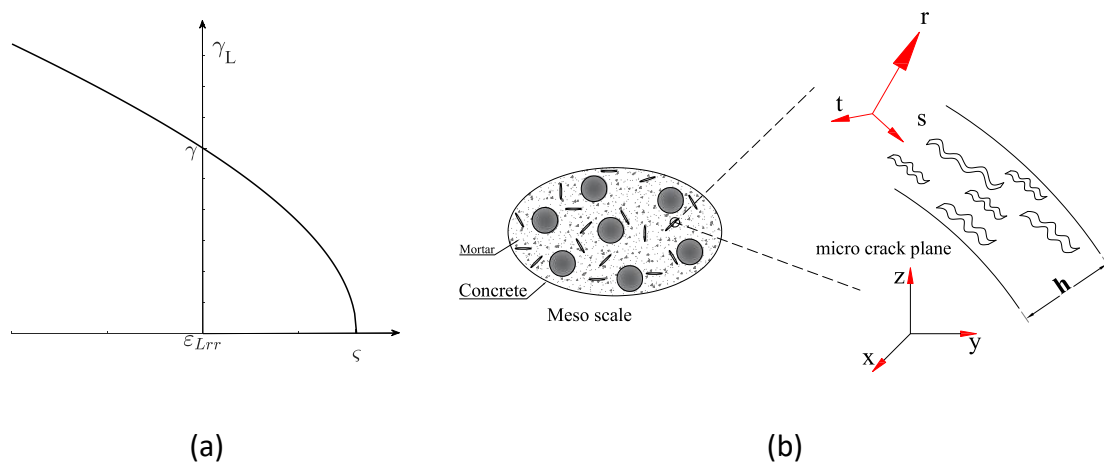


Figure 4-2 Microcracking strain surface, b) parallel set of microcracks

The response of the microcracking evolution function is illustrated in Figure 4-3 for a range of material parameters. This figure shows that the value of c has a strong influence on the post-peak stress behaviour. The actual values of c used in later simulations are calibrated from material constitutive data. The microcrack initiation strain (ε_t) mainly

affects the pre-peak response whilst the strain at the end of softening curve (ε_0) -as with c - affects the post-peak behaviour.

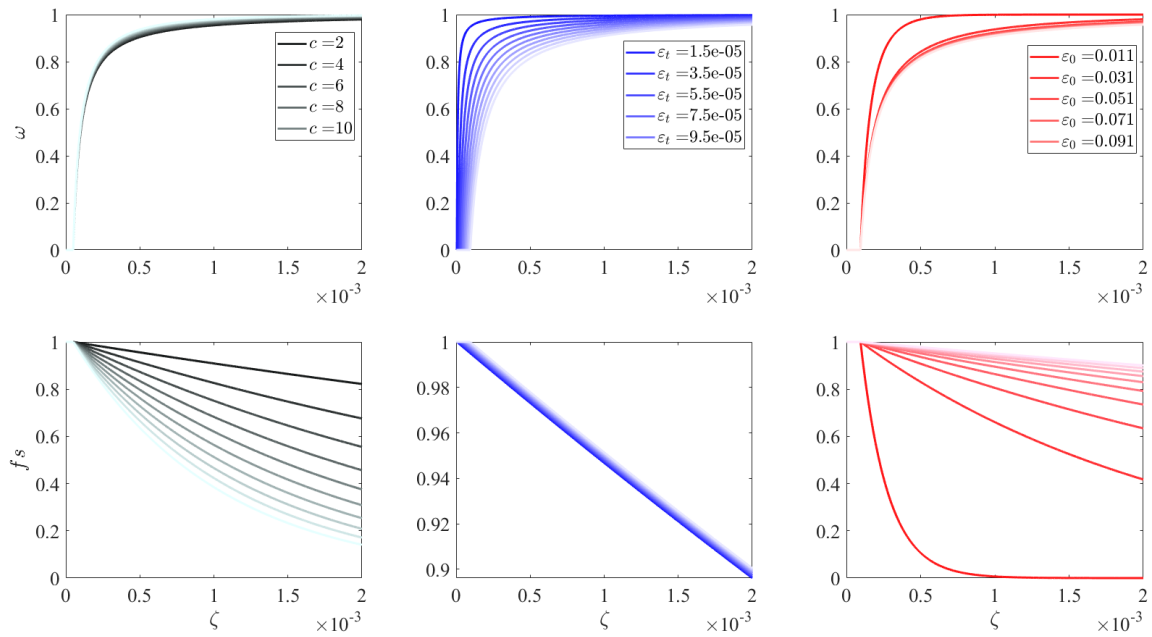


Figure 4-3 Microcracking evolution response with respect to different material parameters.

The effect of the alignment of the microcracks on overall response of an RME is illustrated in the following example. In this example, three scenarios are considered where the microcracks develop at $\psi=0^\circ$, $\psi=45^\circ$ and in randomly distributed orientations. It is assumed that the crack density variable varies from 0 to 1. For the aligned microcrack case, the elastic moduli were computed using the method described by Nemat-Nasser & Hori, 1997. The results are normalized to the representative material parameters as noted in Table 4-1 .

Table 4-1 RME characteristics used for simulation in Figure 4-4

Variables	E (N/mm ²)	ν	f_{ti}	ε_0
Properties	24000	0.15	1	0.001

As shown in Figure 4-4, the material strength and stiffness degraded the most when the microcracks align with the major tensile strain plane. Moreover, the comparison between the normalised secant stiffness matrix component ($\mathbf{M} = \mathbf{D}^{-1} \mathbf{D}_{sec}$) (see Figure 4-4d and f) reveals that the micromechanical formulation simulates anisotropic behaviour due to the microcracks forming in different orientations.

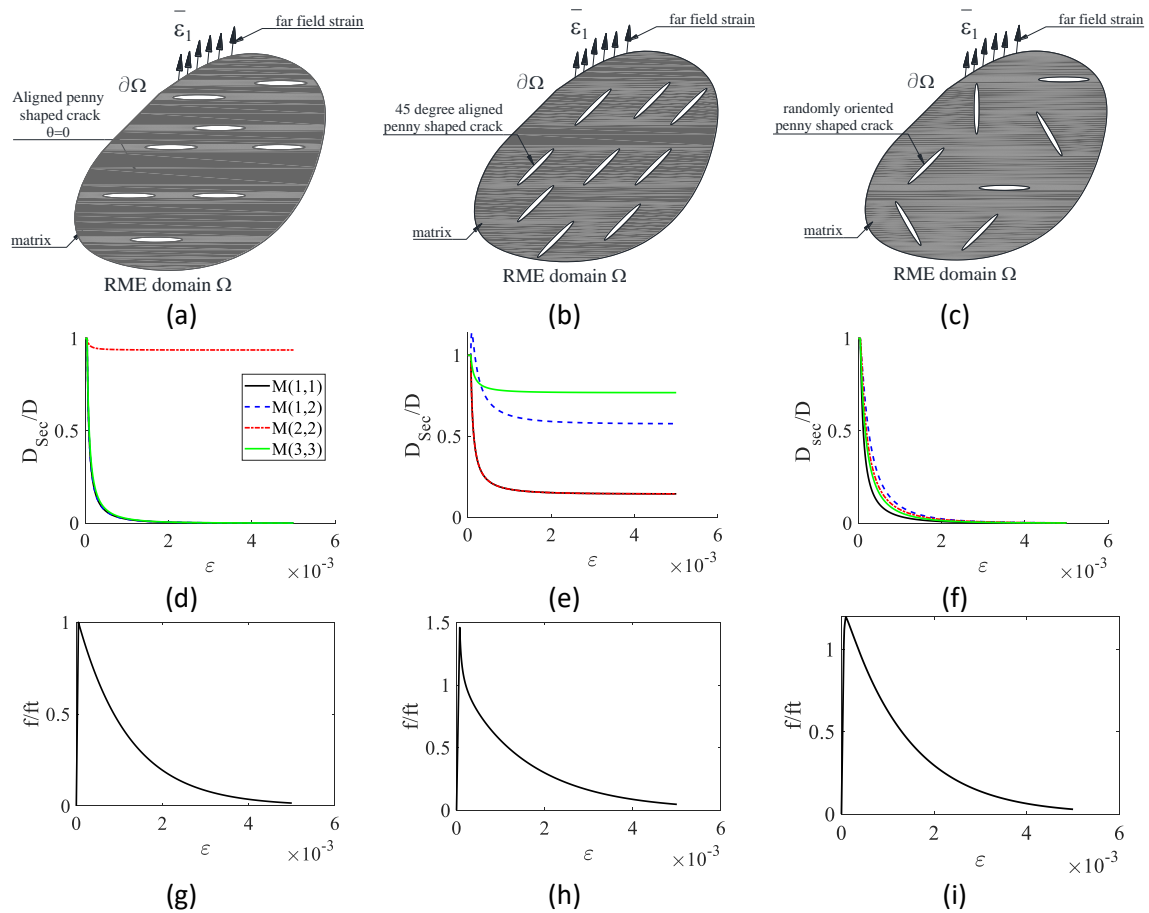


Figure 4-4 RME behaviour under different microcrack configurations, a-c) microcracking alignment, d-f) compliance matrix variation for different microcracking alignments, and g-f) corresponding constitutive behaviour

4-4 Healing simulation

The effect of healing on the mechanical properties is taken into account by restoring the stiffness of the healed material in the local constitutive relationship (equation (4.6)), via the healing variable ($h_v \in [0, \omega]$). This represents the proportion of microcracked material that is healed material at a given time. The evolution of h_v is explained in Section 4-4-1. When healing agent cures in an open microcrack, there is a moment in time when solid material first bridges between the opposing crack faces. This is when mechanical healing of the crack commences, and it is assumed that this bridging material is stress free at the time of formation. This ‘stress free at formation’ condition is assumed to apply to every new increment of bridging material. This assumption is not only consistent with experimental data (Selvarjoo et al. 2020), but also ensures that the simulation of healing does not create spurious energy and therefore does not violate the second law of thermodynamics. Expanding on this issue; when healing is simulated, the stiffness of the

material increases. Thus, if the strain remained constant, the stress and the strain energy would increase. This would violate the second law unless the increase in strain energy was matched by the release of thermal-chemical energy. Since there is no evidence that the stress rises during healing, the surest way to ensure that the model satisfies thermodynamics principles is to introduce a healing strain ($\boldsymbol{\varepsilon}_h$) that evolves such that the stress does not change due to healing alone. Furthermore, this strain simulates the permanent strains associated with solidified healing agent, which prevents microcracks from fully closing. Further detail and mathematical explanation related to discrete crack is explained in (Jefferson & Freeman, 2022). In this thesis, and for the micromechanical model, the method that used to compute $\boldsymbol{\varepsilon}_h$ is described in Section 4-4-2. The model also accounts for the fact that the healed material re-microcracks by employing a second microcracking variable, termed the healed microcracking variable, ($\omega_h \in [0,1]$), which gives the proportion of previously healed material that has re-microcracked. ω_h evolves according to equation (4.9) except that ζ , ε_0 & ε_t are replaced by their healed material counterparts i.e. ζ_h , ε_{h0} & ε_{ht} . Generally, in this Chapter, the subscript (*h*) denotes healed material. This convention is applicable to the rest of the examples presented in this chapter.

The addition of healing and re-microcracking to equation (4.6) leads to the following local constitutive equation:

$$\mathbf{s}_{Lh} = (1 - \omega)\mathbf{D}_L : \boldsymbol{\varepsilon}_L + h_v(1 - \omega_h)\mathbf{D}_{Lh} : (\boldsymbol{\varepsilon}_L - \boldsymbol{\varepsilon}_h) \quad (4.10)$$

where \mathbf{s}_{Lh} is the local stress tensor after healing, and \mathbf{D}_{Lh} the local elasticity matrix of the healed material.

The local strain tensor may be obtained by re-arranging equation (4.10), as follows:

$$\boldsymbol{\varepsilon}_L = [(1 - \omega)\mathbf{D}_L + h_v(1 - \omega_h)\mathbf{D}_{Lh}]^{-1} : [\mathbf{s}_{Lh} + h_v(1 - \omega_h)\mathbf{D}_{Lh} : \boldsymbol{\varepsilon}_h] \quad (4.11)$$

The variable $\boldsymbol{\varepsilon}_\alpha$ is now applied to the additional inelastic strain caused by all microcracking and healing. It is obtained by subtracting the local elastic component from the local strain, remembering that $\boldsymbol{\varepsilon}_\alpha = \boldsymbol{\varepsilon}_L - \boldsymbol{\varepsilon}_{Le}$, where the latter is now given by $\boldsymbol{\varepsilon}_{Le} = \mathbf{C}_L \mathbf{s}_{Lh}$. Thus, the additional inelastic strain is as follows:

Rearranging gives:

$$\boldsymbol{\varepsilon}_\alpha = [((1 - \omega)\mathbf{D}_L + h_v(1 - \omega_h)\mathbf{D}_{Lh})^{-1} : [\mathbf{s}_{Lh} + h_v(1 - \omega_h)\mathbf{D}_{Lh} : \boldsymbol{\varepsilon}_h] - \mathbf{C}_L : \mathbf{s}_{Lh} \quad (4.12)$$

$$\boldsymbol{\varepsilon}_\alpha = [((1 - \omega)\mathbf{D}_L + h_v(1 - \omega_h)\mathbf{D}_{Lh})^{-1} - \mathbf{C}_L] : \mathbf{s}_{Lh} + \left[\frac{(1 - \omega)}{h_v(1 - \omega_h)} \mathbf{C}_{Lh} \cdot \mathbf{D}_L + \mathbf{I}^{2s} \right]^{-1} : \boldsymbol{\varepsilon}_h \quad (4.13)$$

where \mathbf{I}^{2s} is the second order identity tensor, and $\mathbf{C}_{Lh} = \mathbf{D}_{Lh}^{-1}$.

Equation (4.13) shows that the additional microcracking strain has two major components, one (the 1st rhs term) is associated with the local stress, and the other (2nd rhs term) is linked to the healing strain.

The model assumes a static constraint for relating the local stress tensor to the Cartesian stress tensor as follows:

$$\mathbf{s}_{Lh} = \mathbf{N} : \boldsymbol{\sigma} \quad (4.14)$$

where \mathbf{N} is the stress transformation tensor (Jefferson and Bennett, 2010)

The two components of total added strain are now obtained by numerically integrating equation (4.13) around a hemisphere and employing equation (4.15), as follows:

$$\boldsymbol{\varepsilon}_{at} = \frac{1}{2\pi} \oint_S \mathbf{N}_\varepsilon \cdot [((1 - \omega)\mathbf{D}_L + h_v(1 - \omega_h)\mathbf{D}_{Lh})^{-1} - \mathbf{C}_L] \cdot \mathbf{N} : \boldsymbol{\sigma} \quad (4.15)$$

$$\boldsymbol{\varepsilon}_{ah} = \frac{1}{2\pi} \oint_S \mathbf{N}_\varepsilon \cdot \left[\frac{(1 - \omega)}{h_v(1 - \omega_h)} \mathbf{C}_{Lh} \cdot \mathbf{D}_L + \mathbf{I}^{2s} \right]^{-1} : \boldsymbol{\varepsilon}_h \quad (4.16)$$

The method used to evaluate $\boldsymbol{\varepsilon}_h$, which is presented in section 4-4-2, ensures that there is no change in the global stress due to an increment of healing alone. The derivation of the method accounts for interactions between healed microcracks in different directions. The latter interactions were not considered in the method proposed by Davies and Jefferson (2017).

Using equations (4.15) and (4.16) in the overall constitutive relationship (based on equation (4.1) gives

$$\boldsymbol{\sigma} = \mathbf{D}_{sech} : (\boldsymbol{\varepsilon} - \boldsymbol{\varepsilon}_{ah}) \quad (4.17)$$

where \mathbf{D}_{sech} is the equivalent secant stiffness matrix, as given below.

$$\mathbf{D}_{\text{sech}} = (\mathbf{I}^{4s} + \frac{\mathbf{D}}{2\pi} \cdot \left(\frac{1}{2\pi} \oint \oint \mathbf{N}_\varepsilon \cdot [[(1-\omega)\mathbf{D}_L + h_v(1-\omega_h)\mathbf{D}_{Lh}]^{-1} - \mathbf{C}_L] \cdot \mathbf{N} \right)^{-1} \cdot \mathbf{D}) \quad (4.18)$$

where \mathbf{I}^{4s} is fourth order identity tensor.

4-4-1 Time dependent healing evolution

In this work it is assumed that the time taken for the healing agent to fill and start curing is t_{c0} ; thus, in the absence of re-microcracking, the relative proportion of material available for healing (a) is given by:

$$a(t) = \int_{t_{c0}}^t \dot{\omega}(s) ds \quad (4.19)$$

where t is the current time relative to the time at the start of an analysis.

Healing occurs by healing-agent curing in microcracks. The function (equation (4.20)) used to simulate the evolution of the degree of cure ($\phi_h \in [0,1]$) is taken from Selvarajoo et al. (2020) and Freeman & Jefferson (2022a, 2023).

$$\phi_h(t) = (1 - e^{-t_c/\tau}) \quad (4.20)$$

where τ is the curing time parameter, which depends on the chemical properties of the healing agent and the current curing time ($t_c = t - t_{c0}$).

The response of the curing function with different material parameter values is illustrated in Figure 4-5.

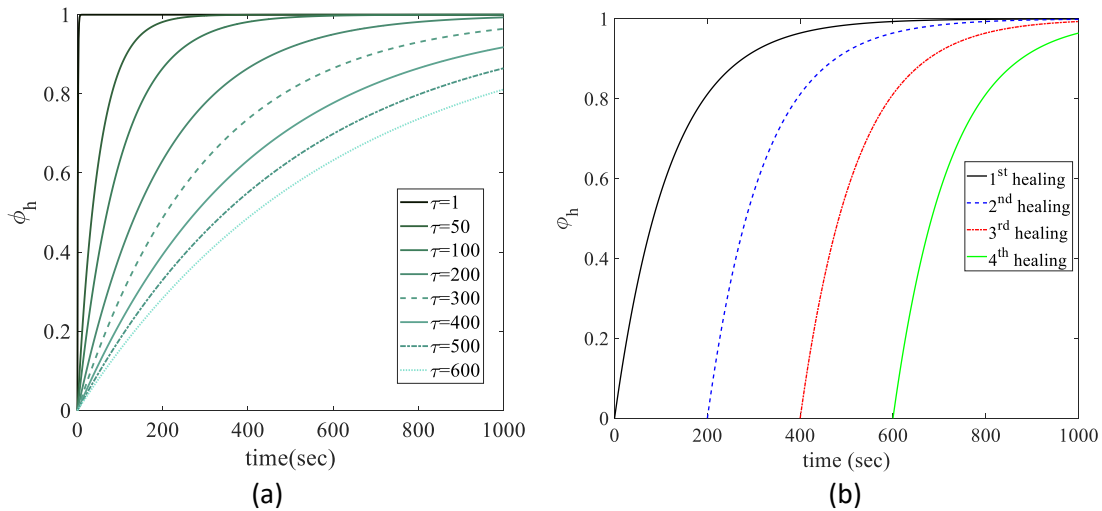


Figure 4-5 Curing function illustration, a) different τ , and b) different healing activation times

With these assumptions, and in the absence of re-microcracking, the degree of healing at time t is given by the following convolutional integral:

$$h_v(t) = \phi_{he} \int_{s=t_{c0}}^t \frac{\partial \omega}{\partial s} (1 - e^{-\frac{t-s}{\tau}}) ds \quad (4.21)$$

where ϕ_{he} is a healing efficiency parameter.

The assumption that the degree of cure matches the degree of healing is different from that used in the macrocrack healing model of Jefferson and Freeman (2022), in which healing was computed from the overlap of curing fronts within a macro-crack. However, in microcracks with relatively small crack opening displacements, the degree of heal may be equated directly to ϕ with little loss of accuracy.

Re-healing is defined as the healing of material that has previously healed and re-microcracked. The present model provides no restriction on the number of cycles of re-microcracking and re-healing. The evolution of the re-healing variable (h_r) is given by the same form of convolutional integral as that used for virgin healed material, given in equation (4.21), except that ω is replaced by ω_h , as follows:

$$h_r(t) = \phi_{he} \int_{t_{hr}}^t \frac{\partial \omega_h}{\partial s} (1 - e^{-t/\tau}) ds \quad (4.22)$$

where t_{hr} is the re-healing activation time.

Introducing (4.21) and (4.22) into equation (4.10) gives:

$$\begin{aligned} \mathbf{s}_{Lh}(t) = & (1 - \omega) \mathbf{D}_L : \boldsymbol{\varepsilon}_{Lh}(t) + \phi_{he} \int_s^t \frac{\partial \omega}{\partial s} \left(1 - e^{-\frac{t-s}{\tau}}\right) (1 - \omega_h(s)) \mathbf{D}_{Lh} : (\boldsymbol{\varepsilon}_{Lh}(t) - \boldsymbol{\varepsilon}_h(s)) ds \\ & + \phi_{he} \sum_{i=1}^n \int_{s_i}^t \frac{\partial \omega_{h_i}}{\partial s} \left(1 - e^{-\frac{t-s_i}{\tau}}\right) (1 - \omega_{h_i}(s)) \mathbf{D}_{Lh} : (\boldsymbol{\varepsilon}_{Lh}(t) - \boldsymbol{\varepsilon}_h(s_i)) ds \end{aligned} \quad (4.23)$$

where subscript i denotes the number of re-healing cycles of re-microcracked material.

Evaluating the second term in equation (4.23) requires the evolution of each parameter to be tracked and stored through time for each healing cycle. This potentially has a high computational cost and a considerable computer storage demand. Therefore, to avoid this computationally costly and inconvenient process, an averaging scheme was developed that introduced an equivalent microcracking parameter (ω_{heq}).

Through this homogenization approach, it is assumed that for an RME of unit area, the microcracked, healed, re-microcracked and re-healed have the relative areas illustrated in Figure 4-6. It is assumed that the re-microcracking variable is relative to the virgin healing proportion of material. The total healed material (h), at any one time, is the sum of the virgin healed proportion of material minus the re-microcracked portion, i.e. ($h = h_v(1 - \omega_h)$). The effect of re-healing on the reduction of the re-microcracking variable is shown in equation (4.24). In this case instead of having multiple portions of healed, re-healed or re-microcracked, the equivalent RME state would be shown in terms of healed and equivalent microcracked variables (ω_{heq}) as depicted in Figure 4-6. The key assumptions for this homogenisation technique were adopted from Jefferson & Freeman (2022) and adjusted for the micromechanical framework as follows:

- The re-healing process is considered in a way that healing agent is supplied instantaneously; therefore, any re-microcracked material within the RME is assumed to be curing.
- The curing process for re-healing material is the same as that for the virgin healing material.

It is assumed that at a specific time, the portion of healed material and re-healed material should be equal to the overall undamaged portion of healed material.

$$h_v(t)(1 - \omega_{heq}) = h_v(1 - \omega_h) + h_r \quad (4.24)$$

ω_{heq} , named the healed-microcracking variable, reduces when re-healing occurs and increases when re-microcracking occurs. $h_v(t)$ represents the limit of virgin healed material in terms of increasing ω .

By introducing the new equivalent re-cracking variable, equation (4.23) becomes:

$$\mathbf{s}_{Lh}(t) = (1 - \omega)\mathbf{D}_L: \boldsymbol{\varepsilon}_{Lh}(t) + h_v(t)(1 - \omega_{heq}(t))\mathbf{D}_{Lh}: (\boldsymbol{\varepsilon}_{Lh}(t) - \boldsymbol{\varepsilon}_h(t)) \quad (4.25)$$

After a healing update, the microcrack evolution of healed material is calculated, noting that the effective strain for healed material (ζ_h) is derived based on the increment of strain this material experienced after healing commenced.

The effective microcracking strain variable for re-microcracking is obtained from:

$$\zeta_{heff} = \zeta(\epsilon_L - \epsilon_h) \quad (4.26)$$

ζ_h evolves according to the healed equivalent of the loading-unloading conditions given in equation (4.8).

Figure 4-6 shows schematically the changing state of the material during successive microcracking-healing cycles.

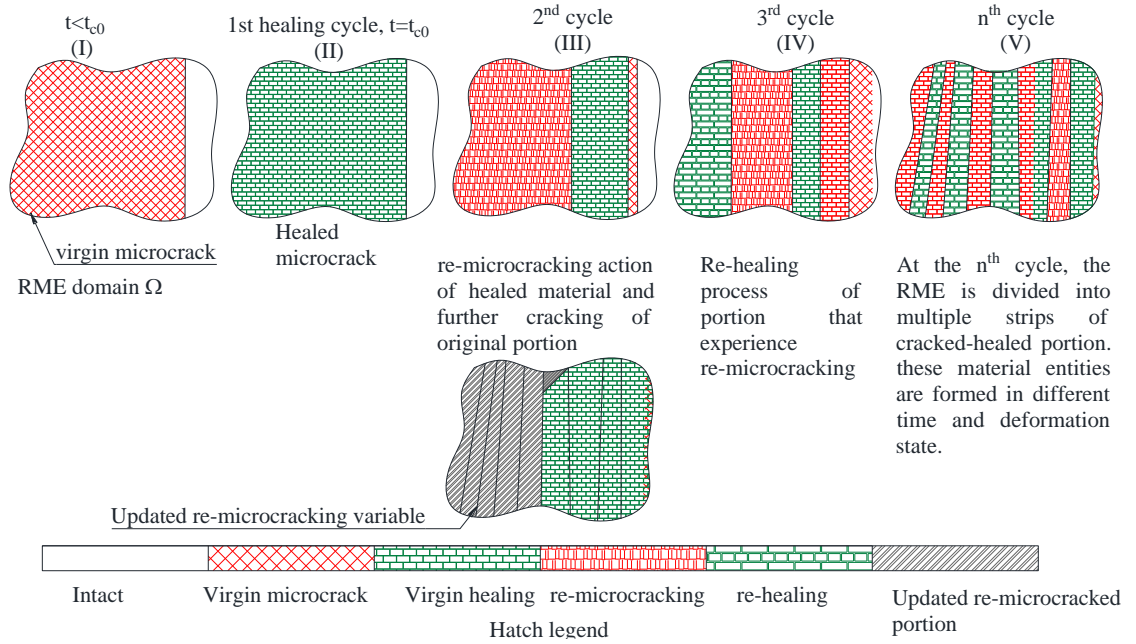


Figure 4-6. schematic representation of material states in successive microcracking and healing cycles.

4-4-2 Healing strain computation

Once healing commences, the healing agent is in a liquid state and starts to harden (cure) inside an open crack. This means that the healed portion of the material within the RME has an eigen strain denoted ϵ_h (healing strain). The healing agent curing process occurs in a stress-free condition as mathematically described in equation (4.10).

Introducing the healing strain into the local constitutive equation ($\mathbf{S}_{Lh}^* = \mathbf{D}_{Lh} : (\epsilon_L - \epsilon_h)$) for the healing component of material with the local stress tensor (\mathbf{s}_{Lh}^*) ensures that -during healing- the stress state does not change. This implies that the second thermodynamic law is also satisfied.

In former studies, the healing strain (ϵ_h) was calculated for an instantaneous healing event, during which the loading was constant. In this case, at each crack plane, the healing strain was obtained from the following equation (Davies & Jefferson, (2017):

$$\epsilon_h = C_L(1 - \omega_c)^{-1}s \quad (4.27)$$

where ω_c is microcracking variable at the moment that healing commences and here s is the current transformed local stress tensor. This zero change in local stress is only considered for a healing increment. Also, in the previous derivation, the zero stress change condition was not checked for all local crack planes. However, due to the interactions between cracks, the above equation might not fully satisfy the 2nd law of thermodynamic, especially for cases in which healing occurs under loaded conditions. The following example illustrates the above-mentioned flaws. For different loading conditions, as well as for different healing initiation times, the constitutive response is computed. The results, given in Figure 4-7, show the changes in the both the local and global stresses during healing step that occur when the healing strain is calculated using the method described by Davies & Jefferson (2017). In this figure, the results of computations undertaken using equations (4.10, (4.17, and (4.27) for a monotonic loading path and three different loading-unloading paths are presented for three different activation times. The mechanical parameters employed in this study are given in Table 4-2.

Table 4-2 Mechanical parameter for controlling the stress-free condition

Variables	E (N/mm ²)	E_h (N/mm ²)	ν, ν_h	f_{t_i}, f_{th} (N/mm ²)	t_{c_0} (s)
Properties	24000	24000	0.15	1	100, 200, and 400

As shown in Figure 4-7 the normal stress (denoted in the figure) changes significantly during the healing step (denoted by subscript $i - 1$ to i) for some cases. This stress change is much higher if healing commences when microcracking is well advanced (e.g. $\omega > 0.9$). According to Figure 4-7, for the loading-unloading scenario, the stress change during the healing step reduces from load path 1 to load path 3. This indicates that Davies and Jefferson's formulation introduces less error when healing occurs at low microcracking levels and in unloaded conditions.

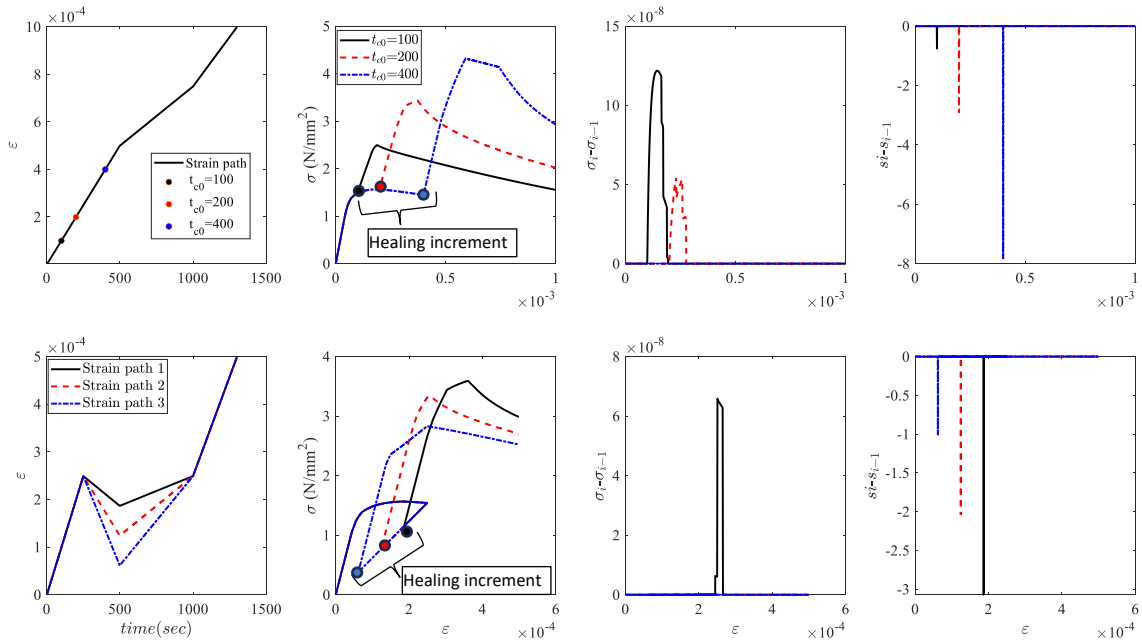


Figure 4-7 Illustration of stress-strain responses and stress changes during a healing increment, in global and local coordinates according to the method of Davies & Jefferson (2017).

The computed healing-increment stress changes for two contrasting cases are shown in Figure 4-8. (i) is for a fully unloaded condition and (ii) is for a scenario where the original material is almost fully microcracked when healing commences.

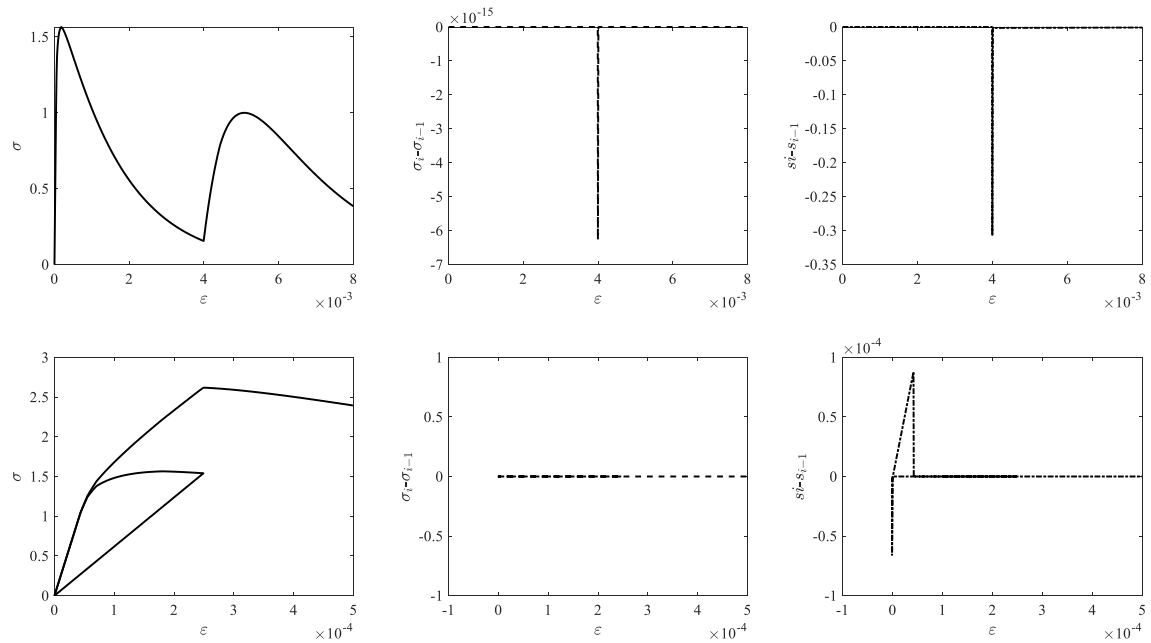


Figure 4-8 Stress state at healing step for fully microcracked and fully unloaded case

The above observation indicates that the approach to the calculation of the healing strain tensor needed to be modified in order to maintain the zero stress change condition

during a healing step. The revised approach, described below, accounts for the interactions between microcrack planes when healing occurs in open microcracks..

In the new method the local healing strain is derived by satisfying the zero-stress condition for the local crack; thus, during a healing increment, $\mathbf{s}_{Lh}^*(t)$: as given below, should not change.

$$h_v(t)(1 - \omega_h(t))\mathbf{D}_{Lh}(\boldsymbol{\varepsilon}_L(t) - \boldsymbol{\varepsilon}_h(t)) = \mathbf{s}_{Lh}^*(t) \quad (4.28)$$

Also, the healing strain for a set of healed microcracks should create no change in the Cartesian stress tensor during a healing increment. The healing strain tensor, in Cartesian coordinates for a set of healed microcracks, is derived from equation (4.29). This equation introduces a set of interaction factors which modify the local healing strains from those obtained given by equation (4.16). These modification factors may be determined by solving this equation (4.30). Converting the equation (4.3) in numerical form (equation (4.32)) gives 6 equations with 87 unknowns as noted below.

$$\boldsymbol{\varepsilon}_{ah} = \boldsymbol{\varepsilon} - \mathbf{D}_{sech}^{-1} \boldsymbol{\sigma}_{i-1} \quad (4.29)$$

$$\boldsymbol{\varepsilon}_{ah} = \frac{1}{2\pi} \oint_S \mathbf{N}_\varepsilon \cdot \left[\frac{(1 - \omega)}{h_v(1 - \omega_h)} \mathbf{C}_{Lh} \cdot \mathbf{D}_L + \mathbf{I}^{2s} \right]^{-1} \boldsymbol{\alpha} : \boldsymbol{\varepsilon}_h \quad (4.30)$$

$$\boldsymbol{\varepsilon}_{ah} = \sum_{id=1}^{29} \mathbf{N}_{\varepsilon_{id}} \cdot \left[\frac{(1 - \omega_{id})}{h_{v_{id}}(1 - \omega_{h_{id}})} \mathbf{C}_{Lh} \cdot \mathbf{D}_L + \mathbf{I}^{2s} \right]^{-1} \boldsymbol{\alpha}_{id} : \boldsymbol{\varepsilon}_{h_{id}} \quad (4.31)$$

Assuming that $\mathbf{N}_{\varepsilon_{id}} \cdot \mathbf{N}_{\varepsilon_{id}} \cdot \left[\frac{(1 - \omega_{id})}{h_{v_{id}}(1 - \omega_{h_{id}})} \mathbf{C}_{Lh} \cdot \mathbf{D}_L + \mathbf{I}^{2s} \right]^{-1}$ is a coefficient matrix for each direction considered (i.e.

each spherical integration direction), the revised system is as follows:

$$\sum_{id=1}^{29} \begin{bmatrix} C_{11}^{id} & C_{12}^{id} & C_{13}^{id} \\ C_{21}^{id} & C_{22}^{id} & C_{23}^{id} \\ C_{31}^{id} & C_{32}^{id} & C_{33}^{id} \\ C_{41}^{id} & C_{42}^{id} & C_{43}^{id} \\ C_{51}^{id} & C_{52}^{id} & C_{53}^{id} \\ C_{61}^{id} & C_{62}^{id} & C_{63}^{id} \end{bmatrix} \begin{bmatrix} \varepsilon_{h_1}^{id} \\ \varepsilon_{h_2}^{id} \\ \varepsilon_{h_3}^{id} \end{bmatrix} \boldsymbol{\alpha}_{id} = \begin{bmatrix} \varepsilon_{Gh_1} \\ \varepsilon_{Gh_2} \\ \varepsilon_{Gh_3} \\ \varepsilon_{Gh_4} \\ \varepsilon_{Gh_5} \\ \varepsilon_{Gh_6} \end{bmatrix} \quad (4.32)$$

Expanding the above series leads to following 6 equations:

$$\begin{bmatrix} C_{11}^1 \varepsilon_{h_1}^1 + C_{12}^1 \varepsilon_{h_2}^1 + C_{13}^1 \varepsilon_{h_3}^1 + C_{21}^2 \varepsilon_{h_1}^2 + C_{22}^2 \varepsilon_{h_2}^2 + C_{23}^2 \varepsilon_{h_3}^2 & \dots & C_{11}^{29} \varepsilon_{h_1}^{29} + C_{12}^{29} \varepsilon_{h_2}^{29} + C_{13}^{29} \varepsilon_{h_3}^{29} \\ C_{21}^1 \varepsilon_{h_1}^1 + C_{22}^1 \varepsilon_{h_2}^1 + C_{23}^1 \varepsilon_{h_3}^1 + C_{31}^2 \varepsilon_{h_1}^2 + C_{32}^2 \varepsilon_{h_2}^2 + C_{33}^2 \varepsilon_{h_3}^2 & \dots & C_{21}^{29} \varepsilon_{h_1}^{29} + C_{22}^{29} \varepsilon_{h_2}^{29} + C_{23}^{29} \varepsilon_{h_3}^{29} \\ C_{31}^1 \varepsilon_{h_1}^1 + C_{32}^1 \varepsilon_{h_2}^1 + C_{33}^1 \varepsilon_{h_3}^1 + C_{41}^2 \varepsilon_{h_1}^2 + C_{42}^2 \varepsilon_{h_2}^2 + C_{43}^2 \varepsilon_{h_3}^2 & \dots & C_{31}^{29} \varepsilon_{h_1}^{29} + C_{32}^{29} \varepsilon_{h_2}^{29} + C_{33}^{29} \varepsilon_{h_3}^{29} \\ C_{41}^1 \varepsilon_{h_1}^1 + C_{42}^1 \varepsilon_{h_2}^1 + C_{43}^1 \varepsilon_{h_3}^1 + C_{51}^2 \varepsilon_{h_1}^2 + C_{52}^2 \varepsilon_{h_2}^2 + C_{53}^2 \varepsilon_{h_3}^2 & \dots & C_{41}^{29} \varepsilon_{h_1}^{29} + C_{42}^{29} \varepsilon_{h_2}^{29} + C_{43}^{29} \varepsilon_{h_3}^{29} \\ C_{51}^1 \varepsilon_{h_1}^1 + C_{52}^1 \varepsilon_{h_2}^1 + C_{53}^1 \varepsilon_{h_3}^1 + C_{61}^2 \varepsilon_{h_1}^2 + C_{62}^2 \varepsilon_{h_2}^2 + C_{63}^2 \varepsilon_{h_3}^2 & \dots & C_{51}^{29} \varepsilon_{h_1}^{29} + C_{52}^{29} \varepsilon_{h_2}^{29} + C_{53}^{29} \varepsilon_{h_3}^{29} \\ C_{61}^1 \varepsilon_{h_1}^1 + C_{62}^1 \varepsilon_{h_2}^1 + C_{63}^1 \varepsilon_{h_3}^1 + C_{61}^2 \varepsilon_{h_1}^2 + C_{62}^2 \varepsilon_{h_2}^2 + C_{63}^2 \varepsilon_{h_3}^2 & \dots & C_{61}^{29} \varepsilon_{h_1}^{29} + C_{62}^{29} \varepsilon_{h_2}^{29} + C_{63}^{29} \varepsilon_{h_3}^{29} \end{bmatrix} = \begin{bmatrix} \varepsilon_{Gh_1} \\ \varepsilon_{Gh_2} \\ \varepsilon_{Gh_3} \\ \varepsilon_{Gh_4} \\ \varepsilon_{Gh_5} \\ \varepsilon_{Gh_6} \end{bmatrix} \quad (4.33)$$

Rearranging the above equation gives:

$$\begin{bmatrix} C_{11}^1 & C_{12}^1 & C_{13}^1 & C_{21}^2 & C_{22}^2 & C_{23}^2 & \dots & C_{11}^{29} & C_{12}^{29} & C_{13}^{29} \\ C_{21}^1 & C_{22}^1 & C_{23}^1 & C_{31}^2 & C_{32}^2 & C_{33}^2 & \dots & C_{21}^{29} & C_{22}^{29} & C_{23}^{29} \\ C_{31}^1 & C_{32}^1 & C_{33}^1 & C_{41}^2 & C_{42}^2 & C_{43}^2 & \dots & C_{31}^{29} & C_{32}^{29} & C_{33}^{29} \\ C_{41}^1 & C_{42}^1 & C_{43}^1 & C_{51}^2 & C_{52}^2 & C_{53}^2 & \dots & C_{41}^{29} & C_{42}^{29} & C_{43}^{29} \\ C_{51}^1 & C_{52}^1 & C_{53}^1 & C_{61}^2 & C_{62}^2 & C_{63}^2 & \dots & C_{51}^{29} & C_{52}^{29} & C_{53}^{29} \\ C_{61}^1 & C_{62}^1 & C_{63}^1 & C_{61}^2 & C_{62}^2 & C_{63}^2 & \dots & C_{61}^{29} & C_{62}^{29} & C_{63}^{29} \end{bmatrix}_{6 \times 87} \begin{bmatrix} \alpha_1 \varepsilon_{h_1}^1 \\ \alpha_1 \varepsilon_{h_2}^1 \\ \alpha_1 \varepsilon_{h_3}^1 \\ \alpha_2 \varepsilon_{h_1}^2 \\ \alpha_2 \varepsilon_{h_2}^2 \\ \alpha_2 \varepsilon_{h_3}^2 \\ \vdots \\ \alpha_{29} \varepsilon_{h_1}^{29} \\ \alpha_{29} \varepsilon_{h_2}^{29} \\ \alpha_{29} \varepsilon_{h_3}^{29} \end{bmatrix}_{87 \times 1} = \begin{bmatrix} \varepsilon_{Gh_1} \\ \varepsilon_{Gh_2} \\ \varepsilon_{Gh_3} \\ \varepsilon_{Gh_4} \\ \varepsilon_{Gh_5} \\ \varepsilon_{Gh_6} \end{bmatrix}_{6 \times 1} \quad (4.34)$$

The coefficient matrix size of this equation is 87×6 with 87 strain components and 29 modification factors as unknowns. The other constraint that needs to be satisfied is that the stress state at each local crack plane should also not change. Applying this local condition to the computation of the local healing strain for a finite healing step results in a nonlinear set of equations (4.35) that are solved using a Newton Raphson iterative procedure:

$$\begin{cases} \omega(\zeta(\varepsilon_L - \varepsilon_{h_i})) = 1 - \frac{(1 - \omega_{h_{i-1}})h_{i-1} + \Delta h_i}{h_{v_i}} \\ h_{v_i} \left(1 - \omega(\zeta(\varepsilon_L - \varepsilon_{h_i})) \right) (\varepsilon_L - \varepsilon_{h_i}) = h_{v_{i-1}} \left(1 - \omega(\zeta(\varepsilon_L - \varepsilon_{h_{i-1}})) \right) \end{cases} \quad (4.35)$$

where Δh_i is the additional healing increment at the current healing step. The subscript (i) denotes the current step. The variables at the former step (i-1) are known. The above equations are solved for ε_{h_i} . Subsequently the derived ε_{h_i} variables are substituted into equation (4.34) to determine the vector of microcracking interaction coefficient factors (α). Equation (4.34) is an under determined system of equations which has an infinite number of solutions. This may be resolved by applying the least squares constraint or singular value decomposition (SVD) method. Here, the SVD scheme is adopted.

An example is presented in order to compare the difference in responses obtained using the modified healing strain update with the method presented by Davies & Jefferson (2017). In this example the strain path and material parameters (Table 4-2), are the same as those used above for the computation of the responses shown in Figure 4-7 and Figure 4-8. The result of the comparison as shown in Figure 4-9, show that the difference in response computed using the two methods is much higher for the cases where healing commences at high level of the microcracking, as well as when healing under loaded conditions.

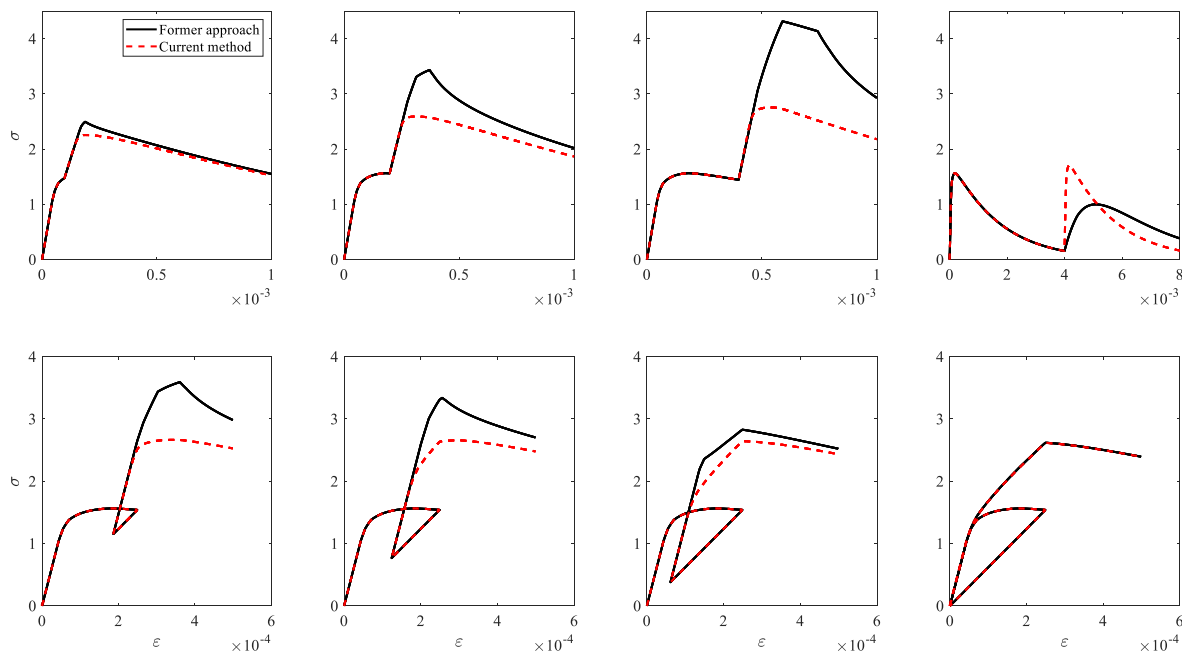


Figure 4-9 Comparing the difference in responses between method with modification factor and without.

4-5 Numerical implementation

The integration over the hemispherical domain is evaluated numerically using Maclaurin's integration rule with 29 sample directions (Stroud, 1973). A study on the accuracy, and effects of varying, the spherical integration rule used for this type of micromechanical model was undertaken by Mihai (2012) The choice of the 29-point integration rule followed the findings from Mihai's study. The evaluation of the spherical integrations represents a significant computational cost, although the nature of the micromechanics model is such that the computations undertaken for each integration direction are relatively in-expensive.

The constitutive relationship (equations (4.16)) is integrated over time using a time stepping procedure in which t_i defines the current time and $\Delta t (= t_i - t_{i-1})$ denotes a time-step.

A recursive scheme proposed by Mergheim & Steinman (2013) is adopted to evaluate the cumulative healing parameter at each time step. By knowing the amount of healed material at a previous step, the total healed material at the next step can be calculated as follows:

Each time step is sub-divided into a healing step and a mechanical step. The following algorithm is used to compute microcracking variables during mechanical step. The Newton Raphson technique is adopted to solve the nonlinear system of equations. The algorithm for deriving the healing variable for each microcrack is given in algorithm box 1.

$$h_{v_{i+1}} = h_{v_i} e^{-\frac{\Delta t}{\tau}} + a_{i+1} (1 - e^{-\frac{\Delta t}{\tau}}) \quad (4.36)$$

Algorithm 1 Computational algorithm for healing variables

<i>If healing = true</i>	if healing is activated at this step
1: for $j = 1$ to n_j	Loop over each direction
2: $a_{v_j} = a_{v_j} + \Delta\omega_j$	Calculate available microcracked material available for healing
3: $h_{v_j} = h_{v_j} e^{-\frac{\Delta t}{\tau}} + a_{v_j} (1 - e^{-\frac{\Delta t}{\tau}})$	Update the healing variable
4: $\omega_{heq_j} = 1 - \frac{(1 - \omega_{h_{j_{i-1}}}) h_{v_{j_{i-1}}} + \Delta h_j}{h_{v_{j_i}}}$	Derive equivalent re-microcracking variable
5: $SL_{i-1} = h_{v_{j_{i-1}}} (1 - \omega_{h_{j_{i-1}}}) D_{Lh}(\varepsilon_{L_{j_{i-1}}} - \varepsilon_{h_{j_{i-1}}})$	Applying the local stress-free condition
6: $\omega_{err} = \omega_{heq_j} - \omega(\zeta_h(\varepsilon_{L_{j_{i-1}}} - \varepsilon_{h_{j_i}}))$	Error due to initial guess for equivalent effective strain
7: $SL_i = h_{v_{j_i}} (1 - \omega_{h_{j_i}}) D_{Lh}(\varepsilon_{L_{j_{i-1}}} - \varepsilon_{h_{j_i}})$	Current local stress field after healing
8: $SL_{err} = SL_i - SL_{i-1}$	Stress difference due to initial guess for local healing strain
9: While $ SL_{err} ^{\wedge} \omega_{err} < tol$	Newton Raphson iteration for finding effective parameters
10: $\zeta_{h_j} = \zeta_{h_j} + \omega_{err} / \frac{\partial \omega}{\partial \zeta_{h_j}}$	Updating the effective strain
11: $\omega_{err} = \omega_{heq_j} - \omega(\zeta_{h_j})$	Updating re-microcrack error
12: $\varepsilon_{h_j} = \varepsilon_{h_j} + (\nabla SL_{err})^{-1} SL_{err}$	Updating healing strain
13: $SL_{err} = SL(\varepsilon_{L_{j_{i-1}}} - \varepsilon_{h_{j_i}})$	Updating local stress difference error

After calculation of local microcrack-healing variables during the healing step process, the global offset strain as well as the microcracking interaction factor is calculated by the method presented in Section 4-4-2

Algorithm 2 Computation algorithm for deriving crack interaction factor.

Global stress free check	if healing is activated at this step
1: for $j = 1$ to n_j	Loop over each direction
2: $\mathbf{A}_j = [(1 - \omega_{j_{i-1}})\mathbf{D}_L + h_{v_{j_i}}(1 - \omega_{heqj})\mathbf{D}_{Lh}]$	Local micro-healing matrix used in line 4 of this algorithm
3: end	
4: $\mathbf{D}_{sech} = \left(\mathbf{I} + \frac{\mathbf{D}_{el}}{2\pi} \sum_{j=1}^{29} \mathbf{N}_{\varepsilon_j}^T [\mathbf{A}_j^{-1} - \mathbf{C}_L] \mathbf{N}_j \right)^{-1} \mathbf{D}_{el}$	Calculate RME stiffness matrix after healing process
5: $\mathbf{D}_{sech} : (\boldsymbol{\varepsilon} - \boldsymbol{\varepsilon}_{ah}) = \boldsymbol{\sigma}_{i-1}$	Impose global stress free condition during healing
6: Solve for $\boldsymbol{\varepsilon}_{ah}$	Deriving the global healing strain
7: $\boldsymbol{\varepsilon}_{ah} = \sum_{j=1}^{n_j} \mathbf{N}_{\varepsilon_j}^T [\mathbf{A}_j^{-1} (h_{v_j}(1 - \omega_{hej})\mathbf{D}_{Lh})] \alpha \boldsymbol{\varepsilon}_{h_j}$	Setting the equation for deriving the microcrack interaction factor
8: Solve for α	

The algorithm developed for computing the stress and updating the microcracking and healing variables at a particular timestep is given in Algorithm box 3. For convenience, Voigt notation is used in the description of algorithm 3.

Algorithm 3 Constitutive driver algorithm

Inpt: $h_{v_{i-1}}, \omega_{h_{i-1}}, \sigma_{i-1}, \Delta \boldsymbol{\varepsilon}, \tau_0, \Delta t$.	Enter, required input parameters
(Mechanical and damage evolution properties)	
1: for $j = 1$ to n_j	Loop over integration direction
2: $\boldsymbol{\varepsilon}_{L_j} = \mathbf{N}_{\varepsilon_j} \boldsymbol{\varepsilon}$	Calculated local strain at each direction
3: $\zeta(\boldsymbol{\varepsilon}_L) = \frac{\varepsilon_{Lrr}}{2} \left[1 + \left(\frac{\mu}{q} \right)^2 \right] + \frac{1}{2q^2} \left(\sqrt{(q^2 - \mu^2)^2 \varepsilon_{Lrr}^2 + 4q^2 \gamma_L^2} \right)$ $\zeta_{eff} = \max(\zeta_{eff_{i-1}}, \zeta(\boldsymbol{\varepsilon}_L))$	Find effective strain parameters
4: Update ω_j	Update microcracking variable
5: end	
6: $\boldsymbol{\sigma} = \left(\mathbf{I} + \frac{\mathbf{D}_{el}}{2\pi} \sum_{i=1}^{29} \mathbf{N}_{\varepsilon_j}^T \frac{\omega_j}{1 - \omega_j} \mathbf{C}_L \mathbf{N}_i \right)^{-1} \mathbf{D}_{el} \boldsymbol{\varepsilon}$	Constitutive formulation with microcracks
7: If healing = true	if healing is activated at this step
8: follow algorithm 1 & 2	Loop over each direction
9: end	
10: mechanical step	Apply mechanical step (by strain or stress increment)
11: for $j = 1$ to n_i	Loop over each microcrack direction
12: $\boldsymbol{\varepsilon}_{L_j} = \mathbf{N}_{\varepsilon_j} (\boldsymbol{\varepsilon} + \Delta \boldsymbol{\varepsilon})$	Calculate local strain after applying load
13: $\zeta_{eff}(\boldsymbol{\varepsilon}_L) = \frac{\varepsilon_{Lrr}}{2} \left[1 + \left(\frac{\mu}{q} \right)^2 \right] + \frac{1}{2q^2} \left(\sqrt{(q^2 - \mu^2)^2 \varepsilon_{Lrr}^2 + 4q^2 \gamma_L^2} \right)$	Find effective strain parameters for original material
14: $\zeta_{heff}(\boldsymbol{\varepsilon}_L - \boldsymbol{\varepsilon}_h) = \frac{\varepsilon_{hrr}}{2} \left[1 + \left(\frac{\mu}{q} \right)^2 \right] + \frac{1}{2q^2} \left(\sqrt{(q^2 - \mu^2)^2 \varepsilon_{hrr}^2 + 4q^2 \gamma_L^2} \right)$ $\zeta_{eff} = \max(\zeta_{eff_{i-1}}, \zeta(\boldsymbol{\varepsilon}_L))$ $\zeta_{heff} = \max(\zeta_{heff_{i-1}}, \zeta_{heff}(\boldsymbol{\varepsilon}_L - \boldsymbol{\varepsilon}_h))$ Update ω_j & ω_{h_j}	Find effective strain parameters for healed material
15: Update ω_j & ω_{h_j}	Update microcracking variables for original and healed
16: $\mathbf{A}_j = [(1 - \omega_j) \mathbf{D}_L + h_{v_j} (1 - \omega_{h_j}) \mathbf{D}_{Lh}]$	Update healing parameters
17: end	
18: $\mathbf{D}_{sech} = \left(\mathbf{I} + \frac{\mathbf{D}_{el}}{2\pi} \sum_{j=1}^{29} \mathbf{N}_{\varepsilon_j}^T [\mathbf{A}_j^{-1} - \mathbf{C}_L] \mathbf{N}_j \right)^{-1} \mathbf{D}_{el}$	Update healed secant stiffness
19: $\boldsymbol{\varepsilon}_{ah} = \sum_{j=1}^{29} \mathbf{N}_{\varepsilon_j}^T [\mathbf{A}_j^{-1} (h_{v_j} (1 - \omega_{h_j}) \mathbf{D}_{Lh})] \boldsymbol{\varepsilon}_{h_j}$	Update homogenized healing strain vector in global coordinate
20: $\boldsymbol{\sigma} = \mathbf{D}_{sech} (\boldsymbol{\varepsilon} - \boldsymbol{\varepsilon}_{gh})$	Calculate stress vector in mechanical step

4-5-1 Calibration

For real cases, the model parameters are calibrated by using experimental data from uniaxial microcracking tests to determine the softening parameters of equation (4.9), such that the peak and post-peak behaviour are captured accurately. Then, the healing-efficiency parameter (ϕ_{he}) is found using data from uniaxial microcracking – healing tests, with ϕ_{he} being calibrated such that the computed overall stiffness recovery matches the corresponding experimental value. The healing activation time is obtained through direct observation. These microcracking and healing parameters are variable since they depend

on the mechanical properties of the overall self-healing system, as well as those of the components, such as microcapsule shells and vascular network channels

4-6 Volumetric response

The proposed methodology is first tested for a volumetric isotropic model. This model is subjected to a volumetric strain increment ($\varepsilon_v = \varepsilon_{xx} + \varepsilon_{yy} + \varepsilon_{zz}$) where both microcracking parameters are calculated directly. The volumetric strain (ε_v) is incremented until $\varepsilon_v=0.003$, at which point healing is initiated. 4 cases are considered to demonstrate the healing response of the proposed formulation, with particular attention on the healing rate-dependency as well as the re-healing potential. The material properties are given in Table 4-3.

Table 4-3. material properties for the volumetric model

Variables	E (N/mm ²)	E_h (N/mm ²)	ν, ν_h	f_{t_i}, f_{th} (N/mm ²)	τ (s)
Properties	24000	12000	0.15	1	60-200

In this example, the response for a single rapid healing case is shown by the dotted grey line (see Figure 4-10). Also, three continuous microcracking-healing scenarios that are shown in continuous black, blue and red line for different types of curing respectively along with a damage only case (continuous grey line) are considered. The model response is depicted in Figure 4-10. The results show how varying the curing time affects the stiffness regain slope as well as the post-peak behaviour. In this example the strain rate is 0.000005/s.

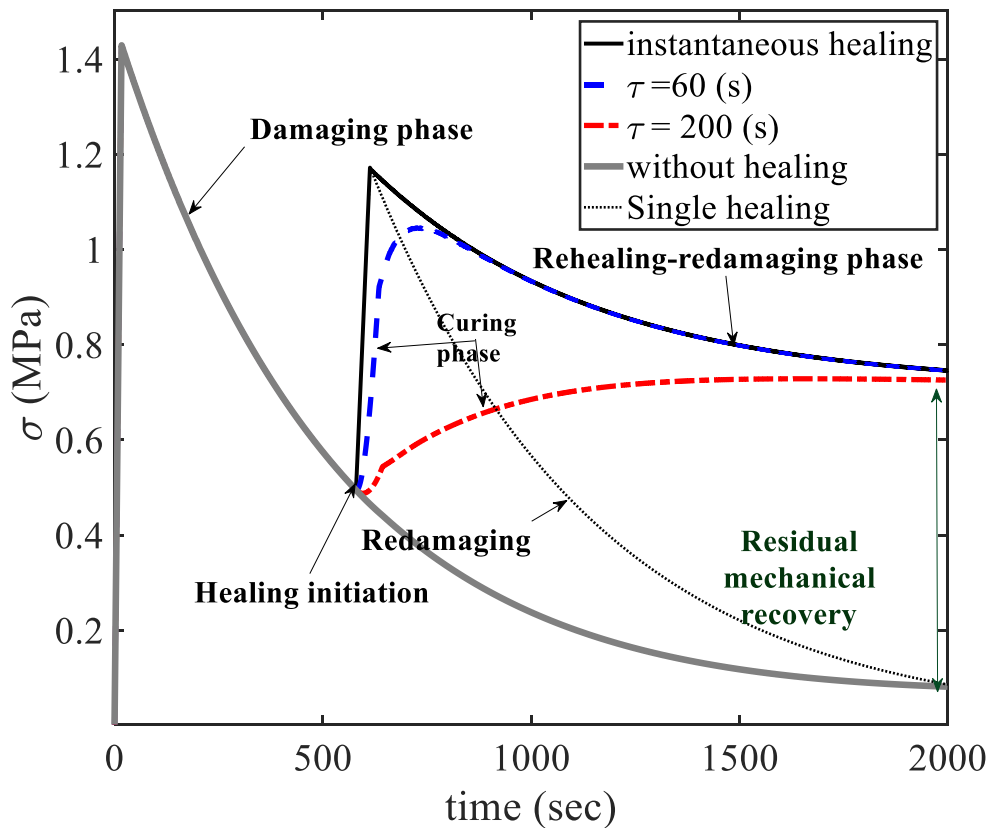


Figure 4-10 Volumetric stress-strain response

4-7 Single point simulations

A series of single-point simulations is presented in this section in order to illustrate the performance of the proposed constitutive model. The material properties used for the simulations are given in Table 4-4. The first example replicates a uniaxial tensile test with an applied strain rate of 5×10^{-6} /s applied in the xx-direction. The simulations were undertaken for a range of curing time parameters (see τ range in Table 2) and healing scenarios. The latter comprise no-healing, single healing, and multiple healing scenarios. 'Multiple healing' means that the mechanism within the model to simulate an unlimited number of simultaneous microcracking and healing steps is active.

The overall responses for each scenario, along with the associated evolutions of the microcracking variables, are given in Figure 4-11.

Table 4-4 Material properties

Variables	E (N/mm ²)	E_h (N/mm ²)	ν, ν_h	f_{t_i}, f_{th} (N/mm ²)	τ (s)
Properties	24000	12000	0.15	1	1-60-200

In this example, healing was assumed to commence when the strain reached 0.003.

The results show that the response is strongly affected by the value of the curing time parameter with the healing response being less abrupt for larger values of τ . It is noteworthy that the responses of the three healed material simulation tend to the same asymptotic stress, which is associated with balanced healing and damage rates.

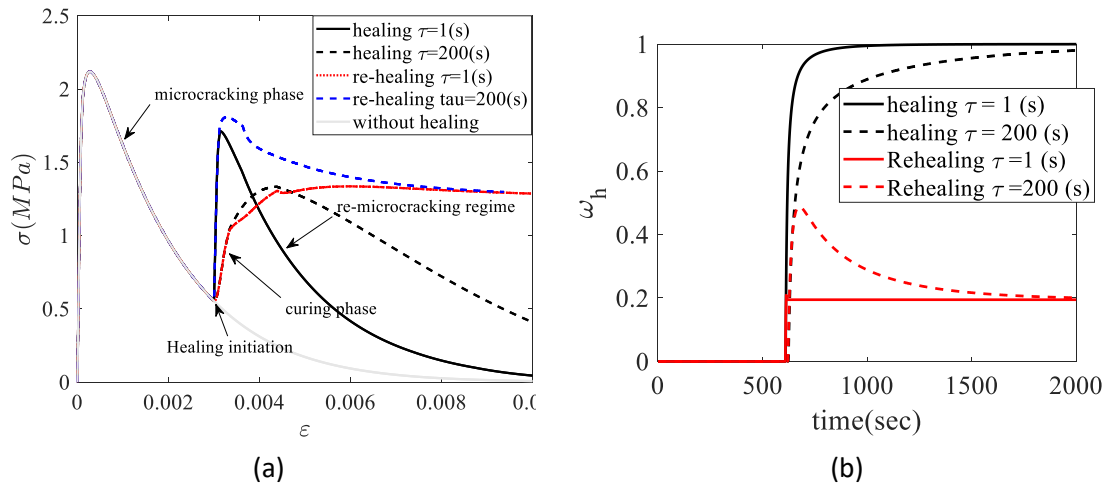


Figure 4-11 Computed uniaxial responses, a) variation of stress with time, b) re-microcracking variables

In order to provide more insight into the behaviour of the model, the variation of the microcracking and healing variables for 4 selected directions have been plotted for all three healing scenarios for the $\tau = 60$ s case in Figure 4-12. The direction numbers correspond to the spherical integration directions given in Appendix B

As may be expected, maximum microcracking occurs in direction 1 which coincides with the loading direction. The microcracking variable in direction 1 (i.e. ω_1) has a value of 0.99 at the time healing initiates; by contrast, the corresponding value of $\omega_{28} = 0.90$. The ω values for the directions that do not correspond with the loading direction illustrate the effect of the local shear strains, as well as the local normal strains, on the degree of microcracking around the hemisphere. As may be expected, the progression of the microcracking and healing responses for the non-coincident directions lag those of direction one, with the lag increasing as the angle between direction 1 and the normal to the local direction under consideration increases. The microcracking and healing variables are visualized in a set of 2D polar plots in Figure 4-12.

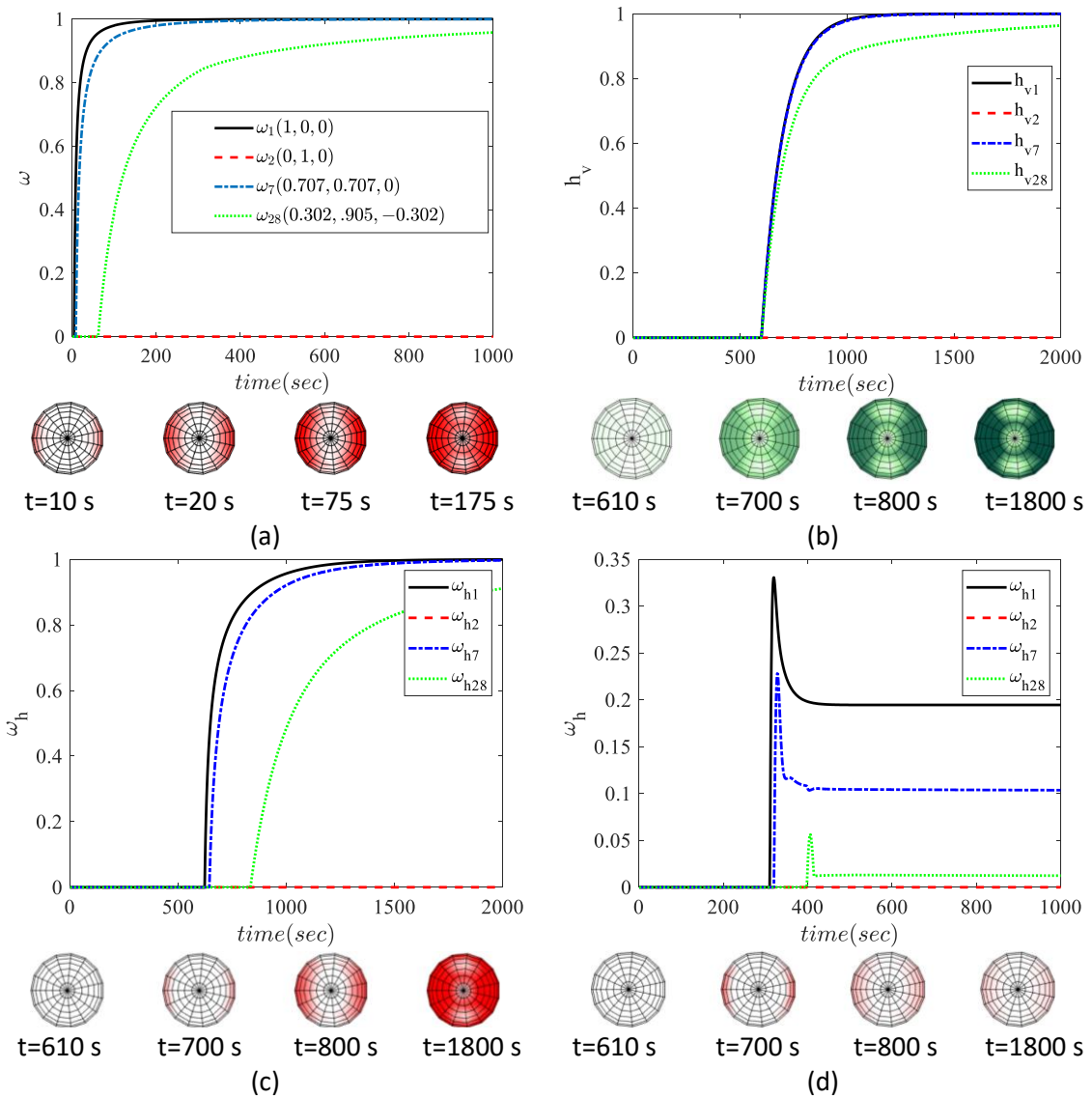


Figure 4-12 Microcracking and healing vectors evolution, a) virgin microcrack b) virgin healing, c) re-microcrack for single healing and d) re-microcracking-re-healing-re-microcracking variables for multiple healing case

4-7-1 Parametric study

The results of a systematic parametric study are now presented in which the model was used to predict the uniaxial response of a self-healing cementitious sample. The reference properties are those given in Table 4-4. The material properties altered sequentially in the study were the curing time, healed material Young’s modulus and healed material strength. The sequence of values used for each parameter are given in Table 4-5. The range of healing scenarios considered are as follows:

- i) single healing under continuous monotonic loading ($\dot{\epsilon} = 5 \times 10^{-6} /s$):
- ii) multiple microcracking-healing under continuous monotonic loading ($\dot{\epsilon} = 5 \times 10^{-6} /s$):

- iii) multiple microcracking-healing events under loading-unloading-reloading conditions (loading $\dot{\epsilon} = 5 \times 10^{-6}$; unloading $\dot{\epsilon} = -5 \times 10^{-6}$; reloading rate varies as shown in figure (III))

Table 4-5 Material properties for parametric study

Case/material properties	values	τ (sec)	E_h (N/mm ²)	f_{th} (MPa)
τ	1, 10, 50, 100, 400	variable	12000	1
E_h/E	0.25, 0.5, 1, 1.5, 2	50	variable	1
f_{th}/f_{t_i}	0.25, 0.5, 1, 1.5, 2	50	12000	variable

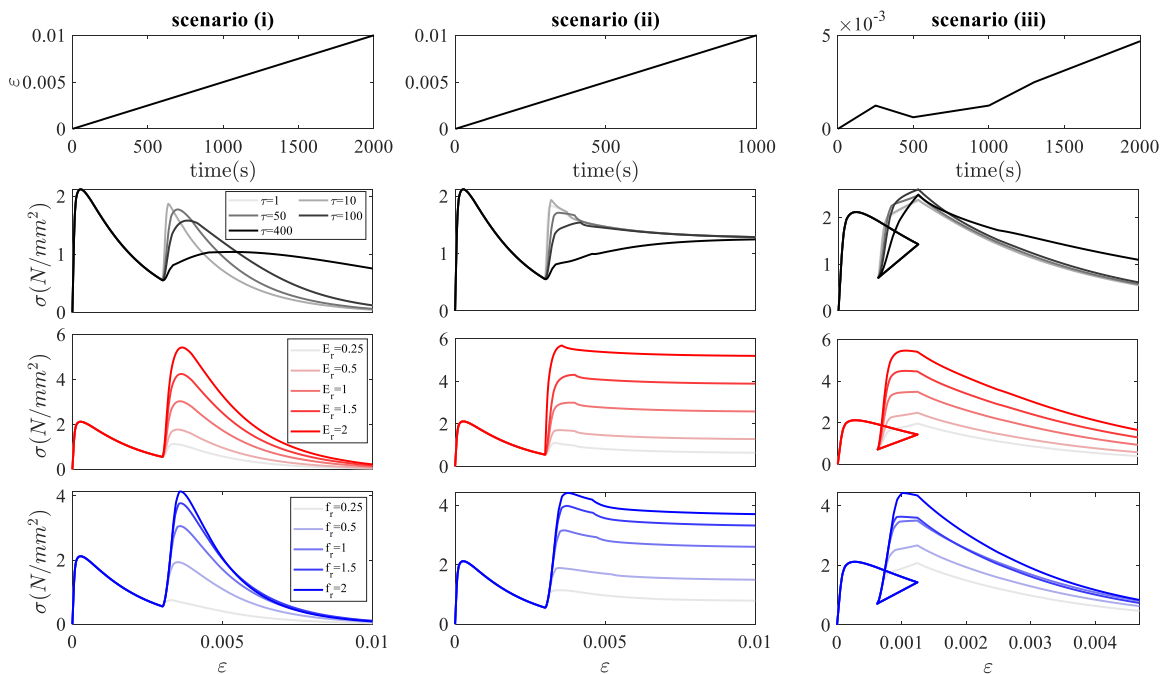


Figure 4-13 Parametric study results

Figure 4-13 presents the predicted mechanical response for all of the cases considered. As shown in this figure, the relative effect of changing each parameter is evident from the graphs, with changes in the healed-material strength and stiffness greatly affecting the post-healed peak load and post-peak softening response. As already mentioned in the earlier example, changing τ has a profound influence on the apparent stiffness and ductility of the post-healed response, with greater values of τ being associated with lower post-healed peak strengths and an apparent more ductile response.

4-7-2 Microencapsulated uniaxial test

The proposed model's ability to replicate the mechanical response of samples formed from a self-healing cementitious material containing microcapsules is assessed by considering the experimental tests on a set of cylindrical samples undertaken by James et al. (2014). In this work, the investigators measured the effects of healing on the elastic modulus of a microencapsulated self-healing cementitious material system. The tests considered material formed with 400-500 μm sized micro-capsules containing sodium silicate at dosages of 0.5% and 1% by volume of the cement paste / concrete /mortar. The tests followed a procedure from ASTM C469 for measuring the static elastic modulus. Each cylindrical sample was loaded axially up to 70% of the nominal compressive strength to order to induce a degree of damage. The samples were then unloaded and allowed to heal for 3 days and then reloaded to fully fracture of specimen.

The material properties used for the simulations are presented in Table 4-6.

Table 4-6 Material properties

Material/properties	E (N/mm ²)	ν	f_{t_i} (N/mm ²)	ϵ_0
Matrix	32430	0.25	1	0.0025
Capsule	3000	0.2	-	
Healing agent	3000	0.2	5	0.0003

The results of the simulations are presented in Figure 4-14, with Figure 4-14a giving the loading protocol and Figure 4-14b the experimental and numerical values of the elastic moduli before and after healing for each case. It is evident from the difference between the initial E values of the control samples and the samples containing microcapsules, that the presence of the microcapsules reduced the stiffness of the material.

The results of the samples with microcapsules shows that the model is able to reproduce the increase in stiffness brought about by healing and capture the effect of increasing the dosage of microcapsules.

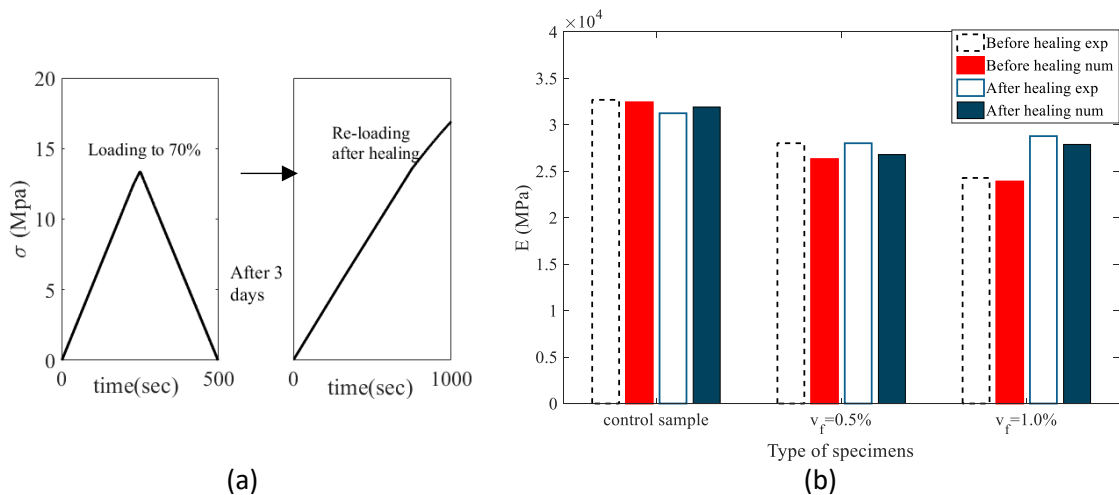


Figure 4-14 Experimental validation, a) loading protocol, b) stiffness recovery comparison

4-8 Conclusions

A new micromechanical model for simulating the response of self-healing cementitious materials has been presented in this chapter. The proposed constitutive formulation captures the time-dependent behaviour of these materials with good accuracy using relatively few physically meaningful material parameters.

The model simulates microcracking and its healing using the assumption that all microcracked material has the potential to be healed. The micromechanics formulation is well suited to simulating distributed cracking and healing systems where the healing material is spread throughout the structural element. This applies to healing systems that use embedded microcapsules and to natural and enhanced autogenous self-healing. The model is not aimed at simulating discrete cracks or systems that use vascular networks, although some aspects of the behaviour of the latter can be captured by the model.

Based on the results, the following conclusions can be drawn:

- the mechanical properties of healed material -often a healing-agent cementitious-matrix composite- greatly affect the post-cracking mechanical response of self-healing materials:
- a series of simulations, including a parametric study, show that the overall microcracking-healing response is strongly dependent on the curing time parameter of the self-healing agent, as well as on the degree of microcracking at which healing is assumed to commence:

- the recursive scheme used to update the healing and re-cracking variables is an effective way to simulate the response of elements to multiple and continuous microcracking-healing cycles in a computationally efficient manner.

Chapter 5

Finite element implementation and boundary value problems

5-1 Introduction

To simulate structures made of self-healing materials, an appropriate constitutive material model has to be implemented in a suitable finite element (FE) program. This implementation allows boundary value problems (BVP) to be solved. The work described in this chapter aims to validate the MM model by assessing its ability to capture the mechanical response of self-healing structural elements, as observed in experiments.

In this chapter, the FE implementation and FE formulation are described in Section 5-2. The micromechanical formulation, that was given in detail in Chapter 4, was coded and added as a material module to the Cardiff University's finite element code, Cardinal. Section 5-3, presents the BVP examples and compares numerical and experimental results. Section 5-4 is devoted to the conclusions.

The cases considered with the model are as follows:

- Single element illustration under different loading paths
- Petersson's (1981) uniaxial test
- 3-point bending test of a beam with and without crystalline admixture (Cibelli et al., 2022)
- 3-point bending test of a beam with a vascular network (Davies et al., 2021)
- Uniaxial test of microencapsulated self-healing systems (Sayadi et al., 2023)

5-2 Finite element implementation

The micromechanics-based self-healing constitutive model was implemented in the finite element code Cardinal, which was developed at Cardiff University. A standard weak form was adopted to evaluate the stiffness matrix at each assembly step. The element is assumed to be an 8-node hexahedron with 24 degrees of freedom as depicted in Figure 5-1.

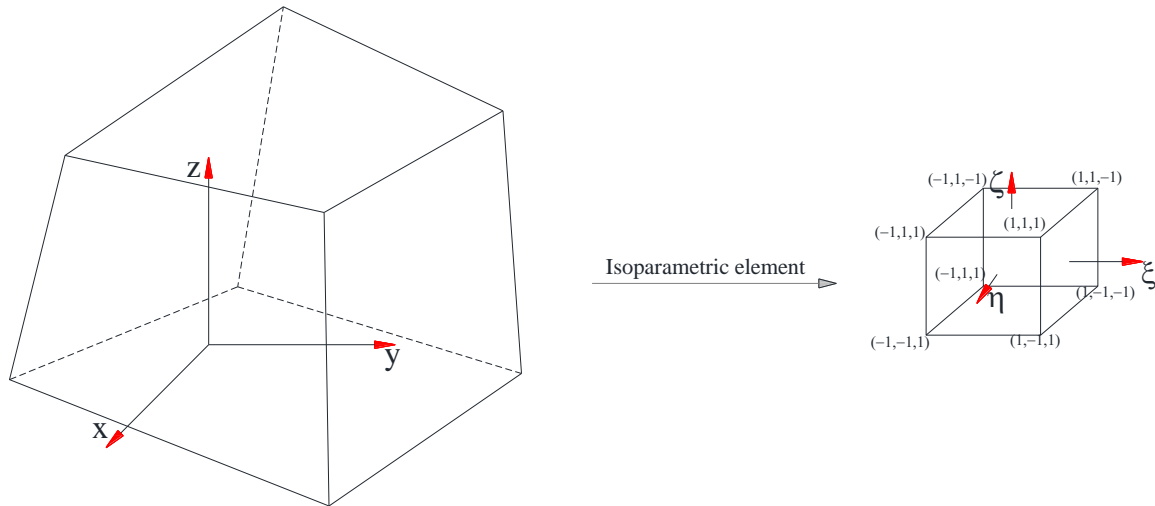


Figure 5-1 8 node hexahedral element

The element shape functions are as follows;

$$N_i(\xi, \eta, \zeta) = \frac{1}{8} (1 + \xi \xi_i)(1 + \eta \eta_i)(1 + \zeta \zeta_i) \quad (5.1)$$

where N is the element shape function. The local coordinates for an isometric element are ξ, η and ζ as shown in Figure 5-1. The subscript i denotes the shape function number associated with the element node number.

Material nonlinearity was considered, and the domain was assumed to be continuous throughout the loading history. The governing equation system in matrix form is given by:

$$\mathbf{K}(\mathbf{u}(\boldsymbol{\varepsilon}))\mathbf{u}(\boldsymbol{\varepsilon}) = \mathbf{F}(\mathbf{u}) \quad (5.2)$$

where \mathbf{u} is the nodal displacement vector, \mathbf{F} is the nodal force vector, $\mathbf{K}(\mathbf{u}(\boldsymbol{\varepsilon}))$ is the global stiffness matrix assembled from each individual element stiffness matrix (\mathbf{k}_e), the latter being given by:

$$\mathbf{k}_e = \int_{\Omega_e} \mathbf{B}^T \mathbf{D}_{sec} \mathbf{B} d\Omega_e \quad (5.3)$$

in which \mathbf{B} is the strain-displacement matrix and \mathbf{D}_{sech} is the material secant stiffness matrix (from equation (4.18)) at each element integration point. The quasi-Newton-based nonlinear solution algorithm was adopted to solve the nonlinear equilibrium equations.

To avoid instability in the solution, particularly near the peaks of the response curve where the tangent of the stress-strain curve approaches zero, a secant stiffness is used when solving the nonlinear systems of equations. In this element, numerical integration of equation 5.3) was undertaken using a standard 2x2x2 Gauss-Legendre integration rule.

In the finite element computations, the element characteristic length (l_e), used in equation (4.9), is derived based on the cube root of the element's volume. This becomes inaccurate when the aspect ratio of an element differs significantly from unity. In this case, a directional characteristic length may be computed using the method described by Alnaas & Jefferson (2016)

5-3 Numerical examples and model validation

In this section, five types of BVP examples are presented to demonstrate the proposed model's ability to capture cracking and crack-healing in cementitious materials. For the cementitious composite example, it is assumed that crack-healing occurs within the matrix. Initially, the nonlinear finite element framework was tested using one cubic finite element. This was to ensure that the constitutive formulation was implemented and coupled with the FE framework correctly. Subsequently, four different experimental test setups were considered with the model. The output from these simulations were then compared with the experimental results. The microcracking and healing variables, as well as the model performance, were observed, and data obtained from the model were analysed. The following table summarises the BVP examples considered in this chapter:

Table 5-1 Summary of the numerical example details

Example	Name	Method	Element type	Number of elements	reference
EX_1	One element	MM*	8 nodes, hexahedron	1	-
EX_2	Petersson	MM	8 nodes, hexahedron	20577	(Petersson, 1981)
EX_3	3-point bending with CA*	MM	8 nodes, hexahedron	2116	(Ferrara et al., 2014)
EX_4	3-point bending with vascular	MM	8 nodes, hexahedron	7068	(Davies et al., 2021)
		EFEM*	8 nodes, hexahedron	7068	
EX_5	Microencapsulated plate	MM	8 nodes, hexahedron	10593	(Sayadi et al., 2023)
		Latice	12DOF Beam	65000	

* Micromechanical formulation, ** finite element with embedded strong discontinuity

5-3-1 One-element illustration

In order to verify the implementation of the model in the FE code, and to illustrate the performance of the model, the predicted response from the model implemented in a single-point constitutive driver program is compared with the response computed with a single 8-noded cubic element with $100 \times 100 \times 100$ mm. The element was subjected to (i) uniaxial tension, (ii) compression with confinement stress and (iii) uniaxial compression. The boundary conditions and element geometry are schematically shown in Figure 5-2.

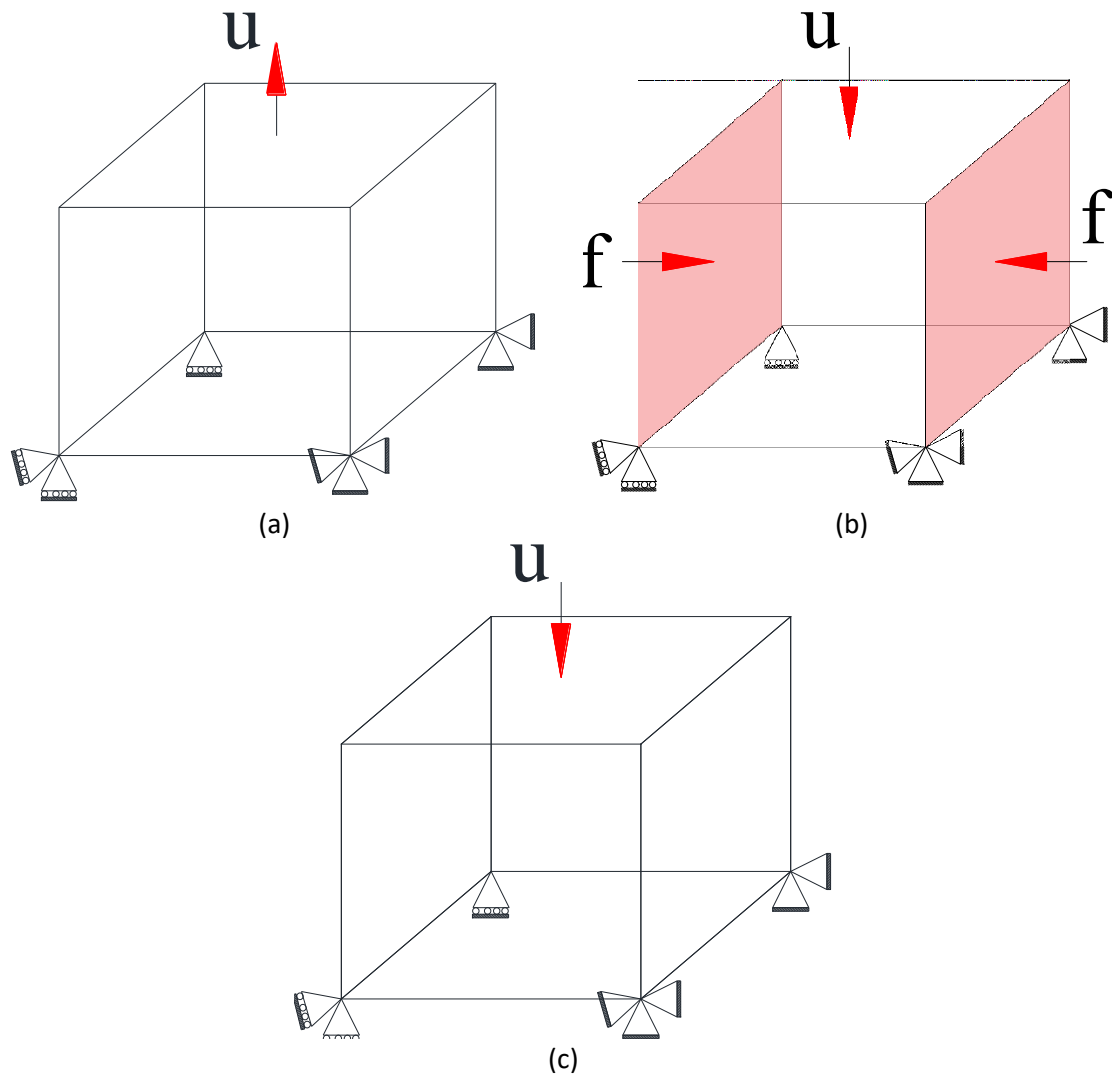


Figure 5-2 The boundary condition for the single element example, a) tension uniaxial, b) confined compression, and c) uniaxial compression

The same parameters used for single-point simulations mentioned in Chapter 4 were adopted for studying the behaviour of the single 3D element with the micromechanical constitutive formulation. The material parameters are given in Table 5-2.

Table 5-2 Material properties used as an input for EX_1.

Material/Properties	$E(N/mm^2)$	ν	$f_{t_i} (N/mm^2)$	ε_0	μ	q
Matrix	24000	0.15	1	0.0067	1.0	1.5

The element was subjected to a monotonic axial displacement of up to 0.006mm for tension and 0.05mm for compression loading path. The $1N/mm^2$ confinement normal stress was assigned for the compression load case, as shown in Figure 5-2b. Healing was initiated when the maximum microcracking variable (ω) reached 0.99. The results are illustrated in Figure 5-3.

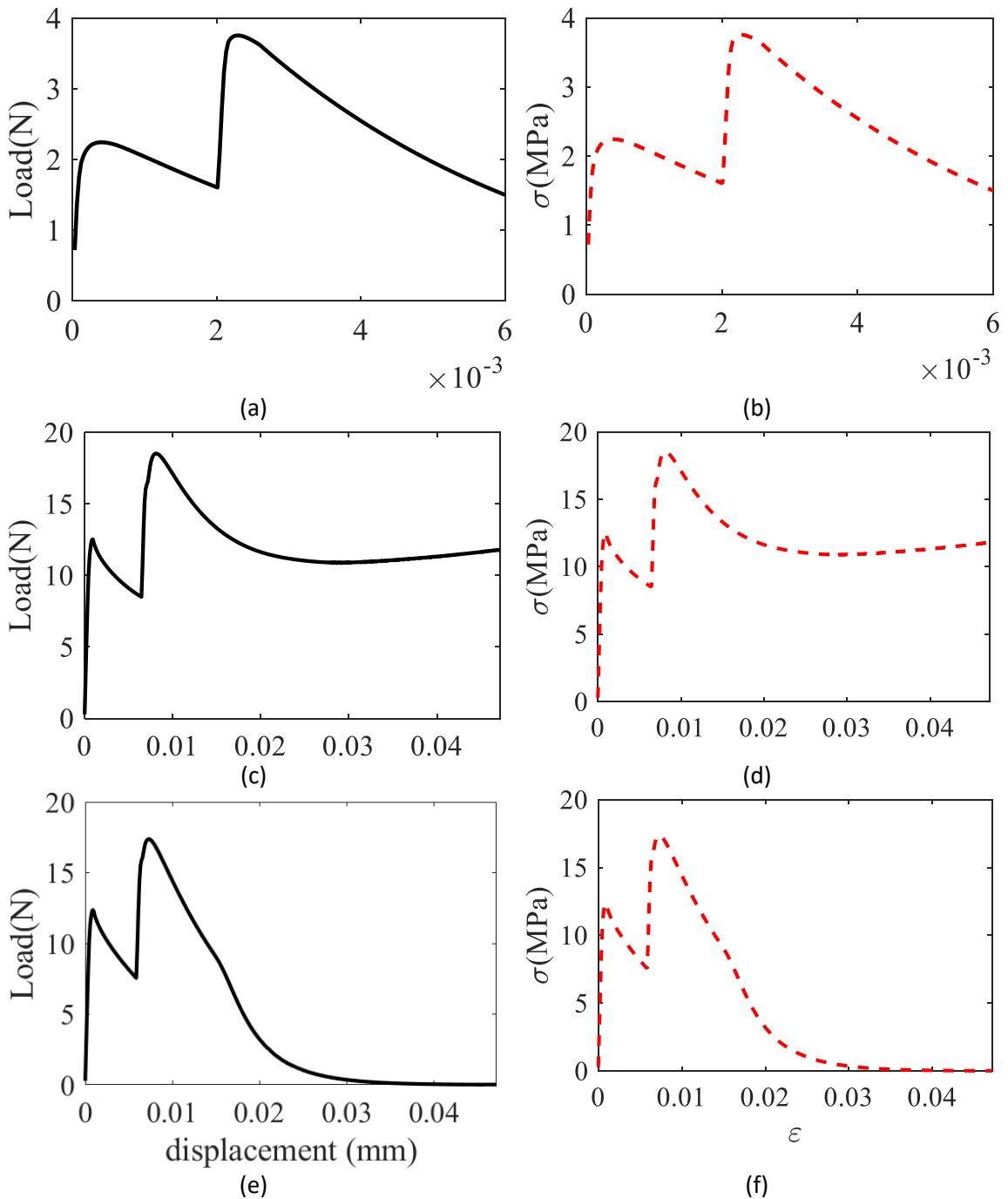


Figure 5-3 Responses computed with one finite element for a range of tension and compression loading paths

The responses presented in Figure 5-3 resemble those of the single-point simulations reported in Chapter 4. This verifies the model implementation.

5-3-2 Petersson test

Petersson (1981) tested a concrete dog-bone-shaped specimen under uniaxial deformation. The specimen's bottom face was fully fixed, and the top face was subjected

to progressive vertical displacements. Petersson reported that a considerable degree of diffuse microcracking occurred during the experiment.

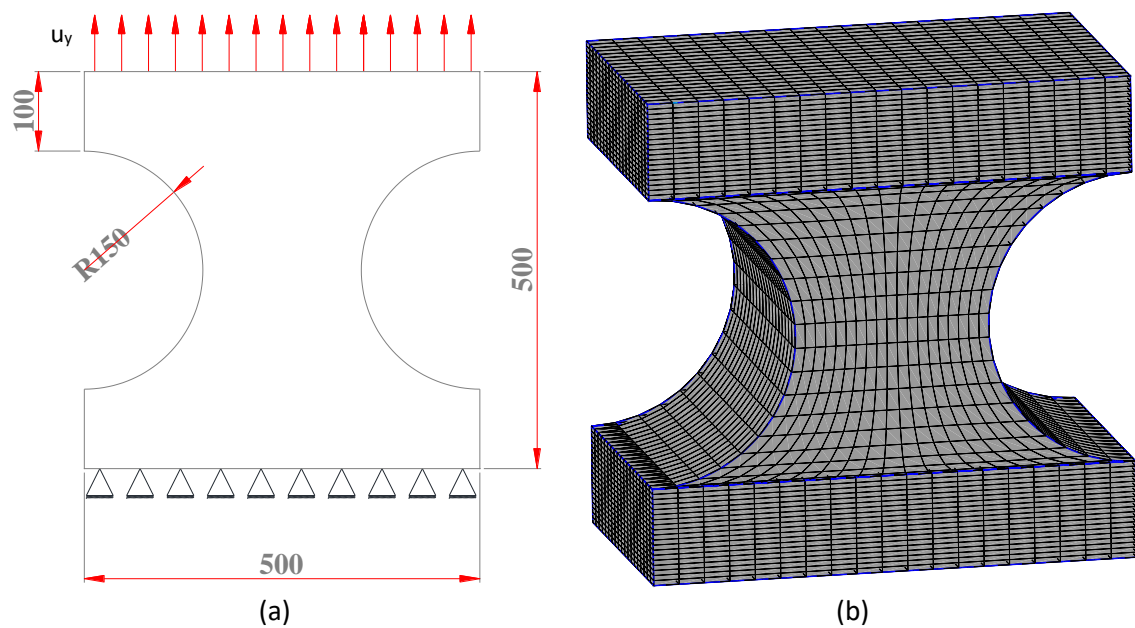


Figure 5-4 Petersson's direct tension test setup a) dimensions and boundary conditions, b) finite element mesh (all dimensions in this figure are in mm)

In this numerical example, the domain was discretised by the transfinite meshing method. The Finite Element mesh employed, which was obtained after a mesh convergence study, is shown in Figure 5.13. The representative mesh used for this simulation comprised 20577 elements and 23200 nodes. As shown in Figure 5-4a, the nodes at the bottom face of the model were fully constrained and the nodes at the top face were subjected to prescribed incremental displacements. The resultant displacement vector was applied progressively to the top-face nodes in 100 increments. The boundary conditions reflected the fact that the specimens were glued to the top and bottom loading platens in the experiments. The micromechanical constitutive material model was assigned to all elements. In this way, all regions of the domain could potentially experience microcracking. In the analysis, body forces due to self-weight were neglected.

The model material parameters are summarised in Table 5-3.

Table 5-3 Peterson specimen material input

Material/Properties	E (N/mm ²)	ν	f_{t_i} (N/mm ²)	ε_0	μ	q
Matrix	38000	0.2	1.8	0.2	1.0	1.5

The global response is shown in Figure 5-5. In this figure, the stress (σ) is the average stress and is assumed to be the normal force divided by the effective area at the neck. The simulated response indicates that the micromechanical model captures the initiation of microcracking and the nonlinear phase. However, the numerical post-peak response is somewhat different from that observed in the experiment.

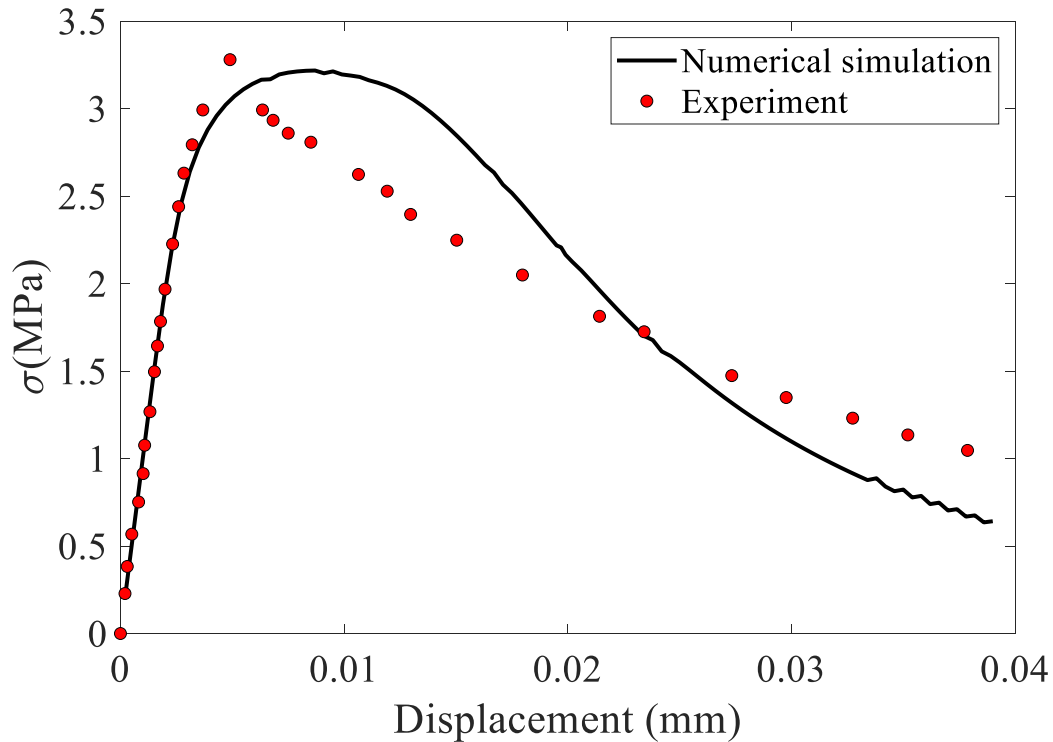


Figure 5-5 Numerical and experimental average stress-displacement responses for the Peterson's experiments

The distribution of normal microcracking variables for all elements is illustrated in Figure 5-6 which represents the cracking progression through the loading history. This figure shows the dispersion as well as localization of nonlinearity throughout the domain. The snapshots of the model are chosen at top surface displacements of 0.002, 0.01 and 0.04 mm for Figure 5-6a, b, and c respectively.

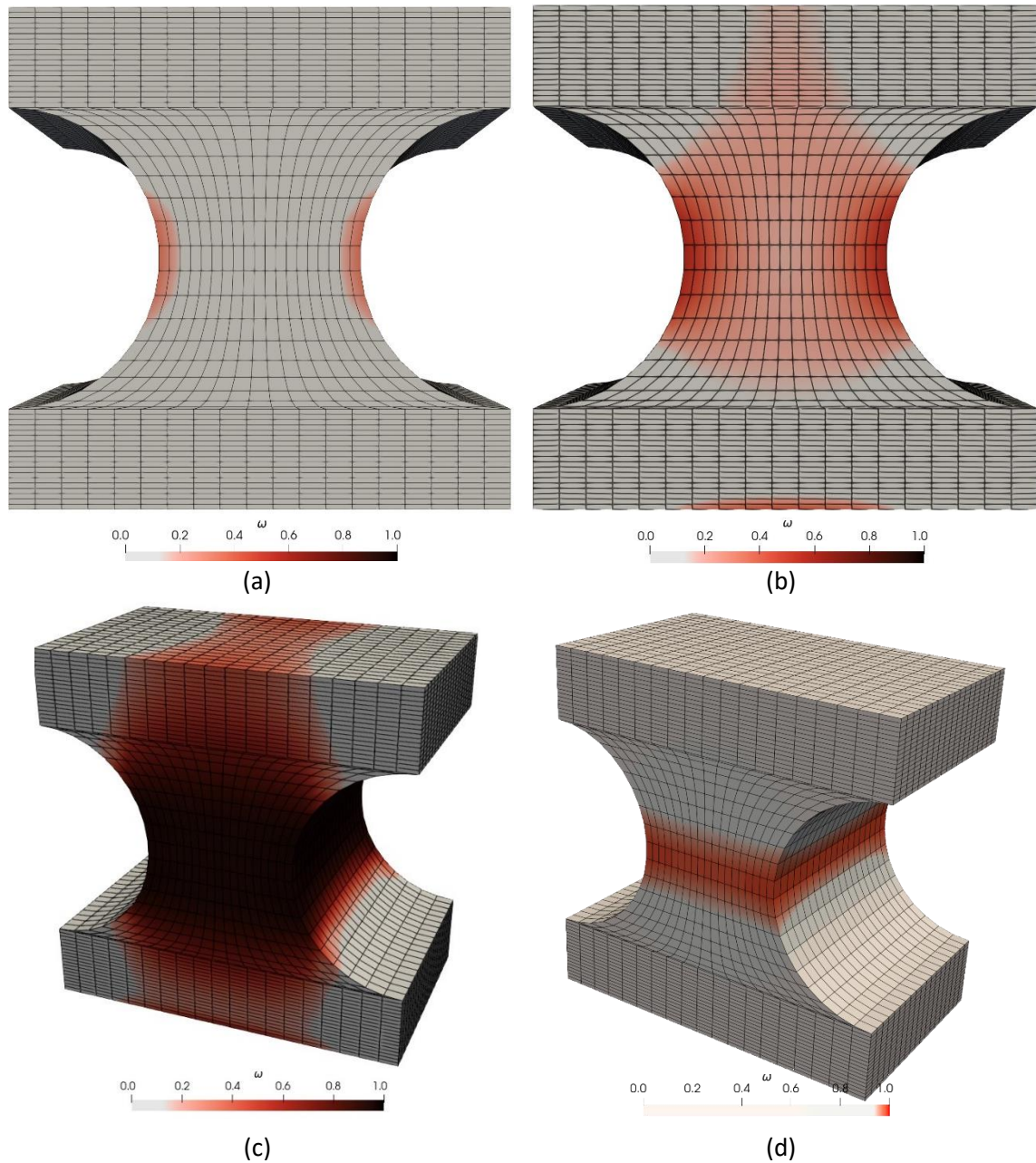


Figure 5-6 Original microcracking distribution, a) elevation view at top displacement equal to 0.002mm, b) displacement equal to 0.01mm, c) displacement equal to 0.04mm, and d) localised damage

In this example, Petersson's experiment was used as the basis of a hypothetical test case in which a microencapsulated self-healing system was added to the dog-bone specimen. It was assumed that, at a specific microcracking threshold, microcapsules are activated and healing commences. As loading resumes, more elements reach the microcracking threshold for initiating healing, which causes multiple cycles of healing, as shown in Figure 5-7b. Also, when the loading resumes microcracking and healing occur simultaneously. The overall response of the system is illustrated in Figure 5-7. It is assumed that healing

materials have the same properties as the matrix and that the curing time constant (τ) is 1 second, which represents a rapid-action healing agent. In this case, the action of re-microcracking and healing occurs very fast. The healing was initiated when the microcrack variable reached 0.995.

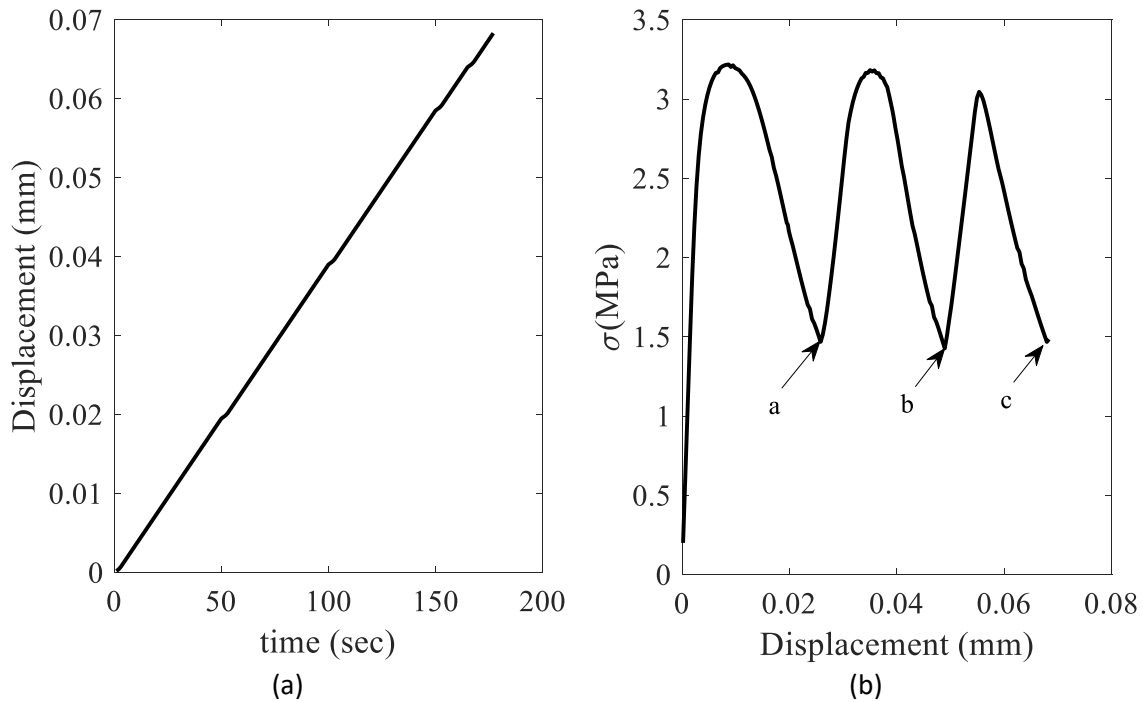


Figure 5-7 Load path and stress-displacement curve, a) load path, and b) stress-displacement curve for the crack-healing case

The healing variables as well as re-microcracking variables at different stages are shown in Figure 5-8. It is shown that -through time- more elements reach the microcracking threshold and participate in the healing process. Figure 5-8d indicates that not all damaged elements participate in the healing process since they are below the trigger criterion. This criterion mimics the stress-based microcapsule triggering condition.

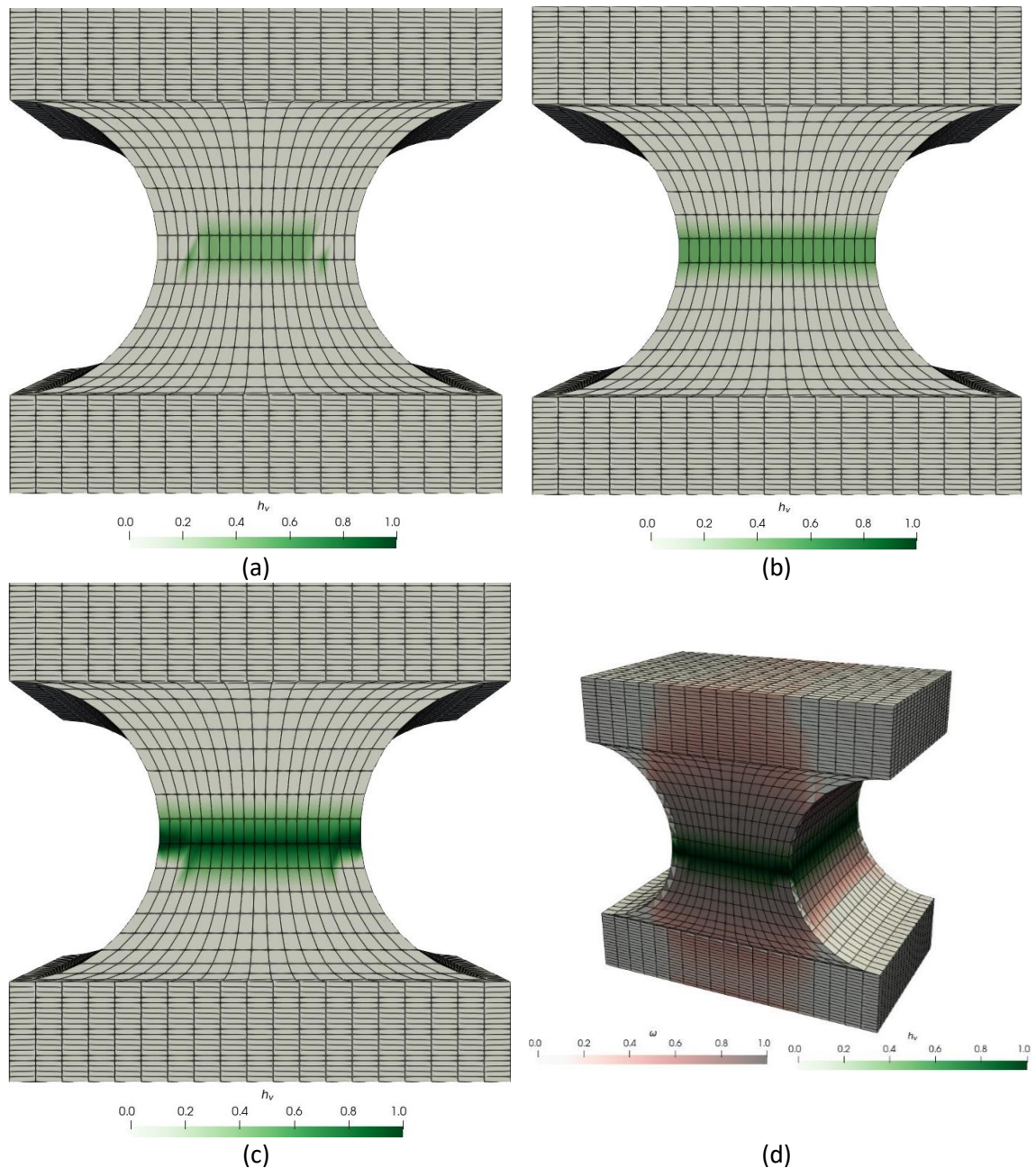


Figure 5-8 Healing state at different prescribed displacements at the top of the specimen, a) 0.04 mm, b) 0.055, c) 0.07, and d) 0.076 mm

The re-microcracking variables show the sequence of healed material experiencing cracking. Also, the overlapping microcracking and healing processes are depicted in Figure 5-9c, which shows re-microcracked elements and their healing status. As expected, not all the healed elements experienced re-microcracking. The re-microcracking evolution affects the global response since the area within each regain cycle reduces as does the degree of strength recovery.

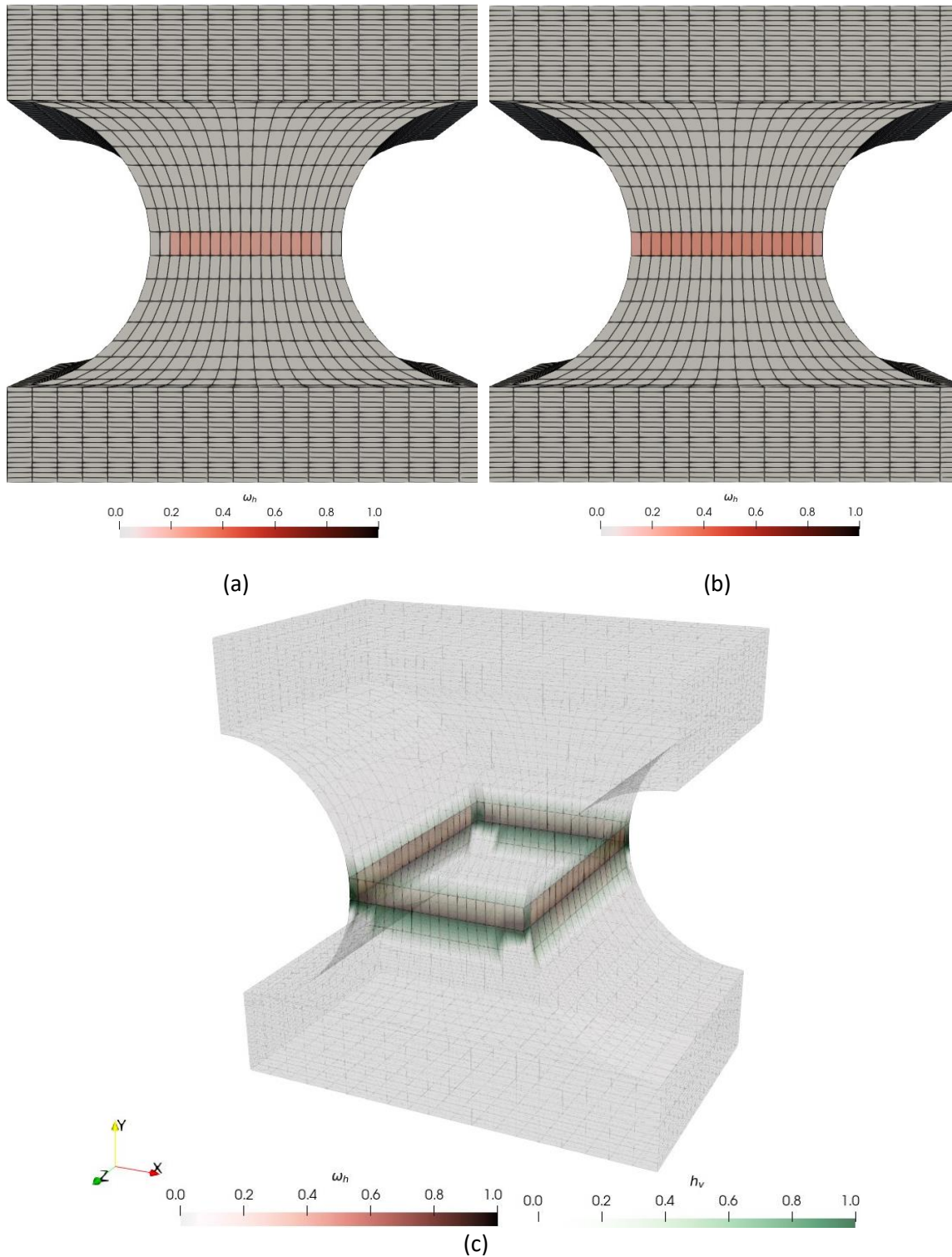


Figure 5-9 Re-microcracking variables distribution at different prescribed displacement, a) elevation view for 0.05 mm, b) elevation view for 0.06mm, and c) 3D isometric view for 0.07mm

5-3-3 3-point bending test CA

The 3-point beam bending experiments conducted by Ferrara et al. (2014) are considered in this example. In these experiments, concrete beams of size 450×100×50 mm (Figure

5-10a), were cast and loaded until the crack mouth opening displacement (CMOD) reached 150 μm and 300 μm for the first and second healing cycles respectively. Some of these beams were formed from a standard concrete mix and others were formed with a concrete containing a proprietary crystalline admixture (CA) (Ferrara et al., 2014), which was assumed to act as an autogenous healing enhancer. After cracking, each sample was stored for 12 months in either, (i) dry air or, (ii) a water curing tank. The beams were then re-loaded until failure. The cases considered in this example are summarised in Table 5-4

Table 5-4 Material properties for EX-3

Case	condition	Designation	E, E_h (N/mm ²)	ν, ν_h	f_{t_i} (N/mm ²)	f_{th} (N/mm ²)	τ (days)	ϕ_{he}
Healing without CA	Dry	WCAD	35000	0.25	0.1	0.5	270	0.01
Healing without CA	Wet	WCAW	35000	0.25	0.3	0.5	270	0.02
Healing with CA	Dry	CAD	35000	0.25	0.45	0.5	135	0.08
Healing with CA	wet	CAW	35000	0.25	0.5	0.5	135	0.1

The material properties used for this example (see Table 5-4) were based on those reported by Di Luzio et al. (2018), Ferrara et al.(2014), and Cibelli et al. (2022). The testing arrangement, specimen geometry, boundary conditions and finite element mesh used for the analysis are illustrated in Figure 8.

Since, at the second cycle for the specimens without CA, no significant healing was observed, only the first healing cycle was considered for the simulations. The second healing cycle was considered for the specimen with CA in the modelling to illustrate the influence of level of the microcracking.

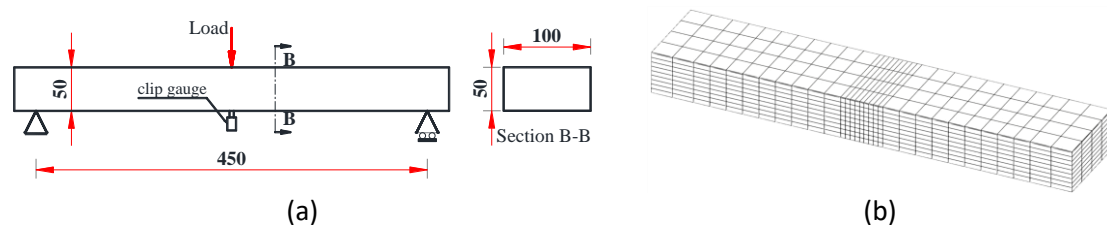


Figure 5-10 a) beam geometry and boundary conditions, b) finite element mesh

Multiple analyses on the reference samples were performed to determine an appropriate mesh and assess mesh convergence. For this purpose, half of the specimen was modelled by using symmetry. Four cases with 336,972,1452 and 2160 elements were

considered. The force-deflection results are plotted in Figure 5-11, and these show that the response of the 1452 element mesh is adequately converged, as shown in Figure 5-11e, in which the responses computed using the 2160 element mesh and 1452 element mesh are almost indistinguishable from each other.

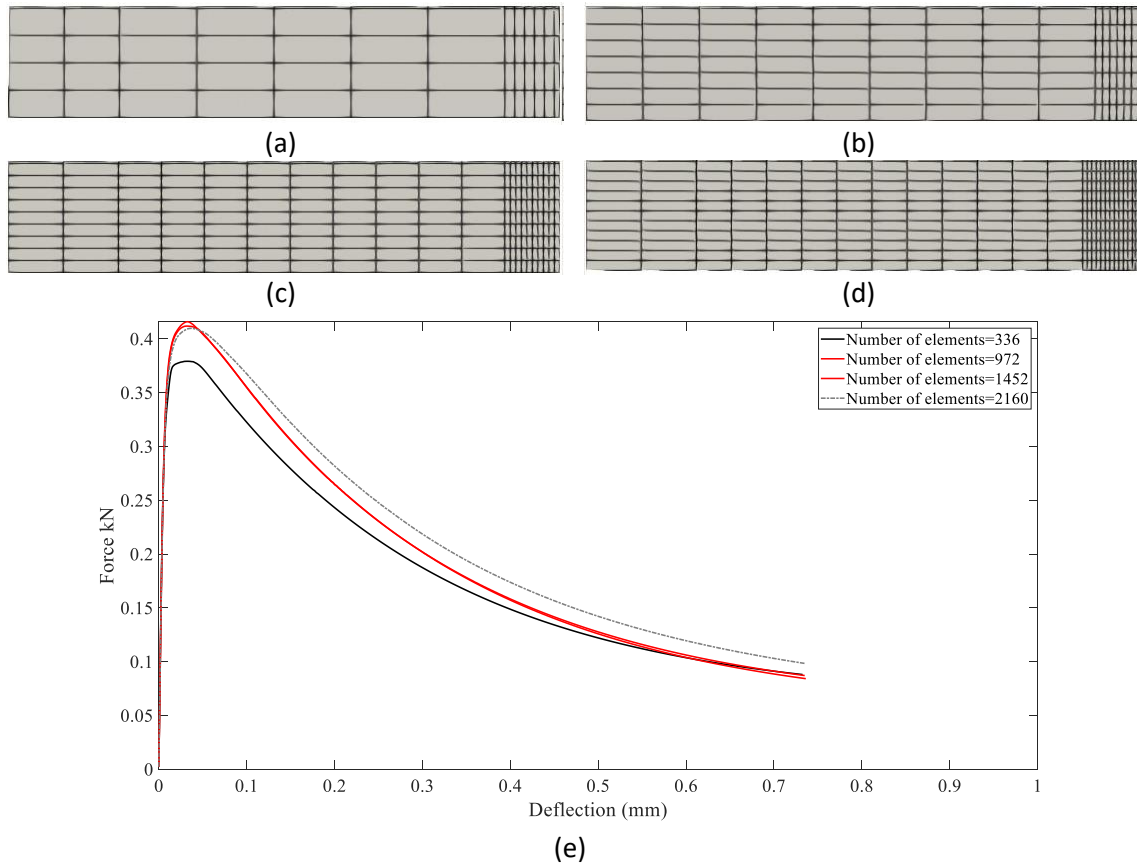


Figure 5-11 Mesh convergence test with different number of elements, a) 336, b) 972, c) 1452, d) 2160, and e) Force-deflection response.

The experimental and numerical responses of the control samples are given in Figure 5-12, which also shows the distribution of selected microcracking variables. The results show that the model is able to simulate the overall response of the control specimens with good accuracy.

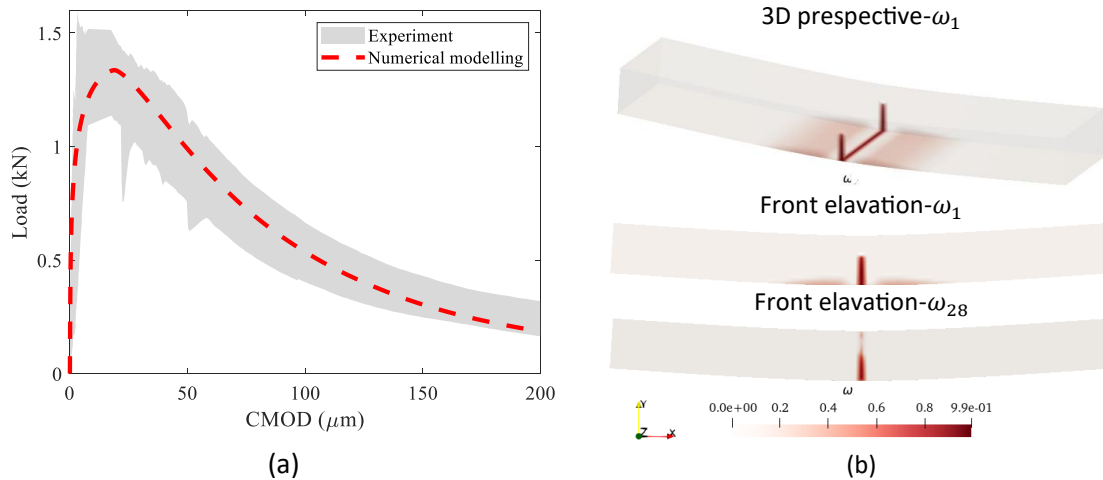


Figure 5-12 Experimental and numerical control beam responses, a) Load v CMOD response, b) microcracking variables at a CMOD of 150

The mean experimental and numerical load-CMOD responses, for the samples without and with CA, are given in Figure 5-13 and Figure 5-14 respectively. In these graphs, the post-curing reloading response commences from the unloading point of the initial cracking stage. In the numerical simulation, the healing process occurs during the unloading - reloading phase. The reloading process includes both elastic recovery and the effects of healing on stiffness and strength. The model does not include a mechanism for capturing the hysteresis in unloading-reloading cycles, which results from the interactions between asperities of opposing crack faces. This occurs in standard concrete and is considered to be a second order effect. A model for simulating this effect may be found in Jefferson (2002) .

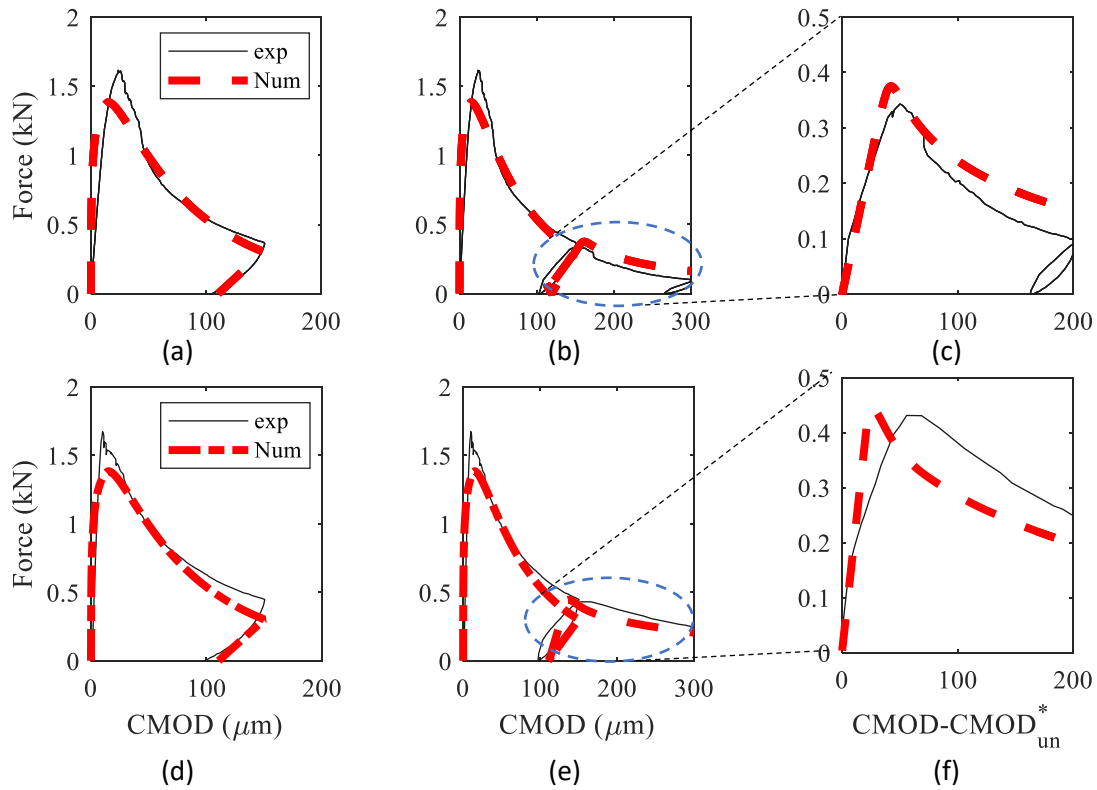


Figure 5-13 Force-CMOD response for WCAD samples (a-c) and WCAW (d-e), a)reference sample loading unloading curve, b) reloading process with healing, c) magnified illustration of (b), d)reference loading-unloading for WCAW, e)reloading with healing and f) magnified illustrating of (e)

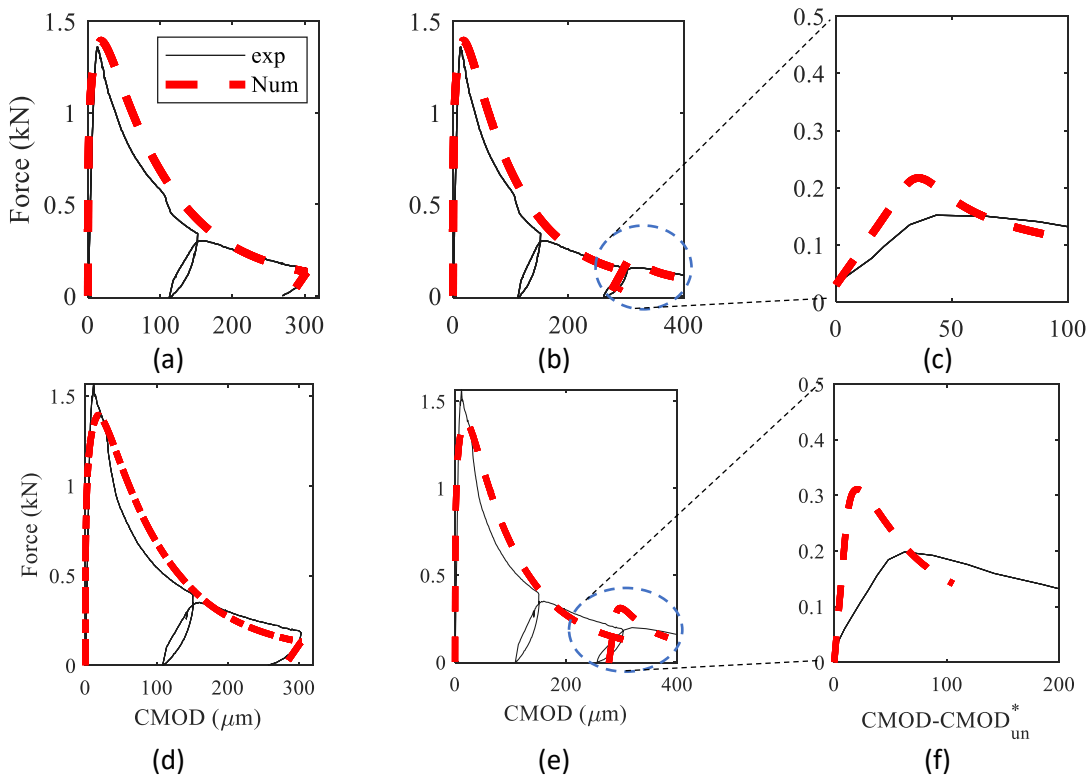


Figure 5-14 Force-CMOD response for samples with CA cured in dry (CAD) (a-c) and wet conditions (d-e) (CAW), a) reference sample loading-unloading curve, b) reloading process with

healing, c) magnified illustration of (b), d) reference loading-unloading for CAW, e) reloading with healing and f) magnified illustrating of (e)

Comparing Figure 5-13b and c with 10e and f, shows that the stiffness and strength recoveries due to healing were significantly less for dry-cured specimens than for the wet-cured specimens without CA. The model captures this difference, although does show a small increase in post-healed strength for dry specimens that was not evident in the corresponding experiment. However, in the wet conditions, the strengths increased by up to 10% compared to strengths at the unloading points. The effect of CA on mechanical recovery shows itself in strength and stiffness regains, as illustrated in Figure 5-14 c and f.

Figure 5-15 shows the distribution of the healing and re-microcracking variables at selected stages of the analysis for the CAW case. Figure 5-15a shows that, at the beginning of reloading stage, the healed material re-damage variable is zero, since, at this time, it had just formed in stress free condition. Subsequently, the material re-microcracks as the loading progresses. Re-microcracking values for the normal crack plane of the healed materials are shown in Figure 5-15 b and c at CMOD=310 and 350 μm respectively. This figure shows that the further damage is localized where healing material was formed.

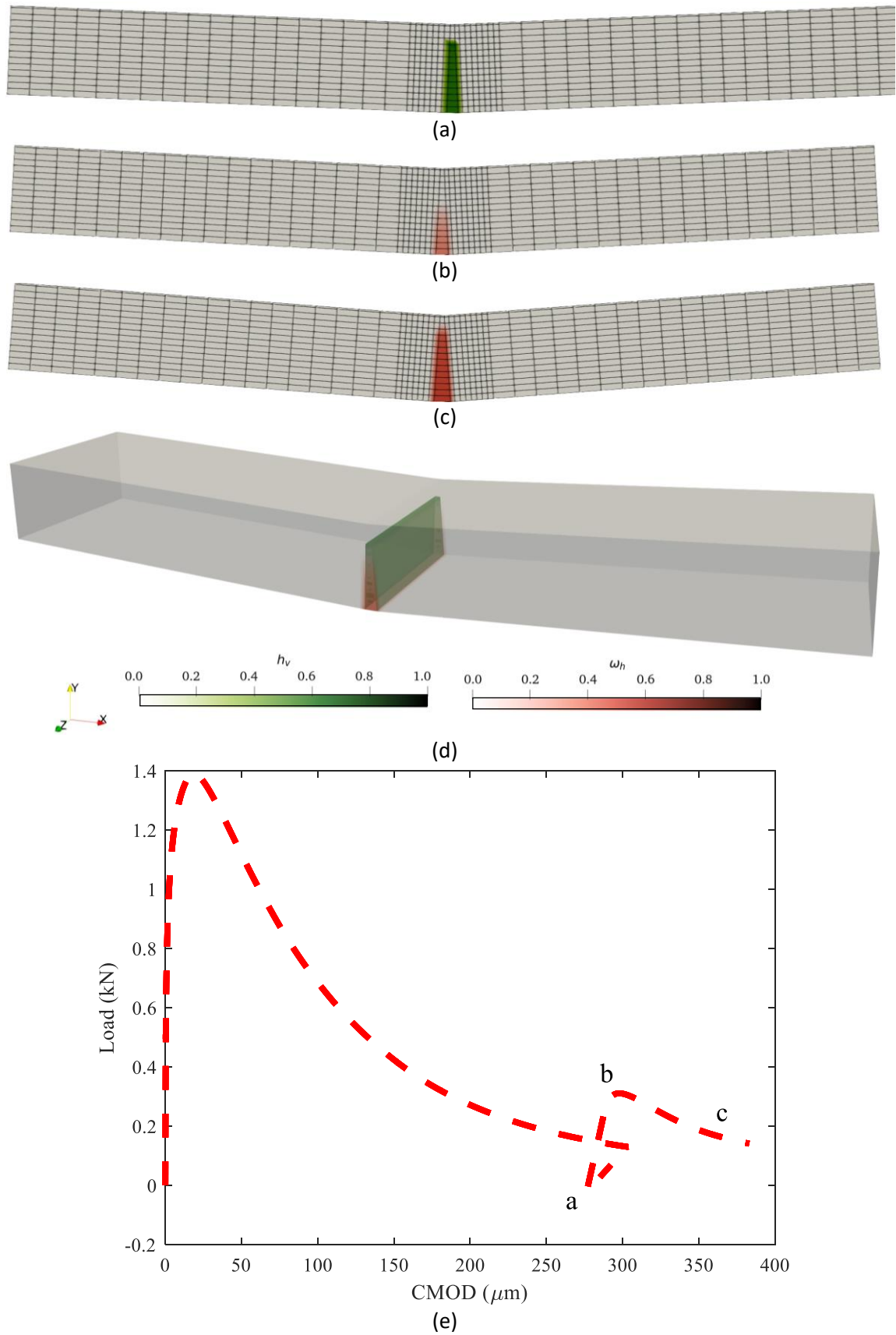


Figure 5-15 Healed material status after reloading a) healing at CMOD=275 μm, b) re-damage at CMOD=310 μm c) re-damage at CMOD=350 μm, d) overlapping damage and healing illustration, and e) the force-CMOD for CAW

5-3-4 3-point bending test vascular

In this example, the three-point bending of a cementitious specimen with an embedded vascular network presented by Davies et al. (2021) was considered. The test setup and specimen dimensions along with the 3D mesh used for simulation are illustrated in Figure 5-16. Another purpose of this example is to compare the response derived from the element with embedded strong discontinuity (EFEM) approach with the results achieved from the micromechanical approach. Therefore, the model geometry and mesh configuration are the same as the model input used by Freeman & Jefferson (2023). As mentioned in Chapter 2, they employed a coupled transport-mechanical model to simulate self-healing along with elements with embedded strong discontinuities. In This model, it is assumed that healing occurs only in a discrete crack and that the overall stiffness matrix is computed by including the healing contribution in the element stiffness matrix.

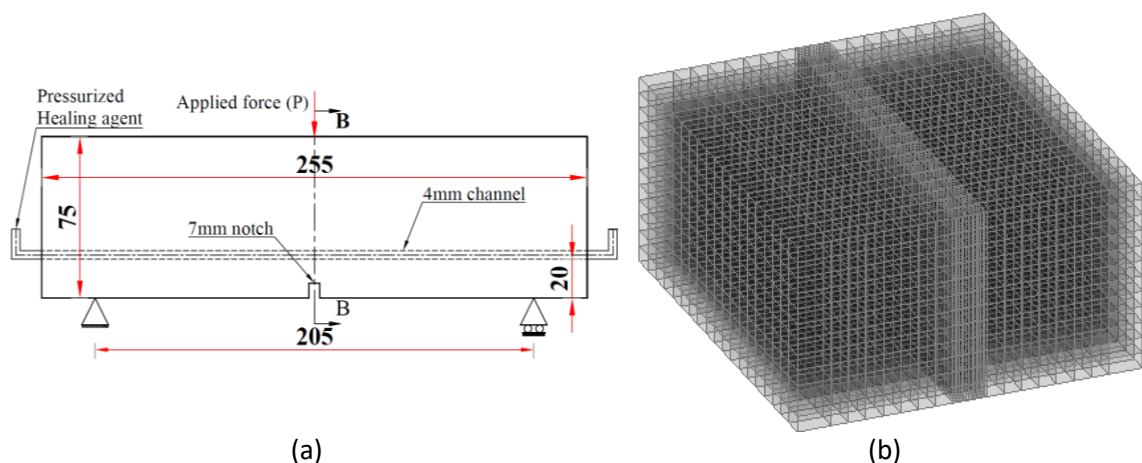


Figure 5-16 Rob's test setup (Davies et al., 2021) , a) dimension and boundary conditions, and b) mesh

The specimen was loaded in three-point bending until a crack mouth opening displacement (CMOD) of 0.3 mm was reached, after which the specimen was unloaded, and left submerged in water for a healing period of one week before being reloaded to failure.

To investigate the mesh sensitivity, two finite element meshes were employed. The coarse mesh comprised 1,950 elements, whereas the fine mesh comprised 7,068 elements. For both cases, the mesh was refined in the vicinity of the line-of-application of the applied displacement in order to more accurately capture the stress in this region. For

the reference sample, the results from analyses with the two different meshes are plotted in Figure 5-17.

For simulating the mechanical regain due to self-healing, the fine mesh configuration (7068 elements) was used. The material mechanical characteristics are noted in Table 5-5. Microcracks started to initiate before the peak, therefore the tensile strengths used as input for the micromechanical model should be less than the ultimate strength reported in the experiment.

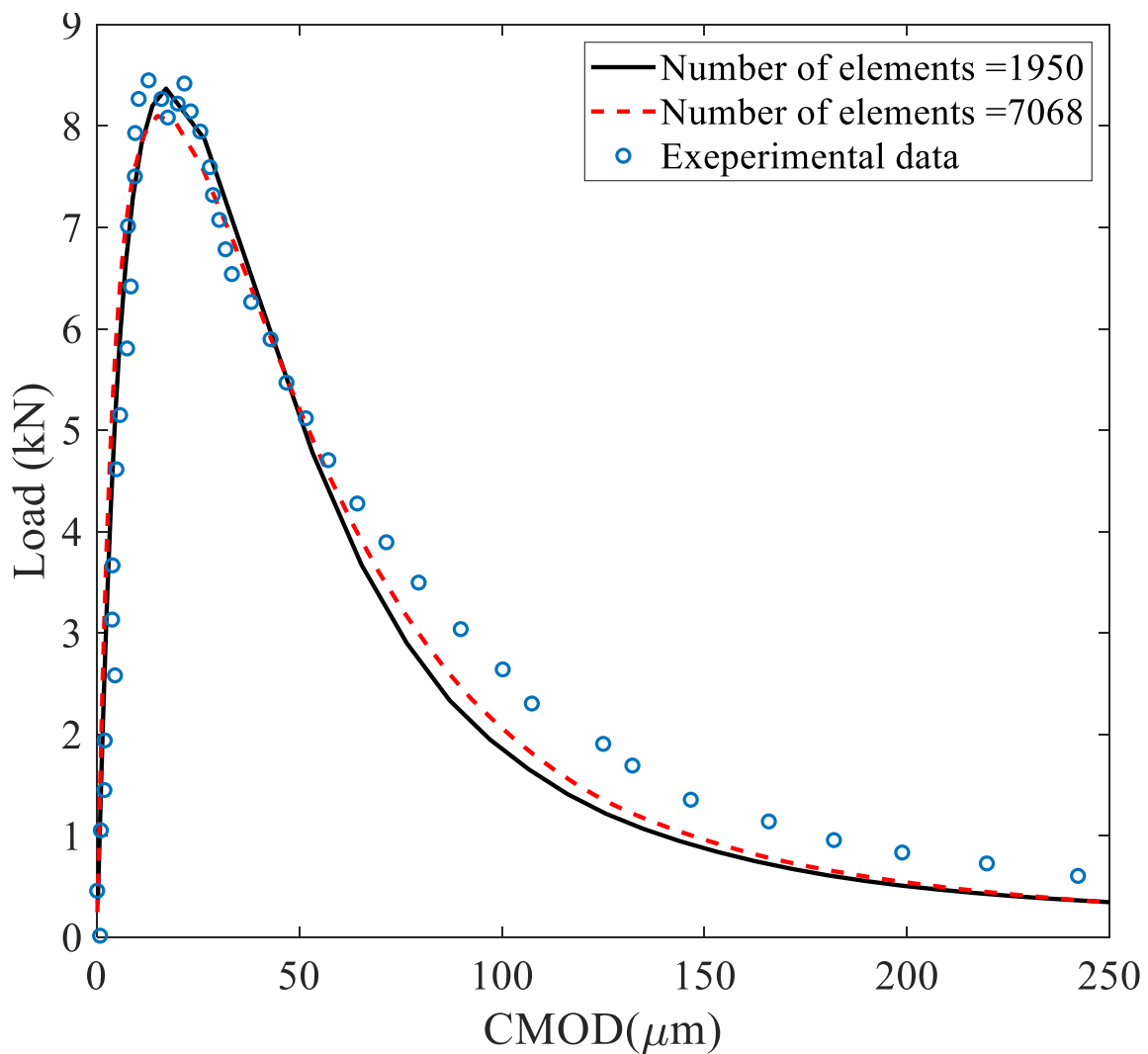


Figure 5-17 Comparing the course and fine mesh response

In this example, the healing agent enters the crack plane through the embedded vascular network. The degree of healing according to the equation described in chapter 4 was calculated after healing period.

Table 5-5 Mechanical properties

Material/Properties	$E(N/mm^2)$	ν	$f_{t_i} (N/mm^2)$
Matrix	30000	0.2	3
Healing material	8505.0	0.2	0.2

The results presented in Figure 5-18 show the Load-CMOD responses for both the EFEM and MM approaches. The results indicate that the numerical simulation captured both microcracking effects and healing with acceptable accuracy. Also, the simulation suggests that the MM model captures the pre-peak effect much more accurately than the post-peak, when judged against the experimental data. However, the MM methods tends to overestimate the post-peak behaviour because is does not consider macro-cracking. The MM model also gives more detailed information about the microcracking and healing processes via the time evolution of the microcracking, healing, and re-microcracking variables. The contour plot in Figure 5-19 shows how matrix virgin microcracking evolves through the loading history. At a CMOD of $250\mu m$, when healing commenced, all microcracks that intersected the embedded vascular network engaged in the healing process.

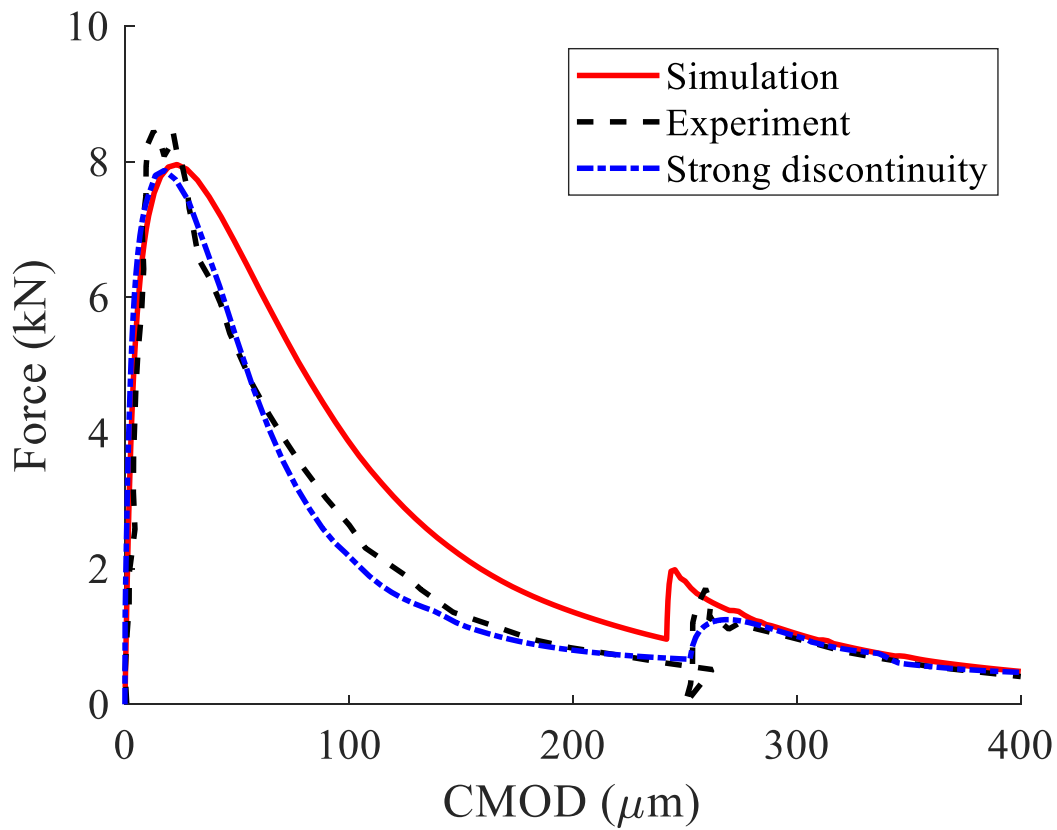


Figure 5-18 Force-CMOD curve for self-healing cases

According to the experiment, as expected, due to the presence of a notch in the middle of the beam, cracking localized in the vicinity of the notch and the healing agent was transported to the main localized crack. This suggests that the elements in the middle of the beam should be subjected to healing as shown in Figure 5-20a.

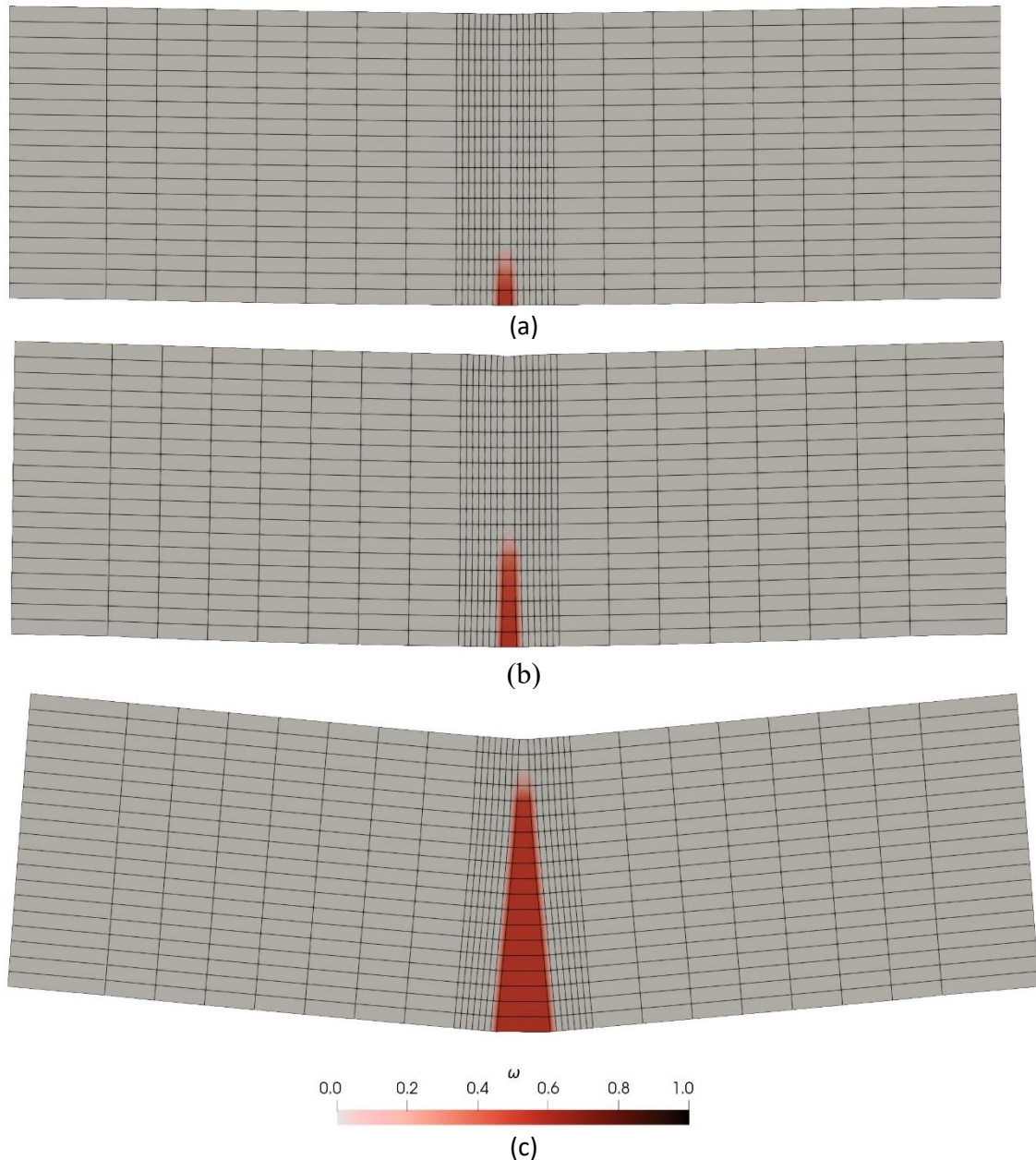


Figure 5-19 Matrix damage variables at different CMOD, a) 50 μm , b) 100 μm , and c) 200 μm

As reloading resumes, the healed materials contribute to the load bearing capacity. This healed material may also undergo re-microcracking. Since, healed materials formed in a stress-free condition, they experienced first cracking when the difference between applied local strain and healing strain ($\varepsilon_L - \varepsilon_h$) on any directional healed microcracks reaches the threshold that is defined for re-microcracking criterion. The progression of re-microcracking and overlapping crack-healing processes is illustrated in Figure 5-20.

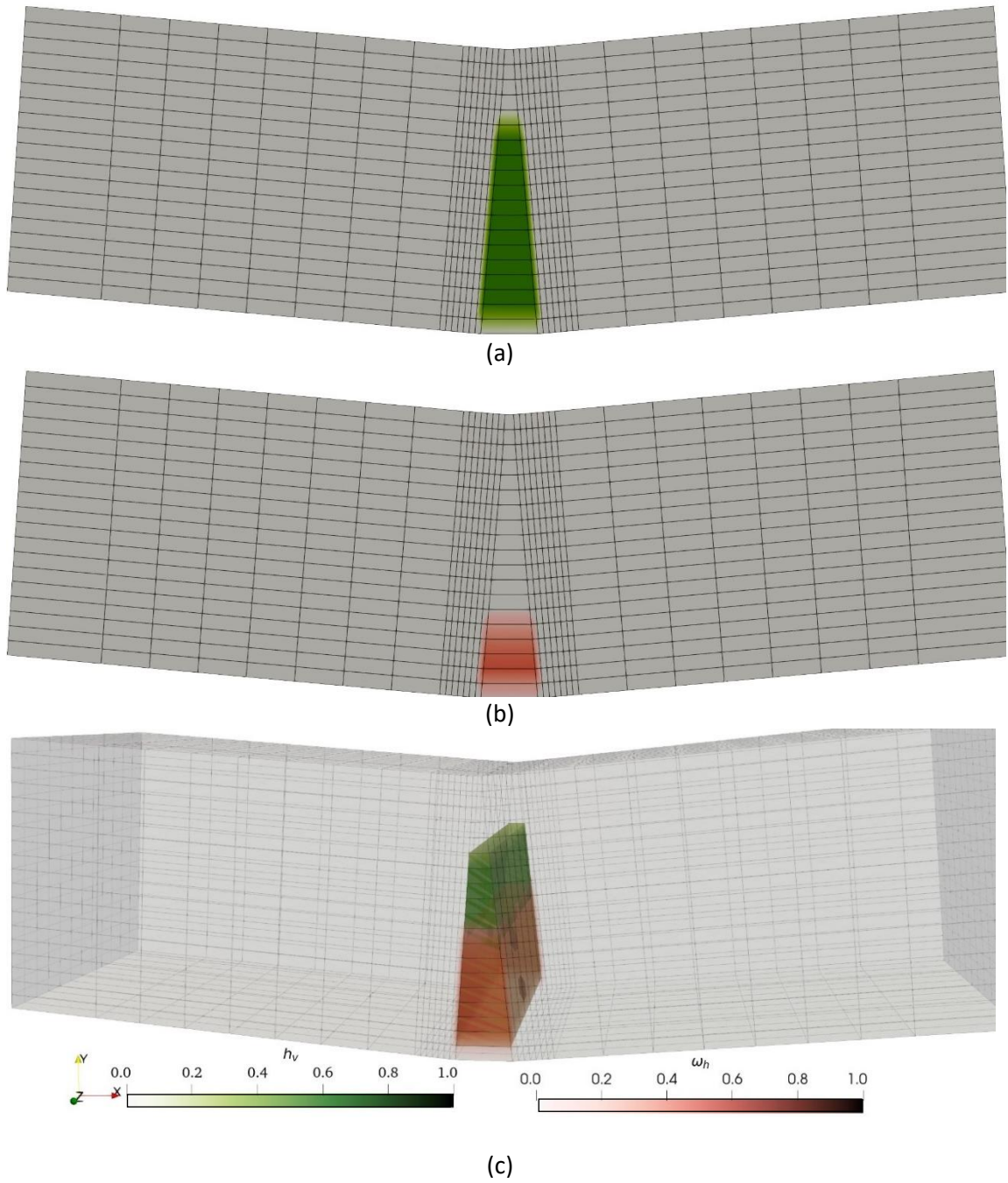


Figure 5-20 Healing and re-microcracking variables at different CMOD, a) 250 μm , b) 290 μm , and c) 300 μm

5-3-5 Encapsulated self-healing_ Lattice vs micromechanics

In this example, both the enhanced Lattice method and micromechanical approach were employed to simulate the mechanical response of specimens formed from encapsulated self-healing cementitious materials. This example explores the difference in global response between the homogenised (MM) continuum and explicit mesoscale representation methods.

A self-healing cementitious mortar with 63.5% aggregate and 2.5 % microcapsules, by volume, was considered to examine how self-healing affects the response of a uniaxial tensile test. A 40mmx40mm square 2D domain was used for the comparison (the analysis was carried out in 3D with a nominal mesh thickness of 1mm), in which the prescribed boundary conditions and meshing type are schematically shown in the Figure 5-21. The top surface displacement was applied at a rate of 0.0001mm/sec (0.000025mm/mm/sec for the strain path) such that healing would be initiated when the applied boundary displacement reached 0.075 mm. Here, it is assumed that healing occurred instantaneously.

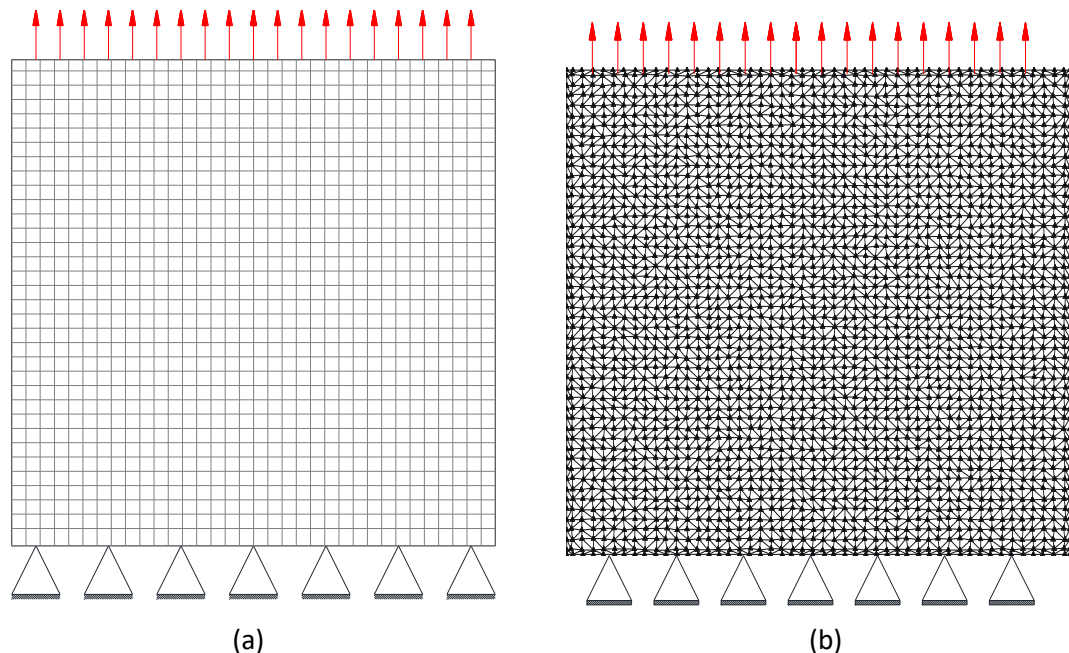


Figure 5-21 Boundary condition and meshing type, a) structured mesh, and b) Dulane triangulation

The Mori-Tanaka approach was employed to derive the elastic properties of the RME in the continuum MM model which used the constitutive formulation described in Chapter 4. The lattice mesh was generated using a pixel-based framework for the aggregate phase

to determine microcapsule geometry and location. The shape of the microcapsules was created using the Bresenham algorithm (Bresenham, 2010), which rasterizes the shell of the microcapsules in the pixel-based domain. The centre of each capsule was chosen such that there was no overlap between neighbouring microcapsules and the aggregate particles. The algorithm randomly distributed microcapsules within the composite cementitious domain. The material mechanical properties and geometry are presented in Table 5-6 and Figure 5-22 respectively. In this example, it is assumed that for the Lattice model, the aggregate particles remain elastic throughout the simulation.

Table 5-6 Material mechanical properties.

Material/Properties	$v_f\%$	$E(N/mm^2)$	$f_{t_i}(MPa)$	ε_t
Matrix-interface	33.0	30000	4	0.00015
Aggregate	63.5	49000	-	-
Microcapsules	2.5	30	0.1	-
Healing agent	-	30000	3.0	0.00015

It is worth reminding that the parameter ε_t , given in Table 5-6, is the microcracking strain parameter used for the micromechanical model.

In the lattice approach, the total number of nodes and elements was chosen to be fine enough to capture the microstructure features as well as the crack propagation. In total, the mesh contained 61366 nodes and 181960 elements.

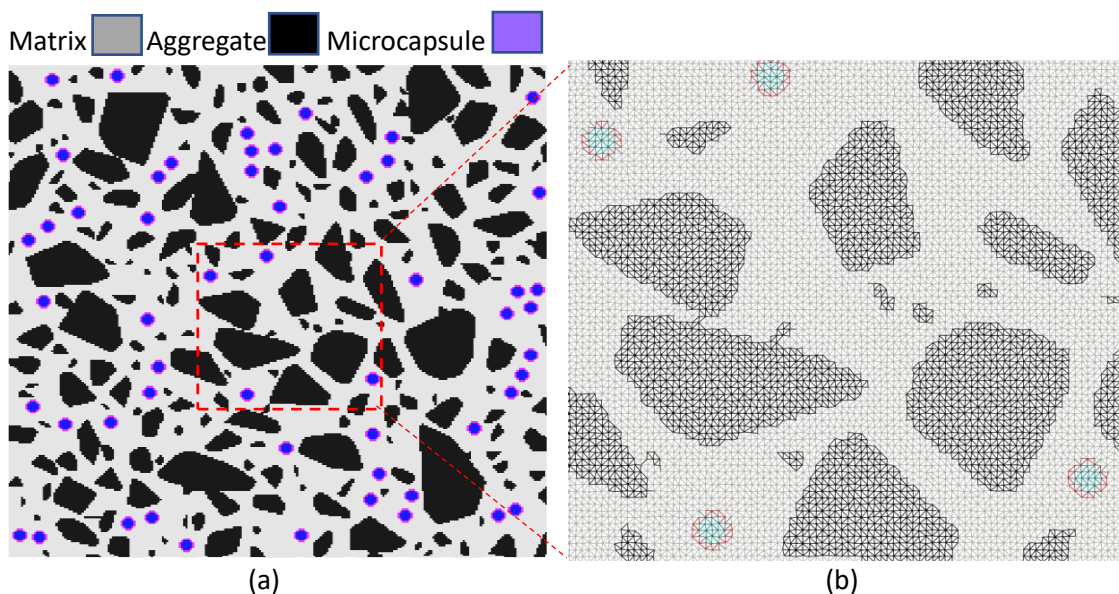


Figure 5-22 Considered RVE for: a) computational microstructure, b) Lattice mesh in the highlighted region

In this study, it was assumed that the bond between microcapsules and cement was perfect. It was also assumed that a given capsule ruptures when it is intersected by a propagating crack. To compare the crack pattern with and without healing, the system was solved for both scenarios.

The calculated responses derived from the two proposed methods are presented in Figure 5-23. The slope of the force-displacement curve indicates that the overall stiffness of the RME calculated from both the Lattice and MM methods are close to each other. Figure 5-23 shows the average stress versus average strain responses for the MM and Lattice approaches with and without the healing. For the Lattice method, the average stress is defined by dividing the normal reaction force to the section area of the specimen. The average strain is defined as calculation of normal displacement to the sample length. The crack patterns of the control and healing cases are presented in Figure 5-25 and Figure 5-26 respectively.

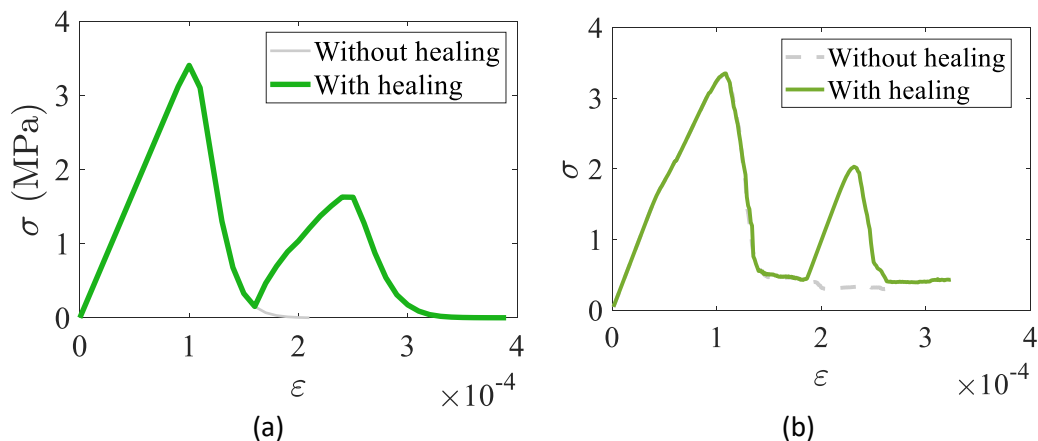


Figure 5-23 Uniaxial responses, a) MM approach, and b) Lattice approach

To have a clear visualization of the fracture pattern for the lattice model, a morphological operation (Comer, 1999) was performed to eliminate single dispersed damaged elements from the Lattice method. In this way, the main continuous crack was isolated from regions of diffuse cracking. This helped with crack tracking and with the comparison of principal crack paths. Through this method, single damaged elements with no adjacent damaged elements would be removed. This method retains damaged elements that form continuous cracks. Figure 5-24 illustrates the morphological operations.

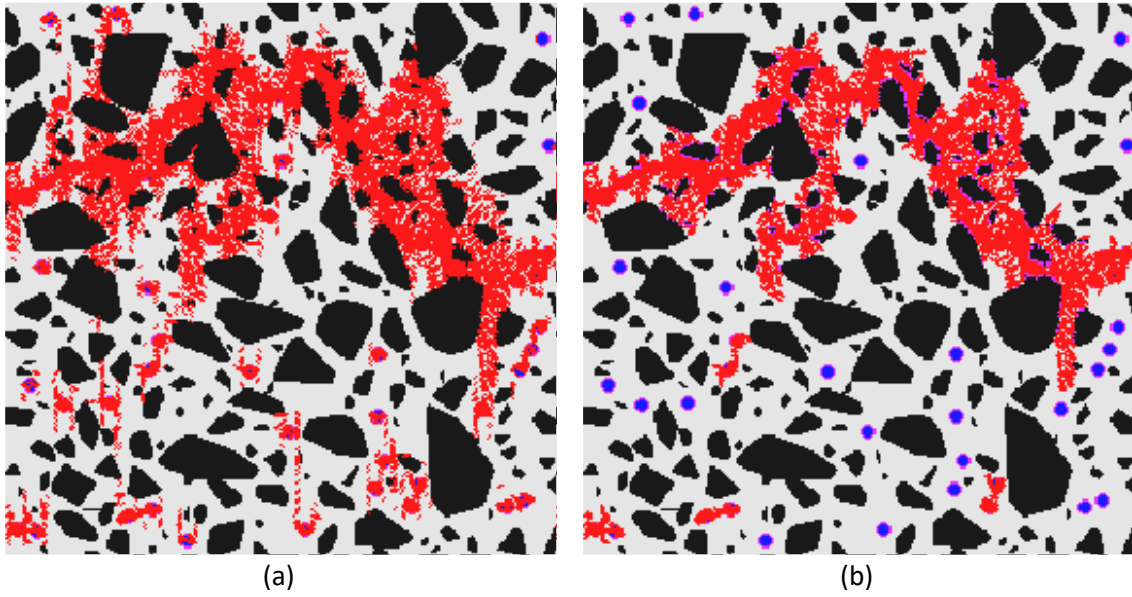


Figure 5-24 The rendering of the crack pattern generated by morphological operations at the collapsed stage, a) without the operation, and b) after the operation.

Figure 5-25 shows the crack pattern as well as normal to the crack direction of the microcracking variable distribution over the domain at two different stages.

For the sake of clarity, only the distribution of microcracking variables with values greater than 0.7 are shown in Figure 5-25d.

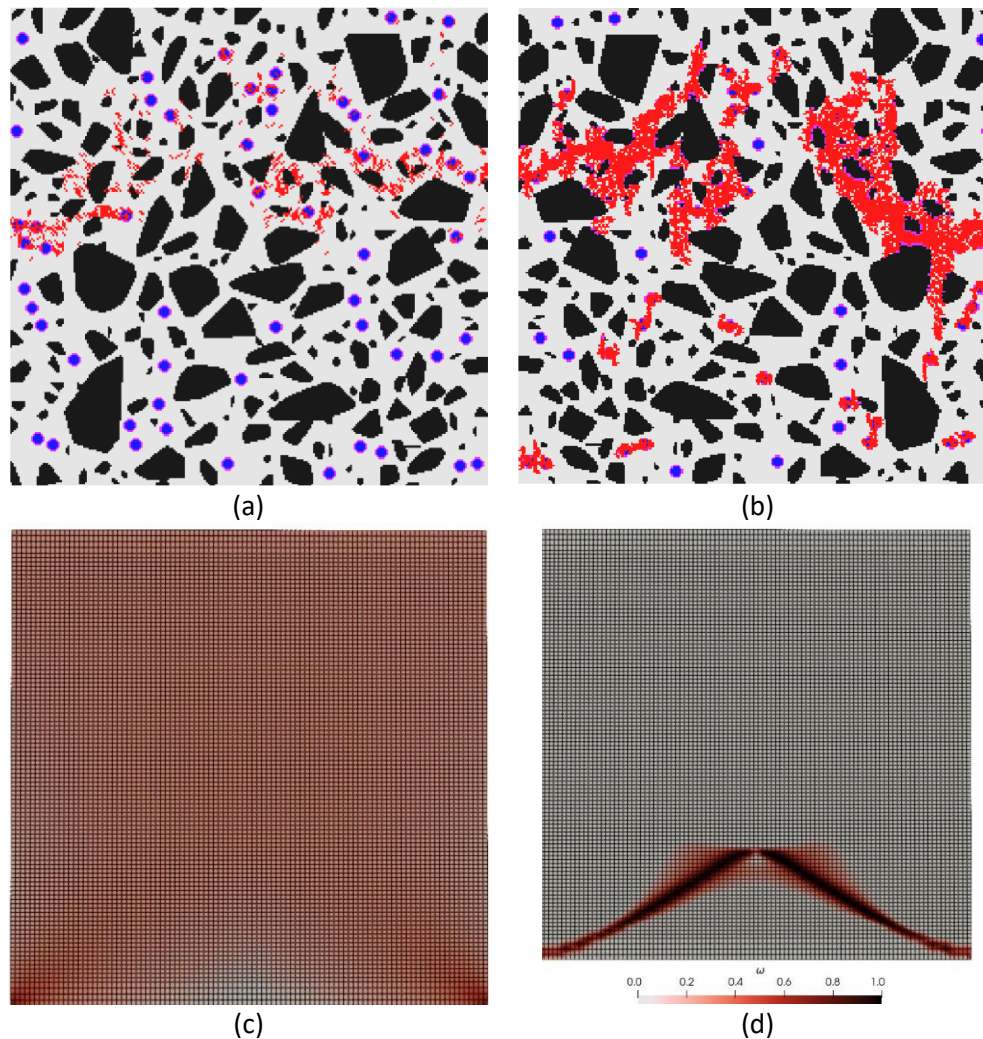


Figure 5-25 Crack pattern and microcracking variable (ω_1) distribution at different strains level, a) Lattice method at $\varepsilon=0.00005$, b) Lattice method at $\varepsilon=0.00015$, c) MM method at $\varepsilon=0.00005$ and d) MM method at $\varepsilon=0.00015$

Figure 5-25 shows that the microcracking distribution over the domain derived from the micromechanical approach is different from that of the explicit lattice approach, despite the similarity of the predicted global average stress-strain responses. This pattern is also visible in the re-microcracking variable distribution and re-fracture pattern of the lattice elements. In addition, the localization of microcracking variables shows the influence of the applied boundary conditions, in which the horizontal displacement is considered to be fixed at the lower face of the specimen. The meso- and micro- scale fracture patterns show that, for the experiments with specimens glued at one end, the heightened stresses and cracks are concentrated in the vicinity of the fixed base region. To avoid this, dog-bone-shaped samples are recommended. It is worth noting that, as mentioned above, a high number of nodes and elements were required for the explicit representation of the

microstructures. Consequently, the computational costs for the Lattice method were relatively high compared to those of the MM approach, in which the total number of elements was 10953. For further investigation of the crack patterns at micro- and meso-scales, experimental data obtained using DiC (digital image correlation) would be useful for validating the lattice method.

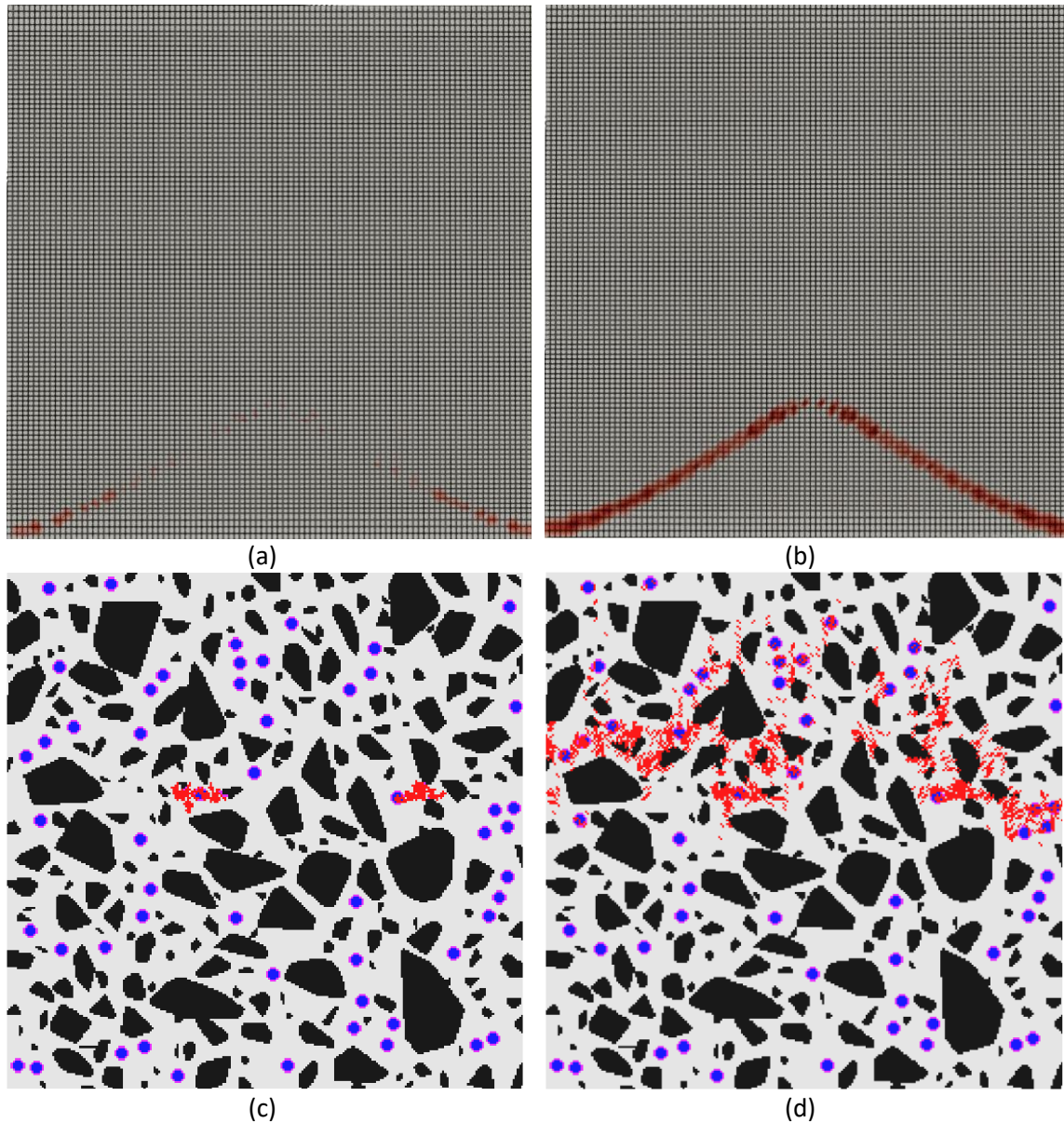


Figure 5-26 The crack pattern after healing and re-microcracking variables. a) MM method at $\varepsilon=0.0002$, b) MM method $\varepsilon=0.0003$ c) Lattice method at $\varepsilon=0.0002$, and d) Lattice method $\varepsilon=0.00025$

5-4 Conclusions

The 3D finite element implementation of the proposed constitutive formulation for capturing rate-dependent crack-healing in cementitious materials was described in this chapter. Different boundary value problems and experimental setups were modelled. The numerical prediction was validated using the data from experiment. The model's capability to capture crack-healing behaviour and its affect on the overall mechanical characteristics of structures formed from self-healing cementitious materials was evaluated. Based on the results, the following conclusions can be drawn:

- The proposed model can simulate different types of self-healing scenarios and can replicate the behaviour of structural elements undergoing simultaneous microcracking and healing.
- Relatively few physically and chemically meaningful parameters are required for both the MM and Lattice approaches to simulate the self-healing systems.
- The stiffness and strength regains observed in experiments on self-healing cementitious materials can be predicted with a good accuracy by both the MM and Lattice models.
- Meso- and micro- structures of cementitious composites, and their cracking and healing behaviour, can be modelled explicitly by the Lattice method. Healing effects can alter crack propagation paths.
- The MM approach, which simulates diffusive microcracking and healing, is applicable to microencapsulated systems. Macrocracking behaviour can be simulated with the MM model but the idealisation becomes increasingly inaccurate as the degree of macrocracking progresses.
- The computational costs of the MM approach are much less than those of the Lattice method.

Chapter 6

Conclusion and recommendations for future work

The main aim of this research was the development of a robust widely applicable formulation for capturing the mechanical behaviour of biomimetic self-healing cementitious materials. The focus was on a mechanistic approach to the constitutive and element formulations. This chapter briefly summarises the objectives mentioned in the introductory part of this thesis as well as how they were achieved. For both the Lattice and micromechanical (MM) methods, the implementation, validation and main outcomes are discussed. The conclusions and the model performance are summarised in Section 6-1. Throughout the research, there were multiple options for model extensions and enhancements, which would be worth pursuing in the future. These are considered in section 6-2.

6-1 Discussion and conclusions

The main conclusions from this study are given below.

The investigations reported in this thesis were carried out to identify the mechanisms and processes involved in self-healing. The mechanical regain due to self-healing, from micro scale to macro scale, and its effect on overall stress-strain responses were studied. Considerable effort was devoted to developing a mathematical description of these processes using ‘a science-based approach’. This was initially proposed in the SMARTINCS research grant agreement 860006.

The TUDelft Lattice model, which was specifically developed to simulate the micro and mesostructural response of cementitious materials, was enhanced to capture time-dependent self-healing behaviour.

- Crack-healing was accounted for using a time dependent element recovery approach accompanied by a unique method for ensuring that nodal forces remain constant during the healing process. The upgraded lattice system is able to evaluate and assess the mechanical response of different self-healing systems. This approach gives valuable information related to the fracture zone as well as the amount of healing agent required for self-healing. The latter is particularly useful for engineers considering design applications.
- The proposed lattice model was validated against experimental results. The behaviour of a three-point bending test of a beam as well as uniaxial tension test of a cube equipped with vascular network and microcapsules under different loading and healing conditions were replicated. The numerical results showed good agreement with the experimental observations.
- Using the MM approach, the differences between responses computed using directional microcracking and aligned microcracks were highlighted. It was shown that a formulation with aligned microcracks perpendicular to a loading direction predicts a greater reduction in the mechanical properties of a representative solid with increasing loading than in formulations with other directional configurations.

- A novel rate dependent micromechanical formulation was developed to capture microcrack-healing action in self-healing cementitious systems. The re-healing and re-microcracking processes are included in this model. The model is focused on mechanical regain due to the self-healing action and is coupled with numerically convenient form of diffusion-advection process during curing phase of the healing materials. The model shows that mechanical properties of healing materials as well as the curing rate strongly affect the constitutive behaviour of the system after healing.
- The micromechanical constitutive formulation gives information related to the micromechanical variables and the healed portion of those microcracks through time. The formulation and healing variables are developed in a way that, during the healing process, the stress states at the local crack level and global level do not change. This required the solution of an underdetermined nonlinear system of equations. The curing and loading rate at the time of healing, affect the evolution of the healing and re-microcracking variables.
- The performance of the proposed MM constitutive formulation was explored using single-point stress-strain paths in a parametric study. The model was also validated through replication of a compression test on a cementitious specimen with an embedded encapsulated self-healing system.
- The MM constitutive model was implemented in a finite element code to simulate boundary value problems. Specifically, the material constitutive model was added to a 3D standard hexahedral element in Cardiff's Cardinal finite element program. The comparison between the single point constitutive response and the results derived from the one single 8-noded element verified the implementation of the model.
- Four types of boundary value problems were considered with the model. The results shows that the proposed model can capture diffuse microcracking and give an accurate prediction of the overall responses of the systems considered. Two different types of self-healing experiment, in which the curing regime and model geometry were varied, were simulated. The overall numerical results were in a good agreement with the experimental observations.

- The self-healing micromechanical model is mainly applicable to diffusive crack-healing systems such as encapsulation-based self-healing systems or self-healing systems with additives such as crystalline admixtures. The numerical model can capture the initiation and propagation of microcracks and observed post peak behaviour with a good accuracy.
- The lattice model may be used to inform the micromechanical parameters as well as predict crack initiation. Also, the explicit microstructural representation helps to identify the healing potential throughout the domain. However, the micromechanical constitutive approach gives a reliable computationally efficient method for simulating self-healing composite systems.

6-2 Recommendations for future work

Throughout this research work multiple potential future developments were identified. These are summarised below.

The healing efficiency and its dependence on the level of the damage were treated as material constants, which were input into the model. The reduction of healing efficiency with the level of microcracking could be formulated using a mechanistic approach.

Currently, it is assumed that the supply of healing agent and agent transport driving force (e.g. capillary force) are sufficient to ensure that healing agent is present in all microcracks and discrete cracks at the time of healing. In reality, this may or may not be the case. Therefore, there would be benefit in adding healing agent transport to a coupled version of the model via integration of transport governing equations, and associated transport finite elements, with either the micromechanical model or the Lattice model. This coupled model would be able determine the availability of healing materials within a cracked region.

The current micromechanical self-healing model could be extended and coupled with the element with strong discontinuity, already present in the FE code, to simulate the merging of microcracks into one or more macro cracks and thereby capture post-peak behaviour after healing with a better accuracy.

Healing under smooth and/or rough contact might affect the results. The current method does not consider these mechanisms. It would be worth investigating the healing process

during contact and studying the stress field before and after healing using a combined experimental-numerical study.

The current approach assumes that healing materials reach and completely fill cracked regions immediately after healing initiation. However, impediments such as air bubbles within the network channels as well as weak triggering or weak release of healing agent from the capsules may alter the self-healing process. These mechanisms would be worth investigating and including in a future model.

Experimental observation shows that healing in fibre-reinforced self-healing cementitious materials is greater than in comparable plain specimens because crack-widths are smaller in the former and healing tends to increase with decreasing crack width. The proposed formulation potentially could be extended and to fibre-reinforcement self-healing materials.

Some experimental studies have been devoted to assessing the mechanical regain in self-healing systems. However, for the validation of numerical models, a wide range of experimental data is needed. Although a significant amount of data exists for vascular network systems, there is much less available for the encapsulated self-healing systems and self-healing systems with bacteria. A future combined experimental-numerical study aimed at gathering such data would be valuable.

A substantial experimental studies is needed to investigate the crack pattern before and after healing in different length scale especially in systems with heterogeneity. This information is useful to validate the numerical simulations as well as to determine the accuracy of homogenization techniques.

References

- Abaimov, S. G., Trofimov, A., Sergeichev, I. V, & Akhatov, I. S. (2019). Multi-step homogenization in the Mori-Tanaka-Benveniste theory. *Composite Structures*, 223, 110801. <https://doi.org/https://doi.org/10.1016/j.compstruct.2019.03.073>
- Abu Al-Rub, R. K., & Darabi, M. K. (2012). A thermodynamic framework for constitutive modeling of time- and rate-dependent materials. Part I: Theory. *International Journal of Plasticity*, 34. <https://doi.org/10.1016/j.ijplas.2012.01.002>
- Abu Al-Rub, R. K., Darabi, M. K., Little, D. N., & Masad, E. A. (2010). A micro-damage healing model that improves prediction of fatigue life in asphalt mixes. *International Journal of Engineering Science*, 48(11). <https://doi.org/10.1016/j.ijengsci.2010.09.016>
- Achour, M., Bignonnet, F., Barthélémy, J.-F., Rozière, E., & Amiri, O. (2020). Multi-scale modeling of the chloride diffusivity and the elasticity of Portland cement paste. *Construction and Building Materials*, 234, 117124. <https://doi.org/https://doi.org/10.1016/j.conbuildmat.2019.117124>
- Ahmed, A., & Sanada, K. (2019). Micromechanical modeling and experimental verification of self-healing microcapsules-based composites. *Mechanics of Materials*, 131, 84–92. <https://doi.org/https://doi.org/10.1016/j.mechmat.2019.01.020>
- Alessandro, F., E., B. J., & Nicola, N. (2018). Lattice Discrete Particle Modeling of Concrete under Compressive Loading: Multiscale Experimental Approach for Parameter Determination. *Journal of Engineering Mechanics*, 144(8), 4018058. [https://doi.org/10.1061/\(ASCE\)EM.1943-7889.0001480](https://doi.org/10.1061/(ASCE)EM.1943-7889.0001480)
- Alfano, G. (2006). On the influence of the shape of the interface law on the application of cohesive-zone models. *Composites Science and Technology*, 66(6). <https://doi.org/10.1016/j.compscitech.2004.12.024>
- Alfano, G., & Sacco, E. (2006). Combining interface damage and friction in a cohesive-zone model. *International Journal for Numerical Methods in Engineering*, 68(5). <https://doi.org/10.1002/nme.1728>

References

- Alnaas, W. F., & Jefferson, A. D. (2016). A robust method for the simulation of quasi-brittle materials. *Proceedings of the Institution of Civil Engineers: Engineering and Computational Mechanics*, 169(3). <https://doi.org/10.1680/jencm.15.00019>
- Alsheghri, A. A., & Abu Al-Rub, R. K. (2016). Finite element implementation and application of a cohesive zone damage-healing model for self-healing materials. *Engineering Fracture Mechanics*, 163. <https://doi.org/10.1016/j.engfracmech.2016.06.010>
- Athanasiadis, I., Wheeler, S. J., & Grassl, P. (2018). Hydro-mechanical network modelling of particulate composites. *International Journal of Solids and Structures*, 130–131. <https://doi.org/10.1016/j.ijsolstr.2017.10.017>
- Barbero, E. J., Greco, F., & Lonetti, P. (2005). Continuum Damage-Healing Mechanics with application to self-healing composites. *International Journal of Damage Mechanics*, 14(1), 51–81. <https://doi.org/10.1177/1056789505045928>
- Barrett, R., Berry, M., Chan, T. F., Demmel, J., Donato, J., Dongarra, J., Eijkhout, V., Pozo, R., Romine, C., & van der Vorst, H. (1994). Templates for the Solution of Linear Systems: Building Blocks for Iterative Methods. In *Templates for the Solution of Linear Systems: Building Blocks for Iterative Methods*. <https://doi.org/10.1137/1.9781611971538>
- Bazant, Z. P. (1984). MICROPLANE MODEL FOR STRAIN-CONTROLLED INELASTIC BEHAVIOUR.
- Bažant, Z. P., Belytschko, T. B., & Chang, T. (1984). Continuum Theory for Strain-Softening. *Journal of Engineering Mechanics*, 110(12). [https://doi.org/10.1061/\(asce\)0733-9399\(1984\)110:12\(1666\)](https://doi.org/10.1061/(asce)0733-9399(1984)110:12(1666))
- Bažant, Z. P., & Oh, B. H. (1983). Crack band theory for fracture of concrete. *Matériaux et Constructions*, 16(3). <https://doi.org/10.1007/BF02486267>
- Bazant, Z. P., Xi, Y., & Reid, S. G. (1991). Statistical Size Effect in Quasi-Brittle Structures: I. Is Weibull Theory Applicable? *Journal of Engineering Mechanics*, 117(11). [https://doi.org/10.1061/\(asce\)0733-9399\(1991\)117:11\(2609\)](https://doi.org/10.1061/(asce)0733-9399(1991)117:11(2609))
- Benveniste, Y. (1987). A new approach to the application of Mori-Tanaka's theory in composite materials. *Mechanics of Materials*, 6(2), 147–157. [https://doi.org/https://doi.org/10.1016/0167-6636\(87\)90005-6](https://doi.org/https://doi.org/10.1016/0167-6636(87)90005-6)

References

- Bernard, O., Ulm, F.-J., & Lemarchand, E. (2003). A multiscale micromechanics-hydration model for the early-age elastic properties of cement-based materials. *Cement and Concrete Research*, 33(9), 1293–1309. [https://doi.org/https://doi.org/10.1016/S0008-8846\(03\)00039-5](https://doi.org/https://doi.org/10.1016/S0008-8846(03)00039-5)
- Böhm, H. J. (1998). A short introduction to basic aspects of continuum micromechanics. *Cdl-Fmd Report*, 3.
- Bolander, J. E., & Saito, S. (1998). Fracture analyses using spring networks with random geometry. *Engineering Fracture Mechanics*, 61(5), 569–591. [https://doi.org/https://doi.org/10.1016/S0013-7944\(98\)00069-1](https://doi.org/https://doi.org/10.1016/S0013-7944(98)00069-1)
- Borst, R. de, Remmers, J. J. C., Needleman, A., & Abellan, M.-A. (2004). Discrete vs smeared crack models for concrete fracture: bridging the gap. *International Journal for Numerical and Analytical Methods in Geomechanics*, 28(7–8), 583–607. <https://doi.org/https://doi.org/10.1002/nag.374>
- Bresenham, J. E. (2010). Algorithm for computer control of a digital plotter. *IBM Systems Journal*, 4(1). <https://doi.org/10.1147/sj.41.0025>
- Budiansky, B., & O'connell, R. J. (1976). Elastic moduli of a cracked solid. *International Journal of Solids and Structures*, 12(2), 81–97. [https://doi.org/https://doi.org/10.1016/0020-7683\(76\)90044-5](https://doi.org/https://doi.org/10.1016/0020-7683(76)90044-5)
- Caggiano, A., Etse, G., Ferrara, L., & Krelani, V. (2017). Zero-thickness interface constitutive theory for concrete self-healing effects. *Computers & Structures*, 186, 22–34. <https://doi.org/https://doi.org/10.1016/j.compstruc.2017.02.005>
- Caner, F. C., & Bažant, Z. P. (2013). Microplane Model M7 for Plain Concrete. I: Formulation. *Journal of Engineering Mechanics*, 139(12). [https://doi.org/10.1061/\(asce\)em.1943-7889.0000570](https://doi.org/10.1061/(asce)em.1943-7889.0000570)
- Cappellesso, V., di Summa, D., Pourhaji, P., Prabhu Kannikachalam, N., Dabral, K., Ferrara, L., Cruz Alonso, M., Camacho, E., Gruyaert, E., & De Belie, N. (2023). A review of the efficiency of self-healing concrete technologies for durable and sustainable concrete under realistic conditions. *International Materials Reviews*, 1–48. <https://doi.org/10.1080/09506608.2022.2145747>

- Cervera, M., Barbat, G. B., Chiumenti, M., & Wu, J. Y. (2022). A Comparative Review of XFEM, Mixed FEM and Phase-Field Models for Quasi-brittle Cracking. In *Archives of Computational Methods in Engineering* (Vol. 29, Issue 2). <https://doi.org/10.1007/s11831-021-09604-8>
- Cervera, M., & Chiumenti, M. (2006). Smearred crack approach: Back to the original track. In *International Journal for Numerical and Analytical Methods in Geomechanics* (Vol. 30, Issue 12). <https://doi.org/10.1002/nag.518>
- Chang, Z. (2019). *Lattice model for numerical analysis of fracture process of concrete material under various loading conditions*. <https://doi.org/10.21012/fc10.235704>
- Chang, Z., Liang, M., Xu, Y., Schlangen, E., & Šavija, B. (2022). 3D concrete printing: Lattice modeling of structural failure considering damage and deformed geometry. *Cement and Concrete Composites*, 133. <https://doi.org/10.1016/j.cemconcomp.2022.104719>
- Chang, Z., Zhang, H., Liang, M., Schlangen, E., & Šavija, B. (2022). Numerical simulation of elastic buckling in 3D concrete printing using the lattice model with geometric nonlinearity. *Automation in Construction*, 142. <https://doi.org/10.1016/j.autcon.2022.104485>
- Chang, Z., Zhang, H., Schlangen, E., & Šavija, B. (2020). Lattice Fracture Model for Concrete Fracture Revisited: Calibration and Validation. In *Applied Sciences* (Vol. 10, Issue 14). <https://doi.org/10.3390/app10144822>
- Chen, J., & Ye, G. (2019). A Lattice Boltzmann single component model for simulation of the autogenous self-healing caused by further hydration in cementitious material at mesoscale. *Cement and Concrete Research*, 123, 105782. <https://doi.org/https://doi.org/10.1016/j.cemconres.2019.105782>
- Chen, Q., Ju, J. W. W., Zhu, H. H., & Yan, Z. G. (2022). Stochastic Micromechanics-Based Probabilistic Damage and Repair Models for Cementitious Composites. In *Handbook of Damage Mechanics: Nano to Macro Scale for Materials and Structures: Second Edition: Volume 1* (Vol. 1). https://doi.org/10.1007/978-3-030-60242-0_50
- Chen, Q., Li, W., & Jiang, Z. (2022). Theoretical estimation of the elastic moduli of self-healing concrete relevant to the evolution of cracks closing due to crystallization- and

- precipitation-based mechanism. *Journal of Building Engineering*, 58. <https://doi.org/10.1016/j.jobbe.2022.104995>
- Chen, Q., Liu, X., Zhu, H., Ju, J. W., Yongjian, X., Jiang, Z., & Yan, Z. (2021). Continuum damage-healing framework for the hydration induced self-healing of the cementitious composite. *International Journal of Damage Mechanics*, 30(5). <https://doi.org/10.1177/1056789520968037>
- Cibelli, A., Pathirage, M., Cusatis, G., Ferrara, L., & Di Luzio, G. (2022). A discrete numerical model for the effects of crack healing on the behaviour of ordinary plain concrete: Implementation, calibration, and validation. *Engineering Fracture Mechanics*, 263, 108266. <https://doi.org/https://doi.org/10.1016/j.engfracmech.2022.108266>
- Comer, M. L. (1999). Morphological operations for color image processing. *Journal of Electronic Imaging*, 8(3). <https://doi.org/10.1117/1.482677>
- Cornelissen, H. A. W., Hordijk, D. A., & Reinhardt, H. W. (1985). EXPERIMENTAL DETERMINATION OF CRACK SOFTENING CHARACTERISTICS OF NORMALWEIGHT AND LIGHTWEIGHT CONCRETE. *Heron*, 31(2).
- Cusatis, G., Pelessone, D., & Mencarelli, A. (2011). Lattice Discrete Particle Model (LDPM) for failure behavior of concrete. I: Theory. *Cement and Concrete Composites*, 33(9). <https://doi.org/10.1016/j.cemconcomp.2011.02.011>
- Darabi, M. K., Abu Al-Rub, R. K., & Little, D. N. (2012). A continuum damage mechanics framework for modeling micro-damage healing. *International Journal of Solids and Structures*, 49(3–4). <https://doi.org/10.1016/j.ijsolstr.2011.10.017>
- Davies, R., & Jefferson, A. (2015). The simulation of inelastic matrix strains in cementitious materials using micromechanical solutions. *Engineering Fracture Mechanics*, 133, 191–210. <https://doi.org/https://doi.org/10.1016/j.engfracmech.2014.10.010>
- Davies, R., & Jefferson, A. (2017). Micromechanical modelling of self-healing cementitious materials. *International Journal of Solids and Structures*, 113–114, 180–191. <https://doi.org/https://doi.org/10.1016/j.ijsolstr.2017.02.008>

- Davies, R., Jefferson, T., & Gardner, D. (2021). Development and Testing of Vascular Networks for Self-Healing Cementitious Materials. *Journal of Materials in Civil Engineering*, 33(7). [https://doi.org/10.1061/\(asce\)mt.1943-5533.0003802](https://doi.org/10.1061/(asce)mt.1943-5533.0003802)
- De Belie, N., Gruyaert, E., Al-Tabbaa, A., Antonaci, P., Baera, C., Bajare, D., Darquennes, A., Davies, R., Ferrara, L., Jefferson, T., Litina, C., Miljevic, B., Otlewska, A., Ranogajec, J., Roig-Flores, M., Paine, K., Lukowski, P., Serna, P., Tulliani, J. M., ... Jonkers, H. M. (2018). A Review of Self-Healing Concrete for Damage Management of Structures. In *Advanced Materials Interfaces* (Vol. 5, Issue 17). <https://doi.org/10.1002/admi.201800074>
- De Borst, R., Crisfield, M. A., Remmers, J. J. C., & Verhoosel, C. V. (2012). *Nonlinear finite element analysis of solids and structures*. John Wiley & Sons.
- DESRUMAUX, F., MERAGHNI, F., & BENZEGGAGH, M. L. (2001). Generalised Mori-Tanaka scheme to model anisotropic damage using numerical Eshelby tensor. *Journal of Composite Materials*, 35(7), 603–624.
- Di Luzio, G., & Cusatis, G. (2009a). Hygro-thermo-chemical modeling of high performance concrete. I: Theory. *Cement and Concrete Composites*, 31(5). <https://doi.org/10.1016/j.cemconcomp.2009.02.015>
- Di Luzio, G., & Cusatis, G. (2009b). Hygro-thermo-chemical modeling of high-performance concrete. II: Numerical implementation, calibration, and validation. *Cement and Concrete Composites*, 31(5). <https://doi.org/10.1016/j.cemconcomp.2009.02.016>
- Di Luzio, G., Ferrara, L., & Krelani, V. (2014). A numerical model for the self-healing capacity of cementitious Composites. *Computational Modelling of Concrete Structures - Proceedings of EURO-C 2014*, 2. <https://doi.org/10.1201/b16645-83>
- Di Luzio, G., Ferrara, L., & Krelani, V. (2018). Numerical modeling of mechanical regain due to self-healing in cement based composites. *Cement and Concrete Composites*, 86. <https://doi.org/10.1016/j.cemconcomp.2017.11.006>
- Dutta, S., & Chandra Kishen, J. M. (2018). Progressive damage through interface microcracking in cementitious composites: A micromechanics based approach.

References

- International Journal of Solids and Structures*, 150, 230–240.
<https://doi.org/https://doi.org/10.1016/j.ijsolstr.2018.06.017>
- Dutta, S., & Kishen, J. M. C. (2019). Micromechanical Damage Model for Plain Concrete Considering Propagation of Matrix Microcracks. *Physical Mesomechanics*, 22(2), 96–106. <https://doi.org/10.1134/S1029959919020024>
- Eshelby, J. D., & Peierls, R. E. (1957). The determination of the elastic field of an ellipsoidal inclusion, and related problems. *Proceedings of the Royal Society of London. Series A. Mathematical and Physical Sciences*, 241(1226), 376–396. <https://doi.org/10.1098/rspa.1957.0133>
- Eshelby, J. D., & Peierls, R. E. (1959). The elastic field outside an ellipsoidal inclusion. *Proceedings of the Royal Society of London. Series A. Mathematical and Physical Sciences*, 252(1271), 561–569. <https://doi.org/10.1098/rspa.1959.0173>
- Feng, X.-Q., Qin, Q.-H., & Yu, S.-W. (2004). Quasi-micromechanical damage model for brittle solids with interacting microcracks. *Mechanics of Materials*, 36(3), 261–273. [https://doi.org/https://doi.org/10.1016/S0167-6636\(03\)00021-8](https://doi.org/https://doi.org/10.1016/S0167-6636(03)00021-8)
- Feng, Y., Wu, D., Stewart, M. G., & Gao, W. (2023). Past, current and future trends and challenges in non-deterministic fracture mechanics: A review. In *Computer Methods in Applied Mechanics and Engineering* (Vol. 412). <https://doi.org/10.1016/j.cma.2023.116102>
- Ferrara, L., Krelani, V., & Carsana, M. (2014). A “fracture testing” based approach to assess crack healing of concrete with and without crystalline admixtures. *Construction and Building Materials*, 68. <https://doi.org/10.1016/j.conbuildmat.2014.07.008>
- Ferrara, L., Van Mullem, T., Alonso, M. C., Antonaci, P., Borg, R. P., Cuenca, E., Jefferson, A., Ng, P. L., Peled, A., Roig-Flores, M., Sanchez, M., Schroefl, C., Serna, P., Snoeck, D., Tulliani, J. M., & De Belie, N. (2018). Experimental characterization of the self-healing capacity of cement based materials and its effects on the material performance: A state of the art report by COST Action SARCOS WG2. In *Construction and Building Materials* (Vol. 167, pp. 115–142). <https://doi.org/10.1016/j.conbuildmat.2018.01.143>

References

- Freeman, B. L., Bonilla-Villalba, P., Mihai, I. C., Alnaas, W. F., & Jefferson, A. D. (2020). A specialised finite element for simulating self-healing quasi-brittle materials. *Advanced Modeling and Simulation in Engineering Sciences*, 7(1), 32. <https://doi.org/10.1186/s40323-020-00171-4>
- Freeman, B. L., & Jefferson, A. (2023). A 3D Coupled Finite-Element Model for Simulating Mechanical Regain in Self-Healing Cementitious Materials. *Journal of Engineering Mechanics*, 149(7), 04023038.
- Freeman, B. L., & Jefferson, A. D. (2022). A 3D coupled chemo-mechanical model for simulating transient damage-healing processes in self-healing cementitious materials. In *Computational Modelling of Concrete and Concrete Structures*. <https://doi.org/10.1201/9781003316404-14>
- Freeman, B. L., & Jefferson, T. (2020). The simulation of transport processes in cementitious materials with embedded healing systems. *International Journal for Numerical and Analytical Methods in Geomechanics*, 44(2), 293–326. <https://doi.org/https://doi.org/10.1002/nag.3017>
- G., W., & Stroud, A. H. (1973). Approximate Calculation of Multiple Integrals. *Mathematics of Computation*, 27(122). <https://doi.org/10.2307/2005635>
- Gardner, D., Jefferson, A., Hoffman, A., & Lark, R. (2014). Simulation of the capillary flow of an autonomic healing agent in discrete cracks in cementitious materials. *Cement and Concrete Research*, 58, 35–44. <https://doi.org/https://doi.org/10.1016/j.cemconres.2014.01.005>
- Gilabert, F. A., Garoz, D., & Paepegem, W. Van. (2017). Macro- and micro-modeling of crack propagation in encapsulation-based self-healing materials: Application of XFEM and cohesive surface techniques. *Materials & Design*, 130, 459–478. <https://doi.org/https://doi.org/10.1016/j.matdes.2017.05.050>
- Gitman, I. M., Askes, H., & Sluys, L. J. (2007). Representative volume: Existence and size determination. *Engineering Fracture Mechanics*, 74(16). <https://doi.org/10.1016/j.engfracmech.2006.12.021>

References

- Han, K., Ju, J. W. W., Zhu, Y., Zhang, H., Chang, T. S., & Wang, Z. (2021). Mechanical responses of microencapsulated self-healing cementitious composites under compressive loading based on a micromechanical damage-healing model. *International Journal of Damage Mechanics*, 30(10). <https://doi.org/10.1177/10567895211011239>
- Han, K., Ju, J. W., Zhang, H., Zhu, Y., Chang, T.-S., & Wang, Z. (2021). Mechanical response analysis of self-healing cementitious composites with microcapsules subjected to tensile loading based on a micromechanical damage-healing model. *Construction and Building Materials*, 280. <https://doi.org/10.1016/j.conbuildmat.2021.122251>
- Han, T., Wang, X., Li, D., Li, D., Xing, F., Han, N., & Li, Z. (2021). Uniaxial deformation characteristics and mechanical model of microcapsule-based self-healing cementitious composite. *Construction and Building Materials*, 274. <https://doi.org/10.1016/j.conbuildmat.2020.121227>
- Hill, R. (1965). Continuum micro-mechanics of elastoplastic polycrystals. *Journal of the Mechanics and Physics of Solids*, 13(2), 89–101. [https://doi.org/https://doi.org/10.1016/0022-5096\(65\)90023-2](https://doi.org/https://doi.org/10.1016/0022-5096(65)90023-2)
- Hu, C., & Li, Z. (2014). Micromechanical investigation of Portland cement paste. *Construction and Building Materials*, 71, 44–52. <https://doi.org/https://doi.org/10.1016/j.conbuildmat.2014.08.017>
- Huang, X., & Karihaloo, B. L. (1993). MICROMECHANICAL MODELLING OF THE TENSILE BEHAVIOUR OF QUASI-BRITTLE MATERIALS. In *Advances in Engineering Plasticity and its Applications*. <https://doi.org/10.1016/b978-0-444-89991-0.50037-8>
- James, G., M., H. M., Tyson, R., Michele, B., Ayman, O., & Somayeh, A. (2014). Dicyclopentadiene and Sodium Silicate Microencapsulation for Self-Healing of Concrete. *Journal of Materials in Civil Engineering*, 26(5), 886–896. [https://doi.org/10.1061/\(ASCE\)MT.1943-5533.0000892](https://doi.org/10.1061/(ASCE)MT.1943-5533.0000892)
- Jefferson, A., & Bennett, T. (2007). Micro-mechanical damage and rough crack closure in cementitious composite materials. *International Journal for Numerical and Analytical Methods in Geomechanics*, 31, 133–146. <https://doi.org/10.1002/nag.551>

- Jefferson, A. D. (2002). Tripartite Cohesive Crack Model. *Journal of Engineering Mechanics*, 128(6). [https://doi.org/10.1061/\(asce\)0733-9399\(2002\)128:6\(644\)](https://doi.org/10.1061/(asce)0733-9399(2002)128:6(644))
- Jefferson, A. D. (2003). Craft—a plastic-damage-contact model for concrete. I. Model theory and thermodynamic considerations. *International Journal of Solids and Structures*, 40(22), 5973–5999. [https://doi.org/https://doi.org/10.1016/S0020-7683\(03\)00390-1](https://doi.org/https://doi.org/10.1016/S0020-7683(03)00390-1)
- Jefferson, A. D., & Bennett, T. (2010). A model for cementitious composite materials based on micro-mechanical solutions and damage-contact theory. *Computers & Structures*, 88(23), 1361–1366. <https://doi.org/https://doi.org/10.1016/j.compstruc.2008.09.006>
- Jefferson, A. D., & Freeman, B. L. (2022). A crack-opening-dependent numerical model for self-healing cementitious materials. *International Journal of Solids and Structures*, 244–245, 111601. <https://doi.org/https://doi.org/10.1016/j.ijsolstr.2022.111601>
- Jefferson, T., Javierre, E., Freeman, B., Zaoui, A., Koenders, E., & Ferrara, L. (2018). Research Progress on Numerical Models for Self-Healing Cementitious Materials. *Advanced Materials Interfaces*, 5(17), 1701378. <https://doi.org/https://doi.org/10.1002/admi.201701378>
- Jendele, L., Cervenka, J., Saouma, V., & Pukl, R. (2001). On the choice between discrete or smeared approach in practical structural FE analyses of concrete structures. *International Conference on Analysis of Discontinuous Deformation*, 4.
- Joseph, C., Gardner, D., Jefferson, T., Isaacs, B., & Lark, B. (2011). Self-healing cementitious materials: A review of recent work. In *Proceedings of Institution of Civil Engineers: Construction Materials* (Vol. 164, Issue 1). <https://doi.org/10.1680/coma.900051>
- Kanellopoulos, A., Giannaros, P., & Al-Tabbaa, A. (2016). The effect of varying volume fraction of microcapsules on fresh, mechanical and self-healing properties of mortars. *Construction and Building Materials*, 122. <https://doi.org/10.1016/j.conbuildmat.2016.06.119>
- Königsberger, M., Hlobil, M., Delsaute, B., Staquet, S., Hellmich, C., & Pichler, B. (2017). Hydrate failure in ITZ governs concrete strength: A micro-to-macro validated

References

- engineering mechanics model. *Cement and Concrete Research*, 103. <https://doi.org/10.1016/j.cemconres.2017.10.002>
- Königsberger, M., Pichler, B., & Hellmich, C. (2013a). Micromechanics of ITZ–Aggregate Interaction in Concrete Part I: Stress Concentration. *Journal of the American Ceramic Society*, 97. <https://doi.org/10.1111/jace.12591>
- Königsberger, M., Pichler, B., & Hellmich, C. (2013b). Micromechanics of ITZ–Aggregate Interaction in Concrete Part II: Strength Upscaling. *Journal of the American Ceramic Society*, 97. <https://doi.org/10.1111/jace.12606>
- Königsberger, M., Pichler, B., & Hellmich, C. (2020). Multiscale poro-elasticity of densifying calcium-silicate hydrates in cement paste: An experimentally validated continuum micromechanics approach. *International Journal of Engineering Science*, 147, 103196. <https://doi.org/https://doi.org/10.1016/j.ijengsci.2019.103196>
- Krajcinovic, D. (1996). *Damage mechanics*. Elsevier.
- Labuz, J. F., Shah, S. P., & Dowding, C. H. (1985). Experimental analysis of crack propagation in granite. *International Journal of Rock Mechanics and Mining Sciences And*, 22(2). [https://doi.org/10.1016/0148-9062\(85\)92330-7](https://doi.org/10.1016/0148-9062(85)92330-7)
- Levasseur, S., Weleman, H., & Kondo, D. (2015). A microcracks-induced damage model for initially anisotropic rocks accounting for microcracks closure. *International Journal of Rock Mechanics and Mining Sciences*, 77, 122–132. <https://doi.org/https://doi.org/10.1016/j.ijrmms.2015.03.011>
- Li, W., Dong, B., Yang, Z., Xu, J., Chen, Q., Li, H., Xing, F., & Jiang, Z. (2018). Recent Advances in Intrinsic Self-Healing Cementitious Materials. *Advanced Materials*, 30(17). <https://doi.org/10.1002/adma.201705679>
- Li, W., Jiang, Z., Yang, Z., & Yu, H. (2016). Effective mechanical properties of self-healing cement matrices with microcapsules. *Materials & Design*, 95, 422–430. <https://doi.org/https://doi.org/10.1016/j.matdes.2016.01.124>
- Logan, D. L. (2002). *A first course in the finite element method* (Vol. 4). Thomson.
- Luhar, S., Luhar, I., & Shaikh, F. U. A. (2022). A Review on the Performance Evaluation of Autonomous Self-Healing Bacterial Concrete: Mechanisms, Strength, Durability, and

References

- Microstructural Properties. In *Journal of Composites Science* (Vol. 6, Issue 1).
<https://doi.org/10.3390/jcs6010023>
- Lv, L. Y., Zhang, H., Schlangen, E., Yang, Z., & Xing, F. (2017). Experimental and numerical study of crack behaviour for capsule-based self-healing cementitious materials. *Construction and Building Materials*, 156.
<https://doi.org/10.1016/j.conbuildmat.2017.08.157>
- Malvern, L. E. (1969). *Introduction to the mechanics of a continuous medium*.
<https://api.semanticscholar.org/CorpusID:121437978>
- Mauludin, L. M., & Oucif, C. (2019). The effects of interfacial strength on fractured microcapsule. *Frontiers of Structural and Civil Engineering*, 13(2), 353–363.
<https://doi.org/10.1007/s11709-018-0469-3>
- Mergheim, J., Possart, G., & Steinmann, P. (2012). Modelling and computation of curing and damage of thermosets. *Computational Materials Science*, 53(1).
<https://doi.org/10.1016/j.commatsci.2011.09.013>
- Mergheim, J., & Steinmann, P. (2013). Phenomenological modelling of self-healing polymers based on integrated healing agents. *Computational Mechanics*, 52(3).
<https://doi.org/10.1007/s00466-013-0840-0>
- Mihai, I. (2012). *Micromechanical constitutive models for cementitious composite materials, PhD thesis, Cardiff University*.
- Mihai, I. C., & Jefferson, A. D. (2011). A material model for cementitious composite materials with an exterior point Eshelby microcrack initiation criterion. *International Journal of Solids and Structures*, 48(24), 3312–3325.
<https://doi.org/https://doi.org/10.1016/j.ijsolstr.2011.08.001>
- Mihai, I. C., & Jefferson, A. D. (2013). Smoothed contact in a micromechanical model for cement bound materials. *Computers & Structures*, 118, 115–125.
<https://doi.org/https://doi.org/10.1016/j.compstruc.2012.11.002>
- Mihai, I. C., & Jefferson, A. D. (2017). A micromechanics based constitutive model for fibre reinforced cementitious composites. *International Journal of Solids and Structures*, 110–111, 152–169. <https://doi.org/https://doi.org/10.1016/j.ijsolstr.2017.01.032>

References

- Mori, T., & Tanaka, K. (1973). Average stress in matrix and average elastic energy of materials with misfitting inclusions. *Acta Metallurgica*, 21(5), 571–574. [https://doi.org/https://doi.org/10.1016/0001-6160\(73\)90064-3](https://doi.org/https://doi.org/10.1016/0001-6160(73)90064-3)
- Mura, T. (1982). Micromechanics of defects in solids. In *Micromechanics of defects in solids*. <https://doi.org/10.1007/978-94-011-9306-1>
- Nemat-Nasser, S., & Hori, M. (1993). *Micromechanics: overall properties of heterogeneous materials*. Elsevier.
- Nemat-Nasser, S., & Hori, M. (2013). *Micromechanics: overall properties of heterogeneous materials*. Elsevier.
- Němeček, J., Králík, V., & Vondřejc, J. (2013). Micromechanical analysis of heterogeneous structural materials. *Cement and Concrete Composites*, 36, 85–92. <https://doi.org/https://doi.org/10.1016/j.cemconcomp.2012.06.015>
- Nguyen-Sy, T., Nguyen, T.-K., Dao, V.-D., Le-Nguyen, K., Vu, N.-M., To, Q.-D., Nguyen, T.-D., & Nguyen, T.-T. (2020). A flexible homogenization method for the effective elastic properties of cement pastes with w/c effect. *Cement and Concrete Research*, 134, 106106. <https://doi.org/https://doi.org/10.1016/j.cemconres.2020.106106>
- Noghabai, K. (1999). Discrete versus Smeared versus Element-Embedded Crack Models on Ring Problem. *Journal of Engineering Mechanics*, 125(3). [https://doi.org/10.1061/\(asce\)0733-9399\(1999\)125:3\(307\)](https://doi.org/10.1061/(asce)0733-9399(1999)125:3(307))
- Ortiz, M. (1985). A constitutive theory for the inelastic behavior of concrete. *Mechanics of Materials*, 4(1). [https://doi.org/10.1016/0167-6636\(85\)90007-9](https://doi.org/10.1016/0167-6636(85)90007-9)
- Ortiz, M. (1988). Microcrack coalescence and macroscopic crack growth initiation in brittle solids. *International Journal of Solids and Structures*, 24(3). [https://doi.org/10.1016/0020-7683\(88\)90031-5](https://doi.org/10.1016/0020-7683(88)90031-5)
- Oucif, C., Voyiadjis, G. Z., Kattan, P. I., & Rabczuk, T. (2019). Investigation of the super healing theory in continuum damage and healing mechanics. *International Journal of Damage Mechanics*, 28(6). <https://doi.org/10.1177/1056789518799822>

References

- Pensée, V., Kondo, D., & Dormieux, L. (2002). Micromechanical Analysis of Anisotropic Damage in Brittle Materials. *Journal of Engineering Mechanics-Asce - J ENG MECH-ASCE*, 128. [https://doi.org/10.1061/\(ASCE\)0733-9399\(2002\)128:8\(889\)](https://doi.org/10.1061/(ASCE)0733-9399(2002)128:8(889))
- Petersson, P.-E. (1981). *Crack growth and development of fracture zones in plain concrete and similar materials*. Lund Inst. of Tech.(Sweden). Div. of Building Materials.
- Pichler, B., & Hellmich, C. (2011). Upscaling Quasi-Brittle Strength of Cement Paste and Mortar: A Multi-Scale Engineering Mechanics Model. *Cement and Concrete Research*, 41, 467–476. <https://doi.org/10.1016/j.cemconres.2011.01.010>
- Pichler, B., Hellmich, C., A. Mang, H., & Aaaa, A. (2007). A combined fracture-micromechanics model for tensile strain-softening in brittle materials, based on propagation of interacting microcracks. *International Journal for Numerical and Analytical Methods in Geomechanics*, 31(2), 111–132. <https://doi.org/https://doi.org/10.1002/nag.544>
- Ponnusami, S. A., Krishnasamy, J., Turteltaub, S., & van der Zwaag, S. (2018). A cohesive-zone crack healing model for self-healing materials. *International Journal of Solids and Structures*, 134. <https://doi.org/10.1016/j.ijsolstr.2017.11.004>
- Ponnusami, S. A., Krishnasamy, J., Turteltaub, S., & van der Zwaag, S. (2019). A micromechanical fracture analysis to investigate the effect of healing particles on the overall mechanical response of a self-healing particulate composite. *Fatigue and Fracture of Engineering Materials and Structures*, 42(2). <https://doi.org/10.1111/ffe.12929>
- Ponnusami, S. A., Turteltaub, S., & van der Zwaag, S. (2015). Cohesive-zone modelling of crack nucleation and propagation in particulate composites. *Engineering Fracture Mechanics*, 149, 170–190. <https://doi.org/https://doi.org/10.1016/j.engfracmech.2015.09.050>
- Ponte Castañeda, P. (2002). Second-order homogenization estimates for nonlinear composites incorporating field fluctuations: I—theory. *Journal of the Mechanics and Physics of Solids*, 50(4), 737–757. [https://doi.org/https://doi.org/10.1016/S0022-5096\(01\)00099-0](https://doi.org/https://doi.org/10.1016/S0022-5096(01)00099-0)

References

- Qian, Z. (2012a). Multiscale Modeling of Fracture Processes in Cementitious Materials. In *Civil engineering*.
- Qian, Z. (2012b). Multiscale Modeling of Fracture Processes in Cementitious Materials. *Human Molecular Genetics - HUM MOL GENET*.
- Qian, Z., Schlangen, E., Ye, G., & Van Breugel, K. (2017). Modeling Framework for Fracture in Multiscale Cement-Based Material Structures. In *Materials* (Vol. 10, Issue 6). <https://doi.org/10.3390/ma10060587>
- Qian, Z., Ye, G., Schlangen, E., & van Breugel, K. (2011). 3D Lattice Fracture Model: Application to Cement Paste at Microscale. *Key Engineering Materials*, 452–453, 65–68. <https://doi.org/10.4028/www.scientific.net/KEM.452-453.65>
- Quayum, Md. S., Zhuang, X., & Rabczuk, T. (2015). Computational model generation and RVE design of self-healing concrete. *Frontiers of Structural and Civil Engineering*, 9, 383–396. <https://doi.org/10.1007/s11709-015-0320-z>
- Rashid, Y. R. (1968). Analysis of prestressed concrete pressure vessels. *Nucl.Eng.Des.*, 7(484).
- Reuss, A. (1929). Berechnung der Fließgrenze von Mischkristallen auf Grund der Plastizitätsbedingung für Einkristalle . *ZAMM - Journal of Applied Mathematics and Mechanics / Zeitschrift Für Angewandte Mathematik Und Mechanik*, 9(1). <https://doi.org/10.1002/zamm.19290090104>
- Rodríguez, C. R., de Mendonça Filho, F. F., Mercuri, L., Gan, Y., Rossi, E., Anglani, G., Antonaci, P., Schlangen, E., & Šavija, B. (2020). Chemo-physico-mechanical properties of the interface zone between bacterial PLA self-healing capsules and cement paste. *Cement and Concrete Research*, 138. <https://doi.org/10.1016/j.cemconres.2020.106228>
- Rots, J. G., Nauta, P., Kusters, G. M. A., & Blaauwendraad, J. (1985). SMEARED CRACK APPROACH AND FRACTURE LOCALIZATION IN CONCRETE. *Heron*, 30(1).
- Sanahuja, J., Dormieux, L., & Chanvillard, G. (2007). Modelling elasticity of a hydrating cement paste. *Cement and Concrete Research*, 37(10), 1427–1439. <https://doi.org/https://doi.org/10.1016/j.cemconres.2007.07.003>

- Sanz-Herrera, J. A., Aliko-Benitez, A., & Fadrique-Contreras, A. M. (2019). Numerical investigation of the coupled mechanical behavior of self-healing materials under cyclic loading. *International Journal of Solids and Structures*, *160*, 232–246. <https://doi.org/https://doi.org/10.1016/j.ijsolstr.2018.10.029>
- Šavija, B., Farias, J., Polder, R., & Schlangen, E. (2012). *Lattice model as a tool for modelling transport phenomena in cement based composites*.
- Šavija, B., Feiteira, J., Araújo, M., Chatrabhuti, S., Raquez, J.-M., Van Tittelboom, K., Gruyaert, E., De Belie, N., & Schlangen, E. (2016). Simulation-Aided Design of Tubular Polymeric Capsules for Self-Healing Concrete. *Materials (Basel, Switzerland)*, *10*(1). <https://doi.org/10.3390/ma10010010>
- Sayadi, S., Ricketts, E., Schlangen, E., Cleall, P., Mihai, I., & Jefferson, A. (2023). Effect of microstructure heterogeneity shapes on constitutive behaviour of encapsulated self-healing cementitious materials. *MATEC Web of Conferences*, *378*. <https://doi.org/10.1051/mateconf/202337809004>
- Schimmel, E. C., & Remmers, J. J. C. (2006). Development of a constitutive model for self-healing materials. In *Delft Aerospace Computational Science, Report DACS-06-003*.
- Schlangen, E. (2022). M&S highlight: Schlangen and van Mier (1992), Simple lattice model for numerical simulation of fracture of concrete materials and structures. *Materials and Structures*, *55*(3), 95. <https://doi.org/10.1617/s11527-022-01932-w>
- Schlangen, E., & Garboczi, E. J. (1996). New method for simulating fracture using an elastically uniform random geometry lattice. *International Journal of Engineering Science*, *34*(10), 1131–1144. [https://doi.org/https://doi.org/10.1016/0020-7225\(96\)00019-5](https://doi.org/https://doi.org/10.1016/0020-7225(96)00019-5)
- Schlangen, E., & van Mier, J. G. M. (1992). Simple lattice model for numerical simulation of fracture of concrete materials and structures. *Materials and Structures*, *25*(9), 534–542. <https://doi.org/10.1007/BF02472449>
- Selvarajoo, T., Davies, R. E., Freeman, B. L., & Jefferson, A. D. (2020). Mechanical response of a vascular self-healing cementitious material system under varying loading

References

- conditions. *Construction and Building Materials*, 254. <https://doi.org/10.1016/j.conbuildmat.2020.119245>
- Selvarajoo, T., Davies, R. E., Gardner, D. R., Freeman, B. L., & Jefferson, A. D. (2020). Characterisation of a vascular self-healing cementitious material system: Flow and curing properties. *Construction and Building Materials*, 245. <https://doi.org/10.1016/j.conbuildmat.2020.118332>
- Sharma, M., & Bishnoi, S. (2020). Influence of properties of interfacial transition zone on elastic modulus of concrete: Evidence from micromechanical modelling. *Construction and Building Materials*, 246, 118381. <https://doi.org/https://doi.org/10.1016/j.conbuildmat.2020.118381>
- Shields, Y., De Belie, N., Jefferson, A., & Van Tittelboom, K. (2021). A review of vascular networks for self-healing applications. *Smart Materials and Structures*, 30(6), 063001. <https://doi.org/10.1088/1361-665x/abf41d>
- Shojaei, A., & Voyiadjis, G. Z. (2023). Statistical continuum damage healing mechanics (SCDHM). *International Journal of Damage Mechanics*, 32(6). <https://doi.org/10.1177/10567895231172537>
- Singla, A., Šavija, B., Sluys, L. J., & Romero Rodríguez, C. (2022). Modelling of capillary water absorption in sound and cracked concrete using a dual-lattice approach: Computational aspects. *Construction and Building Materials*, 320, 125826. <https://doi.org/https://doi.org/10.1016/j.conbuildmat.2021.125826>
- Subramanian, H., & Mulay, S. S. (2020). Continuum damage–healing-based constitutive modelling for self-healing materials: application to one-dimensional cyclic loading cases. *International Journal of Advances in Engineering Sciences and Applied Mathematics*, 12(1–2). <https://doi.org/10.1007/s12572-020-00266-6>
- van Breugel, K. (1995). Numerical simulation of hydration and microstructural development in hardening cement-based materials (I) theory. *Cement and Concrete Research*, 25(2). [https://doi.org/10.1016/0008-8846\(95\)00017-8](https://doi.org/10.1016/0008-8846(95)00017-8)
- Van der Giessen, E. (2019). Micromechanics & emergence in time. *European Journal of Mechanics, A/Solids*, 75. <https://doi.org/10.1016/j.euromechsol.2019.01.003>

References

- van Mier, J. G. M. (2012). Concrete fracture: A multiscale approach. In *Concrete Fracture: A Multiscale Approach*. <https://doi.org/10.1201/b12968>
- van Mier, J. G. M. (2017). Fracture Processes of Concrete. In *Fracture Processes of Concrete*. <https://doi.org/10.1201/b22384>
- Van Mier, J. G. M., & Van Vliet, M. R. A. (2001). Uniaxial tension test for the determination of fracture parameters of concrete: State of the art. *Engineering Fracture Mechanics*, 69(2). [https://doi.org/10.1016/S0013-7944\(01\)00087-X](https://doi.org/10.1016/S0013-7944(01)00087-X)
- Van Tittelboom, K., & De Belie, N. (2013). Self-healing in cementitious materials-a review. *Materials*, 6(6). <https://doi.org/10.3390/ma6062182>
- Vidya Sagar, R., Raghu Prasad, B. K., Nazreen, S., & Singh, R. K. (2019). Modeling mode-I fracture process in concrete at meso-scale: Computational aspects of lattice model and a comparison between results of two dimensional lattice simulation and acoustic emission measurements. *Engineering Fracture Mechanics*, 210, 257–278. <https://doi.org/https://doi.org/10.1016/j.engfracmech.2018.05.044>
- Voigt, W. (1889). Ueber die Beziehung zwischen den beiden Elasticitätsconstanten isotroper Körper. *Annalen Der Physik*, 274(12). <https://doi.org/10.1002/andp.18892741206>
- Voyiadjis, G. Z., Oucif, C., Kattan, P. I., & Rabczuk, T. (2022). Damage and Nonlinear Super Healing with Application to the Design of New Strengthening Theory. In *Handbook of Damage Mechanics: Nano to Macro Scale for Materials and Structures: Second Edition: Volume 1* (Vol. 1). https://doi.org/10.1007/978-3-030-60242-0_87
- Voyiadjis, G. Z., Shojaei, A., & Li, G. (2011). A thermodynamic consistent damage and healing model for self healing materials. *International Journal of Plasticity*, 27(7). <https://doi.org/10.1016/j.ijplas.2010.11.002>
- Voyiadjis, G. Z., Shojaei, A., Li, G., & Kattan, P. (2012). Continuum damage-healing mechanics with introduction to new healing variables. *International Journal of Damage Mechanics*, 21(3). <https://doi.org/10.1177/1056789510397069>
- Willam, K. J., & Carol. (2014). *DISCRETE VERSUS SMEARED CRACK ANALYSIS*. <https://api.semanticscholar.org/CorpusID:150376154>

References

- Wu, L., Meng, S., & Du, S. (1997). The overall response of composite materials with inclusions. *International Journal of Solids and Structures*, 34(23). [https://doi.org/10.1016/S0020-7683\(96\)00195-3](https://doi.org/10.1016/S0020-7683(96)00195-3)
- Wu, M., Johannesson, B., & Geiker, M. (2012). A review: Self-healing in cementitious materials and engineered cementitious composite as a self-healing material. In *Construction and Building Materials* (Vol. 28, Issue 1). <https://doi.org/10.1016/j.conbuildmat.2011.08.086>
- Xu, Y., Gan, Y., Chang, Z., Wan, Z., Schlangen, E., & Šavija, B. (2022). Towards understanding deformation and fracture in cementitious lattice materials: Insights from multiscale experiments and simulations. *Construction and Building Materials*, 345, 128409. <https://doi.org/https://doi.org/10.1016/j.conbuildmat.2022.128409>
- Xue, C., Li, W., Li, J., Tam, V. W. Y., & Ye, G. (2019). A review study on encapsulation-based self-healing for cementitious materials. *Structural Concrete*, 20(1). <https://doi.org/10.1002/suco.201800177>
- Yang, Q. S., Tao, X., & Yang, H. (2007). A stepping scheme for predicting effective properties of the multi-inclusion composites. *International Journal of Engineering Science*, 45(12). <https://doi.org/10.1016/j.ijengsci.2007.07.005>
- Zemskov, S. v, Jonkers, H. M., & Vermolen, F. J. (2011). Two analytical models for the probability characteristics of a crack hitting encapsulated particles: Application to self-healing materials. *Computational Materials Science*, 50(12), 3323–3333. <https://doi.org/https://doi.org/10.1016/j.commatsci.2011.06.024>
- Zhang, H., Šavija, B., Chaves Figueiredo, S., Lukovic, M., & Schlangen, E. (2016). Microscale Testing and Modelling of Cement Paste as Basis for Multi-Scale Modelling. In *Materials* (Vol. 9, Issue 11). <https://doi.org/10.3390/ma9110907>
- Zhang, H., Šavija, B., & Schlangen, E. (2018). Towards understanding stochastic fracture performance of cement paste at micro length scale based on numerical simulation. *Construction and Building Materials*, 183, 189–201. <https://doi.org/https://doi.org/10.1016/j.conbuildmat.2018.06.167>

References

- Zhang, W., Zheng, Q., Ashour, A., & Han, B. (2020). Self-healing cement concrete composites for resilient infrastructures: A review. In *Composites Part B: Engineering* (Vol. 189). <https://doi.org/10.1016/j.compositesb.2020.107892>
- Zhang, Y., & Zhuang, X. (2018). A softening-healing law for self-healing quasi-brittle materials: Analyzing with strong discontinuity embedded approach. *Engineering Fracture Mechanics*, *192*, 290–306. <https://doi.org/https://doi.org/10.1016/j.engfracmech.2017.12.018>
- Zhou, S., Jia, Y., & Wang, C. (2020). Global Sensitivity Analysis for the Polymeric Microcapsules in Self-Healing Cementitious Composites. *Polymers*, *12*, 2990. <https://doi.org/10.3390/polym12122990>
- Zhou, S., Zhu, H., Ju, J. W., Yan, Z., & Chen, Q. (2017). Modeling microcapsule-enabled self-healing cementitious composite materials using discrete element method. *International Journal of Damage Mechanics*, *26*(2). <https://doi.org/10.1177/1056789516688835>
- Zhou, S., Zhu, H., Yan, Z., Ju, J. W., & Zhang, L. (2016). A micromechanical study of the breakage mechanism of microcapsules in concrete using PFC2D. *Construction and Building Materials*, *115*, 452–463. <https://doi.org/https://doi.org/10.1016/j.conbuildmat.2016.04.067>
- Zhu, H., Zhou, S., Yan, Z., Ju, J. W., & Chen, Q. (2015). A two-dimensional micromechanical damage-healing model on microcrack-induced damage for microcapsule-enabled self-healing cementitious composites under tensile loading. *International Journal of Damage Mechanics*, *24*(1), 95–115. <https://doi.org/10.1177/1056789514522503>
- Zhu, H., Zhou, S., Yan, Z., Ju, J. W., & Chen, Q. (2016). A two-dimensional micromechanical damage–healing model on microcrack-induced damage for microcapsule-enabled self-healing cementitious composites under compressive loading. *International Journal of Damage Mechanics*, *25*(5), 727–749. <https://doi.org/10.1177/1056789516641593>
- Zhu, Q., Kondo, D., & Shao, J. (2008). Micromechanical analysis of coupling between anisotropic damage and friction in quasi brittle materials: Role of the homogenization

References

- scheme. *International Journal of Solids and Structures - INT J SOLIDS STRUCT*, 45, 1385–1405. <https://doi.org/10.1016/j.ijsolstr.2007.09.026>
- Zhu, Q. Z., Kondo, D., & Shao, J. F. (2009). Homogenization-based analysis of anisotropic damage in brittle materials with unilateral effect and interactions between microcracks. *International Journal for Numerical and Analytical Methods in Geomechanics*, 33(6), 749–772. <https://doi.org/https://doi.org/10.1002/nag.741>
- Zhu, Q. Z., & Shao, J. F. (2015). A refined micromechanical damage-friction model with strength prediction for rock-like materials under compression. *International Journal of Solids and Structures*, 60. <https://doi.org/10.1016/j.ijsolstr.2015.02.005>
- Zhu, Q. Z., Shao, J. F., & Kondo, D. (2011). A micromechanics-based thermodynamic formulation of isotropic damage with unilateral and friction effects. *European Journal of Mechanics - A/Solids*, 30(3), 316–325. <https://doi.org/https://doi.org/10.1016/j.euromechsol.2010.12.005>
- Zienkiewicz, O., Taylor, R., & Zhu, J. Z. (2013). The Finite Element Method: its Basis and Fundamentals: Seventh Edition. In *The Finite Element Method: its Basis and Fundamentals: Seventh Edition*. <https://doi.org/10.1016/C2009-0-24909-9>

Appendix A

Elastic tensors component

For an ideal Hookean solid, the elastic compliance tensors (**D**) assuming that the material is isotropic is derived from following equation using the Lamé constant (λ) and the shear modulus (μ).

$$\mathbf{D} = \lambda \mathbf{I}^2 \otimes \mathbf{I}^2 + 2\mu \mathbf{I}^{4s} \quad (\text{A.1})$$

where \mathbf{I}^2 and \mathbf{I}^{4s} are second order tensor and symmetric part of the fourth order identity tensor respectively. λ and μ are individually referred to as Lamé's constant. The following equation shows the calculation of \mathbf{I}^{4s} .

$$\mathbf{I}^{4s} = I_{ijkl}^{4s} = \delta_{ik}\delta_{jl} = 0.5(\delta_{ik}\delta_{jl} + \delta_{il}\delta_{jk}) + 0.5(\delta_{ik}\delta_{jl} - \delta_{il}\delta_{jk}) \quad (\text{A.2})$$

In this equation, the δ is the Kronecker delta, and i and j are the indices. The Kronecker delta is one if $i = j$ and is equal to zero if $i \neq j$.

In Matrix and vector notation (Voigt), the above tensor (**D**) in a 3D Cartesian coordinate may be presented in a 6x6 matrix as follows:

$$\mathbf{D} = \frac{E}{(1+\nu)} \begin{bmatrix} \frac{1-\nu}{1-2\nu} & \frac{\nu}{1-2\nu} & \frac{\nu}{1-2\nu} & 0 & 0 & 0 \\ & \frac{1-\nu}{1-2\nu} & \frac{\nu}{1-2\nu} & 0 & 0 & 0 \\ & & \frac{1-\nu}{1-2\nu} & 0 & 0 & 0 \\ & & & 0.5 & 0 & 0 \\ & & & & 0.5 & 0 \\ \text{sym} & & & & & 0.5 \end{bmatrix} \quad (\text{A.3})$$

Appendix B

Eshelby tensor

The constraint displacement field is expressed in terms of the Green's function of the elastic body as follows.

$$u_c(\mathbf{x}) = \int_{\Omega} \boldsymbol{\sigma} \cdot \mathbf{n}(\mathbf{x}') G(\mathbf{x}, \mathbf{x}') d\Omega \quad (\text{B.1})$$

Employing the strain derivation equation from displacement field ($0.5(\nabla u + \nabla u^T)$), lead to calculation of the constraint strain as follows.

$$\boldsymbol{\varepsilon}_c(\mathbf{x}) = 0.5 \int_{\Omega} [\boldsymbol{\sigma} \cdot \mathbf{n}(\mathbf{x}') \otimes \nabla G(\mathbf{x}, \mathbf{x}') + \boldsymbol{\sigma} \cdot \mathbf{n}(\mathbf{x}') \otimes \nabla G(\mathbf{x}, \mathbf{x}')^T] d\Omega \quad (\text{B.2})$$

Assuming a fourth order auxiliary tensor (\mathcal{C}) which relates the stress and displacement field gradient gives

$$\nabla u_c(\mathbf{x}) = -\mathcal{C} : \boldsymbol{\sigma} \quad (\text{B.3})$$

Substituting (B.3) in Eshelby's theory ($\mathbf{S} : \boldsymbol{\varepsilon} = \boldsymbol{\varepsilon}_c$) gives

$$\mathbf{S}(\mathbf{x}) = -0.5 \mathbf{D} \cdot (\mathcal{C} + \mathcal{C}^T) \quad (\text{B.4})$$

For a system with a spherical elastic inclusion, the Eshelby fourth order tensor is derived from following equation using Einstein notation

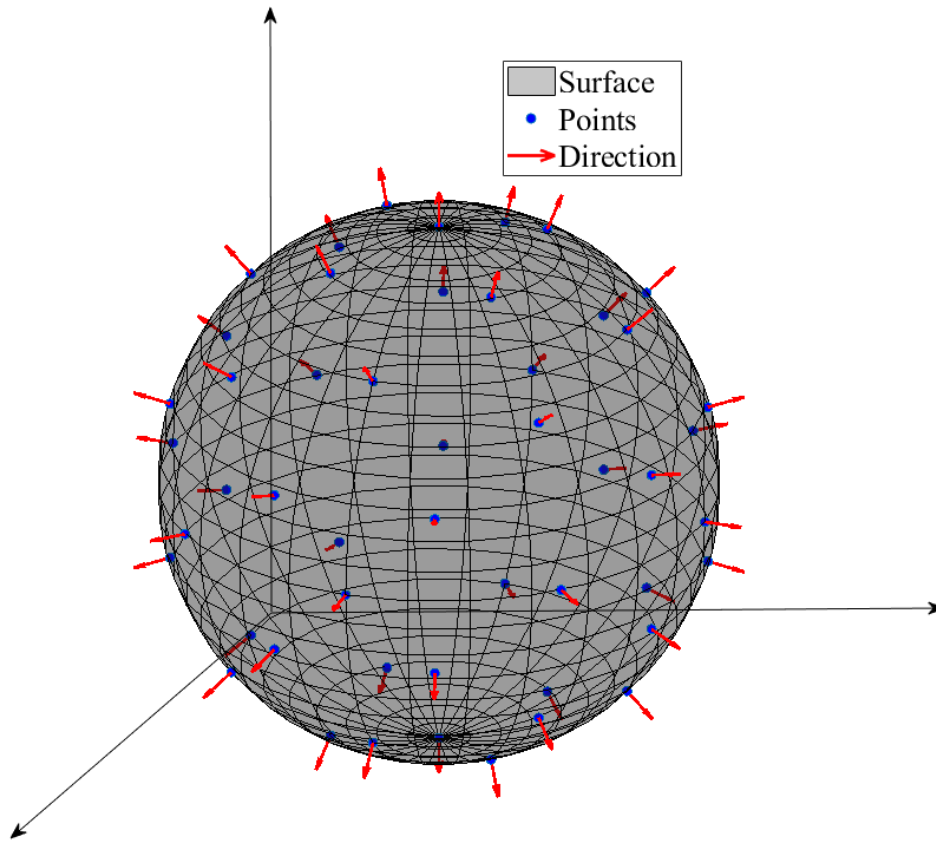
$$S_{ijkl} = \frac{5\nu - 1}{15(1 - \nu)} \delta_{ij} \delta_{kl} + \frac{4 - 5\nu}{15(1 - \nu)} (\delta_{ik} \delta_{jl} + \delta_{il} \delta_{jk}) \quad (\text{B.5})$$

Appendix C weights and corresponding direction for numerical integration

The following table shows the coordinates and the weights for the directional integration over the sphere. These coordinates and points are illustrated in Figure C-1.

Dir	(x,y,z)	weight	Dir	(x,y,z)	weight
1	(1,0,0)	0.0254	16	$(\frac{\sqrt{3}}{3}, \frac{\sqrt{3}}{3}, -\frac{\sqrt{3}}{3})$	0.04219
2	(0,1,0)	0.0127	17	$(\frac{\sqrt{3}}{3}, \frac{\sqrt{3}}{3}, \frac{\sqrt{3}}{3})$	0.04219
3	(0,0,1)	0.0127	18	$(\frac{\sqrt{11}}{11}, -\frac{\sqrt{11}}{11}, -\frac{3\sqrt{11}}{11})$	0.04035
4	(0,-1,0)	0.0127	19	$(\frac{\sqrt{11}}{11}, \frac{\sqrt{11}}{11}, -\frac{3\sqrt{11}}{11})$	0.04035
5	(0,0,-1)	0.0127	20	$(\frac{\sqrt{11}}{11}, -\frac{3\sqrt{11}}{11}, -\frac{\sqrt{11}}{11})$	0.04035
6	$(\frac{\sqrt{2}}{2}, -\frac{\sqrt{2}}{2}, 0)$	0.04515	21	$(\frac{\sqrt{11}}{11}, -\frac{3\sqrt{11}}{11}, \frac{\sqrt{11}}{11})$	0.04035
7	$(\frac{\sqrt{2}}{2}, \frac{\sqrt{2}}{2}, 0)$	0.04515	22	$(\frac{\sqrt{11}}{11}, -\frac{\sqrt{11}}{11}, \frac{3\sqrt{11}}{11})$	0.04035
8	$(0, -\frac{\sqrt{2}}{2}, -\frac{\sqrt{2}}{2})$	0.02257	23	$(\frac{\sqrt{11}}{11}, \frac{\sqrt{11}}{11}, \frac{3\sqrt{11}}{11})$	0.04035
9	$(0, -\frac{\sqrt{2}}{2}, \frac{\sqrt{2}}{2})$	0.02257	24	$(\frac{3\sqrt{11}}{11}, -\frac{\sqrt{11}}{11}, -\frac{\sqrt{11}}{11})$	0.04035
10	$(0, \frac{\sqrt{2}}{2}, -\frac{\sqrt{2}}{2})$	0.02257	25	$(\frac{3\sqrt{11}}{11}, -\frac{\sqrt{11}}{11}, \frac{\sqrt{11}}{11})$	0.04035
11	$(0, \frac{\sqrt{2}}{2}, \frac{\sqrt{2}}{2})$	0.02257	26	$(\frac{3\sqrt{11}}{11}, \frac{\sqrt{11}}{11}, -\frac{\sqrt{11}}{11})$	0.04035
12	$(\frac{\sqrt{2}}{2}, 0, -\frac{\sqrt{2}}{2})$	0.04515	27	$(\frac{3\sqrt{11}}{11}, \frac{\sqrt{11}}{11}, \frac{\sqrt{11}}{11})$	0.04035
13	$(\frac{\sqrt{2}}{2}, 0, \frac{\sqrt{2}}{2})$	0.04515	28	$(\frac{\sqrt{11}}{11}, \frac{3\sqrt{11}}{11}, -\frac{\sqrt{11}}{11})$	0.04035
14	$(\frac{\sqrt{3}}{3}, -\frac{\sqrt{3}}{3}, -\frac{\sqrt{3}}{3})$	0.04219	29	$(\frac{\sqrt{11}}{11}, \frac{3\sqrt{11}}{11}, \frac{\sqrt{11}}{11})$	0.04035
15	$(\frac{\sqrt{3}}{3}, -\frac{\sqrt{3}}{3}, \frac{\sqrt{3}}{3})$	0.04219			

(a)



(b)

Figure C-1 Schematic numerical points, a) 3D figure, b) direction and weight for numerical integration

Appendix D

Tensorial notation

The following tensorial notation (Table D-1) is used in continuum mechanics, damage continuum mechanics and micromechanical approaches. The equivalent Einstein summation convention is mentioned. In this table α is a scalar, \mathbf{a} and \mathbf{b} are first order tensors, \mathbf{A} , \mathbf{B} and \mathbf{C} are second order tensors; \mathbf{D} , \mathbf{E} and \mathbf{F} are fourth order tensors.

Table D-1 Tensorial notation

Direct tensor notation	Summation convention	Operation symbol
$\mathbf{A} = \mathbf{a} \otimes \mathbf{b}$	$\mathbf{A}_{ij} = \mathbf{a}_i \mathbf{b}_j$	\otimes is dyadic product
$\mathbf{D} = \mathbf{A} \otimes \mathbf{B}$	$\mathbf{D}_{ijkl} = \mathbf{A}_{ij} \mathbf{B}_{kl}$	
$\alpha = a \cdot b$	$\alpha = a_i b_i$	\cdot is dot product
$\mathbf{C} = \mathbf{A} \cdot \mathbf{B}$	$\mathbf{C}_{ik} = \mathbf{A}_{ij} \mathbf{B}_{jk}$	
$\mathbf{F} = \mathbf{D} \cdot \mathbf{E}$	$\mathbf{F}_{ijmn} = \mathbf{D}_{ijkl} \mathbf{E}_{klmn}$: is tensor contraction
$\alpha = \mathbf{A} : \mathbf{B}$	$\alpha = \mathbf{A}_{ij} \mathbf{B}_{ij}$	
$\mathbf{B} = \mathbf{D} : \mathbf{A}$	$\mathbf{B} = \mathbf{D}_{ijkl} \mathbf{A}_{kl}$	